SCINTILLATOR PURIFICATION AND STUDY OF LIGHT PROPAGATION IN A LARGE LIQUID SCINTILLATION DETECTOR

Michael Clinton Johnson

A DISSERTATION

PRESENTED TO THE FACULTY

OF PRINCETON UNIVERSITY

IN CANDIDACY FOR THE DEGREE

OF DOCTOR OF PHILOSOPHY

RECOMMENDED FOR ACCEPTANCE

BY THE DEPARTMENT OF

CHEMICAL ENGINEERING

June 1998

ABSTRACT

The Counting Test Facility (CTF) was a large-scale liquid scintillation detector which contained 4.8 m^3 of organic liquid scintillator. The CTF was designed to test some concepts important to the successful operation of the Borexino experiment prior to its construction. Borexino is planned as a larger detector containing 300 m^3 of scintillator, and it will be used for the detection of solar neutrinos. This thesis is concerned with two of these concepts: the ability to measure the radiopurity level of a liquid scintillator and improve it if necessary and the need to understand light propagation in the scintillator.

The work in this thesis concerning scintillator purity centers on the design, construction, and operation of a pilot-sized purification plant. This plant was designed to remove radioactive contamination and optical impurities from the scintillator if initial concentrations were too great. The plant employed water extraction, nitrogen stripping, distillation, and filtration for this purification. The CTF was able to place stringent enough limits on the ^{238}U, ^{232}Th, and ^{14}C concentrations in the scintillator that the Borexino project could proceed. The purification system was very effective at removing ^{85}Kr and ^{210}Po from the scintillator, and other unidentified impurities were also removed.

This thesis was also concerned with the study of light propagation in large scintillation detectors. It is important to understand the mechanisms of light propagation in a large scintillation detector in order to predict the detector's performance. For this thesis, light propagation was studied in three scintillator mixtures: pseudocumene, PPO-pseudocumene, and bis-MSB-PPO-pseudocumene. These investigations utilized milliliter-sized samples in commercial spectrophotometers and limited aperture radon sources in the CTF detector. The

experiments showed that scattering occurs in the scintillator due to absorption and reemission of light by scintillator components and Rayleigh scattering in the solvent. Monte Carlo simulation using parameters determined in measurements with milliliter-sized samples was also used to examine light scattering. The simulated results agreed well with the experimental ones, confirming that Monte Carlo simulation is an effective means of extrapolating small-scale measurements for application to a large scintillation detector.

ACKNOWLEDGMENTS

The completion of this thesis would not have been possible without the assistance of several people during my time at Princeton. First I would like to thank my adviser Jay Benziger for guiding my studies and showing me what is required in order to conduct effective research while allowing me the freedom to develop these abilities on my own. My friends and colleagues in the Princeton group of the Borexino collaboration were invaluable, and this work would have been impossible without them: Mark Chen, Fred Loeser, Nick Darnton, Laura Cadonati, Bruce Vogelaar, Cynthia Murphy, and Frank Calaprice. I would also like to thank Albert Young for his assistance with the decay time measurements. My friends Rob, Dan, Doug, and Jill, and my sister Hydee have contributed to this thesis by helping me maintain a positive attitude during my graduate school career. Finally, I want to thank my parents for their support, especially while I was writing my thesis.

Lasciate ogne speranza, voi ch'intrate.

Dante *The Divine Comedy: Inferno* III.9.

TABLE OF CONTENTS

LIST OF FIGURES

Chapter 7

LIST OF TABLES

CHAPTER 1: INTRODUCTION

The work presented in this thesis is part of the larger efforts of the Borexino collaboration. The Borexino collaboration is a multi-national group of over fifty scientists, and its largest manpower and financial resources come from Italy, Germany, and the United States. The goal of the collaboration is to construct and operate the Borexino solar neutrino detector. Borexino is a large liquid scintillation detector which will contain 300 tons of liquid scintillator. When radiation impinges on the scintillator of a scintillation detector, it causes the emission of scintillation light. This light is received by phototubes surrounding the scintillator and the incident radiation is thereby detected. Borexino is designed specifically to detect solar neutrinos, and the details of the experiment are considered in Chapter 2 of this thesis.

Because of the size and complexity of Borexino, its construction requires a large investment of personnel and economic resources. A smaller prototype of Borexino, the Counting Test Facility (CTF), was built to test several concepts crucial to the success of the larger experiment without requiring so large an expense. The CTF was a five ton liquid scintillation detector. Construction of Borexino is continuing based on the successful resolution of several questions by the CTF. These questions include the ability of a liquid scintillator to meet stringent requirements for radioactive and optical purity and the need to ensure that light propagation inside a large scintillation detector allows the position of scintillation events inside the detector to be pinpointed.

The CTF not only served as a prototype of Borexino, but it was an important experiment in its own right. The CTF allowed measurement of radioactivity at low levels unattainable with other instruments. It also allowed the measurement of light propagation on a longer distance scale than is possible with commercial devices. The

work described in this thesis was performed as part of the CTF program. It can be divided into two major segments: purification of the scintillator and understanding the propagation of light inside it.

The purity of the liquid scintillator was a major concern of the CTF. The scintillator needed to be free of both radioactive and optical impurities. The CTF was designed to demonstrate that a liquid scintillator could meet the stringent purity requirements and that this purity could be maintained over a period of years. The scintillator was examined as it was received and purification operations were carried out to improve its purity. Construction of a pilot-sized plant for this purification required a major effort by the Princeton group of the collaboration. The assembly and operation of this plant are discussed in Chapter 3. The successful removal of contaminants from the scintillator and the ultimate purity levels obtained are detailed. The scintillator is shown to meet the purity requirements of Borexino.

The other major part of this thesis deals with light propagation in the scintillator. The study of light propagation involves tracking the scintillation photons from their point of emission until they are either lost or detected at the phototubes. Knowledge of light propagation is very important in the CTF and Borexino because it can affect positional reconstruction and α-β separation in the detectors. As explained in Chapter 2, these techniques are used to reduce the radioactive background. Positional reconstruction allows the location of an event in the detector to be pinpointed. Events in the outer portion of the scintillator can be discarded and this region can be used as shielding so that the background rate in the inner portion of the scintillator is extremely low. Positional reconstruction is based on measuring the difference in the times of flight of photons from the event to phototubes in various locations. It is most accurate when the photons travel directly from the event to the phototubes. If they are scattered, that is undergo a change in direction, they will take

longer to arrive at a given phototube than the distance from the event location to the phototube requires. This causes inaccuracy in the reconstruction. Identification of α scintillation events reduces the background in the detector because neutrino events have a β signature and the α events can be discarded. The separation of α and β events is also based on the arrival time of photons at the phototubes. Emission following α excitation results in more photons at long times than does that from β excitation. Light scattering lengthens photon flight paths and makes differentiation between the two types of events more difficult.

Because of the importance of understanding how much scattering takes place in the scintillator and what mechanisms cause this scattering, this thesis concentrates on these subjects. Theoretical background on the emission and scattering of light in a liquid scintillator is covered in Chapter 4. Light propagation in the scintillator is studied in several ways. Small-scale measurements made using milliliter-sized samples with commercially available absorption and fluorescence spectrophotometers are reported in Chapter 5. The optical properties of liquid scintillators are commonly measured in this manner. This chapter examines what the small-scale measurements really tell us about the scintillator. Through comparison of absorption and elastic scattering results, it is shown that apparent absorption at wavelengths outside the main absorption band of a compound is due to elastic scattering. This has important implications for light propagation in a large scintillation detector because light at these wavelengths is never lost and only undergoes changes of direction in the scintillator. Based on the investigations in Chapter 5, it is concluded that the major scattering mechanisms in a liquid scintillator are absorption of light by scintillator components followed by its isotropic reemission and elastic Rayleigh scattering by the scintillator solvent.

Although measurements like those described in Chapter 5 are certainly accurate for the small samples with which they are performed, application of these measurements to the prediction of light propagation in a large detector is not necessarily straightforward. Scattering and absorption effects which are negligible at a distance of 1 cm (the size of the sample cuvettes in the small-scale measurements) may become important at distances of 1 – 2 m (the size of the CTF). The CTF provided a unique opportunity to examine light propagation on a large distance scale. Chapter 6 describes the insertion of limited aperture radon sources into the CTF so that light scattering in the detector could be measured. Light could only escape from the limited aperture of the sources. Phototubes viewing the opaque portion of the source could only receive light if it was scattered, while those viewing the clear aperture received direct and scattered light. By comparing the amounts of light received by the two classes of phototubes, the amount of scattering in the detector is quantified.

Monte Carlo simulation has been proposed as a method to apply small-scale scintillator optical property measurements to the prediction of the behavior of a large detector. The light scattering data collected in the CTF provides a means to test this ability of the simulation. In Chapter 7, a Monte Carlo is used to predict the light propagation in the CTF. Input parameters for the simulation are obtained from small-scale measurements described in Chapter 5. The simulation is able to accurately model the light propagation in the detector and reproduce the experimental light scattering results of Chapter 6. This success confirms that Monte Carlo simulation is an effective means to scale scintillator optical properties measured on a small-scale for use in large detectors.

The main conclusions of this thesis can be summarized as follows: Organic liquid scintillators inherently contain low concentrations of radioactive impurities, and

these concentrations can be reduced further by appropriate purification operations. Scattering of light in a liquid scintillator is caused by absorption and reemission of light by scintillator components on a short distance scale and by Rayleigh scattering in the scintillator solvent on a longer distance scale. Monte Carlo simulation is an effective means of utilizing small-scale scintillator optical property measurements to predict light propagation in large detectors. These conclusions are discussed in greater detail in the bulk of this thesis, and data are presented to support them.

CHAPTER 2: SOLAR NEUTRINOS, BOREXINO, AND THE CTF

Borexino is a solar neutrino experiment. Neutrinos are particles produced in some nuclear reactions. Among these reactions are some of those which occur during nuclear fusion in the sun. By measuring the flux of solar neutrinos reaching the earth, we can learn more about the mechanism of those fusion reactions. Borexino is not the first solar neutrino experiment; existing solar neutrino detectors have measured a solar neutrino flux less than that predicted by current solar models. This is referred to as the "solar neutrino problem".

Borexino can play an important role in increasing our understanding of this "problem" because of its ability to measure ^{7}Be neutrinos at a "high" rate. The heart of the Borexino detector is a 100 ton fiducial volume of organic liquid scintillator. The scattering of electrons in the scintillator by neutrinos will result in scintillation which will be detected by an array of photomultiplier tubes surrounding the fiducial volume. Light emission in the scintillator is also caused by other ionizing radiation (e.g. γ-rays, radioactive decay, etc.). The background due to other sources must be extremely low so as not to overwhelm the neutrino signal.

In order to test the radiopurity of the scintillator to be used in Borexino, the Counting Test Facility (CTF) was constructed. This low-level counting experiment consists of 5 tons of organic scintillator viewed by 100 phototubes. In addition to providing a way to measure the radioactivity inherent in a liquid organic scintillator, purification procedures to reduce the background were also tested. The CTF also served as a tool to measure the optical properties of the organic scintillator. These scintillation decay time and light scattering properties are of critical importance because one of the main techniques for background reduction is through the use of positional reconstruction of events. By measuring the time of flight of photons from an event to

various phototubes, the location of the event can be determined. Deviations from direct photon flight paths between an event and the phototubes degrade the positional resolution of the detector, and thus the ability to discern true neutrino events from background. Because of this, the knowledge of how light propagates through the scintillator is of crucial importance.

A. Solar Neutrinos

The existence of neutrinos was first hypothesized by Pauli in 1930 to provide a means for spin and angular momentum conservation in reactions such as

$$^{14}C \rightarrow {}^{14}N + e^- + \bar{\nu}_e \qquad (2.1)$$

where $\bar{\nu}_e$ is an antineutrino. The hypothetical particle had a spin of 1/2 to balance that of the electron in eq 2.1. Neutrino existence was validated in 1934 by Fermi's quantitative theory of β-decay, and they were first detected experimentally in 1956.[1] Neutrinos are produced in β^+-decay, and antineutrinos are produced in β^--decay.

Neutrinos interact with other matter through weak nuclear forces. (The other types of interactions known to exist are gravitational, electromagnetic, and strong nuclear forces.) There are three flavors of neutrinos and antineutrinos – electron, muon, and tauon (ν_e, ν_μ, and ν_τ). The neutrino-electron reaction cross-sections for the three neutrino flavors at the energy of interest for Borexino have been calculated to be 59.3×10^{-46} cm^2 for electron neutrinos and 12.6×10^{-46} cm^2 for muon and tauon neutrinos.[2] For comparison, the reaction cross section between a proton and a neutron, which interact through the strong nuclear force, is approximately 10^{-24} cm^2. The neutrino flavors differ in their reaction cross-sections with an electron. The electron neutrino has a larger cross-section because it can interact through a charged current interaction involving exchange of a $W^\pm$ boson as well as a neutral current interaction

involving a Z^0 boson. The other flavors can only react through neutral current interactions.

Since their discovery, neutrinos have become important in the study of solar fusion. Mankind has been interested in the sun, the source of earth's energy, for ages. Although many explanations have been presented for the sun's energy production mechanism, it was only with the discovery of nuclear fusion in the early twentieth century that a viable hypothesis was produced. This current theory holds that the sun, and the other stars as well, are fueled by nuclear fusion taking place in their cores.[3]

A standard solar model (SSM) has been developed to describe the reactions taking place in the sun. This model consists of numerous differential equations which describe the nuclear reactions which produce energy in the core of the sun, the transport of this energy to its outer regions, and the hydrostatic equilibrium of the sun whereby the gravitational forces affecting it are exactly balanced by internal radiative and particle pressures to keep it from collapsing on itself. These equations are solved numerically to predict a profile of conditions throughout the sun. Input data for these calculations include initial chemical abundances in the sun and the radiative opacity of the sun which are deduced by solar astronomy and an equation of state which relates pressure and density. The SSM makes many predictions about occurrences in the core of the sun. Neutrinos, because of their weak interactions, can travel unabated from the solar core to earth, where we can measure them. Through measurement of the solar neutrino flux, we can learn about conditions in the solar core and make comparisons with those predicted by the SSM.

Neutrinos are produced in the solar core by nuclear reactions. The major source of solar energy is believed to be through the fusion of hydrogen to helium. Because of the incredibly high temperatures which exist in the sun's core, matter exists there in a plasma state, where all atoms are ionized and hydrogen exists in the form of protons.

Several steps exist in the fusion process which converts four protons into a helium nucleus. One process by which this occurs is known as the pp chain (for proton-proton) and the reactions which occur in it are shown in Table 2.1. It can be seen that neutrinos are products of several of these reactions, and that these neutrinos have different energies depending on the reaction in which they are produced. The relative number of neutrinos produced in these reactions are also shown in Table 2.1 as termination percentages. The largest number of neutrinos comes from the pp reaction. These neutrinos possess a range of energies, with a maximum energy of 0.42 MeV. Neutrinos are also produced in reactions involving ^{7}Be. These particles have discrete energies of either 0.861 MeV (90%) or 0.383 MeV (10%). Higher energy neutrinos are produced by the pep reaction. These neutrinos are easier to detect, but their flux is lower. The highest energy neutrinos are produced in ^{8}B and hep reactions, but these reactions are rather rare as can be seen in Table 2.1. The standard solar model predicts the neutrino production expected in the solar core. By knowing the interaction cross section with matter here on earth, the number of solar neutrinos detected on earth by a neutrino detector can be predicted. Expected neutrino fluxes on earth calculated from the SSM are listed in Table 2.2.

The standard solar model has been tested through the measurement of solar neutrinos. The first solar neutrino experiment[4] was constructed at the Homestake Gold Mine in South Dakota in the 1960's. This experiment detects neutrinos through the reaction

$$\nu_e + {}^{37}\mathrm{Cl} \rightarrow e^- + {}^{37}\mathrm{Ar} \qquad (2.2)$$

The threshold energy for this reaction is 0.814 MeV; all neutrinos with energies greater than the threshold can be detected. All the solar neutrino types except the pp variety can be detected through this reaction, but the detector is primarily sensitive to ^{8}B neutrinos. The experiment is located in an old mine, approximately one mile under the earth's

Table 2.1. The pp chain in the sun. The average number of pp neutrinos produced per termination in the sun is 1.85. For all other neutrino sources, the average number of neutrinos produced per termination is equal to (the termination percentage / 100).

Reaction	(neutrino nomenclature)	Termination† (%)	ν energy (MeV)
$p + p \rightarrow {}^2H + e^+ + \nu_e$	(pp)	100	≤ 0.420
or			
$p + e^- + p \rightarrow {}^2H + \nu_e$	(pep)	0.4	1.442
${}^2H + p \rightarrow {}^3He + \gamma$		100	
${}^3He + {}^3He \rightarrow \alpha + 2\,p$		85	
or			
${}^3He + {}^3He \rightarrow {}^7Be + \gamma$		15	
${}^7Be + e^- \rightarrow {}^7Li + \nu_e$	(^{7}Be)	15	(90%) 0.861 (10%) 0.383
${}^7Li + p \rightarrow 2\,\alpha$		15	
or			
${}^7Be + p \rightarrow {}^8B + \gamma$		0.02	
${}^8B \rightarrow {}^8Be^* + e^+ + \nu_e$	(^{8}B)	0.02	< 15
${}^8Be^* \rightarrow 2\,\alpha$		0.02	
or			
${}^3He + p \rightarrow {}^4He + e^+ + \nu_e$	(hep)	0.00002	≤ 18.77

†The termination percentage is the fraction of terminations of the pp chain, $4p \rightarrow a + 2e^+ + 2\nu_e$, in which each reaction occurs. The results are averaged over the model of the current sun. Since in essentially all terminations at least one pp neutrino is produced and in a few terminations one pp and one pep neutrino are created, the total of pp and pep terminations exceeds 100%. From Bahcall.[2]

Table 2.2. Calculated solar neutrino fluxes. From Bahcall.[2]

Source	Flux (10^{10} cm^{-2} s^{-1})
pp	6.0 (1 ± 0.02)
pep	0.014 (1 ± 0.05)
hep	8×10^{-7}
^{7}Be	0.47 (1 ± 0.15)
^{8}B	5.8×10^{-4} (1 ± 0.37)
^{13}N	0.06 (1 ± 0.50)
^{15}O	0.05 (1 ± 0.58)
^{17}F	5.2×10^{-4} (1 ± 0.46)

surface. It was constructed there because the rock above it provides shielding from cosmic rays which can also produce ^{37}Ar. This need for shielding from cosmic radiation (as well as other radioactivity) is common to all solar neutrino experiments. The experiment consists of a large tank of perchloroethylene (C_2Cl_4). When chlorine atoms are struck by neutrinos, argon is formed as in eq 2.2. This gaseous argon is extracted, and used to calculate the neutrino flux. Periods of time on the order of one to three months are required in order to generate an amount of argon gas sufficient for measurement.

The Homestake (or Chlorine) experiment has operated for more than two decades and enough data has been obtained for good statistical reliability. The results have consistently shown about one-third the expected number of solar neutrinos. This can be seen in Figure 2.1, where the number of neutrinos expected based on the standard solar model is shown along with the number of neutrinos detected in several runs of the experiment. In this figure the ordinate is labeled in terms of SNU (Solar Neutrino Unit), which has units of events per target atom per second and is defined so that one SNU equals 10^{-36} s^{-1}. This discrepancy between the observed and predicted neutrino fluxes has come to be known as the "solar neutrino problem".

Many explanations have been proposed for this difference between theory and experiment. Some have involved modifications to the standard solar model. These modifications include enhanced elemental diffusion, convective instabilities, or a solar interior greatly deficient in heavy elements. None of these modifications have successfully resolved the matter. Experimental support of the SSM has also come from recent helio-seismology measurements.[5] The neutrino interaction cross-sections have been checked by many researchers. The cross-sections could still be incorrect because of the types of measurements involved in checking them, but this is unlikely. A

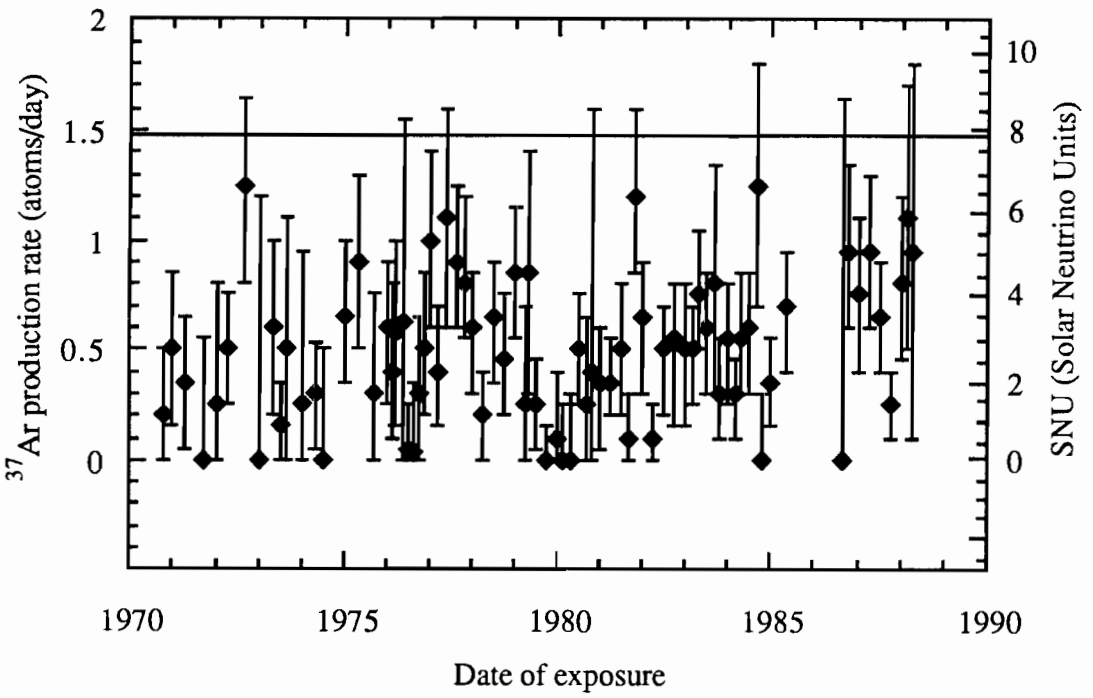

Figure 2.1. Observational results from the chlorine solar neutrino experiment. This figure shows the results from several runs of the chlorine experiment and includes statistical error bars for the points. The line at 7.9 SNU represents the prediction of the SSM. For more detail see the articles by Davis.[6,7] From Bahcall.[2]

remaining possibility is the existence of new physics which is not accounted for in the current predictions.

One type of new physics under consideration is the MSW effect[8] (for Mikhayev, Smirnov, and Wolfenstein), which hypothesizes interconversion between the various neutrino flavors. This conversion would change some of the electron neutrinos into the less easily detectable tauon and muon neutrinos, and it could explain the observed discrepancy. The interconversion would be caused by oscillations between different mass eigenstates of the neutrino, and neutrinos must have mass if these oscillations are to occur. The standard model of electroweak interactions predicts that neutrinos are massless, and if the MSW effect can be shown to exist, it will require a revision of the standard model. Experiments have been performed to measure the neutrino mass, but have only resulted in upper limits being put on this mass.

As the Homestake experiment continues to collect data, other solar neutrino experiments are in operation and even more are planned. Two experiments are based on the interaction of neutrinos with gallium in the following reaction.

$$\nu_e + {}^{71}\mathrm{Ga} \rightarrow e^- + {}^{71}\mathrm{Ge} \qquad (2.3)$$

The threshold energy of this reaction is 0.233 MeV, so all types of neutrinos produced in the pp chain can be detected. The GALLEX experiment,[9] which began operation in 1990, is located in the Labotatori Nazionali del Gran Sasso (LNGS) in Italy. These laboratories are located under the Appenine Mountains to provide cosmic ray shielding. In GALLEX, the gallium is present in the form of an aqueous solution of gallium chloride. The germanium produced by neutrino interactions forms the volatile compound $GeCl_4$ and can be extracted from the gallium chloride liquid and counted to provide a measure of the neutrino flux. Several runs of one to three months duration have allowed GALLEX to obtain good statistical error estimates on the experimental data. The SAGE experiment[10] (Soviet-American Gallium Experiement) uses metallic

gallium for neutrino detection. This experiment is located underground in the Baksan Neutrino Observatory in Russia. Several data runs have also been completed in this experiment, in which germanium produced through neutrino interactions is extracted through a complicated procedure and counted to measure the neutrino flux.

Another solar neutrino detector which saw operation was the Kamiokande experiment,[11] located in the Kamioka Mine under the Japanese Alps. This detector did not rely on a nuclear reaction as the chlorine and gallium experiments do, but detected the particles through neutrino-electron scattering in a water target. If the scattered electrons have a velocity greater than c/n, where c is the speed of light and n is the refractive index of water, Čerenkov light is produced. High energy neutrinos can scatter electrons with sufficient velocity to produce Čerenkov light, which was detected with phototubes. Kamiokande was mostly sensitive to ^{8}B neutrinos. The experiment began operation in 1985 and collected data for several years. Another similar experiment has just been constructed at the same location. This experiment is much larger, and is known as Superkamiokande.[12] It should produce results on the solar neutrino flux in early 1998. Another detector based on detection of Čerenkov light is under construction in the Sudbury Mine in Canada. The SNO experiment[13] (Sudbury Neutrino Observatory) will detect Čerenkov light from ultrapure heavy water (D_2O) and will begin data collection in 1998.

These other solar neutrino experiments have provided additional measurements of the solar neutrino flux, and none of them has observed as many neutrinos as the standard solar model predicts it should. The gallium experiements have reported a flux of 0.54 ± 0.12 the expected amount, and in Kamiokande 0.50 ± 0.10 of the expected flux was observed.[14]

None of the solar neutrino experiments discussed above has been designed to specifically detect the ^{7}Be neutrinos. The measurement of the ^{7}Be neutrino flux is

important because one conclusion consistent with all the experimental solar neutrino data collected thus far is the almost complete suppression of the ^{7}Be neutrino flux on earth. Such a suppression is possible under the MSW hypothesis because neutrinos of different energies have different probabilities of flavor conversion. The Borexino solar neutrino experiment has been designed to measure the ^{7}Be neutrino flux using a liquid scintillation detector. The work described in this thesis has been undertaken as part of the Borexino experiment.

B. The Borexino Experiment

Borexino was first conceptualized in 1987. At that time, the experiment was visualized in terms of using a tri-methylborate scintillator to detect solar neutrinos. The consideration of this substance resulted in the name Borexino. The tri-methylborate was later dropped from consideration, and by 1991 design work was being carried out for Borexino as a liquid organic scintillation detector. Borexino has been designed with the specific goal of detecting ^{7}Be solar neutrinos. Construction of Borexino began in 1996 and early results should be available by 2001. Several tests have been performed to prove the viability of the Borexino concept. The most important of these has been the operation of the Counting Test Facility (CTF), which will be discussed in more detail in a separate section.

Borexino is a liquid scintillator detector. Liquid scintillation detectors have been used for decades to measure radioactivity, although Borexino extends the concept to a much larger scale than that of a normal scintillation detector. In scintillation detectors, impinging radiation causes excitation of the scintillator solvent. The solvent then transfers this excitation energy to one or more solutes (or fluors) which release the energy as ultraviolet or visible light with a high efficiency. This light is monitored by detectors surrounding the scintillator and provides a measure of the incident radiation.

Borexino will contain 300 tons of liquid scintillator in a transparent spherical vessel eight meters in diameter, of which 100 tons will be defined as a fiducial voume. This scintillator containment vessel will be surrounded by shielding liquid and viewed by approximately 2000 photo-multiplier tubes (PMTs). The scintillator solvent will be an aromatic liquid, 1,2,4-trimethyl benzene (pseudocumene or PC). The fluor will be 2,5-diphenyloxazole (PPO) at a concentration of approximately 1.5 g/L, with the possible addition of a second fluor, bis-methylstyrylbenzene (bis-MSB), at a concentration of approximately 20 mg/L. The shielding liquid will be a combination of high-purity water and pseudocumene in two separate shells, as seen in Figure 2.2, a schematic diagram of Borexino. The scintillator containment vessel is surrounded by a pseudocumene buffer. This buffer is contained inside a stainless steel sphere which is immersed in high-purity water.

In Borexino neutrinos will be detected through electron-neutrino scattering. Neutrinos can interact with electrons in the scintillator solvent. This electron-neutrino scattering causes the ejection of electrons from the solvent molecules and the ejected electrons act as β-particles in the scintillator. An electron receives the largest possible amount of energy from the neutrino if the neutrino recoils backwards after the collision. In all other cases, the electron will receive less energy. A measure of the energy transferred to the electron can be obtained by monitoring the amount of light produced in the scintillator. Electrons ejected through scattering by neutrinos with a discrete energy, such as the ^{7}Be neutrinos, will have a variety of energies, but there will be a Compton-like edge in their energy spectrum corresponding to an elastic collision. This edge can be seen at 0.66 MeV in the calculated spectrum for 0.881 MeV ^{7}Be neutrinos shown in Figure 2.3. In an elastic collision, the neutrino recoils directly backwards with an energy of 0.221 MeV while the electron has 0.66 MeV imparted to it. The appearance of this edge will be important in the confirmation of candidate neutrino events. The the

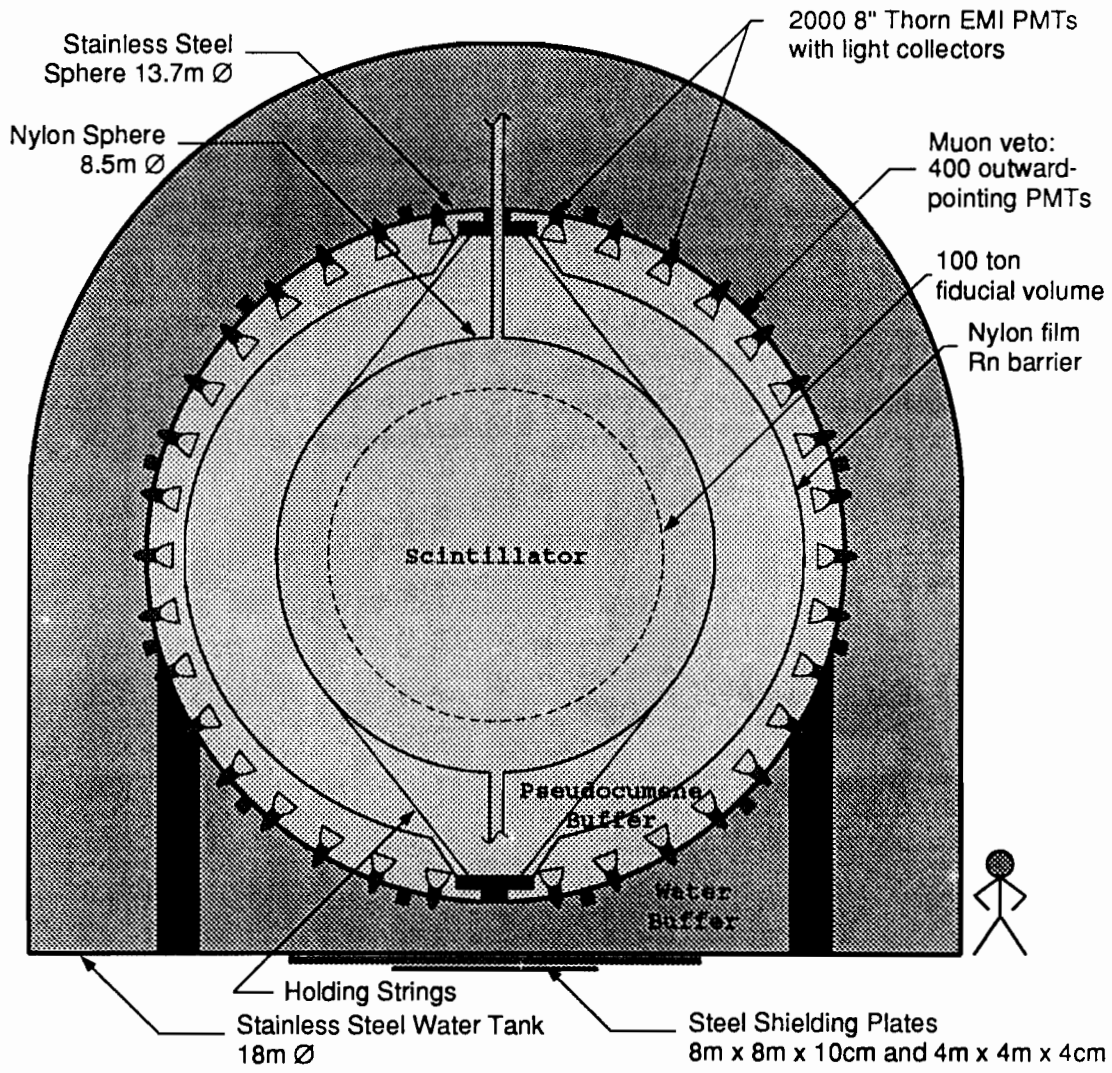

Figure 2.2. Schematic diagram of Borexino. The important conceptual pieces of Borexino are shown here, including the nylon scintillator containment vessel, the stainless steel sphere with photomultiplier tubes, and the outer shielding water tank. From the Princeton NSF proposal.[15]

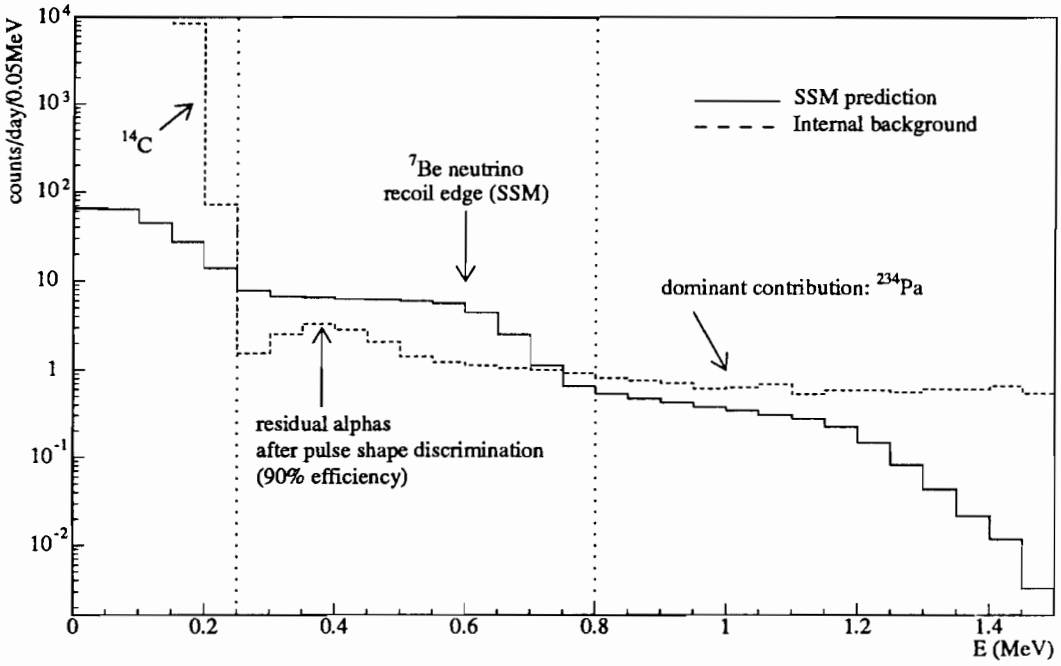

Figure 2.3. Borexino spectrum. Estimate of internal background and SSM neutrino signal in a 100-ton fiducial volume. The dotted vertical lines indicate the ^{7}Be "neutrino window" range of energies.

detection of neutrinos through electron scattering involves an important difference from earlier radiochemical experiments. Those experiments could only detect electron neutrinos, while Borexino can detect the other neutrino flavors, albeit with a reduced signal.

Electrons scattered by neutrinos are not the only particles which will cause light emission in the Borexino scintillator. Any other radiation incident on the scintillator will also result in light emission which is very difficult, a priori, to tell from that emitted due to neutrino-electron scattering. Making this even more challenging is the fact that the neutrino event rate is very low. The predicted ^{7}Be neutrino rate, based on the standard solar model, is 0.5 events per day per ton of scintillator. If less neutrinos are seen than predicted, as in other solar neutrino experiments, this rate will be even lower. Because of this low event rate, the rate of all other radioactive events affecting the scintillator, known as background events, must be kept at a level where they do not overwhelm the neutrino signal. The background requirements which must be met if Borexino is to be successful are very stringent.

Background events can be divided into two main types. External background comes from outside the scintillator containment vessel. Some sources of external background are cosmic radiation and emission of γ-rays and particle radiation from rock walls surrounding the experiment, steel used in constructing the experiment, and from the PMTs. Additional external background can result from radioactivity in the shielding liquid around the scintillator.

There are four major strategies for reducing the number of external background events: shielding, use of radiopure materials, purification and cleaning, and definition of a fiducial volume. Shielding from cosmic radiation is provided by approximately one mile of rock above the experiment (4000 m water equivalent) due to its location in the LNGS under the Appenine Mountains. The liquid surrounding the scintillator

containment vessel acts as shielding to reduce radiation from rock walls, steel tanks, and PMT components. All the materials for use in Borexino have undergone stringent radiopurity checks. This has included work on development of a more radiopure glass for the PMTs (Schott 8246 glass which has one-tenth the radioactivity of normal glasses[16]), selection of more radiopure concrete components for use in support structures, and study of coating materials for the tank containing the shielding liquid. All the tanks and other structures to be used in Borexino will be extensively cleaned to remove radioactive contaminants in the form of dust and grease that may be present on their surfaces. Purification can be used to reduce the radioactivity of the shielding liquid. This radioactivity, already at very low levels by ordinary standards and only significant in the context of Borexino, can be caused by dissolved ionic impurities containing radionuclides such as ^{238}U, ^{232}Th, and their daughters, as well as soluble radioactive gases such as ^{222}Rn. The definition of a fiducial volume consists of using some of the scintillator itself as shielding. In this scheme, the position of an event in the scintillator must be identified. Only events in a certain inner volume of the scintillator (the fiducial volume) are accepted and the rest of the scintillator is used as shielding material. For this method to be effective, it must be possible to determine the position of an event.

Internal background comes from the scintillator itself. The main causes of internal background are radioactive contaminants dissolved in the scintillator and radionuclides in the scintillator components. The major contaminants are those listed for the shielding liquid, as well as ^{40}K and ^{85}Kr. ^{14}C is a radionuclide present in the organic scintillator components. The ^{14}C events are of low energy, but there is a tail to the ^{14}C energy spectrum. This tail leaks into the ^{7}Be neutrino energy window and can provide a large background if the concentration of ^{14}C is too high.

Through Monte Carlo simulation, radiopurity standards necessary for the success of Borexino have been calculated.[17] Some of these requirements are listed in Table 2.3. The internal background levels must be minimized through selection of radiopure materials and purification. It is believed that organic liquids have a level of radiopurity sufficient to meet the ^{14}C requirement (the ^{14}C:^{12}C ratio is estimated to be $10^{-20} - 10^{-21}$ in petroleum products[18]). Fluors must also be found that do not contain too much ^{14}C, although the requirements are less strict in this case because much less fluor than solvent will be present in the scintillator. If dissolved radioactive impurites are present , it is possible to remove them by using water extraction and distillation for solid impurities and nitrogen stripping for gaseous impurities.

The calculated effect of the backgrounds at the levels mentioned on the energy spectrum of detected events in Borexino above can be seen in Figure 2.3. If the background levels assumed in these calculations cannot be met, Borexino will have a difficult time producing any useful measurements. Predicting the attainment of these background levels was a very difficult task because it required measuring radioactivities at a level of sensitivity unobtainable with current equipment. As a result, the Counting Test Facility (CTF) was constructed. Its purpose was to be a low-level counting experiment in which the radiopurity and background reduction goals necessary for Borexino could be tested.

C. The Counting Test Facility (CTF)

The CTF[18] can be thought of as a small version of Borexino, and a schematic drawing of it is shown in Figure 2.4. It consists of 4.8 tons of liquid scintillator contained in a spherical nylon vessel two meters in diameter. The scintillator containment vessel is surrounded by 1000 tons of purified water for shielding and is viewed by 100 PMTs. This vessel is located in the middle of a cylindrical tank 11

Table 2.3. Radiopurity requirements for Borexino. Radioisotopes which have been identified as potential contaminants in Borexino are listed, along with sources of contamination, and stategies for reducing contamination. Ambient concentrations of the radioisotopes are also presented to illustrate the stringency of the Borexino requirements. From Benziger et al.[19]

Radioisotope	Source	Typical Concentration	Tolerable Level	Strategy for reduction
^{14}C	Cosmogenic bombardment of ^{14}N	$^{14}C/^{12}C \leq 10^{-12}$	$^{14}C/^{12}C \leq 10^{-18}$	Petroleum derivative (old carbon)
^{7}Be	Cosmogenic bombardment of ^{12}C	$3x10^{-2}$ Bq/ton-carbon	$< 10^{-6}$ Bq/ton-carbon	Distillation or underground storage
^{222}Rn	Air and Emanation from materials	100 radon atoms/cm^3-air	1 radon atom/ton scintillator	Nitrogen stripping
^{210}Pb	Surface contamination			Positional discrimination
^{238}U, ^{232}Th	Suspended dust, Organometallic	2×10^{-5} g/g-dust	$< 10^{-16}$ g/g-scintillator	Water extraction or distillation
^{40}K	Dust or Contaminant in fluor	2×10^{-6} g/g-dust	$< 10^{-13}$ g/g in scintillator $< 10^{-11}$ g/g in fluor	Water extraction of fluor solution
^{39}Ar, ^{42}Ar	Air			Nitrogen stripping
^{85}Kr	Air			Nitrogen stripping

Figure 2.4. Schematic diagram of the CTF. Shown here are the shielding water tank, the scintillator containment vessel, and the phototube support structure. The phototube support structure is a set of six rings, on which the phototubes are oriented so that they view the scintillator containment vessel. Plumbing is connected at the top and bottom of the scintillator containment vessel to allow circulation of scintillator for filling, emptying, and purification. The nylon strings resist the buoyant force caused by the density difference between water and scintillator. The winch system allows vertical positioning of the scintillator containment vessel as the nylon strings stretch under load. The steel plate under the center of the shielding water tank is to provide additional shielding from the underground surfaces; the scintillator containment vessel is centered 4.5 m above the bottom of the shielding water tank and there is less water shielding below than in any other direction.

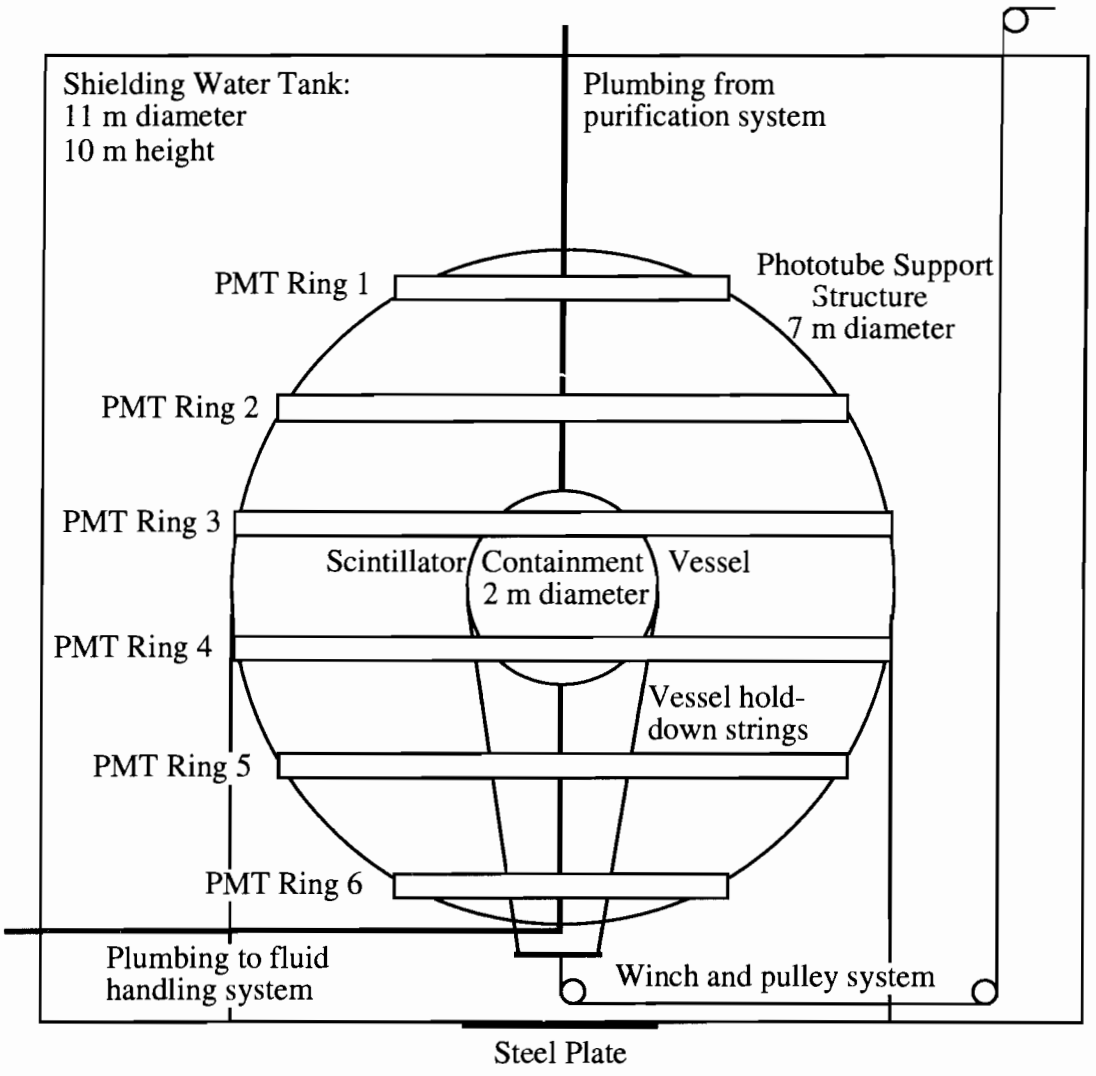
Shielding Water Tank:
11 m diameter
10 m height
Plumbing from
purification system
PMT Ring 1
Phototube Support
Structure
7 m diameter
PMT Ring 2
PMT Ring 3
Scintillator
Containment
2 m diameter
Vessel
PMT Ring 4
Vessel hold-
down strings
PMT Ring 5
PMT Ring 6
Plumbing to fluid
handling system
Winch and pulley system
Steel Plate

Figure 2.4.

meters in diameter and 10 meters in height. The shielding water is contained inside this tank. The shielding water tank is the large blue structure in Figure 2.5. Inside the tank, the scintillator containment vessel is surrounded by a phototube support structure seven meters in diameter as depicted in Figure 2.6. The CTF scintillator consists of a pseudocumene solvent containing 1.5 g/L of PPO. Because this organic scintillator is less dense than water, the scintillator containment vessel has a net buoyant force, and a hold-down mechanism is required to keep it in place. Such a mechanism is provided by the sixteen nylon strings that can be seen looping over the scintillator containment vessel in Figure 2.6.

Construction of the CTF began in 1993 in Hall C of the LNGS. During that year, the shielding water tank, the water purification plant, and the fluid handling system for scintillator were constructed. In 1994, the phototube support structure was built and the PMTs were mounted. A plumbing system for the purified water and the data collection electronics were also completed during that period. The nylon inner vessel was also installed in 1994. Filling of the entire shielding water tank, including the inner vessel, with water began during December of that year. Assembly of the scintillator purification system began in January 1995. In February, before completion of this system, one ton of scintillator was introduced to the inner vessel. Data were taken with this one ton for approximately one month and the remaining four tons of scintillator were added in April. Data were taken in this configuration for two months, enough time to allow some radon introduced into the inner vessel during the filling process to decay and some limits to be placed on the radioactivity levels in the scintillator.[20,21] The ^{238}U level was found to be $4.2 \pm 2.0 \times 10^{-16}$, the ^{232}Th level was found to be $2.5 \pm 1.0 \times 10^{-16}$, and the ^{14}C:^{12}C ratio was found to be $1.45 \pm 0.01 \times 10^{-18}$. These results indicated that the radiopurity goals of Borexino

Figure 2.5. The CTF water shielding tank. This photograph was taken in Hall C of the LNGS. The large blue structure is the water shielding tank of the CTF. The scintillator purification system is located in the cleanroom on top of the tank which can be reached via the stairway on the outside of the tank. Some parts of the scintillator fluid handling system can be seen in the foreground.

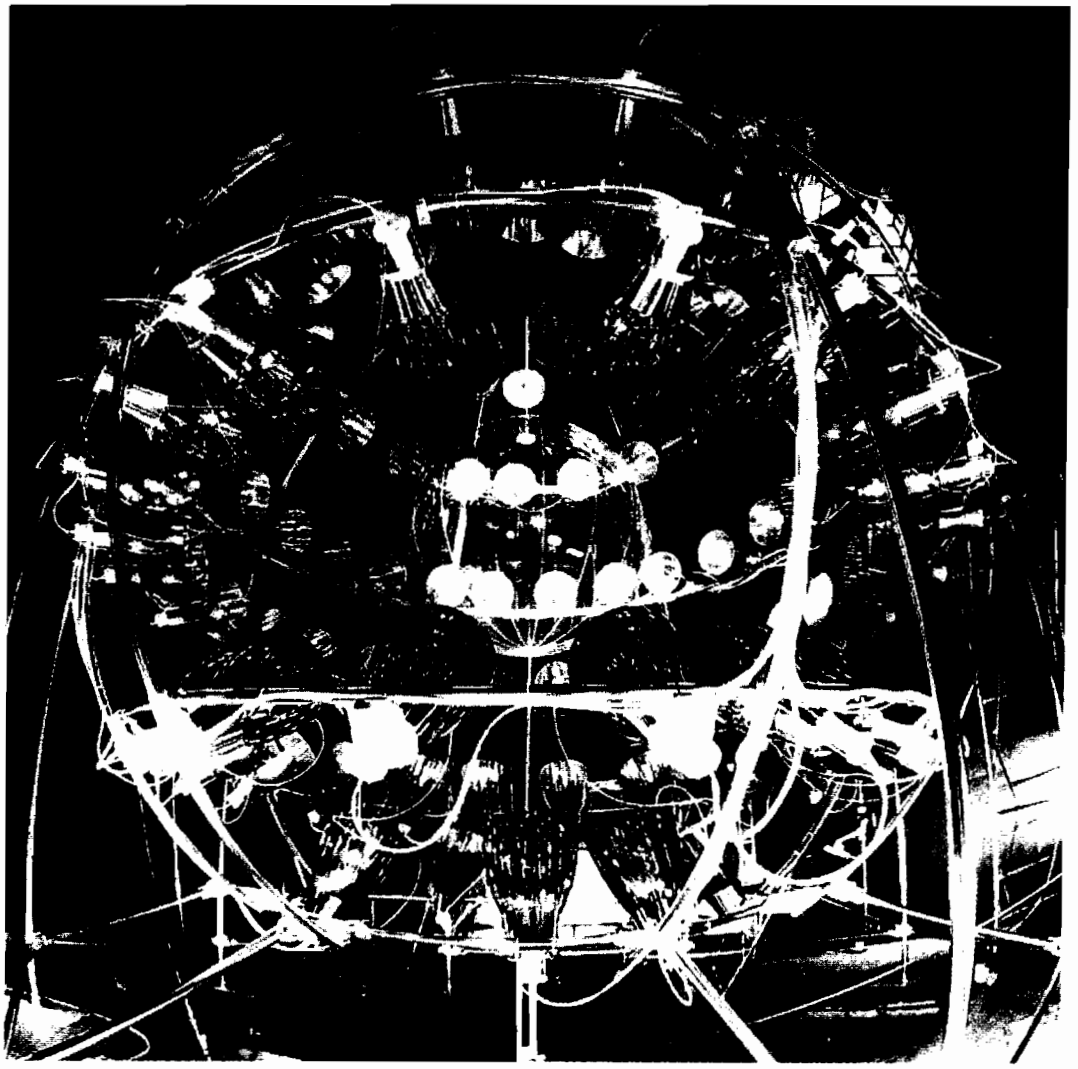

Figure 2.6. Interior of the CTF. This photograph was taken inside the water shielding tank before it was filled with purified water.[20] The scintillator containment vessel can be seen at the center of the phototube support structure. The plumbing for scintillator circulation, the nylon hold-down strings, and the phototube cabling are also visible.

could be achieved, but some issues were raised that had not been fully appreciated previously.

Results from the CTF indicated that radon was major contaminant which had to be monitored closely. After the initial filling of the inner vessel, the scintillator sat for two months to allow radon introduced during the filling process to decay. ^{222}Rn has a 5.5 day mean lifetime, and the ^{222}Rn level decayed from 10^5 counts per day to less than 10 counts per day after two months. Unfortunately, after the radon decayed, radioactive radon daughters remained in the scintillator as internal background. Radon in the shielding water was also a concern, because the level of radioactivity in the water proved to be 10 – 20 times greater than that predicted before construction of the experiment. A water purification system[23] began operation before the initial filling of the shielding water tank in December 1994. This system consisted of a reverse osmosis unit, a deionization unit, 0.1 μm filtering to remove particulates, and nitrogen stripping. The nitrogen stripping portion was modified in mid-1995 to increase the efficiency of radon stripping from the shielding water, but radon levels still remained higher then anticipated. One possible explanation is the existence of radon emanation sources inside the shielding water tank unaccounted for in the initial modeling.

Operation of the scintillator purification system began in June 1995, with the nitrogen stripping of the scintillator. Water extraction was operated from July to August, and vacuum distillation from September to December. These operations showed that some reduction of radioactive contamination in the scintillator was possible, although the presence of small amounts of radon in the stripping nitrogen was found to be a problem.[17] The scintillator purification system is located on top of the shielding water tank inside a cleanroom which can be seen in Figure 2.5.

The optical properties of the CTF scintillator were examined in a series of experiments beginning in early 1996. These experiments involved the insertion of

radon sources into the inner vessel. These measurements were first carried out for the pseudocumene-PPO scintillator in January and February. In March, fifteen percent of the PPO was removed by distillation to determine if PPO was a major source of ^{14}C contamination. This was followed by the addition of approximately 20 mg/L of bis-MSB to the mixture, and the optical experiments were repeated. In July and August, the scintillator in the inner vessel was replaced by water. Data were taken in this configuration, and the water was then displaced with pure pseudocumene. Because the vessel was never rinsed thoroughly during this procedure, there was a small amount of residual PPO. The PPO concentration after addition of the pure pseudocumene was found to be 0.2 ppm (as compared to 1.5 parts per thousand initially). The optical measurements were repeated again for this scintillator mixture. These measurements with almost pure pseudocumene are important because of the possibility of using a pure pseudocumene shielding buffer in Borexino. In late August, the pseudocumene was again replaced with water in preparation for tests with a new scintillator consisting of a phenylxylylethane (PXE) solvent and a p-terphenyl fluor. This scintillator was introduced in November 1996, and studies to determine its radiopurity continued until August 1997.

The CTF has been a useful tool for conducting experiments on potential scintillator mixtures, both in terms of radiopurity and optical properties. It has also allowed the testing of different fluid handling and purification methods. Because of the importance of the data collected in the CTF and the relavance of CTF data to work in this thesis, it is worthwhile to examine the data collection capabilities of the CTF.

Light emitted by the CTF scintillator is collected by 100 Thorn EMI 9351 photo-multiplier tubes (PMTs). These PMTs have 8 inch diameter cathodes and their coverage area is extended through the use of Winston light cones.[24] These light collectors are designed as "truncated string cones" and are optimized for very good acceptance for

light coming from the inner vessel and very poor acceptance for light from regions outside the inner vessel. The collection end of the light cones is 50 cm in diameter and this provides a 30 percent coverage of the inner vessel. These phototubes are capable of detecting single photons. In the CTF, the 100 PMTs are arranged in six rings, as shown in Figures 2.4 and 2.7. Although there are 100 PMTs, there are only 64 electronic channels for data collection. Because of this, 72 PMTs are arranged in pairs and the other 28 have a dedicated channel. A channel with two PMTs registers a hit when either of the PMTs receives a photon. The 36 pairs are arranged so that the two PMTs are adjacent and in the same ring to minimize the uncertainty in the position of a photon strike.

Each electronic channel has a time-to-digital converter (TDC) and an analog-to-digital converter (ADC). The TDC contains a counter and converts elapsed time into a digital signal. The ADC converts the analog current signal from the PMT(s) into a digital signal which can be used by the data computer. There is also an auxiliary channel with the same components connected to each main channel. When a PMT receives a photon, as determined by the charge at the anode exceeding a threshold value, the data collection activity is begun. If enough PMTs (the number of hit PMTs necessary to constitute an event is known as the trigger level) receive a photon in a certain time window, then the activity is considered to be an event. In most cases an event is defined as six PMTs receiving photons within a 30 nanosecond window (the sixth PMT must be hit within 30 ns of the first PMT being hit). This trigger level discrimination is necessary because each PMT has a dark rate of approximately 1000 Hz, but the tubes only register light at the same time if a real event occurs. If the number of PMTs receiving light is insufficient in the alloted time, the data collection registers reset to zero.

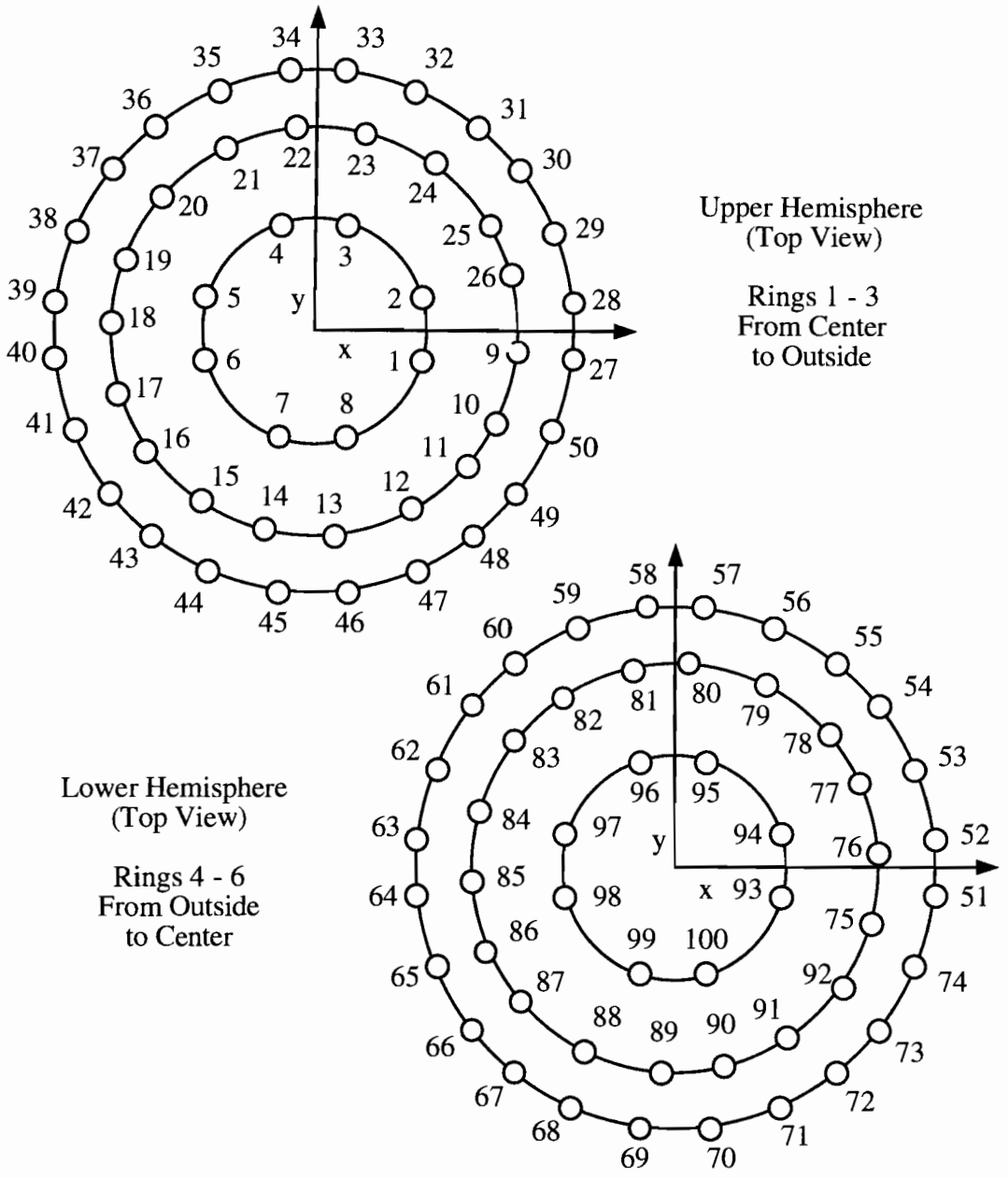

Figure 2.7. CTF PMT map. A schematic of the PMT locations in the CTF. The numbering system in ring 2 (tubes 9 – 26) goes clockwise instead of counterclockwise like the other rings. Data from Manno.[25]

Once it has been determined that an event is occuring, the TDC in each channel begins counting from the time when the sixth PMT received a photon. Thus the time of photon arrival at the first five PMTs will be negative. The TDCs record the time of arrival of the first photon at their respective channel. Additional photon hits do not affect the TDC data. The ADC in each channel records the integrated charge received by the PMT(s) in the channel for 100 ns after the initial photon hit. This allows a measure of the total number of photons impinging on the channel's PMT(s) to be determined. If more than 20 photons strike the PMT(s), the ADC becomes saturated. The TDC and ADC that record this data are known as the group 1 data recorders.

When a group 1 event occurs (any random event), a hardware timer begins running. If a second event occurs within 8 milliseconds, the TDCs and ADCs in the auxiliary channels are activated and record data in a similar manner. These converters are known as group 2 data recorders. The use of separate TDCs and ADCs for group 2 events is necessary because the events happen much more quickly than it is possible to store the results. If not for the use of two sets of data recorders, events with a close coincidence would be lost because the TDCs and ADCs would still be processing data from the previous event. The TDC and ADC data for each channel and each event are stored on magnetic tape from which they can be analysed.

Sophisticated data analysis techniques can be applied to the CTF data after a data collection run is finished. The length of a run can vary from about one hour to several days, depending on the rate of activity in the scintillator containment vessel and on how soon the data need to be analyzed. The analysis software allows events to be discriminated from one another based on many factors. Energy cuts are one form of discrimination. Very high energy events, such as muons (a form of cosmic radiation) passing through the detector, are discernable by the immense amount of charge collected by the ADCs (corresponding to many photon hits). Muon events also have a distinct

up-down asymmetry; more photons are received by PMTs in the bottom hemisphere than by those in the upper region. Very low energy events (below 0.2 MeV) can be attributed to ^{14}C activity, although many of these events are excluded by a six PMT trigger.

It is possible to discriminate between α and β events in the scintillator by calculating the percentage of the total ADC signal received (summed over all channels) as a function of time. An α particle causes a larger ionization density in the scintillator, and as a result, a larger percentage of the total charge is located in the tail of the signal, at longer times. The different pulse shape responses of the PMTs to α and β events are shown in Figure 2.8. In laboratory measurements, it was found that 4 percent of the total charge produced by an α event occurred between 48 and 500 ns. A β or γ event has only 1% of its total charge after 48 ns. In the laboratory measurements, over 99% of α events could be correctly identified as such by this method with less than 1% of β events being misidentified. The effectiveness dropped to approximately 97 percent in the CTF for 751 keV electron equivalent α's and to 90 - 97% for α's of lower energy. Misidentification of β's increased to 2.5% and 10% respectively.[21] This degradation in performance was due to some optical properties of a large scale scintillator that will be discussed in Chapter 3.

Identification of coincidence events is also a powerful tool in the analysis of CTF data. The coincidence time between a group 1 event and the corresponding group 2 event is especially useful in identifying the decay of ^{214}Bi and ^{214}Po. These nuclides are daughters of ^{222}Rn and are commonly encountered in the CTF. ^{214}Bi decays by emitting a β-particle (along with a γ-ray in most cases) with a lifetime of 28.4 minutes, while ^{214}Po decays through emission of an α-particle with a lifetime of 236 μs. Thus, β emission followed by α emission with a mean coincidence time of 236 μs strongly suggests the existence of this decay chain. The ^{222}Rn level in the CTF is measured

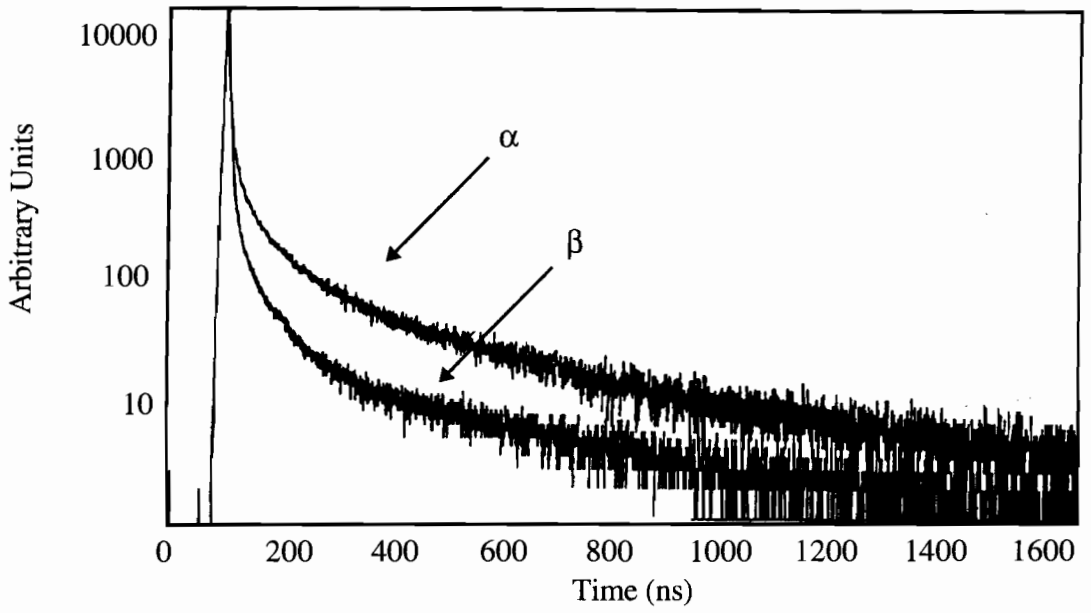

Figure 2.8. Pulse shape analysis for α - β discrimination. Comparison of the PMT signals from α and β events shows the larger amount of charge in the tail of the α, making it possible to differentiate between the two types of events. From Bellini.[16]

through this decay coincidence. Coincidences are also important in identification of the ^{85}Kr decay chain, in which 0.43% of the ^{85}Kr atoms decay by β emission to a metastable state of ^{85}Rb. This metastable state emits a γ-ray with a lifetime of 1.46 μs and makes possible the detection of ^{85}Kr through the coincidence method.

Positional resolution is another very important method of event discrimination which can be applied through software analysis. Positional resolution in the CTF is based on the measurement of photon arrival times at various photo tube locations. This reconstruction is quite simple in an ideal situation in which all the photons are emitted instantaneously upon the occurance of an event and travel directly from the event to a photo tube. If the time of flight from such an ideal event to each phototube was known, it would take the data from only three PMTs to specify the position of the event. The time of flight from the event to a PMT would specify a spherical three-dimensional surface, and the intersection of the surfaces from three tubes would indicate the position of the event.

The reality of the CTF is quite different from this ideal case. The timing information as recorded by the TDCs does not provide an actual flight time from an event to each photo tube. The TDC data only provide information on differences in the time of arrival of photons at different PMTs. This means that even for the ideal events considered above data from at least four photo tubes would be required to locate an event position.

In an ideal event, all the energy is deposited at one point in the scintillator. Energy in a real event is deposited along the track of the ionizing radiation which caused it. These tracks are discussed again in Chapter 4. The length of an ionization track depends upon the type and energy of the ionizing radiation. Uncertainty in event reconstruction increases as the length of the ionization track grows longer.

Many other non-idealities are inherent in a real scintillation detector. Not all the photons are emitted by the scintillator at the same time. This is because the scintillator components have finite decay times. The decay time is the mean time during which a molecule remains in an excited electronic state before relaxing to the ground state and releasing energy. A scintillator is designed to minimize this decay time, and the CTF scintillator has a decay time of about 3.5 ns. A decay time of 3.5 ns corresponds to an uncertainty in the position of an event with respect to a given PMT of approximately 10 cm. Scintillator decay time will be considered in more detail in Chapters 4 and 5.

There is also uncertainty, known as jitter, in the photoelectron transit time in the PMTs. This transit time is the amount of time it takes for the PMT to produce a signal after a photon impinges on the photocathode. The jitter in the CTF photo tubes is approximately 1 ns. This adds an additional uncertainty of nearly 3 cm to the position of an event with respect to a specific PMT. Monte Carlo simulations taking the finite scintillator decay time and photo tube jitter into account predict that positional resolution to within 10 cm can be achieved for a β event by using all the available TDC data (i.e. using more than the minimum number of phototubes necessary).

In the ideal case, the photon was assumed to travel in a direct straight-line path from the event to the PMT which detected it, but this does not necessarily happen. There are many mechanisms by which a photon can be scattered or undergo a change of direction in its flight path. Scattering mechanisms include including absorption and reemission by the scintillator solvent or fluor, and elastic Rayleigh scattering by the scintillator components and the nylon scintillator containment vessel. Photon flight paths can also be changed by refraction at the scintillator-water interface, reflection at this interface, and reflection from the glass of the PMTs. These processes will be considered in detail in Chapter 4, but are mentioned here to stress the fact that they make positional reconstruction in the CTF more difficult. Depending on where the scattering

occurs, it can change the arrival time at a phototube by up to 30 ns. Because a change of this magnitude adds a significant uncertainty to the location of an event, it is important to determine how much scattering occurs in a large-scale scintillation detector and at what length scale this scattering takes place. The quantitative description of light scattering is one of the major goals of this thesis.

Some of the non-idealities in the positional reconstruction are due to the data collection electronics. The TDCs only record the timing of the first photon to hit a PMT. Because of this, photons other than the first cannot be used to aid in reconstruction. A small amount of uncertainty is added because some of the channels contain two PMTs. It is not possible to determine which of the two photo tubes was hit by a photon. This effect is minimized by placing the tubes which share electronic channels adjacent to each other.

The position of an event in the CTF is reconstructed using a computer algorithm. The software uses a fitter to determine the spatial coordinates for the event which maximize a likelihood function. This function is based on time of flight to each PMT. It includes the use of an effective refractive index applied to the entire flight path (as opposed to separate indices for scintillator and water) and a probability distribution function (PDF) for the time of arrival at a PMT. Initially the PDF was calculated from Monte Carlo simulations of the CTF, but later versions of the fitter contain a PDF based on experimental data from radioactive sources placed inside the inner vessel. Positional resolution in the CTF was predicted to be approximately 10 – 12 cm for 1 MeV events. Experimentally, the resolution has been determined to be 10 – 15 cm. This degradation, even with the use of the experimentally determined PDF, has been caused by optical effects which were not appreciated in the simulations upon which the initial estimates were based.

Positional resolution is necessary in order to define a fiducial volume in Borexino, and the definition of the fiducial volume is necessary to reduce the background in Borexino to an acceptable level. The ability to obtain satisfactory positional resolution is dependent on an understanding of the optical properties of the scintillator. These optical properties also influence the α - β separation possible in the detector, especially because they affect the timing of light emission,. The understanding of these properties is crucial to the success of the experiment.

References

1. Williams, W. S. C. *Nuclear and Particle Physics*; Clarendon Press: Oxford, 1991.

2. Bahcall, J. N. *Neutrino Astrophysics*, Cambridge University Press: Cambridge, 1989.

3. Bethe, H. A. *Phys. Rev.* **1939**, *55*, 434.

4. Cleveland, B. T. *Nucl. Phys. B* **1995**, *38*, 47.

5. Basu, S.; Christensen-Dalsgaard, J.; Schon, J.; Thompson, M. J.; Tomczyk, S. *Astrophys. J.* **1996**, *460*, 1064.

6. Mikhayev, S.; Smirnov, A. *Sov. J. Nucl. Phys.* **1985**, *42*, 913.

7. Davis, R.; Harmer, D. S.; Hoffman, K. C. *Phys. Rev. Lett.* **1968**, *20*, 1205.

8. Bahcall, J. N.; Davis, R. *Science* **1976**, *191*, 264.

9. Anselmann, P. *Phys. Lett. B* **1995**, *342*, 440.

10. Abdurashitov, J. *Phys. Lett. B* **1994**, *328*, 234.

11. Fukuda, Y. *Phys. Rev. Lett.* **1994**, *77*, 1683.

12. Takita, M. In *Frontiers of Neutrino Astrophysics*, Suzuki, Y.; Nakamura, K., Eds.; Universal Academy: Tokyo, 1993, p 147.

13. Chen, H. H. *Phys. Rev. Lett.* **1985**, *55*, 1534.

14. Bludman, S. A.; Hata, N.; Kennedy, D. C.; Langacker, P.G. University of Pennsylvania preprint, UPR-0516T (revised), 1992.

15. Benziger, J. B.; Calaprice, F. P.; Chen, M. C.; Eisenstein, R. A.; Vogelaar, R. B. NSF Borexino Proposal, Princeton, 1996.

16. Bellini, G. Memo on Borexino Project, Milano, 1995.

17. Benziger, J. B.; Calaprice, F. P.; Lowry, M;.Vogelaar, R. B. NSF Borexino Proposal, Princeton, 1992.

18. Benziger, J. B.; Calaprice, F. P.; Chen, M. C.; Darnton, N.; Johnson, M. C.; Loeser, F.; Vogelaar, R. B. "Purification System for a Low-Background Liquid Scintillation Detector", in preparation.

19. Borexino Collaboration. "A Large Scale Low Background Liquid Scintillation Detector: The Counting Test Facility at Gran Sasso", *Nucl. Inst. and Meth. A* , in press.

20. Ragavan, R. S. *Science* **1995**, *267*, 45.

21. Borexino Collaboration. "Ultra-low Background Measurements in a Large Volume Underground Experiment", *Astroparticle Phys.*, in press.

22. Borexino Collaboration. "Measurement of the 14C Abundance in a Low-Background Liquid Scintillator, *Phys. Lett. B*, in press.

23. Balata, M. *Nucl. Inst. and Meth. A* **1996**, *370*, 605.

24. Winston, R.; Welford, W. T. *High Collection Nonimaging Optics*; Academic Press: New York, 1989.

25. Manno, I. "Event Reconstruction in the CTF", Milan, 1995.

CHAPTER 3: SCINTILLATOR PURIFICATION

One of the major goals of the CTF was to test the concept of scintillator purification. Purification operations took place throughout a major portion of the life of the CTF, and the success of these operations was essential in showing the validity of the Borexino concept. Scintillator purification was mentioned briefly in Chapter 2, but it will be considered in greater detail here because the purification work constituted a major effort in this thesis. The CTF purification operations had two major goals: preservation of the scintillator optical properties and removal of radioactive contaminants from the scintillator. Both of these goals had to be achieved in order for the CTF to be a successful prototype of Borexino.

A. Contaminants of Concern for Borexino

1. Contaminants Affecting Optical Properties

Molecules present in the liquid scintillator other than the solvent and the fluor(s) can have a significant effect on its optical properties. These impurities affect the scintillator in two ways: Some contaminants absorb the light produced by the scintillator and prevent it from reaching the photo-multiplier tubes. Others act as quenchers and interfere with the emission of light from the scintillator molecules. Many impurities cause a combination of these effects. The mechanisms of absorption and quenching are considered in detail in Chapter 4.

Organic molecules are the most common type of optical impurity. They can enter the scintillator during the initial mixing if they are present as trace components in the solvent and fluor(s). They can also be introduced into the scintillator after it is inside the scintillator containment vessel of the CTF due to the degradation of scintillator components. Degradation can be caused by the oxidation of the

components or by their polymerization. This type of degradation can be seen visually after a few months in scintillator left exposed to air and light. It should be much less significant in a dark, oxygen-free environment like that of the CTF.

Inorganic compounds can also contribute to reduction of the scintillator optical properties. Oxygen, in addition to causing oxidation of scintillator components, is a powerful quencher of scintillator fluorescence. Substances in the scintillator which are subject to phase separation are also potential contaminants. Water is the most likely impurity of this nature. It can be introduced into the scintillator by diffusion through the nylon membrane of the scintillator containment vessel or by direct contact during water extraction purification operations (see Section 3.B). Water is dissolved in the scintillator up to a saturation level of 100 ppm at 20°C.[1] If the temperature of saturated scintillator decreases, the water can phase separate and form tiny droplets. These droplets would severely degrade the optical properties inside the detector due to the scattering they would cause.

Although the exact formulas of the organic impurities which impair the optical performance of the detector are not known, purification strategies for removal of general classes of these contaminants have been developed. The removal of oxygen and water from the scintillator is also possible using purification techniques.

2. Radioactive Contaminants

Radioactive contaminants are of even greater concern in the CTF than those which degrade its optical properties. The level of radio-impurities in the Borexino scintillator must be very low in order for the experiment to successfully detect solar neutrinos. Low levels of radio contamination are necessary so that decay events from these contaminants do not overwhelm the neutrino signal in the detector. Several potential contaminants[2] are listed in Table 2.3.

^{14}C is a radioactive isotope of carbon that is present in the organic scintillator components. It is produced by the cosmogenic bombardment of ^{14}N, and has a half-life of 5730 years. ^{14}C emits low energy β-particles (maximum energy 0.157 MeV) when it decays to ^{14}N. These β's are of low enough energy that they do not appear in the neutrino energy window (0.250 – 0.800 MeV), but if too many of these decays occur they can produce false events through accidental coincidences. Calculations have shown that the ^{14}C:^{12}C ratio in the scintillator components must be less than 10^{-18} to meet the requirements of Borexino.[3] At the earth's surface, the rate of ^{14}C production is sufficient to result in a ^{14}C:^{12}C ratio of 10^{-12}. This is the ^{14}C:^{12}C ratio present in living organisms and atmospheric CO_2.

The ratio in the scintillator components should be much lower because they are derived from petroleum. Petroleum has been located deep underground, where the cosmic background is highly attenuated, for millions of years. This has allowed time for most of the ^{14}C to decay. A small equilibrium amount of ^{14}C remains due to bombardment of ^{14}N in the petroleum by radiation emitted from the rocks surrounding the petroleum. Because different petroleum reservoirs have different amounts of natural radioactivity, the ^{14}C concentration in petroleum can vary with location. It has been estimated that the ^{14}C:^{12}C ratio in petroleum could be as low as $10^{-19} – 10^{-21}$. Production of ^{14}C activity takes place on a time scale of thousands of years and petroleum can be brought to the earth's surface without immediate contamination by cosmogenic bombardment taking place.

Existing analytical techniques cannot measure the ^{14}C concentration at the required sensitivity, and one of the major goals of the CTF was to show that the ^{14}C level in a petroleum-derived scintillator was as low as predicted. It is important to realize that ^{14}C contamination cannot be removed from the scintillator. If ^{14}C levels

in the scintillator are too high, the only solution is to obtain scintillator derived from a different petroleum source.

Cosmogenic bombardment of ^{12}C produces ^{7}Be, another potential scintillator contaminant. Little ^{7}Be production takes place while the petroleum is underground, but contamination begins when it is brought to the surface. On the Earth's surface, an equilibrium concentration of ^{7}Be is reached. At this concentration, an activity of 2600 decays per day per ton of scintillator is observed. A ^{7}Be level of more than 90% of this equilibrium amount is reached in 180 days, and the ^{7}Be concentration becomes unacceptable for Borexino in less than 5 minutes. ^{7}Be decays to the stable isotope ^{7}Li by electron capture with a half-life of 53 days. In 10% of these decays, a 0.478 MeV γ-ray is emitted, and this energy is in the neutrino window. The acceptable decay rate from ^{7}Be in Borexino is less than 0.1 decays per day per ton of scintillator. The reduction in ^{7}Be contamination can be accomplished in two ways: removal by purification or underground storage. Effective purification methods for the removal of ^{7}Be have been found. In addition, the relatively short half-life of this isotope allows a reduction in its concentration to be achieved by underground storage. When stored underground, ^{7}Be production in the scintillator ceases, and after approximately two years the amount of ^{7}Be will have decayed to an acceptable level.

^{238}U and ^{232}Th may also contaminate the CTF scintillator. The decay chains of these naturally occurring radioactive isotopes are shown in Figure 3.1. The emission of radiation does not stop with the decay of the ^{238}U and ^{232}Th, but continues along the decay chains until the stable ^{206}Pb and ^{208}Pb isotopes are reached, respectively. The uranium chain includes 6 α- and 8 β-decays, and the thorium chain consists of 6 α- and 4 β-decays. Many of the decays in these two chains produce events in the neutrino energy window. If enough time passes, daughter nuclides of the uranium and thorium decay will reach equilibrium concentrations. These

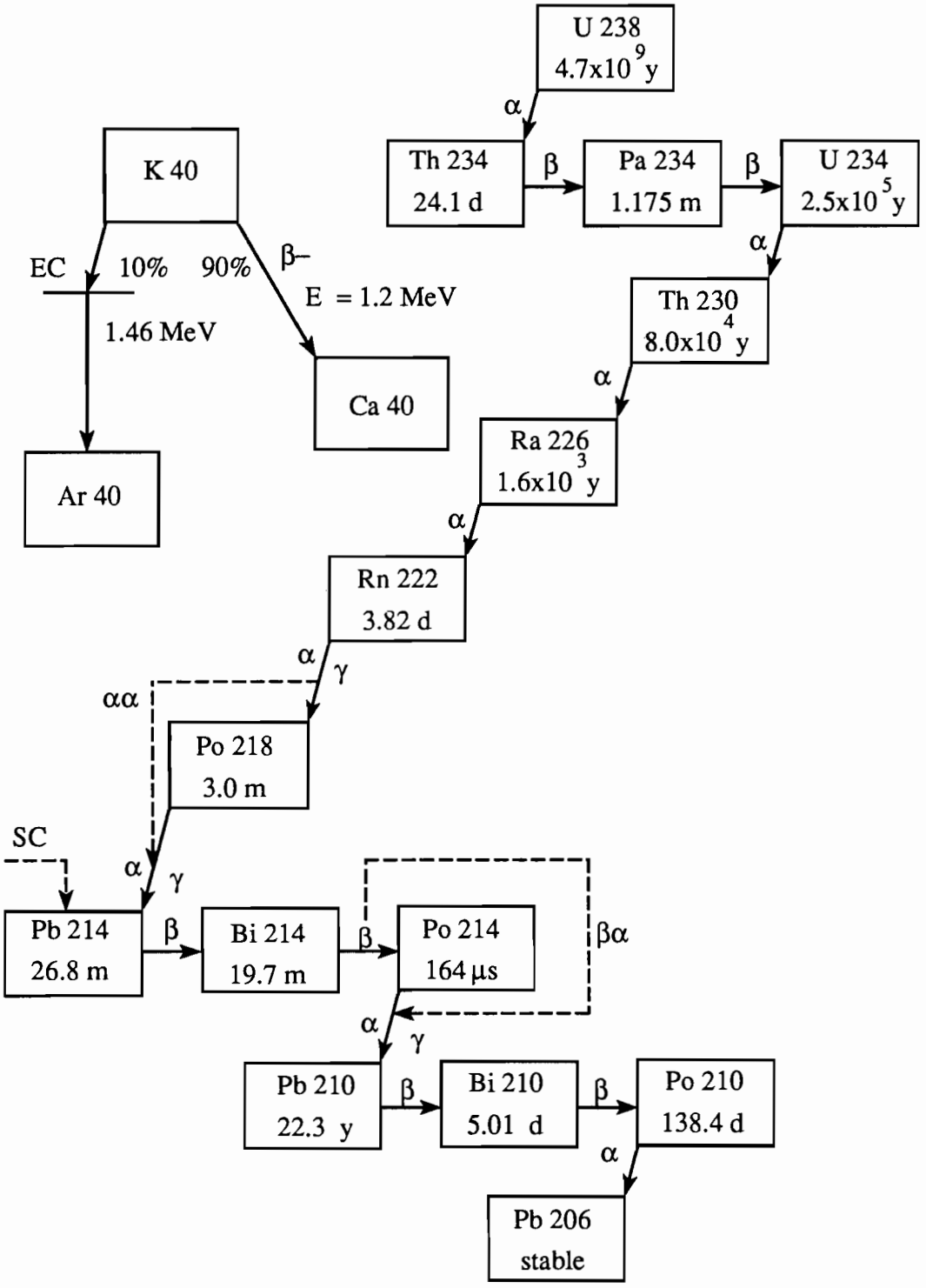

Figure 3.1. Decay chains for ^{238}U, ^{232}Th, and ^{40}K. The half-lives and modes of decay for these potential Borexino contaminants and their daughters are shown here.

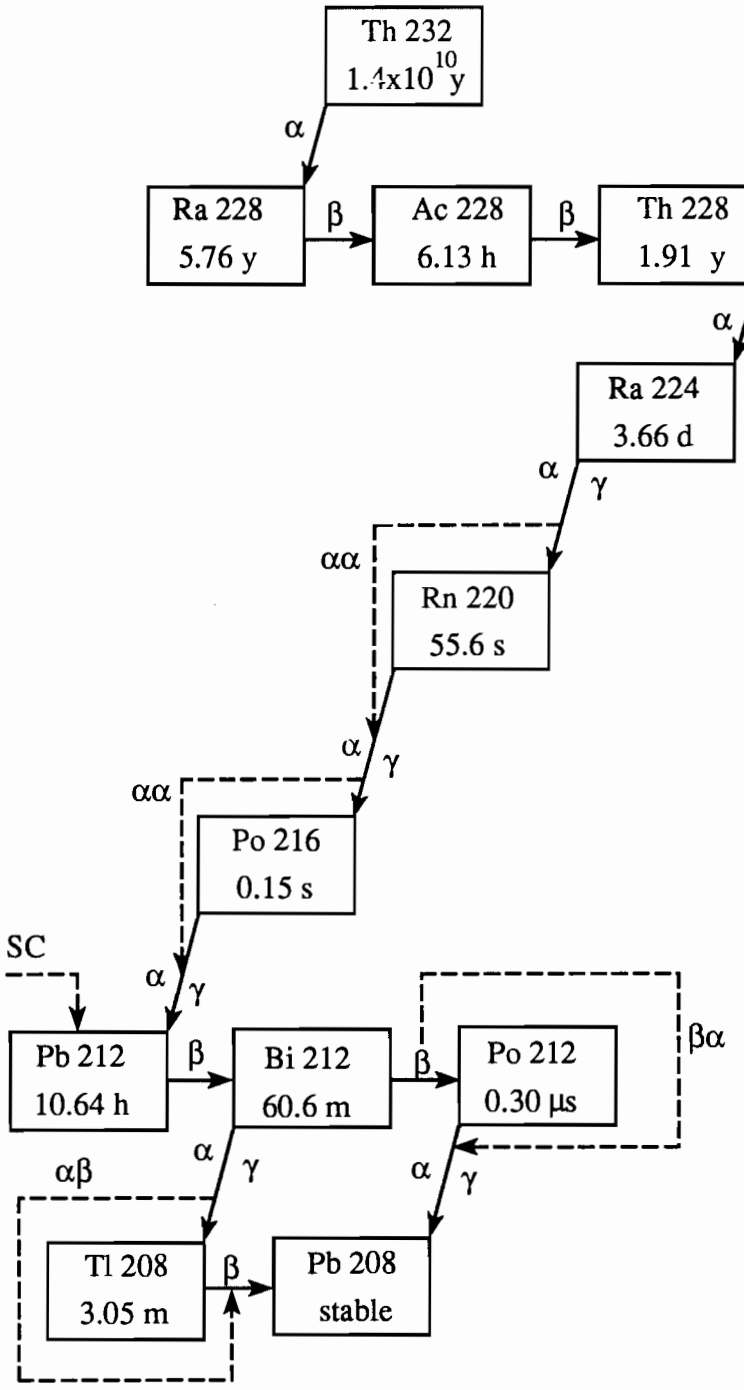

Figure 3.1. (cont.).

concentrations are determined by the rate of production of the daughter from the nuclide prior to it in the decay chain and the decay rate of the daughter. This condition is known as secular equilibrium. Because some of the decay times are very long, it takes some time for secular equilibrium to be established. Secular equilibrium can be disturbed quite easily, and it is most often broken at the long-lived ^{234}U, ^{230}Th, and ^{226}Ra isotopes in the uranium chain. If secular equilibrium does not exist, concentrations of uranium and thorium cannot be deduced from measurements of the concentrations of daughter nuclides.

Uranium and thorium contamination can enter the scintillator in many ways. These materials can be present as dissolved impurities in the scintillator solvent itself. Contamination in this manner is not of major concern because of the extremely low solubility of ionic species and metals in organic liquids such as pseudocumene, although there is a chance for the formation of organo-metallic complexes. Laboratory measurements at Princeton have confirmed this low solubility.[4] Of much greater concern is the presence of these isotopes in dust particles. They are normally present in the form of oxides such as UO_3. The earth's crust contains uranium and thorium at a level of 2×10^{-5} grams per gram of crust material, and any dust from the earth's crust therefore contains them at the same level. The requirement for Borexino is a uranium and thorium level of less than 10^{-16} grams per gram of scintillator. This means that dust contamination must be kept to a level of less than 5 picograms of dust per gram of scintillator or less than 1.5 mg of dust in the 300 tons of scintillator in Borexino. The structural components in the experiment are made from natural materials, and they contain some uranium and thorium. The glass in the phototubes, in particular, is a potential source of radioactive contamination. There is some fear that the radionuclides may leach out of the system components into the scintillator, although this is rather unlikely due to the low solubility of uranium and thorium in the

organic scintillator. Appropriate purification strategies should be able to reduce the uranium and thorium levels in the scintillator if they are initially unacceptable.

^{40}K is another potential metallic contaminant in Borexino. This radioactive isotope of potassium has a half-life of 1.25×10^9 years. It can decay in two ways as seen in its decay chain in Figure 3.1. ^{40}K has a natural abundance of 0.012%. Because potassium makes up 2% of the earth's crust, ^{40}K is present in dust at a level of 10^{-6} g/g. ^{40}K is also associated with living organisms, which contain relatively high amounts of potassium. It has been estimated that one thumbprint contains enough ^{40}K to ruin the Borexino experiment. The ^{40}K limit for Borexino has been set at 10^{-13} g/g of scintillator. A major source of ^{40}K contamination is the fluor component of the scintillator. The fluor contains a large amount of potassium because the potassium can interact chemically with the basic groups on the solute molecule. Because the fluor is present in the scintillator at a low concentration, the ^{40}K limit for it is not as strict as for the overall scintillator. The fluor limit has been set at 10^{-11} grams per gram of fluor. ^{40}K in the scintillator, especially that in the fluor, can be removed by purification operations.

Radioactive gases are another important source of potential contamination for Borexino. Although there are several of these gases, ^{222}Rn is the most troublesome. This radon isotope is part of the uranium decay chain and has a half-life of 3.8 days. It can be introduced into the scintillator when the uranium daughter ^{226}Ra decays, but this route for radon contamination is relatively unimportant. The major risk of radon contamination comes from exposure of the scintillator to air. Outdoor air contains radon at an average level[5] of 20 Bq/m^3 (1 Bq = 1 Becquerel = 1 decay per second). This corresponds to approximately 17 radon atoms per cm^3 of air. The underground air in the LNGS has a higher radon concentration of nearly 100 Bq/m^3. If scintillator is exposed to air, some radon in the air will dissolve in the scintillator. The

partitioning of radon between the two phases can be expressed using the Ostwald coefficient. The Ostwald coefficient for a gas-liquid system is the volume of gas at system temperature T and gas partial pressure P that dissolves per unit volume of liquid. If the gas phase is ideal and the solubility is low, this parameter is independent of P. Wojcik[6] has determined that the Ostwald coefficient of radon in pseudocumene and xylene is 11.5.

Radon can also enter the scintillator by emanation from materials used in constructing the experiment. Any material containing uranium can be a source of this emanation. As the uranium in the materials decays, radon is formed. Because it is a gas, the radon can diffuse out of the material and enter scintillator which is contacting it. For this reason, construction materials with low uranium content must be used. This is especially critical for the nylon scintillator containment vessel which will constantly be in intimate contact with the scintillator.

Radon present in the shielding water of the CTF can also contaminate the scintillator inside the nylon vessel. Radon is approximately 10 times more soluble in scintillator than in water on a molar basis,[7] and radon in the shielding water can diffuse through the nylon vessel and contaminate the scintillator inside it.[8]

The radon level required for Borexino is less than 1 radon atom per ton of scintillator. It is very important to minimize exposure of the scintillator to air and to reduce the number of possible emanation sources in the experiment in order to achieve this goal. Purification procedures for radon removal were developed for the CTF. Radon contamination due to a one-time exposure can also be reduced by allowing the radon to decay with its 5.5 day mean lifetime.

Air exposure can also introduce radioactive gas contaminants other than radon into the scintillator. These include ^{85}Kr, ^{39}Ar, and ^{42}Ar. None of these isotopes occurs naturally, but they have been introduced into the atmosphere by above-ground

nuclear bomb testing and nuclear reactor fuel processing. Air exposure is the only source of these contaminants. ^{85}Kr is present in the atmosphere at a level of 1 Bq/m^3 and decays by emission of a 0.687 MeV β with a half-life of 10.7 years. ^{39}Ar decays by emission of a 0.570 MeV β and has a half-life of 260 years. ^{42}Ar decays by emission of a 0.600 MeV β and has a half-life of 33 years. Purification is necessary to remove these gases from the scintillator if contamination occurs. Waiting for them to decay is not a viable strategy for their removal due to their long half-lives.

Contamination problems posed by ^{222}Rn do not end when the radon decays. There are several daughter nuclides of radon which decay farther until the stable ^{206}Pb isotope is reached. The most important contaminant among these daughters is ^{210}Pb because of its relatively long 22.3 year half-life. While waiting is an effective technique for reducing radon activity in the scintillator, this cannot be effective on a useful time scale for ^{210}Pb activity. Any radon which decays in the scintillator will produce ^{210}Pb contamination. The long life of ^{210}Pb also causes concerns during construction. If construction takes place in a radon-containing atmosphere, radon decays during the assembly can deposit ^{210}Pb on the surfaces of components in the experiment. Scintillator contacting these components can then be contaminated. For this reason it is important to minimize the radon content of the air during construction and the exposure time of component surfaces to air. These surfaces must be cleaned to remove ^{210}Pb before contacting them with scintillator. Because ^{210}Pb is a metallic impurity, its removal should be possible using appropriate techniques.

B. Purification Strategies Used in the CTF

The discussion in the previous section provided a detailed look at the sources of several contaminants expected to be of concern in Borexino. The CTF was constructed in order to show that contamination can be effectively managed in a liquid

scintillation detector. The detector had to demonstrate that the necessary optical properties could be achieved and maintained over a period of years. The CTF was designed to measure the levels of several radioactive contaminants in the liquid scintillator and to test the ability of a purification system to remove them if necessary. It was also expected to show if there were any other unexpected contaminants whose presence could affect the experiment. All of the contaminants mentioned in Section 3.A except ^{14}C can be removed by using appropriate purification methods. Before discussing these methods in detail, it is first important to understand the overall purification concept used in the CTF.

The CTF purification system was designed to purify the scintillator on-line. This meant that the scintillator could be purified after it was introduced into the scintillator containment vessel. During purification, scintillator was removed via a pipe connected to the bottom of the containment vessel. It was then transported to the purification system on top of the shielding water tank by a pump at the top of the tank. After purification operations were performed, the purified scintillator collected in a holding vessel under a low-pressure nitrogen blanket. A small pressure head allowed the scintillator to flow through a pipe back into the top of the containment vessel. This arrangement minimized the stresses on the nylon containment vessel.

The purification system had to be carefully designed and operated so that it did not contaminate the scintillator during attempts at purification. The plant had to be free of dust particle contamination, surface plating of ^{210}Pb, and radon emanation from materials used in its construction. The system had to be air-tight to prevent contamination by radon and other radioactive gases due to air exposure. It was also important that the scintillator optical properties were not degraded during purification operations.

On-line purification is important for maintaining the optical properties of the scintillator over a period of years. The shielding water diffuses slowly through the nylon vessel and can cause scattering problems as outlined in Section 3.A.1. The on-line purification system allows removal of this water before it builds up to potentially harmful levels. The scintillator itself can also degrade over time, and on-line purification allows removal of the degraded portion of the scintillator.

The on-line purification concept is also useful for management of radioactive contaminants. It was recognized that during the initial filling of the detector with scintillator, some contamination could occur. The on-line system would allow removal of this contamination. Slow leaching of contaminants from materials in the detector could result in an eventual buildup that could be removed by an on-line system. The same holds true for radon emanation from construction materials. If the radon emanation levels are too high, the purification system will not be effective because the required processing rate to remove this continual influx of radon will be beyond its capabilities. This is especially true if large amounts of radon emanate from the nylon scintillator containment vessel.

While the on-line purification system is designed to be quite effective, the most desirable approach for obtaining a pure scintillator is to minimize the initial contamination levels in the scintillator as much as possible. For this reason, scintillator purification by means other than the scintillator purification plant was carried out before introducing the liquid into the detector. The pseudocumene solvent for the CTF was obtained fresh from a distillation column at a plant in Sardinia and brought immediately underground at LNGS. Because distillation effectively removes ^{7}Be contamination, as shown by studies at Princeton,[4] and the immediate shipping allowed a negligible amount of time for recontamination, this technique effectively eliminated the ^{7}Be problem. The PPO fluor was also treated prior to the initial filling.

Based on experiments carried out at Princeton[3] which showed that water extraction was an effective method for removing potassium from the fluor, concentrated mixtures of pseudocumene and PPO were purified manually by several batch extractions before the fluor was mixed with the bulk of the solvent. This scintillator was then sparged with nitrogen inside a large holding tank to provide good mixing and to remove radon.

The scintillator purification system designed for the CTF consisted of four basic operations: microfiltration, water extraction, vacuum distillation, and nitrogen stripping. They were chosen for their general efficacy in removing broad classes of contaminants and not for the removal of specific species.

Filtration is included to remove particulate matter which is too large to pass through the pores of the filter. Large dust particles containing uranium, thorium, and potassium can be removed in this manner. The filter with the smallest commercially available pore size, 0.05 μm, is used in the CTF.

Water extraction was implemented to remove impurities which are more soluble in water than in the organic scintillator phase. This includes ionic and polar impurities, as well as dust particles. Uranium and thorium can be removed by this technique, whether present in metallic form or as oxides. Many uranium and thorium daughters can also be removed by water extraction. Water extraction is effective for removing many metal impurities from the scintillator because water can oxidize the metals while the organic cannot. The free energy change upon oxidation is shown in Table 3.1 for several metals which are potential contaminants in Borexino. The large negative free energy values indicate that oxidation is thermodynamically favorable for all the metals listed except lead. The metals for which oxidation is thermodynamically favorable will be effectively removed by water extraction. Another purification technique is needed to remove lead.

Table 3.1. Free energy change upon oxidation of metals. The free energy change for the reaction

$M^0 + n\ H_2O \rightarrow M^{n+}(aq) + n\ (OH)^- + n/2\ H_2$

is listed for several metals. The value for lead is positive, indicating that oxidation of lead is not thermodynamically favorable. The Po number is based on the rather sparse data available for that metal and may not be reliable. Data from the *CRC Handbook*.[9]

Metal	ΔG (kJ/mol)
$K \rightarrow K^+$	-202
$Ra \rightarrow Ra^{2+}$	-399
$U \rightarrow U^{4+}$	-206
$Th \rightarrow Th^{4+}$	-380
$Be \rightarrow Be^{2+}$	-217
$Bi \rightarrow BiO^+$	-146
$Pb \rightarrow Pb^{2+}$	+138
$Po \rightarrow Po^{2+}$	-24

Small dust particles will migrate to the aqueous phase from the organic phase. The change in free energy for a small particle of radius a_p and charge Q moving from phase 1 with dielectric constant ε_1 to phase 2 with dielectric constant ε_2 is

$$\Delta G = -\frac{Q^2}{8\pi\varepsilon_0 a_p}\left[\frac{1}{\varepsilon_1} - \frac{1}{\varepsilon_2}\right] \qquad (4.1)$$

Most dust particles have a net charge, and this equation indicates that their removal from the scintillator having $\varepsilon = 2.27$ to water having $\varepsilon = 80.4$ is energetically favorable.

The purpose of distillation is to remove any impurities having a volatility less than that of the scintillator. In distillation, the scintillator components are vaporized, transported to another vessel, and condensed, while less volatile impurities remain in the vessel in which the vaporization was carried out. Distillation in the CTF purification plant is run under vacuum conditions so that the scintillator will vaporize at lower temperatures. The lower temperatures reduce the likelihood of its thermal degradation and help preserve the scintillator optical properties. A simple one-stage distillation is used in the CTF because the scintillator is a two-component mixture of solvent and fluor, and fluor must not be lost from the scintillator during the distillation. Impurities removed by distillation include dust particles, metallic impurities, organo-metallic complexes, and polymerized scintillator molecules. Because of its ability to remove organic compounds which have a volatility different than that of the scintillator, distillation helps to maintain the scintillator optical properties.

Nitrogen stripping plays several roles in the purification strategy. One obvious function is to remove radioactive gases such as radon, krypton, and argon. When scintillator contaminated with these gases is contacted with nitrogen, the contaminants will partition between the two phases, resulting in the removal of some of the gas from the scintillator. This results in an effective purification of the scintillator, assuming

that the stripping nitrogen is initially free of the radioactive gases. Nitrogen stripping also removes water which was introduced during the water extraction operation from the scintillator. This is important because the scintillator is saturated with water after the extraction and temperatures in the purification plant are normally warmer than in the containment vessel. If the scintillator was returned to the containment vessel without removing the water, water droplets would form as the scintillator cooled. Stripping also removes oxygen from the scintillator.

C. Laboratory Tests of the Efficacy of Purification Processes

i. Maintenance of Optical Properties

The various purification processes have been studied in the laboratory to determine their effect on the optical properties of the scintillator. These results are often quoted in terms of attenuation length. The attenuation length is the distance a beam of light of a certain wavelength can travel through the scintillator before its intensity is reduced by a factor of e. The measurements are commonly made in 1 cm cuvettes using an absorption spectrophotometer. The techniques used to measure these attenuation lengths will be presented in more detail in Chapter 5. Early experiments at Princeton[3] showed that batch distillation of pseudocumene at atmospheric pressure increased its attenuation length at 420 nm from 3.1 m to 7.4 m. Water extraction left the attenuation length essentially unchanged at 3.3 m. This indicates that many of the impurities that absorb light in the pseudocumene are less volatile than it is and can be effectively removed by distillation.

More extensive tests on the effects of purification on scintillator optical properties have since been conducted. The attenuation length of pseudocumene as a function of wavelength is shown in Figure 3.2 for pseudocumene samples which have undergone different distillation procedures. Values are shown for undistilled

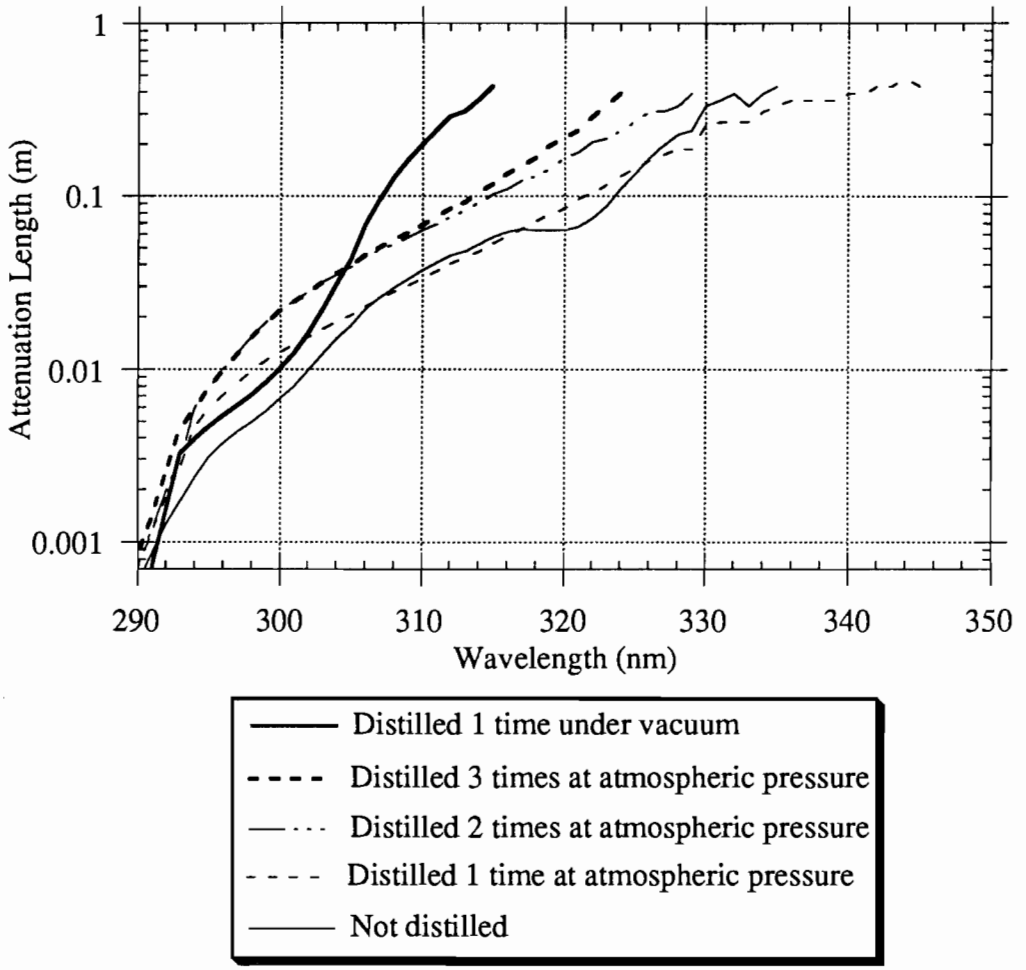

Figure 3.2. Attenuation length in pseudocumene after different distillation treatments. The attenuation length at wavelengths from 290 to 350 nm was measured in pseudocumene samples which had undergone various distillation procedures. Samples included undistilled pseudocumene and pseudocumene which had been distilled once, twice, and three times at atmospheric pressure. A sample distilled under a vacuum of 28.5 inches of water was also examined.

pseudocumene and for the same solvent after one, two, and three distillations at atmospheric pressure. Results after one distillation carried out under a vacuum of 28.5 inches of mercury are also shown. The spectrophotometer used for these measurements cannot accurately measure attenuation lengths of more than 60 cm, and all the curves are terminated when they reach this value. One atmospheric distillation did not significantly improve the attenuation length of the scintillator, and the attenuation length actually became slightly shorter beyond 325 nm. The distillation did remove an impurity indicated by the dip in the attenuation length of the undistilled pseudocumene at 320 nm. The second distillation had a marked effect on the attenuation length, and the third provided a small improvement in optical clarity. The best attenuation lengths above 305 nm came from the sample which was distilled once under vacuum conditions. This indicates that thermal degradation which can occur in the scintillator when it is distilled under atmospheric pressure may be avoided by using the lower temperatures required for vacuum distillation.

The effect of filtration on scintillator optical properties was also explored in the laboratory. Filtration should reduce the number of particulates in the liquid and decrease the scattering which these particles cause, increasing the attenuation length. Attenuation lengths for undistilled pseudocumene are shown in Figure 3.3 before and after filtration with a 0.10 μm polyethylene filter. The filtration increased the attenuation length slightly for this sample. A similar plot is shown in Figure 3.4 for pseudocumene which had been distilled three times at atmospheric pressure. The filtration decreased the attenuation length of the thrice-distilled pseudocumene slightly at long wavelengths. The filtration may be unnecessary after several distillations because most particulate contamination would have been removed by the distillation. The decrease in attenuation length after filtration could be due to a small amount of impurity introduced by contact with the filter, although clean filters were used for the

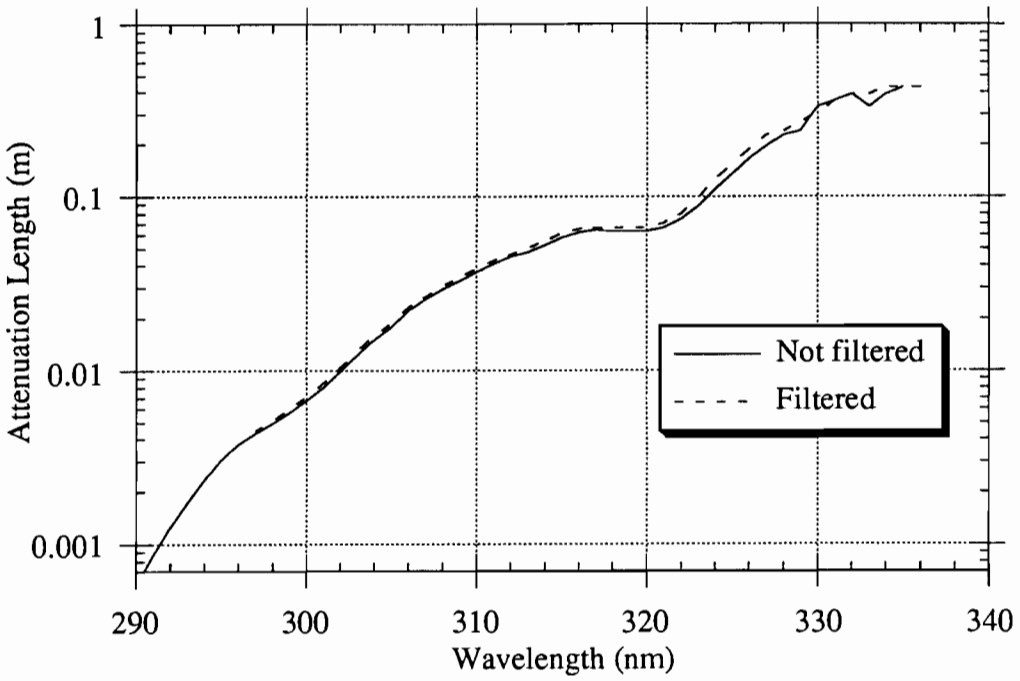

Figure 3.3. Attenuation length in undistilled pseudocumene before and after filtration. The attenuation length at wavelengths from 290 to 350 nm was measured in samples of undistilled pseudocumene. One sample was unfiltered and the other was filtered with a 0.10 μm polyethylene syringe filter.

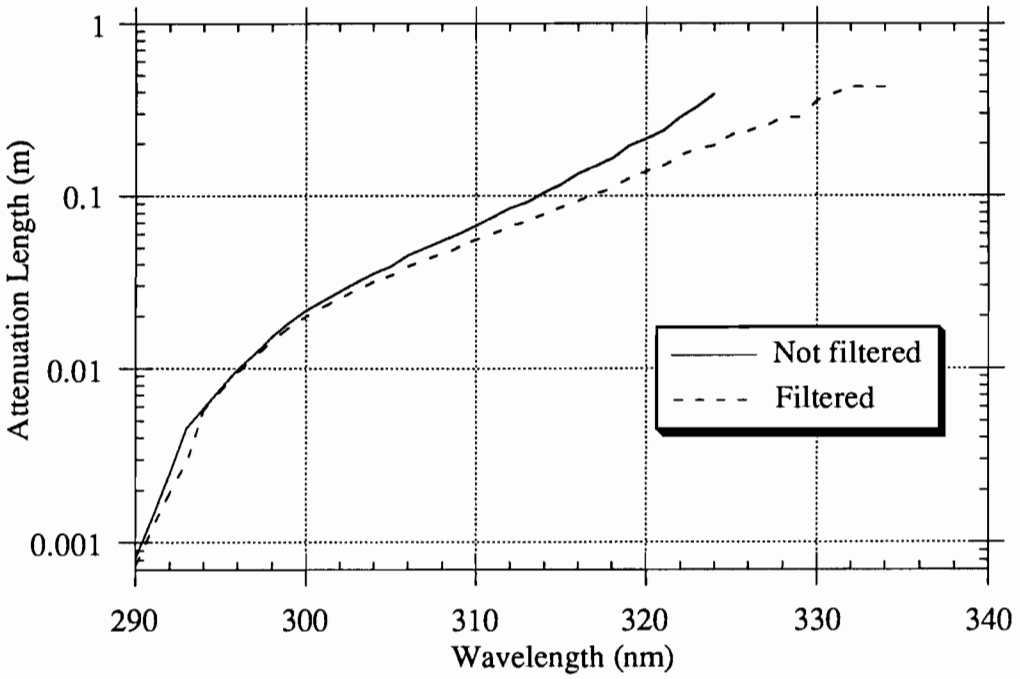

Figure 3.4. Attenuation length in thrice-distilled pseudocumene before and after filtration. The attenuation length at wavelengths from 290 to 350 nm was measured in samples of pseudocumene which had been distilled three times at atmospheric pressure. One sample was unfiltered and the other was filtered with a 0.10 μm polyethylene syringe filter.

operation. The attenuation length in water was found to increase to a much greater extent upon filtration with a 0.22 μm cellulose acetate filter. Filtration may be more effective at increasing the attenuation length in water than in organic scintillator because dust particles have a greater affinity for the aqueous phase.

Nitrogen sparging is very important for obtaining accurate attenuation length measurements in the laboratory, where it is used to remove oxygen from the scintillator samples. The effect of sparging on the attenuation length of pseudocumene can be seen in Figure 3.5, where the attenuation lengths before and after sparging for 10 minutes are shown for undistilled pseudocumene and for pseudocumene which had been distilled three times. The effect is of similar magnitude regardless of any previous distillation treatment of the pseudocumene.

The attenuation length measurements described here indicate that the purification procedures developed for the CTF do not adversely affect the scintillator optical properties. The distillation and nitrogen sparging operations can significantly improve the optical clarity of the liquid. The ability of purification to maintain these properties over time must be tested using the CTF itself.

2. Removal of Radioactive Impurities

Before the CTF purification plant was constructed to test the ability of the purification processes described in Section 3.B to work at extremely low levels (close to those required for Borexino), some of them were tested in the laboratory on a less sensitive scale. Uranium and thorium levels can be measured to a level of 10^{-12} g/g using inductively coupled plasma mass spectroscopy (ICPMS), and potassium contamination can be measured with a sensitivity of 10^{-9} g/g using neutron activation. Neither of these measurements has the sensitivity required for Borexino, but they were useful in setting limits on the contamination in the scintillator prior to operation of the CTF.

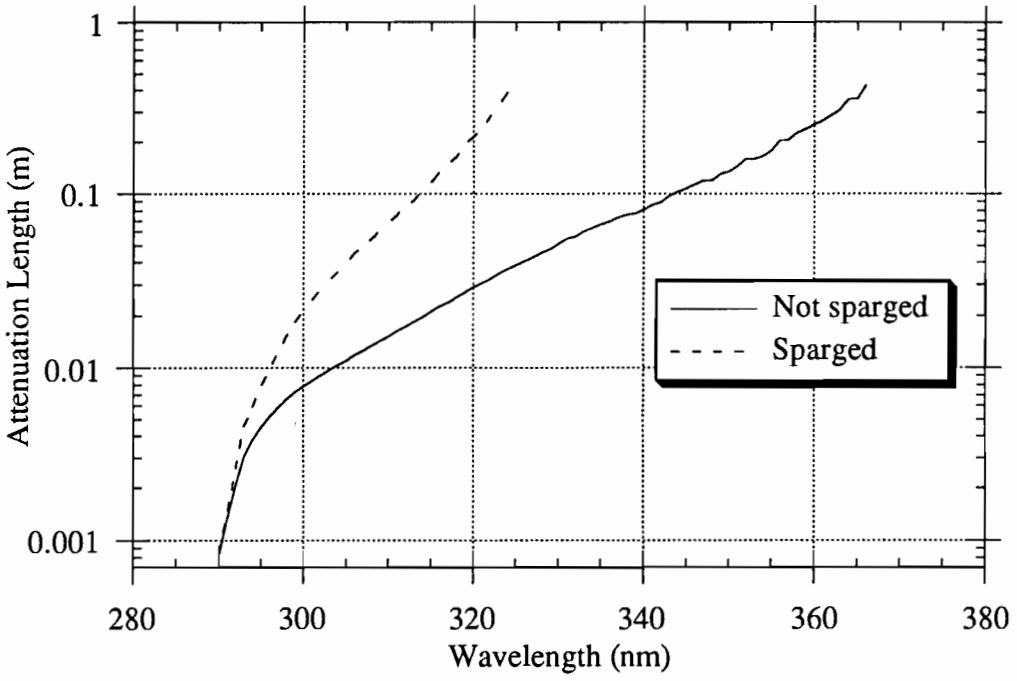

Figure 3.5. Attenuation length in thrice-distilled pseudocumene before and after nitrogen sparging. The attenuation length at wavelengths from 290 to 350 nm was measured in pseudocumene samples which been distilled three times at atmospheric pressure. One sample contained oxygen in equilibrium with the atmosphere. The other was sparged with nitrogen for 10 minutes inside a glove box to remove the oxygen.

The scintillator components pseudocumene and PPO were analyzed using ICPMS and neutron activation prior to any purification operations.[3] The uranium and thorium levels in both components were below the limit of detectability. A ^{40}K level of 2×10^{-6} g/g was found in the PPO. The PPO was water extracted in two ways to attempt to reduce the amount of potassium in it. In one trial, water was contacted with the solid PPO, which is almost insoluble in the water. In the other trial, a concentrated pseudocumene-PPO solution was mixed and shaken with water. While water contacting with solid PPO was ineffective, water extraction of the pseudocumene-PPO mixture reduced the potassium level in the PPO below the sensitivity limit of the neutron activation. This technique was used for pre-purification of the fluor used in the CTF, as described in Section 3.B.

Other experiments were performed to determine the solubility of uranium in the pseudocumene solvent.[3] A sample of uranyl nitrate (10 g) was placed in pseudocumene (100 ml) and the liquid was brought to a boil for 10 minutes. Upon cooling, the uranium level in the pseudocumene was still below the limit of detectability of ICPMS. A sample of water (100 ml) was then prepared by dissolving uranyl nitrate (10 g) in it. This sample was contacted with pseudocumene (100 ml) in a water extraction procedure. After this contacting, the uranium content in the pseudocumene was again below the sensitivity of the measurement. These experiments confirmed that uranium is very insoluble in the organic scintillator and set a limit of $> 10^9$ on the partition coefficient of uranium between water and pseudocumene. The partition coefficient is equal to the ratio of the mass fractions of uranium in the two phases.

The effectiveness of ^{7}Be removal by various purification methods was studied using the Princeton University cyclotron.[4] Pseudocumene samples were irradiated to produce a high concentration of ^{7}Be. This concentration was measured with the use of

a high purity germanium (HPGE) detector. The pseudocumene was then purified using both distillation and water extraction. One distillation step reduced the ^{7}Be concentration by a factor of greater than 1000 to below the limit of detectability of the HPGE instrument. Water extraction also reduced the ^{7}Be concentration, but not as drastically. It took 13 water extraction steps, contacting the scintillator volume with an equal volume of water each time, to achieve the same 1000-fold reduction. This test showed that distillation is a very effective means of removing ^{7}Be from the scintillator.

The measurements discussed above have shown that the purification processes chosen for the CTF scintillator purification system are effective for removing radioactive impurities from the scintillator. The actual purification system had to be operated in order to show that these procedures would remove impurities to the levels required for Borexino.

D. Design of the CTF Scintillator Purification Plant

A scintillator purification plant for the CTF incorporating the four operations discussed in Section 3.B was developed by the Princeton group of the Borexino collaboration with the help of Modular Process Systems, Inc. The engineers from this company utilized the conceptual design and laboratory data on the scintillator system provided by Princeton to size the equipment, design the piping layout, and develop the electrical and control systems. The stainless steel vessels and piping for the plant were constructed by the Allegheny-Bradford Company in Bradford, Pennsylvania. The plant was designed to be mounted inside a $2 \times 6 \times 2.5$ m skid to facilitate its transport overseas. Following construction, the plant was disassembled and sent for final cleaning at specialty cleaning companies: Central Electropolishing Co. in Lawrence, Kansas, and Precision Tube Finishing in Houston, Texas. This cleaning included a

final rinse with clean acid solutions and flushing with deionized water. The cleaned pieces were shipped to Italy inside sealed packages filled with clean nitrogen. Reassembly of the system, installation of the electrical and control systems, and operation of the plant was left to the Princeton scientists.

The selection of construction materials was crucial in the plant design to minimize potential contamination due to radon emanation and formation of particulates. For most of the plant, including the piping and vessels, 316L stainless steel is the material of choice. Stainless steel is relatively radiopure, it does not emanate much radon, and it can be cleaned with acid solutions prior to use. The stainless steel vessels and piping used in the plant were mechanically polished to an Ra 15 finish and then electropolished. (A Ra 15 finish is one in which the average roughness in the surface is 15 microinches.) A highly polished surface is desirable because it reduces the possibility of small particles breaking off from the surface. These particles would enter the scintillator and contaminate it. The manually operated valves in the plant are stainless steel Whitey ball valves, and the control valves are made of the same material. Some vessels in the plant are equipped with sight glasses to provide a view of their interiors, and these sight glasses are made from quartz. Piping connections in the plant are made using VCR metal gasket fittings with silver-plated nickel gaskets and Topline™ fittings using a clamped Teflon gasket. Filter cartridges are made of Teflon. The vessels are sealed by either Teflon-encapsulated viton O-rings or Teflon-polymer sandwich gaskets. In all the seals, scintillator only comes in contact with metal or Teflon. Teflon is a good polymer for use in a system of this nature because the radon emanation rate from it is much less than from other polymers. It is also resistant to acids, allowing them to be used for cleaning of the system. The pumps used in the system have a stainless steel pumping chamber, and the pumping action is provided by a Teflon diaphragm.

A schematic diagram of the purification plant is shown in Figure 3.6. The plant was designed to operate in two modes: water extraction and distillation. In water extraction mode, the scintillator is contacted counter-currently with high purity water, filtered, and stripped with nitrogen before being returned to the scintillator containment vessel. In distillation mode, the scintillator is vacuum distilled, filtered, and stripped with nitrogen. The plant is designed to operate with water extraction as the normal mode of operation. Distillation is to be used occasionally to maintain the optical properties of the scintillator. A piping and instrumentation diagram (P&ID) for the plant is shown in Figure 3.7. This diagram shows the nomenclature of the vessels in the plant, the piping connections between them, the locations of instrumentation, and the control loops to be implemented during operation.

If the purification plant removes a given contaminant completely from the scintillator passing through it, the level of the impurity in the scintillator containment vessel will decrease by a factor of e with each cycle of processing. A cycle is defined as the processing of a volume of scintillator equal to the volume of the containment vessel. This exponential decrease in the contamination level with each cycle will take place if perfect mixing occurs in the containment vessel. Imperfect mixing will alter the reduction from that observed in the ideal case. If the contaminant is not completely removed as scintillator passes through the plant, the reduction will be less than exponential.

The water extraction column is designed to provide five equilibrium stages of contacting between the scintillator and aqueous phases at flow rates of approximately 50 L/hr of scintillator and 10 L/hr of water. This requires a column 2 m tall and 75 mm in diameter; a schematic of this column is shown in Figure 3.8. Water enters 45 cm from the top of the column, and scintillator enters 15 cm from the bottom. The two phases flow counter-currently to each other due to their density difference. (The

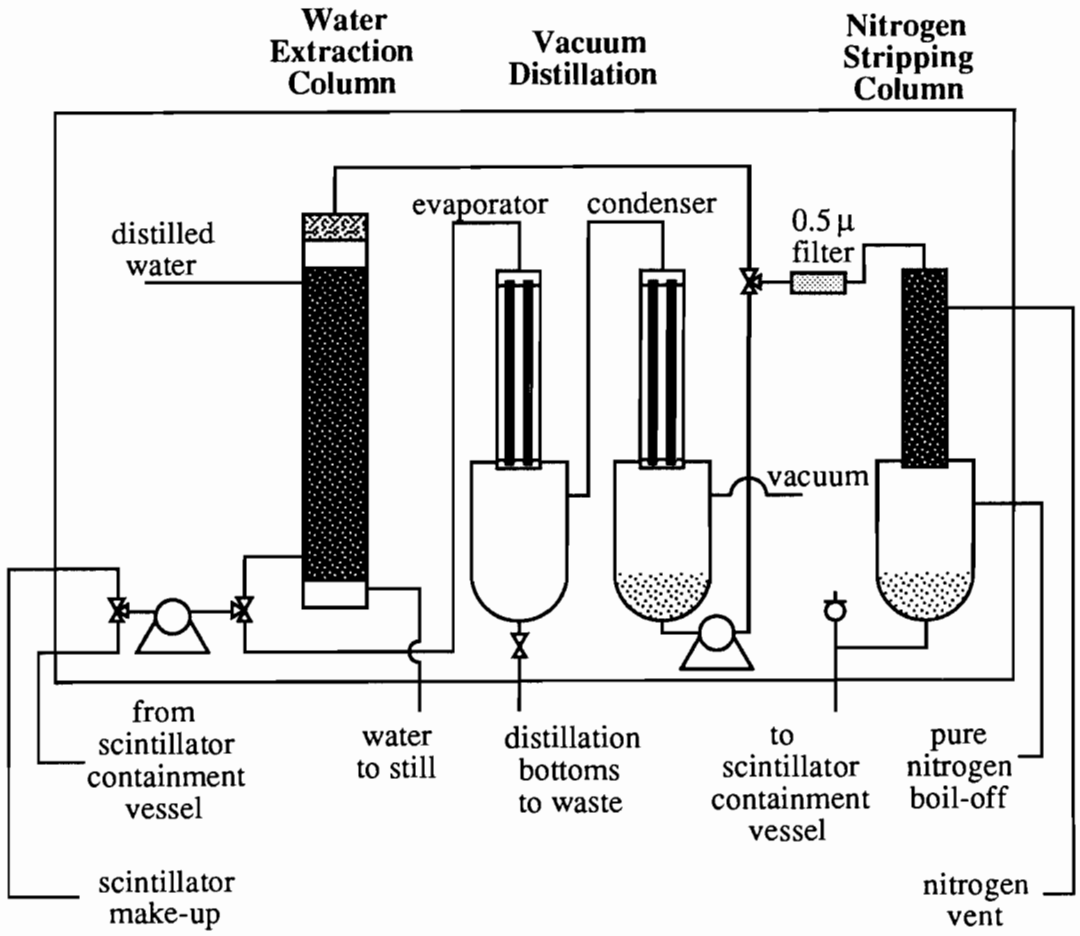

Figure 3.6. Schematic of the purification system in the CTF The scintillator is circulated from the scintillator containment vessel in the detector through either counter-current water extraction or vacuum distillation. The scintillator is then filtered and stripped of water and dissolved gases in a nitrogen stripping column. From Benziger et al.[2]

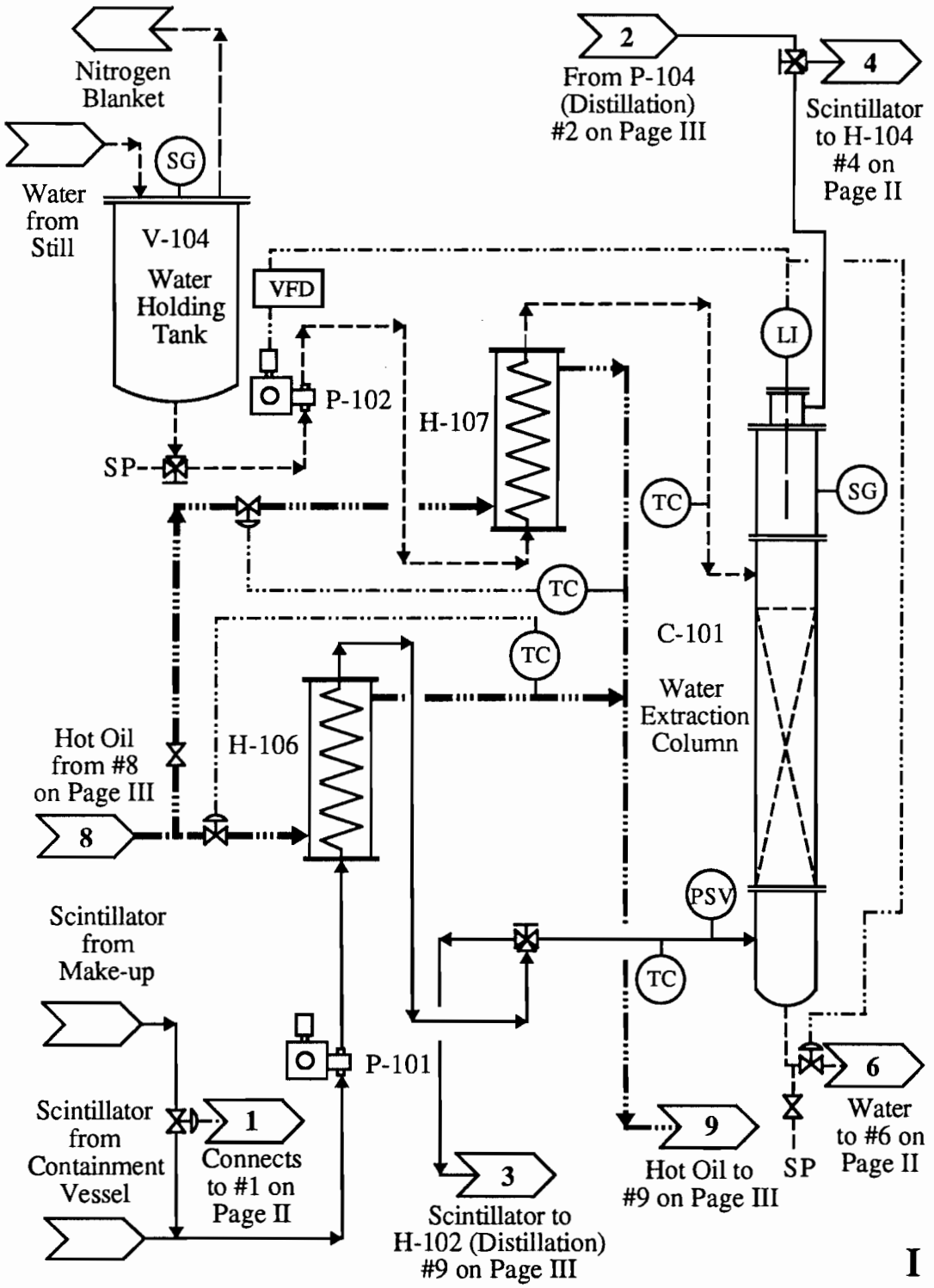

Figure 3.7. Piping and instrumentation diagram (P&ID) for the CTF scintillator purification plant. Part I shows the water extraction portion of the plant.

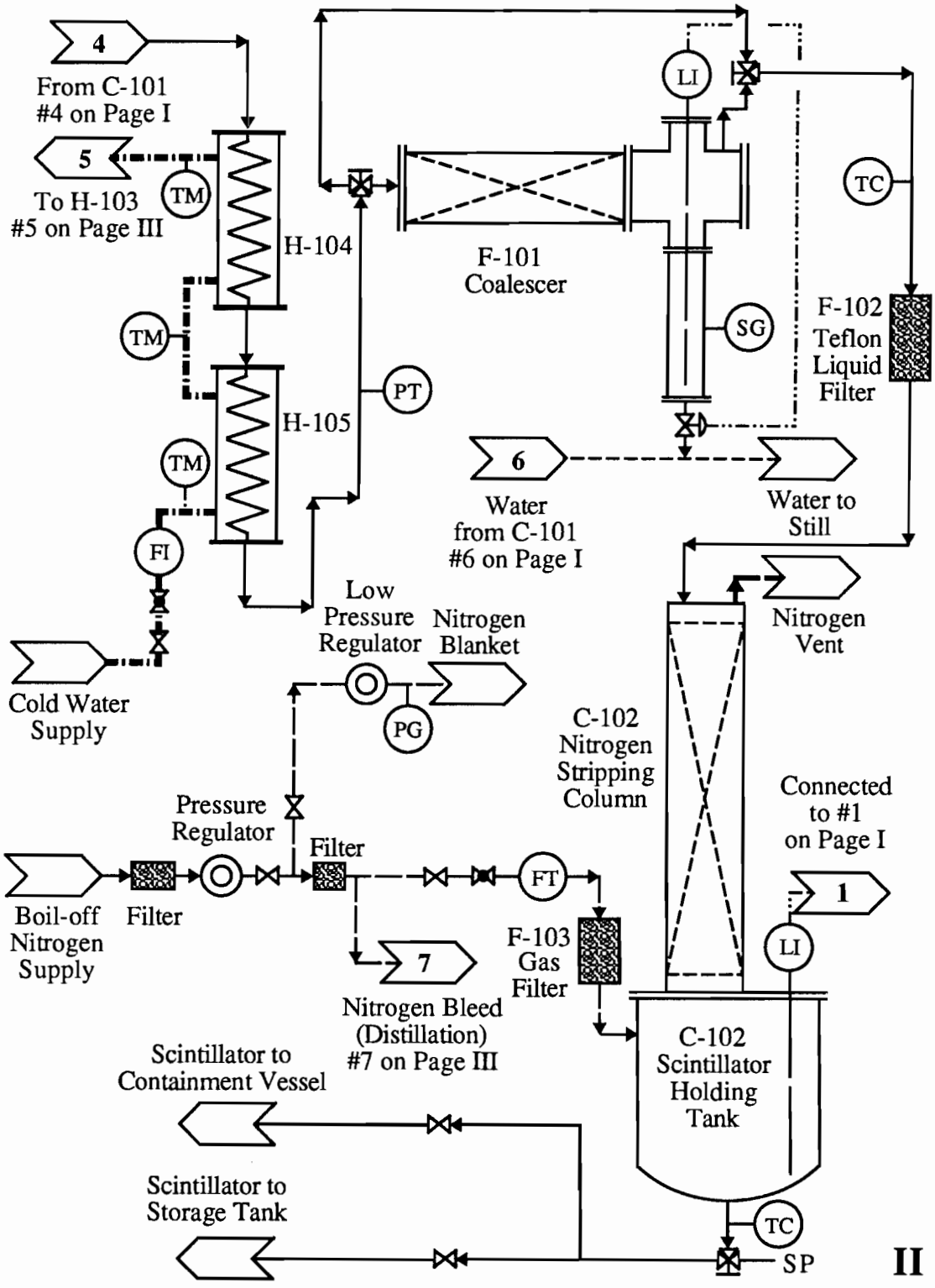

Figure 3.7. (cont.). Part II shows the water coalescer, the nitrogen stripping column, and the boil-off nitrogen distribution system.

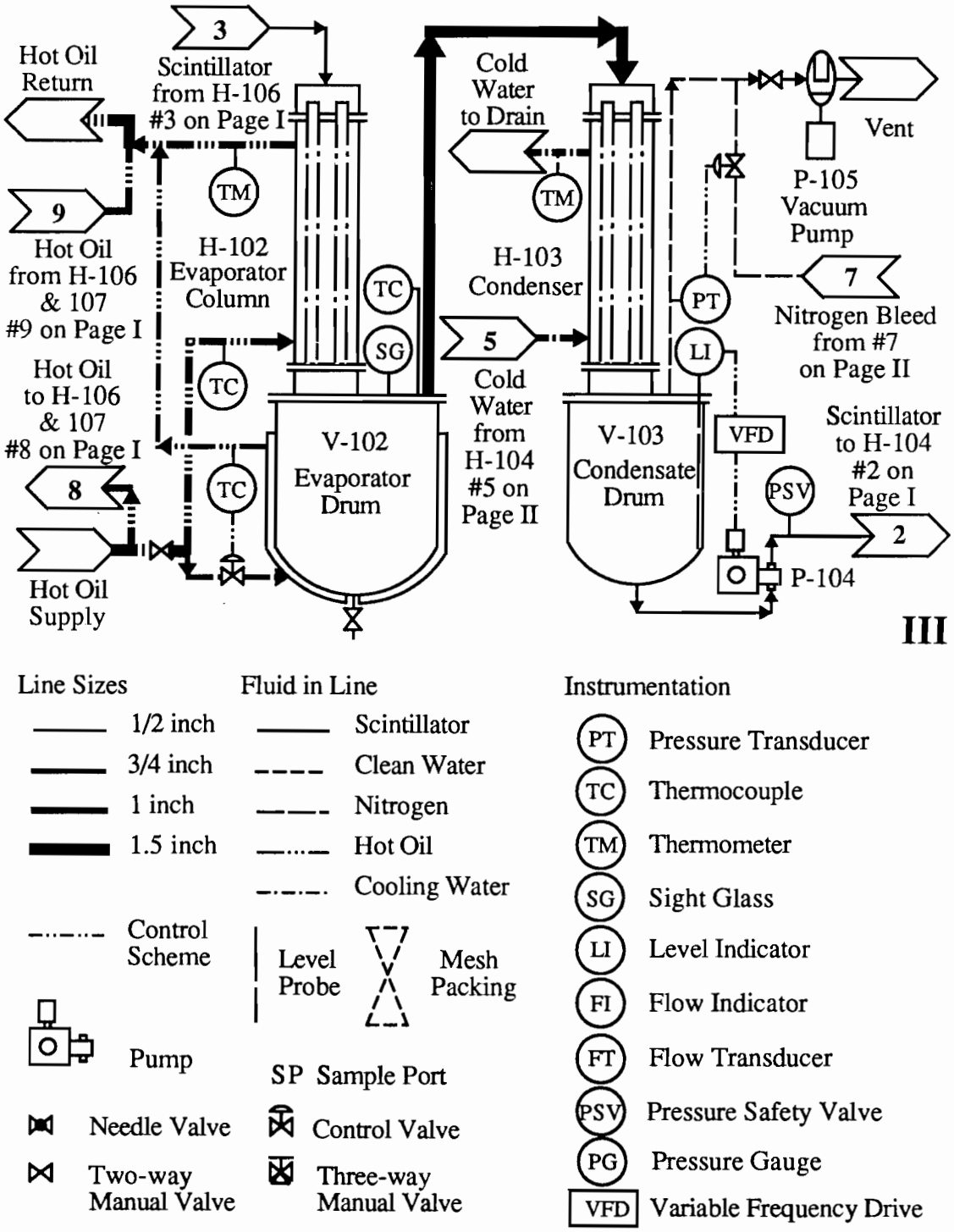

Figure 3.7. (cont.). Part III shows the distillation portion of the plant. The symbols used in the figure are also listed here.

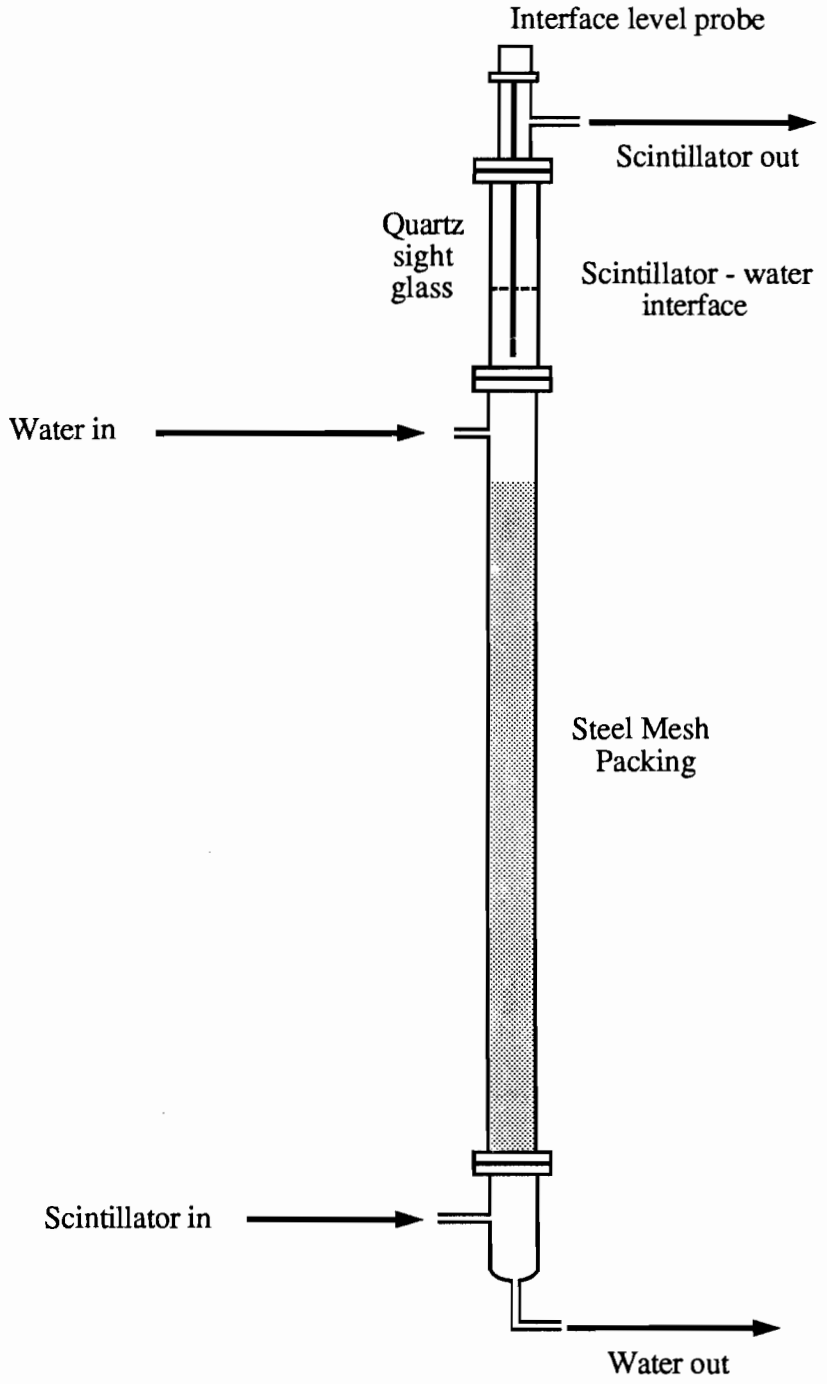

Figure 3.8. Schematic diagram of the water extraction column. The water extraction column was designed to remove impurities from the scintillator by contacting the organic phase with high purity water.

scintillator density is 0.88 that of water.) The column is packed with stainless steel mesh for a length of 130 mm between the two inlets to provide good contacting between the two phases. Water is the continuous phase in this portion of the column, and the scintillator is dispersed. Below the scintillator inlet, the two phases separate due to their immiscibility. Water is removed from the bottom of the column. The two phases also separate at the top of the column, and a scintillator-water interface forms here. The position of this interface is maintained inside a quartz tube through which it can be viewed. A capacitance probe monitors the location of this interface, and provides data to the control system to allow it to adjust the flow rate of the water in order to maintain the position of the interface while the scintillator flow rate remains constant. Scintillator is removed from the top of the column following water extraction.

An examination of Figure 3.7 will show that heat exchangers are located before and after the water extraction column. These heat exchangers are provided to allow for heated water extraction. In this mode of operation, the scintillator and water entering the extraction column are preheated in separate exchangers to approximately 80 °C. Water extraction at elevated temperatures may be favorable because the solubility of ions in water increases with temperature. The heating is provided by hot oil in the jacket of the heat exchanger, while the water and scintillator pass through a coiled tube in each exchanger.

Following heated water extraction, the scintillator is cooled by passing it through two heat exchangers having cooling water flowing through their jackets. Because the solubility of water in pseudocumene increases at higher temperatures, this cooling will cause the formation of many small water droplets. These droplets are to be removed by a water coalescer following the cooling heat exchangers. The water coalescer is a horizontal vessel filled with mesh packing. The water droplets are to

collect on the mesh packing until they form drops large enough that gravity causes them to sink to the bottom of the vessel. The vessel is slightly tilted so that water at the bottom will flow into a quartz collection tube, where its level can be monitored and from which the water can be periodically removed. Water extraction is also followed by nitrogen stripping to remove any residual water.

The quality of the water used in the extraction process is crucial to its success. This water is initially obtained from the CTF water plant,[10] which has been shown to be very effective for removal of ionic impurities. After an initial charge of water is loaded, the water is used in a closed loop. Upon leaving the water extraction column, the water passes to a still, where it is boiled to remove any impurities picked up during the extraction. The distilled water vapor is then condensed and collected in a 50 L tank from which it can be returned to the extraction column. A nitrogen blanket is provided over this tank. This blanket maintains the pressure in the tank as the liquid level changes and prevents radon contamination which would occur if the system was open to the atmosphere. The use of a closed loop minimizes radon contamination in the water. The water still is completely separate from the scintillator distillation plant. The still was obtained separately from the rest of the plant and it is mounted outside the purification skid.

The one stage vacuum distillation is accomplished using an falling film evaporator column and a condenser column, which are shown schematically in Figure 3.9. The nominal processing rate of this unit is 20 L/hr. The falling film evaporator consists of a pipe 65 mm in diameter and 110 cm in height with three 19 mm diameter tubes arranged in a triangular pattern inside it. The walls of the tubes are heated by hot oil flowing in the pipe enclosing them. Scintillator enters at the top of the column and spills into the tubes through V-shaped grooves. The scintillator quickly evaporates as it comes in contact with the hot walls of the tubes. Below the

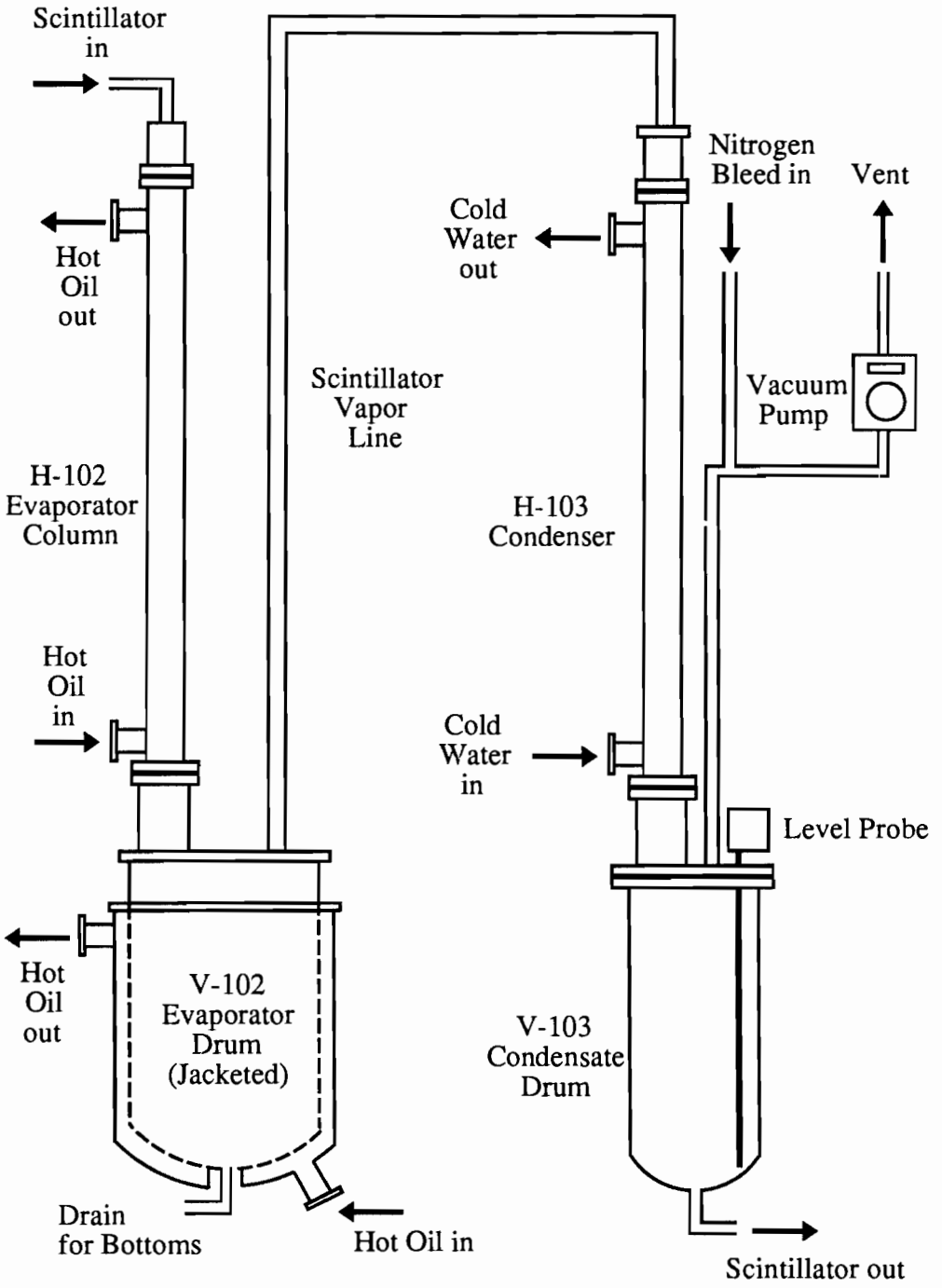

Figure 3.9. Schematic diagram of the vacuum distillation unit. The distillation unit purifies the scintillator by removing contaminants with a volatility less than that of the scintillator components.

evaporator column is a jacketed evaporator drum whose walls are also heated with hot oil. Impurities with low volatility collect here, and they can be purged through a drain in the bottom of the vessel. Scintillator vapor passes through the evaporator drum and to the top of a condenser column. This column is almost identical to the evaporator column, but in the condenser water flows in the pipe enclosing the tubes to provide cooling. The cooling condenses the scintillator, and it collects in a 30 L condensate drum. The liquid level in this drum is monitored with a capacitance level probe. Data from this probe are used to control the speed of a pump which removes scintillator from the drum and returns it to the scintillator containment vessel.

The entire distillation procedure is carried out under vacuum conditions. This vacuum is provided by a mechanical vacuum pump connected to the condensate drum. The arrangement allows a vacuum to be pulled from the evaporator column through to the condensate drum. The vacuum level is monitored by a pressure transducer in the condensate drum. It is controlled by bleeding nitrogen into the system between the condensate drum and the vacuum pump.

During distillation, the scintillator passes through the same heat exchangers as it does during water extraction. The first heat exchanger serves to preheat the scintillator before it enters the evaporator column, and the second pair cools it further following condensation.

After both distillation and water extraction, the scintillator passes through the filter and the nitrogen stripping column before being returned to the scintillator containment vessel. Filtration by the 0.05 μm Teflon filter is provided near the exit of the purification plant in order to remove any particulates which may have become entrained in the scintillator as it passed through the plant.

Nitrogen stripping follows the filtration. It takes place in a column 100 mm in diameter and 100 cm in height as shown schematically in Figure 3.10. This column is

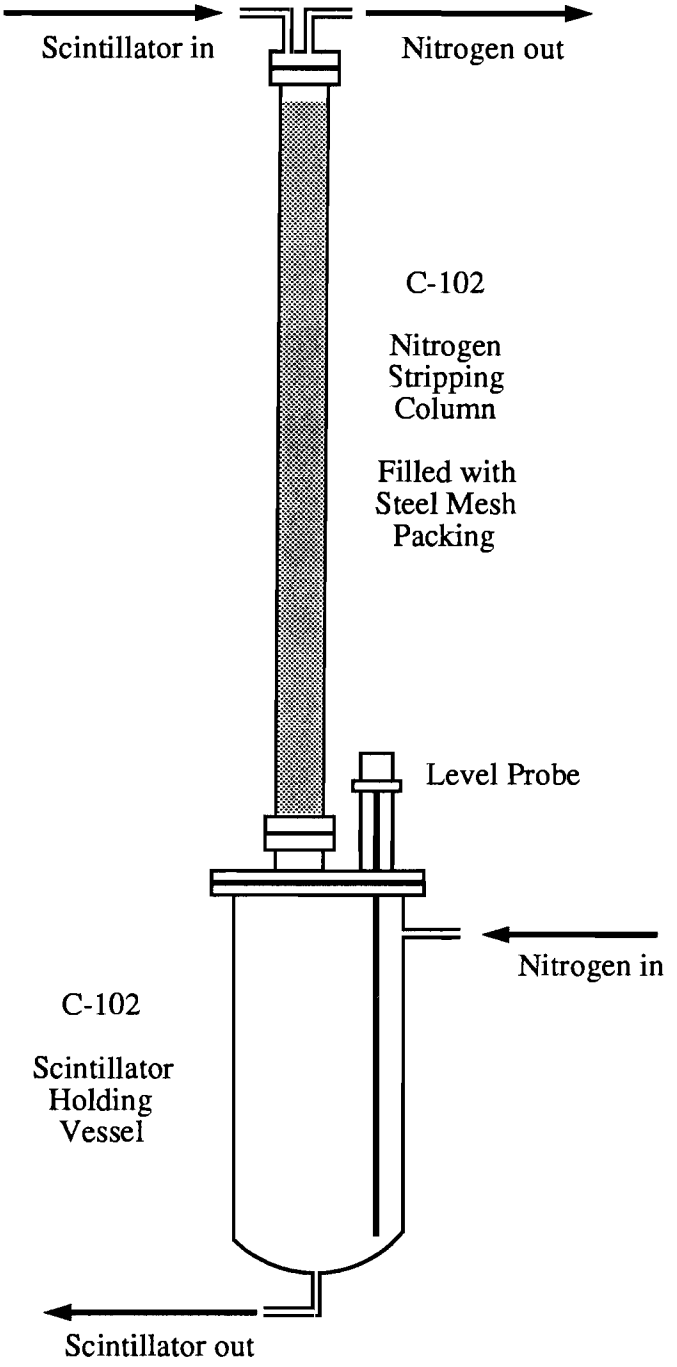

Figure 3.10. Schematic diagram of nitrogen stripping column. The nitrogen stripping column removes gaseous impurities from the scintillator by contacting it with high purity nitrogen.

packed with the same stainless steel mesh which is used in the water extraction column. Scintillator enters at the top of the column and trickles downward over the mesh packing. Nitrogen enters at the bottom of the column and flows counter-currently to the scintillator. The column is designed to give 2 – 3 equilibrium stages for removal of water from the scintillator at 20 °C with flow rates of approximately 50 L/hr of scintillator and 2 – 3 m^3/hr of nitrogen. The stripping reduces the amount of water in the scintillator to less than 10% of its saturation value.

The stripping column design is based on removal of water from saturated scintillator. At saturation, the water dissolved in the scintillator has a chemical potential equal to that of pure liquid water. The solubility of water in pseudocumene is known to be 100 ppm at 20 °C, and this can be used to calculate an activity coefficient at saturation for water in pseudocumene of 1500. If this activity coefficient is assumed to be independent of composition and the water behavior in the gas phase is assumed to follow the ideal gas law, the stripping performance of the column can be predicted. The column was designed to remove water, but it is also effective for removing noble gases. This removal will be somewhat less effective than that of water because, based on the relatively sparse data available on noble gas solubility in pseudocumene, the activity coefficients for these gases in the solvent are less than that of water.

Following nitrogen stripping, the scintillator collects in a 40 L scintillator holding vessel below the stripping column. Scintillator flows back into the scintillator containment vessel under the influence of pressure head; the pressure head in the scintillator holding vessel is very important. The plant is designed to maintain the containment vessel in a fully inflated state at all times in order to preserve its spherical shape. Under design conditions there is a solid column of scintillator from the scintillator holding vessel to the scintillator containment vessel. The height of the

scintillator holding vessel was chosen so that when the scintillator level is maintained inside it, the liquid height causes enough pressure inside the containment vessel to equalize the inward pressure exerted on it by the surrounding shielding water. The required scintillator level is higher than the level of the shielding water because the scintillator is less dense. If the scintillator level rises too high, undesirable stresses are placed on the nylon containment vessel. The scintillator level in the scintillator holding vessel is monitored by a capacitance level probe. The nitrogen pressure above the liquid in the scintillator holding vessel is also quite important because it is transmitted directly to the scintillator containment vessel along with the pressure head caused by the liquid height. Because of this, the pressure drop of the nitrogen through the stripping column and the nitrogen vent line must be minimized, and the pressure above the scintillator holding vessel must be very close to atmospheric. If the scintillator containment vessel is not completely inflated, the liquid pressure head in the scintillator holding vessel is not transmitted to it, but the nitrogen pressure still is.

The purity of the stripping nitrogen is of great importance to the overall effectiveness of the stripping operation. In order to obtain the highest purity nitrogen possible, the stripping nitrogen is provided from the gaseous phase of a liquid nitrogen tank. This boil-off nitrogen should be especially pure because radioactive gas contaminants such as radon and krypton have boiling points higher than that of nitrogen and should preferentially remain in the liquid phase. The nitrogen flow is controlled by a pressure regulator in the purification plant and a needle valve. The flow rate is monitored by measuring the pressure drop across an orifice plate. A second low-pressure regulator at the nitrogen input provides clean blanket nitrogen for the plant.

The purification plant was designed to operate under computer control. This control was provided by a GE Fanuc 90-30 series programmable logic controller

(PLC). The PLC was interfaced with a personal computer to allow programming of the PLC and to provide a graphical display of plant operating conditions. Although the control loops in the plant were specified by Modular Process Systems, the actual programming to implement these schemes was left to the Princeton group. The PLC was programmed using ladder logic commands which proved to be quite versatile.

Data on plant conditions had to be provided to the PLC in order for it to control the system. Some of this instrumentation has been described previously: capacitance level probes in the water extraction column, water coalescer, condensate drum, and scintillator holding vessel; a pressure transducer in the condensate drum; and a nitrogen flow meter. Information is also provided by another pressure transducer in the plumbing after the water extraction column and by eight thermocouples which measure the temperature of the scintillator and hot oil at locations in the plant as shown in Figure 3.7. Additional temperature information is provided by manually read thermometers which measure hot oil and cooling water temperatures. The level probes are Teflon coated to maintain plant cleanliness. The thermocouples and thermometers do not directly contact the fluids in the plant; they are mounted in stainless steel thermowells.

The PLC controls the plant by manipulating the settings of seven control valves and the speeds of two pumps. The control loops in the plant are shown in Figure 3.7. Some of the controlled parameters include the water flow rate through the water extraction column, the flow rate of hot oil through the evaporator drum jacket and the evaporator column, the removal rate of scintillator from the condensate drum, and the amount of nitrogen bleed to maintain the correct vacuum in the condensate drum. The control system was also designed to introduce make-up scintillator to replace any that was lost during purification in order to maintain the liquid level in the scintillator holding vessel at a constant level, but this feature was never implemented.

Other changes to the plant must be made manually. These include adjustment of the rate of scintillator removal from the scintillator containment vessel, adjustment of cooling water flow rate, adjustment of stripping nitrogen flow rate, and conversion of the system from water extraction mode to distillation mode.

E. Assembly and Operation of the Purification Plant

The purification plant was constructed in the United States, disassembled for cleaning, and shipped to Italy in a disassembled condition. A photograph taken during construction of the plant at Allegheny-Bradford is shown in Figure 3.11. Many of the plant vessels are visible in the photograph. The electrical and control systems were not installed in the plant at the time of construction, and no operational tests of the plant were performed prior to its shipment to Italy. The disassembled plant arrived at LNGS in December 1994. The skid in which the plant was to be mounted had arrived previously and was positioned on the top of the water shielding tank. A class 100 cleanroom was constructed around the skid. (A class 100 cleanroom contains less than one hundred 0.1 μm particles per cubic foot.) The purification cleanroom was constructed to minimize contamination of the purification plant by dust when the sealed packaging was opened and the pieces were reassembled. The purification cleanroom can be seen on top of the shielding water tank in Figure 2.5.

The purification plant was assembled in Italy over a period of approximately six months. This included time for cleaning, installation of electrical and control systems, and operational tests of the system. Many modifications to the original plant design were made during this period. The following section describes the assembly and operation of the plant chronologically. Results of the major purification processes will be given in the next section.

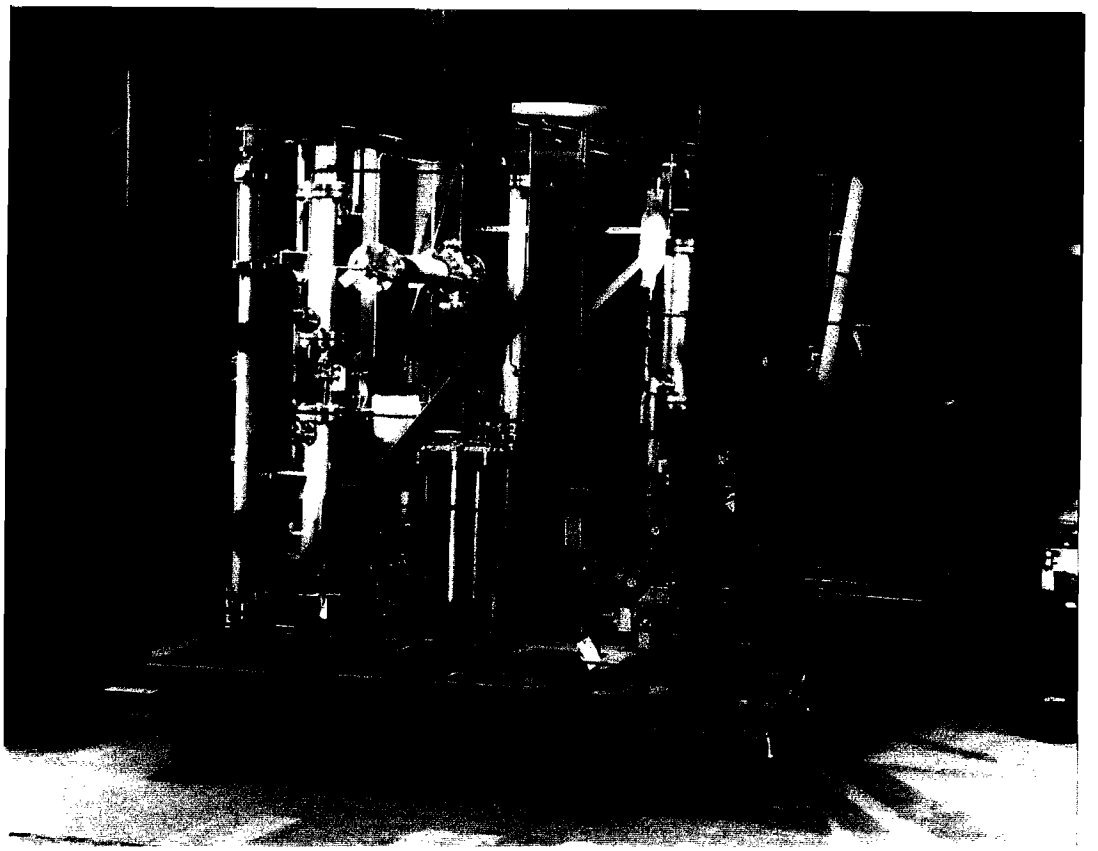

Figure 3.11. Construction of the purification plant at Allegheny-Bradford. Many of the plant vessels, including the distillation unit, the water extraction column, and the nitrogen stripping column can be seen in the photograph.

Assembly of the purification plant began with the installation of the vessels and columns inside the purification cleanroom. The piping and valves, including the control valves, were installed next. The pumps were also installed at this time. High pressure nitrogen was provided to operate the pneumatic control valves. It was connected through a pressure regulator and a manifold of valve actuators controlled by the PLC. During this assembly, efforts were made to minimize contamination of the surfaces inside the plant by opening the sealed equipment packages just prior to installation and capping the exposed ends of piping to prevent dust from entering.

The purification system was cleaned extensively both during and after its assembly. The quartz used in the sight glasses, the Teflon-encapsulated o-rings for the vessel lids, and the Topline™ gaskets were washed in dilute nitric acid prior to use in the plant. The tubing and columns in the plant were cleaned by flowing a dilute nitric acid solution through them. The nitric acid was special high-purity acid obtained from GFS Chemicals, and the solutions were made using deionized water from the CTF water plant. Water used for cleaning the purification plant was produced at a slower rate than usual to ensure thorough removal of radon. The acid solutions were mixed in 50 L polyethylene jugs. A small rotary pump with a Kynar coated pumping chamber was connected to Teflon tubing to form closed loops around different parts of the plant to perform the acid rinsing. A close inspection of the larger vessels in the plant showed the existence of a white powder on their interior surfaces. Because of their large cross-sectional areas, it was difficult to get good cleansing action by flowing an acid solution through these vessels. They were rinsed manually with concentrated nitric acid after their tops were removed. After acid rinsing, the plant was flushed copiously with deionized water and dried by flowing nitrogen through it.

As the purification plant was assembled, many modifications were made to the original design. The nitrogen vent line from the nitrogen stripping column which

discharged the nitrogen outside the cleanroom was originally one-half inch tubing. Calculations showed that the pressure drop for 3 m^3/hr of nitrogen flow through tubing of this diameter was unacceptably high, and the one-half inch tubing was replaced with three-quarter inch tubing to reduce the pressure drop and the overpressure on the scintillator containment vessel. A check valve was installed at the end of this vent line to allow flow in only one direction. It prevented radon-containing air from diffusing in through the vent line when the nitrogen flow was stopped. Cleanliness was not as important for the nitrogen vent line as for other plant plumbing because the nitrogen passing through it was leaving the plant.

Extensive work was also required on the water still used for repurifying the water in the closed loop water extraction process. This still was originally a commercial model. The manufacturer designed the still to operate while exposed to the atmosphere. It was modified to operate under a nitrogen blanket provided from inside the purification cleanroom Figure 3.12 shows a photograph of the water still after these changes were made. After modification, the still was cleaned by distilling water with it several times. The water distilled during this cleaning was discarded.

Installation of the electrical and control systems proceeded concurrently with the physical assembly of the purification plant. The level probes, the pressure transducers, and the nitrogen flow meter were installed after the plant was first reassembled. Swagelok connectors were used to secure the thermocouples in the thermowells. Signal cable was strung from the control room (in the entranceway to the purification cleanroom) to the monitoring devices in the plant. This cable was cleaned with detergent before being used inside the cleanroom. A cable tray was specially cleaned and mounted along the center of the cleanroom to provide a neat appearance inside the plant. Nitrogen lines for the pneumatic control valves were also run in the cable tray. Electric power was provided to the plant in order to operate the

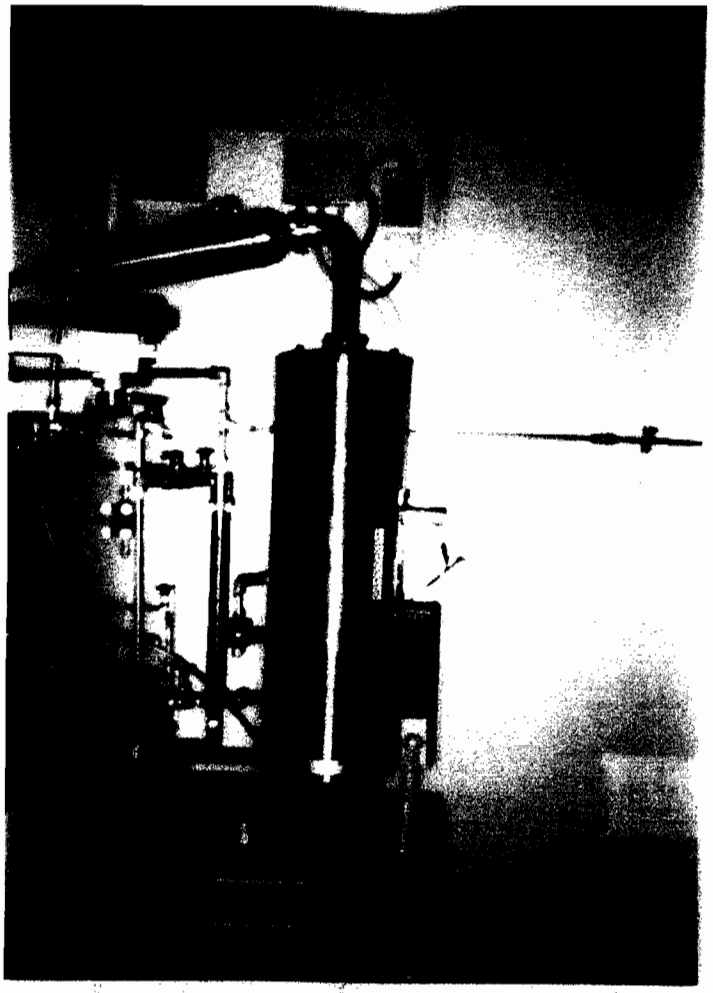

Figure 3.12. Water still. This photograph shows the water still which cleans the water used during the counter-current water extraction process. The water is used in a closed loop, and it is distilled here following contacting with the scintillator to remove any impurities it may have accumulated during the process.

pumps. Relays were mounted on the outside wall of the cleanroom. Control for the pumps was available at control boxes inside the cleanroom and through the PLC in the control room. The relays allowed this remote control to be exercised without passing high currents through the PLC itself.

As the purification system was being assembled and cleaned, the collaboration decided that the time had come to introduce scintillator into the scintillator containment vessel. The containment vessel had been filled with water since December 1994. It was filled with water when the shielding water tank was initially filled . The original plans called for water extraction and nitrogen stripping purification of the scintillator as it was introduced into the containment vessel, but the actual filling procedure was changed because the purification plant was not yet operational. Teflon tubing was run into the purification cleanroom from a 50 L electropolished stainless steel tank outside of the cleanroom and it was connected to the piping leading to the containment vessel. The original purpose of the outside tank was to provide make-up scintillator during purification operations. The outside tank was used to provide the appropriate pressure head during the filling.

One ton of scintillator was added to the scintillator containment vessel in early February 1995, and an equal volume of water was removed from it. Radon contamination during this filling was quite evident. Almost 1000 radon decays per day, as determined by measuring the number of $^{214}Bi - ^{214}Po$ coincidence events, took place in the scintillator after the first ton was introduced. The scintillator was not disturbed for one month, allowing time for the radon to decay. The radon level decreased enough to allow background limits to be placed on uranium and thorium. The filling of the containment vessel with scintillator was completed in late March 1995. Radon was again introduced along with the scintillator, and 35 days were required for the $^{214}Bi - ^{214}Po$ coincidence rate to fall to approximately 2 per day. The

uranium and thorium levels and the ^{14}C:^{12}C ratio in the scintillator were measured again at this time.

As the scintillator containment vessel was filled with scintillator and data were taken in this condition, work on the purification plant proceeded. The water extraction and nitrogen stripping operations were prepared first. It had become evident that operation of the distillation plant would be delayed somewhat because of difficulties in obtaining the hot oil system to provide its heat source. The highest quality water with the lowest possible radon content was desired for the water extraction. At this time the CTF water plant was experiencing difficulty in producing water with the desired low levels of radon. Because of this, the purification plant was modified to allow the stripping of water using its nitrogen stripping column.

Using the purification plant to remove radon from water required the addition of some tubing and valves and a small pump. Great care was taken during the installation of this new plumbing to minimize contamination. A nitrogen stream was blown through any lines broken during the operation to prevent radon-containing air from entering the piping. The new lines were flushed with deionized water to remove particulates after the connections were made. Electropolished stainless steel tubing and stainless steel ball valves were used, and connections were made with stainless steel Swagelok connectors.

In this new mode of operation, water was pumped from the water holding tank inside the purification cleanroom into the water extraction column using the original water pump. The control valve at the bottom of the water extraction column was closed Water filled the extraction column and flowed out the exit normally intended for scintillator. The exiting water bypassed the water coalescer (this bypass was part of the original piping arrangement) and flowed to the top of the nitrogen stripping column. The filter cartridge had to be removed during this operation because it was

made of hydrophobic teflon and did not allow water to flow through it. Water collected in the scintillator holding vessel following nitrogen stripping. The valve between the scintillator holding vessel and the scintillator containment vessel was closed during this operation. The new plumbing made a connection from the scintillator holding vessel to the original water recycle line from the water extraction column as shown in Figure 3.13. The water was removed from the scintillator holding vessel by a small pump added to the water recycle line outside the cleanroom. The water bypassed the water still and was returned to the water holding tank. After the water passed through the nitrogen stripping column a few times, it was collected in the water holding tank. It remained there for more than two months, allowing time for the radon level to decay further.

The nitrogen stripping of water was very valuable for the experience it provided in operating the purification plant in a less critical situation than would be the case for purifying scintillator. The diaphragm pumps used in the plant were metering pumps with adjustable stroke lengths. They were used in the plant because the metering action provides a knowledge of flows through the system based on the stroke settings of the pumps, without the use of flow meters. The relationship between the amount of fluid pumped and the stroke length of the pump was tested by operating the water pump at a constant speed and varying stroke length. The response was found to be linear.

A method was also developed for calibrating the level probes in the system. The probe in the water extraction column was quite easy to calibrate because it could be viewed through the quartz sight tube. The calibration for the probe inside the scintillator holding vessel was somewhat more difficult because the level inside the stainless steel vessel could not be seen. A U-tube device was attached to the sample port at the bottom of the vessel, and the height of liquid in this tube indicated the level

Figure 3.13. Modifications to the plant to allow nitrogen stripping of water.

Portions of the P&ID in Figure 3.7 are shown here along with additions (valves, piping, and a pump) made to allow nitrogen stripping of water. The path followed by the water from the water holding tank (V-104) through the water extraction column (C-101) and into the nitrogen stripping column and scintillator holding vessel (C-102) is shown by the lines with arrows. The water flows through lines following the water extraction column which hold scintillator during normal operation. The control valves at the bottom of the extraction column and the coalescer are closed during water stripping. The water is removed from the stripping column by a new pump near the water still. The water bypasses the still, and is returned to the water holding tank. The control system adjusts the speed of pump P-102 to maintain the water level in the scintillator holding vessel constant. The additions made to the plant are indicated by a dotted background. The coalescer is bypassed during this operation using an existing bypass line. Although the water flows through three heat exchangers during the stripping, they play no role in it and are not shown. Some details of the water still which were not shown in Figure 3.7 are shown in this figure, including its nitrogen blanket and the means by which water is initially obtained from the CTF water plant.

Figure 3.13. Modifications to the plant to allow nitrogen stripping of water.

Portions of the P&ID in Figure 3.7 are shown here along with additions (valves, piping, and a pump) made to allow nitrogen stripping of water. The path followed by the water from the water holding tank (V-104) through the water extraction column (C-101) and into the nitrogen stripping column and scintillator holding vessel (C-102) is shown by the lines with arrows. The water flows through lines following the water extraction column which hold scintillator during normal operation. The control valves at the bottom of the extraction column and the coalescer are closed during water stripping. The water is removed from the stripping column by a new pump near the water still. The water bypasses the still, and is returned to the water holding tank. The control system adjusts the speed of pump P-102 to maintain the water level in the scintillator holding vessel constant. The additions made to the plant are indicated by a dotted background. The coalescer is bypassed during this operation using an existing bypass line. Although the water flows through three heat exchangers during the stripping, they play no role in it and are not shown. Some details of the water still which were not shown in Figure 3.7 are shown in this figure, including its nitrogen blanket and the means by which water is initially obtained from the CTF water plant.

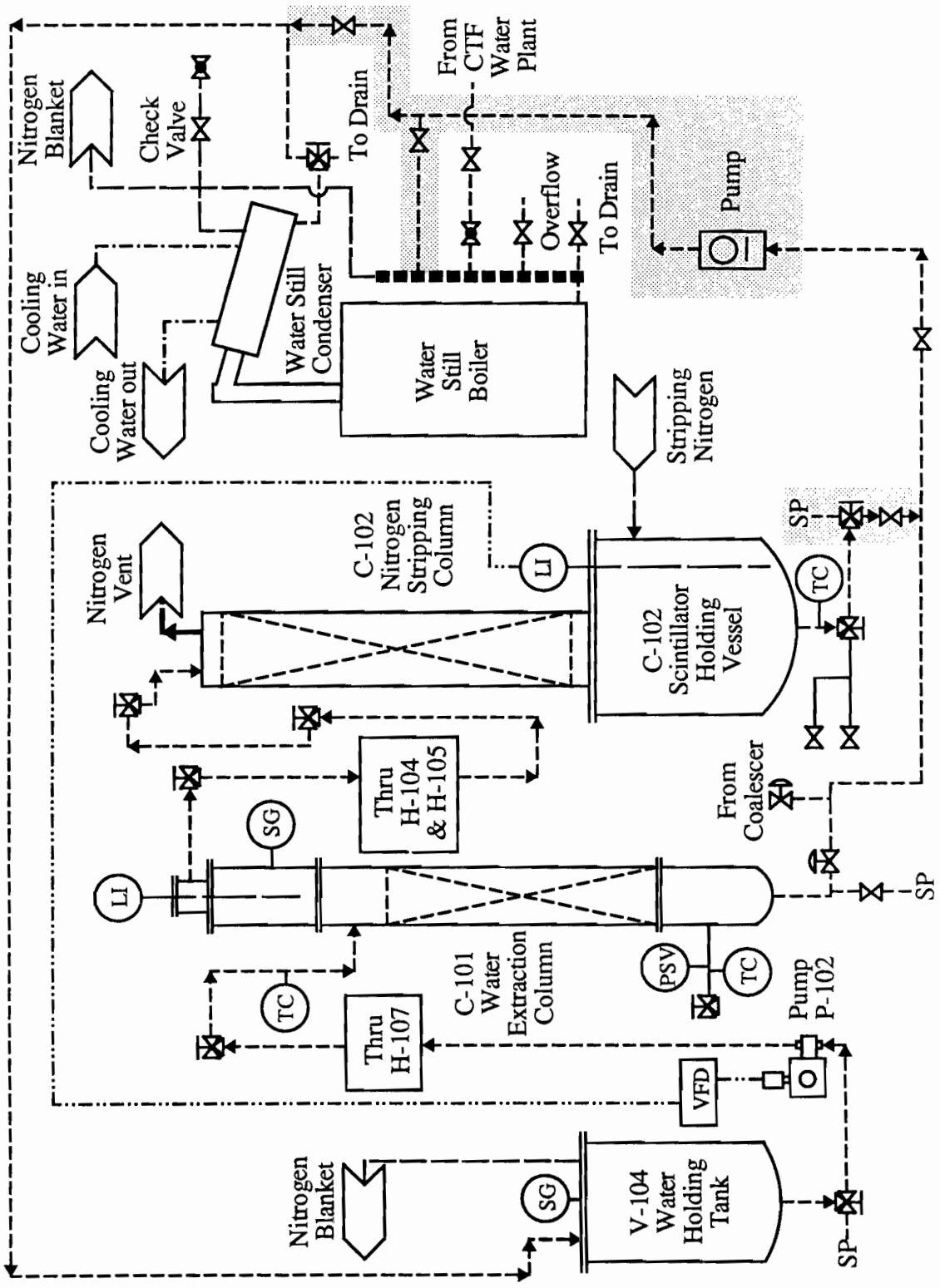
Nitrogen Blanket
Check Valve
To Drain
From CTF Water Plant
Overflow
To Drain
Pump
Cooling Water in
Cooling Water out
Water Still Condenser
Water Still Boiler
Stripping Nitrogen
SP
Nitrogen Vent
C-102 Nitrogen Stripping Column
LI
C-102 Scintillator Holding Vessel
TC
Thru H-104 & H-105
From Coalescer
SG
LI
SP
TC
C-101 Water Extraction Column
PSV
TC
Pump P-102
Thru H-107
VFD
Nitrogen Blanket
SG
V-104 Water Holding Tank
SP

Figure 3.13.

in the vessel. Probe readings at several liquid heights allowed the probe to be calibrated and its electrical current output to be converted to a percent full reading on the computer display. The calibration was only valid for water because scintillator has a different dielectric constant than water and gives a different probe response.

The nitrogen stripping of water also provided an opportunity to test the computer control system. The control system was programmed to control the water level in the scintillator holding vessel. It could adjust the amount of water flowing into the nitrogen stripping column by varying the speed of the original water pump using a variable frequency drive (VFD). The ability of the system to respond to changes in the rate of water removal from the scintillator holding vessel and changes in the water level setpoint were tested. The settings of the proportional-integral-derivative (PID) controller in the PLC software were adjusted using a trial and error procedure to optimize the control of the system.

Purification attempts on the scintillator began in May 1995. The first operation to be tested was nitrogen stripping. For this test, the scintillator flowed through the water extraction part of the plant, but no water was present in the extraction column; the only active operations were filtration and nitrogen stripping. The nitrogen stripping test was initially unsuccessful. The scintillator pump had difficulty drawing scintillator up into the plant, although it eventually succeeded. Unfortunately, scintillator began leaking from some VCR connections in a valve manifold outside the purification cleanroom. Operation was terminated as soon as the leakage was discovered. No scintillator reached the stripping column, but some of the other plant vessels and plumbing were filled with scintillator that had been contaminated by air exposure. The contaminated scintillator was discarded, and an extensive period of leak checking began. A helium leak detector used for high vacuum work was obtained, and the connections in the purification plant were

tightened and adjusted until the entire water extraction portion of the plant was vacuum tight. The outside valve manifold was modified to provide more support for the VCR connections so that they would not work loose in the future. The plant was recleaned by flushing with deionized water and nitrogen before the nitrogen stripping was attempted again.

The second nitrogen stripping effort was much more successful, and the plant was operated in this mode from May 23 to July 5, 1995. The plant behaved nicely, and leaks were no longer evident. The level probe in the scintillator holding vessel was recalibrated for scintillator. The calibration was made using two data points from the U-tube device. No computer control was required during this nitrogen stripping, but the PLC unit did monitor the process and alert the operator if the scintillator level or temperature in the scintillator holding vessel deviated outside preset limits.

Results from the nitrogen stripping showed that the radon level in the scintillator rose as it was processed, although contamination by other radioactive gases was reduced during the operation. This indicated the emanation of radon somewhere in the purification process. Nitrogen stripping was operated for three cycles to allow its effectiveness for removing gas contamination other than radon to be measured. The operation of the plant was then altered in an effort to find the source of the radon emanation. Different sections of the plant were filled with scintillator and isolated by closing the appropriate valves. The scintillator was allowed to sit for 3 – 5 days. It was then returned to the scintillator containment vessel. Any increase in radon upon its return would indicate emanation in that part of the plant. All the emanation tests were negative; no part of the plant showed measurable radon emanation. It was concluded that radon contamination came from the stripping nitrogen itself, probably from an emanation source inside the liquid nitrogen tank. This tank was commercially installed, and it was not cleaned as thoroughly as the rest of the system. It was later

determined that by maintaining the liquid nitrogen level high in the tank, radon contamination during nitrogen stripping was reduced.

Water extraction was the next purification operation to be tested. Initial water extraction took place in a standing water mode. Approximately 8 L of water, which had been in the water holding tank for two months following its stripping with nitrogen, was charged into the extraction column. Scintillator was pumped through the column to provide the contact necessary for extraction. A photograph of the water extraction column during operation is shown in Figure 3.14. The scintillator flowed from the top of the water extraction column to the water coalescer, the filter, and the nitrogen stripping column before it returned to the scintillator containment vessel. Nitrogen stripping was continued during water extraction to remove water from the scintillator. The water in the extraction column was changed every few days during this operation to remove water from the column which may have become contaminated with impurities extracted from the scintillator. The water extraction column was operated in this manner from July 5 to July 21, 1995. During this time the control system was used only for monitoring purposes.

Water extraction was conducted in a counter-current mode from July 21 to August 12, 1995. In this mode, the water in the extraction column was circulated in a closed loop at a flow rate of approximately 5 L/hr, and the scintillator flow continued as before. The control system successfully maintained the level of the scintillator-water interface at the desired position, and the closed water loop performed as expected. Nitrogen stripping was continued during this period. Removal of water from the coalescer proved to be unnecessary because no water collected inside it.

The plant was designed to provide heated water extraction. This mode of operation was attempted after the hot oil system became operational in early August 1995, but it proved to be unsuccessful. The heating and extraction processes worked

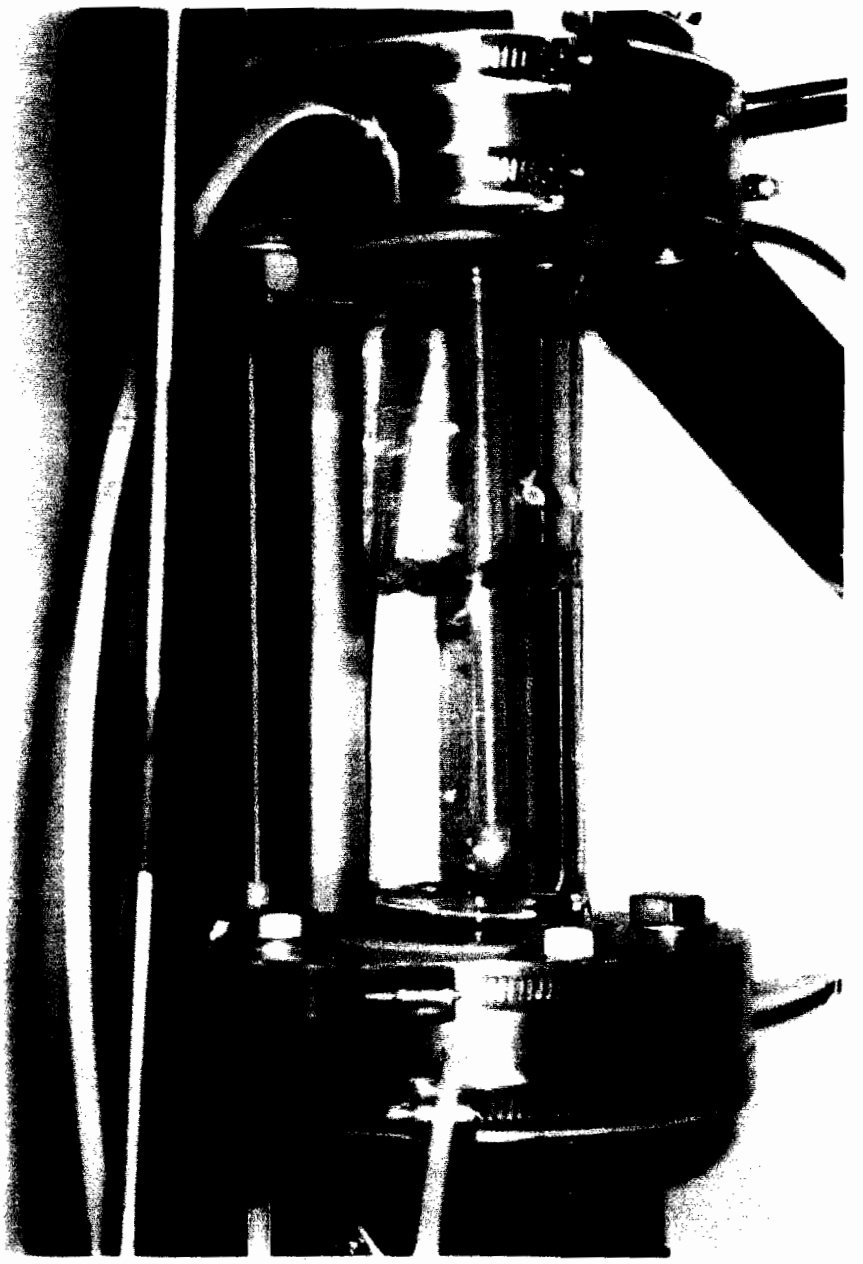

Figure 3.14. Close-up view of the sight tube of the water extraction column. Large droplets of pseudocumene can be seen rising through the water in the bottom section of the quartz sight tube during operation of the water extraction column. The scintillator-water interface and the capacitance level probe can also be seen.

as expected. Due to the higher temperature, water was more soluble in the scintillator, and it phase separated following the cooling heat exchangers. The water coalescer failed to perform correctly, and it did not remove the water droplets from the scintillator. During the operation, the pressure in the lines in the plant increased drastically. This happened because water in the scintillator was trapped by the hydrophobic filter. The flow through the filter became more restricted, and the pressure in the system increased as the scintillator pump continued to process fluid at the same volumetric rate. The plant was quickly shut down, and heated water extraction was abandoned after this unsuccessful trial.

Work continued on the purification plant as the nitrogen stripping and water extraction processes were being tested. At an early stage in the nitrogen stripping operation, it was discovered that the temperature of the scintillator returning to the containment vessel was higher than that of the scintillator leaving it. This was undesirable and steps were taken to minimize the temperature rise. The scintillator piping from the outlet of the scintillator containment vessel to the top of the shielding water tank and the piping inside the purification plant were insulated with foam rubber insulation to minimize heat transfer to the liquid. The heat exchangers after the water extraction column were used during ambient temperature water extraction to cool the scintillator with cold water. The water extraction column, the water coalescer, the stripping column, and the scintillator holding vessel were also insulated. Insulation of the scintillator holding vessel was especially important because temperature fluctuations in the returning scintillator could be seen as the residence time of the scintillator in the vessel varied due to changes in the scintillator flow rate. Some of the insulation installed in the plant can be seen in Figure 3.15.

Progress was also made in preparing the distillation portion of the plant. The hot oil system was installed at the bottom of the shielding water tank for safety

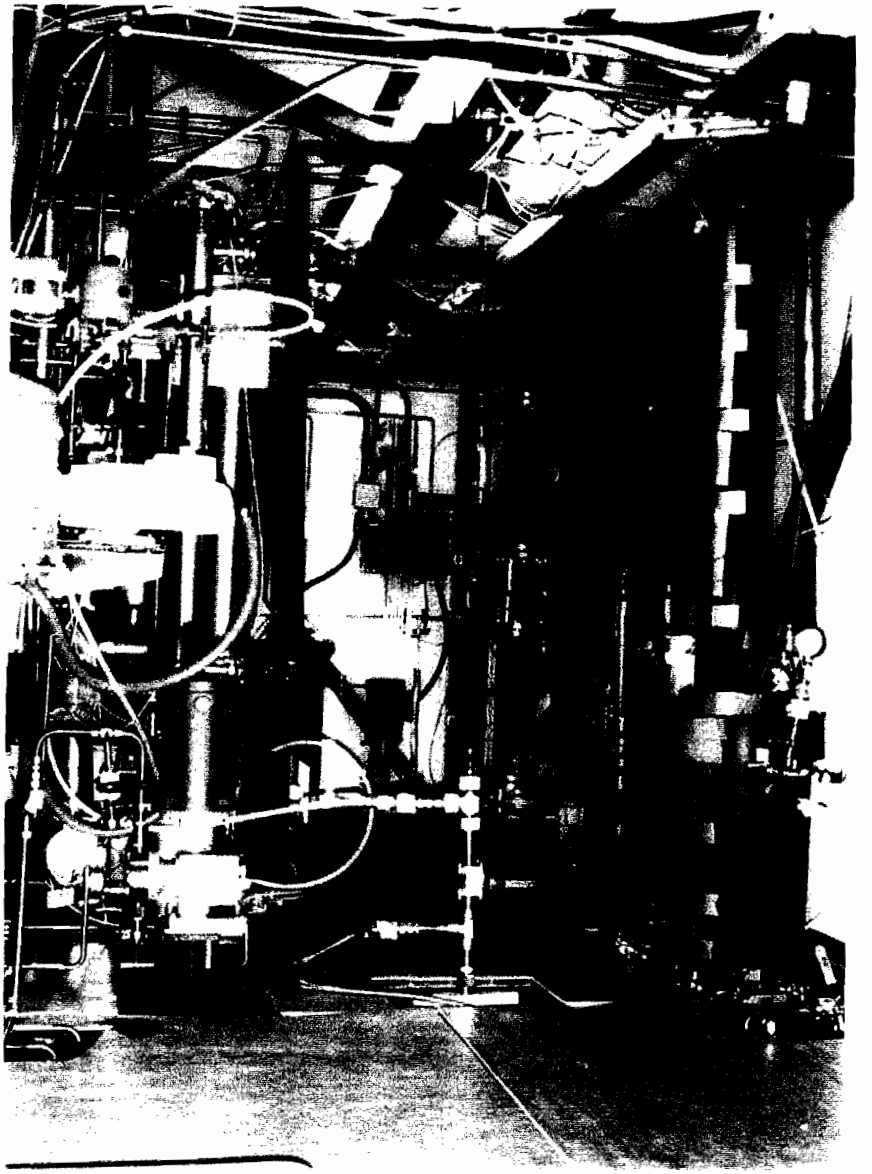

Figure 3.15. View inside the purification cleanroom. The nitrogen stripping column and the scintillator holding vessel can be seen in the foreground to the right. They are covered with foam rubber insulation. The distillation units can be seen on the left side. The evaporator is insulated with foam glass covered by aluminum sheeting. The water holding tank is near the back of the room. The pipe in the central foreground provides access to the scintillator containment vessel.

reasons. Insulated 1.5 inch pipes were run to bring the hot oil to the purification plant on top of the tank. The system was leak checked and tested for its ability to provide heat for distillation. The hot oil was also used to heat water and scintillator in the heated water extraction trial. The piping and vessels inside the cleanroom which transport or contain hot oil and scintillator were insulated with foam glass and covered with sheet aluminum to provide protection for workers from the hot surfaces and to prevent heat loss in the lines. This insulation was installed by an outside contractor. Electric heat tape was wrapped around the 1.5 inch vacuum line between the evaporator drum and the condenser column to provide heating for this line so that scintillator vapor would not condense inside it.

During preparation of the distillation units, that portion of the plant was leak checked with a helium leak detector. Most of the connections were successfully made vacuum tight. Experience from this leak checking, as well as that conducted earlier on the water extraction portion of the plant, indicated that one type of gasket used in the plant did not reliably seal under vacuum conditions. These gaskets consisted of a soft polymer core sandwiched between teflon rings, and were used to seal the flanges where columns attached to vessels or were capped. Because the vacuum sealing of these gaskets was unreliable, there was a fear that radon could enter the plant around them. In order to minimize this threat, a nitrogen atmosphere was provided around each flange sealed with these gaskets. The flange connections were surrounded by metal bands with two small holes in them, as shown in Figure 3.16. These holes served as the inlet and outlet for a nitrogen purge which continually flushed a small amount of gas through the volume inside the bands. Because of the nitrogen purge, any gas that leaked into the plant through the gaskets would be nitrogen.

The control system was also developed further as purification plant operation continued. The initial control codes were written in Princeton prior to assembly of the

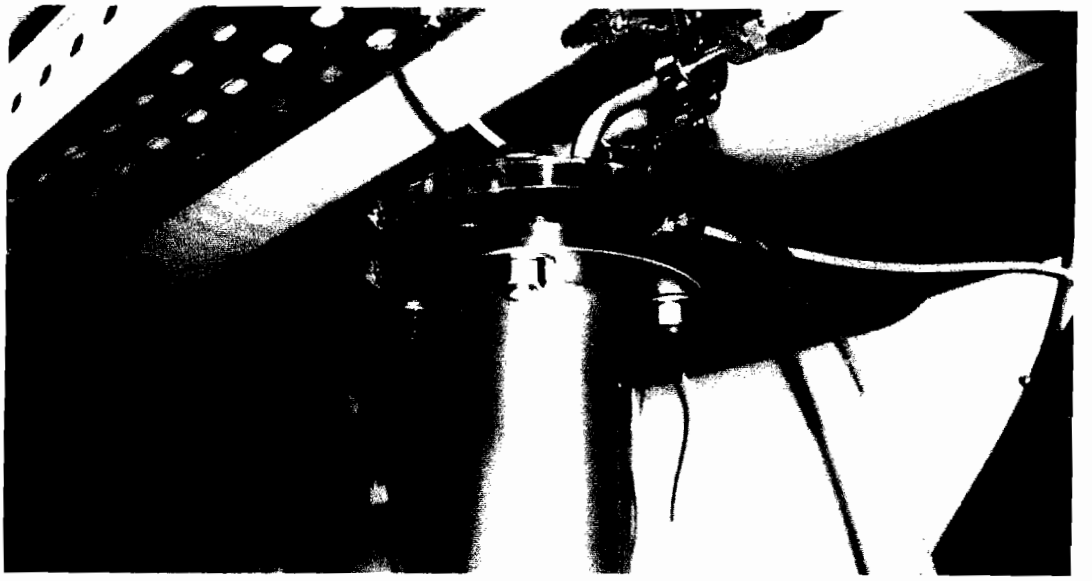

Figure 3.16. Metal bands to provide protection from radon at plant flanges.

Because the teflon sandwich gaskets in the plant were found to be unreliable under vacuum conditions, a nitrogen atmosphere was provided around each flange joint sealed with one of these gaskets. A metal band was attached to each flange joint using silicone adhesive. Two holes in the band allowed a small flow of nitrogen to pass through the volume enclosed by it.

system. Modifications to these codes were made during actual operation, most often when procedures not included in the initial plant design, such as nitrogen stripping of water, were carried out. The control schemes were adjusted to utilize the most accurate data from the plant.

The PLC was also used to establish alarm conditions for plant operation. An alarm condition was defined when a measured system variable reached a level above or below established thresholds. The controller allowed the definition of two stages of alarm. In the first stage, a siren was sounded to alert operating personnel of the problem. If the second stage of the alarm condition was reached, the plant was shut down by the computer to leave it in a safe mode. Alarm conditions were established for several system parameters: the level of scintillator in the scintillator holding vessel, the interface level in the water extraction column, the stripping nitrogen flow rate, the overall pressure in the system piping, and the temperature of the scintillator returning to the scintillator containment vessel. Figure 3.17 shows a view of the control room of the scintillator purification plant.

Following counter-current water extraction, the scintillator was allowed to remain quiescent inside the containment vessel from August 12 to September 28, 1995. This provided time for radon introduced by the stripping nitrogen to decay and for data to be collected on the effectiveness of the water extraction and nitrogen stripping purifications. During this period, work was completed on the distillation system and operational tests using it were conducted. Modifications to the original plant design were made to allow off-line distillation of scintillator so that distillation could be practiced before distilling the scintillator in the containment vessel. The water extraction portion of the plant could continue to process scintillator from the scintillator containment vessel during off-line distillation. A new pump and new plumbing were added to allow withdrawal of scintillator from the 50 L electropolished

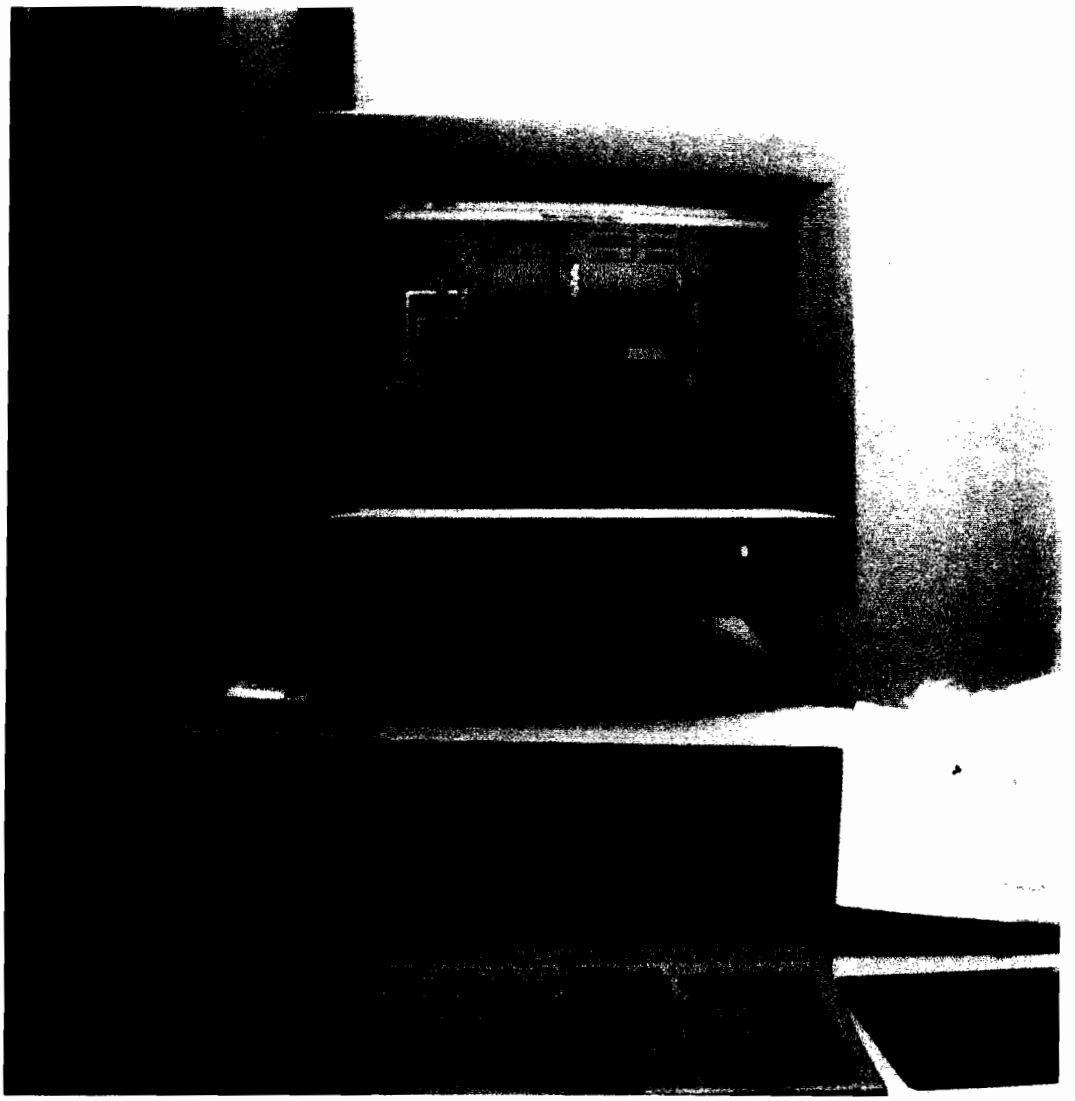

Figure 3.17. Control room of the purification plant. This photograph was taken inside the control room of the purification plant. Some of the PLC modules can be seen mounted on the wall at the left. One of the graphical interface screens used for reporting conditions in the plant can be seen on the personal computer monitor.

stainless steel vessel outside the cleanroom which had been used for the initial filling of the containment vessel. In off-line distillation, the scintillator enters the top of the evaporator column without preheating and passes through the distillation unit as usual. Upon its removal from the condensate drum it is returned to the outside vessel. The piping modifications made for this operation are shown in Figure 3.18. Electrical power was provided for the new pump, and the control system was updated to allow this new mode of plant operation.

Initial efforts with off-line distillation were made using water, and water was pumped to the top of the evaporator column. The distillation of water was unsuccessful. Some water was distilled through the system, but much of it remained in the evaporator drum and the water level in this vessel rose continually. This problem was never successfully resolved. The failure of the unit to distill water can be attributed to its design. The purification plant was designed to distill scintillator, which has a much lower heat capacity than water. Distillation of water required the transfer of more heat in order to vaporize it and the unit was unable to provide this.

After the failure of water distillation, testing was continued using scintillator. Not all of the originally mixed scintillator was needed to fill the scintillator containment vessel, and this scintillator was used to practice distillation. The distillation of scintillator went quite smoothly. A small puddle (approximately 200 ml) of scintillator collected in the bottom of the evaporator drum, but the size of the puddle did not change after the process reached steady-state. The operating pressure in the condensate drum and the temperature of the hot oil were adjusted to obtain optimum performance from the unit. The fluor content of the condensed scintillator was regularly checked using a spectrophotometer to ensure that its concentration was not being depleted. The best operating conditions were found to be a pressure of 50 torr and a hot oil temperature of 150°C. This corresponded to a scintillator vapor

Figure 3.18. Plant modification to allow off-line distillation. This diagram shows part of the P&ID for the plant as in Figure 3.7. Piping and valve additions to allow off-line distillation of scintillator are indicated by a dotted background, and the scintillator path is shown by arrows. A new pump was also added to the system. This pump withdraws scintillator from a 50 L electropolished stainless steel tank outside the purification cleanroom and the scintillator flows to the top of the evaporator column. Distillation proceeds as in Figure 3.7. The hot oil and cooling water lines are unaltered from Figure 3.7, and are not shown here. The control system adjusts the hot oil flow and the speed of pump P-104 as originally designed. The scintillator leaving the condensate drum is returned to the 50 L tank. It is returned through an overflow tube which rises 40 cm inside the tank. With the valves in different positions, scintillator can flow to a large holding tank at the base of the shielding water tank. The connection to the top of the evaporator column was made by detaching the original piping at this point, and the connection must be replaced in the original condition before on-line distillation can take place. Some existing plumbing from the 50 L tank which was to provide make-up scintillator was also used for the off-line distillation.

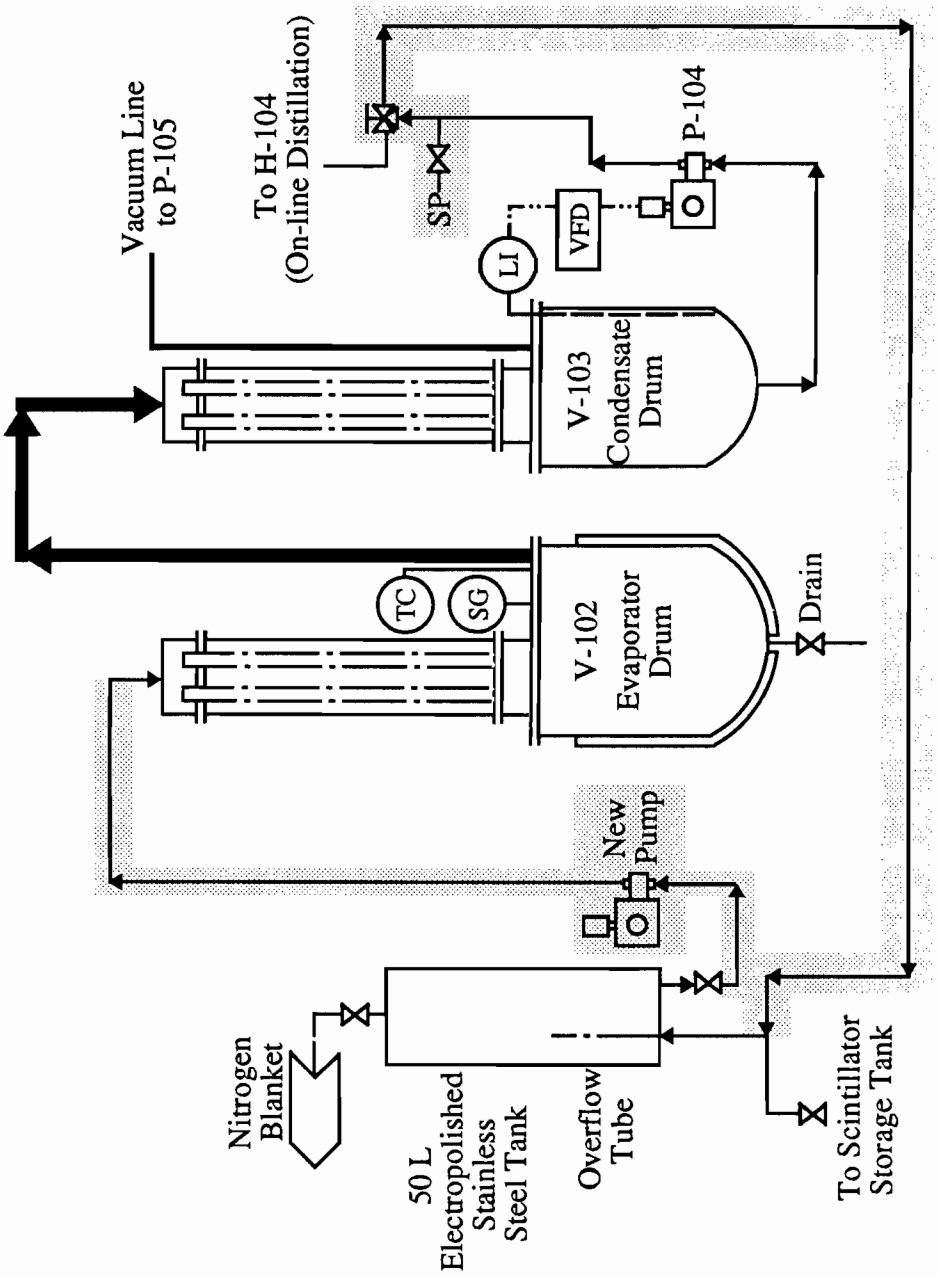
Vacuum Line
to P-105
To H-104
(On-line Distillation)
SP
LI
VFD
P-104
V-103
Condensate
Drum
TC
SG
V-102
Evaporator
Drum
Drain
New
Pump
Nitrogen
Blanket
50 L
Electropolished
Stainless
Steel Tank
Overflow
Tube
To Scintillator
Storage Tank

Figure 3.18.

temperature of 130°C. The level probe in the condensate drum was calibrated during this practice distillation using a U-tube device.

The distillation plant was used to process scintillator from the scintillator containment vessel from September 29 to November 12, 1995. The distillation proceeded smoothly and took place at the operating conditions determined by the off-line trials. The fluor content of the scintillator was monitored during this operation; it remained constant. The bottoms collected in the evaporator drum were purged every few days to remove any impurities which had accumulated there. In order for the bottoms to be purged, distillation had to be stopped. The plant was backfilled with a slight overpressure of nitrogen, and a valve underneath the evaporator drum was opened to allow the bottoms to be blown out. Vacuum was then re-established, and distillation was resumed. The scintillator passed through the filter and the nitrogen stripping column as it returned to the containment vessel. The control system was quite effective at maintaining the temperature and pressure in the distillation unit and the liquid level in the condensate drum at the desired values.

The scintillator remained undisturbed inside the containment vessel for a few months following the distillation operations in November 1995. Some radon which had been introduced to the scintillator during the distillation decayed during this time, and final numbers were obtained for scintillator purity following the purification procedures.

The purification plant was next used in April 1996, when the scintillator was distilled to remove some of the PPO fluor. This test was designed to determine if PPO was the major source of ^{14}C contamination in the scintillator. If a reduction in the ^{14}C level could be achieved by removing some of the PPO, this would indicate that PPO was a major source of this contaminant. The distillation was operated under the same conditions as before, but the bottoms purge was carried out more frequently,

approximately once every two hours. The PPO concentration in the bottoms is enriched so that the PPO there is in equilibrium with the PPO in the vapor phase. Frequent removal of the bottoms disturbs this equilibrium, and a significant percentage of the PPO is removed from the scintillator. The PPO concentration in the bottoms product withdrawn during this operation was above the solubility limit of PPO in pseudocumene at room temperature, and it separated into a solid phase upon cooling.

Plant modifications implemented prior to the PPO removal made bottoms purging less difficult. The outlet from the bottom of the evaporator drum was connected directly to the vacuum pump. This suction line contained a collection flask. When the valves in the line were opened, the bottoms were drawn into the flask. This process is shown schematically in Figure 3.19. The pressure in the distillation unit still had to be raised before purging the bottoms, but a complete shutdown was not necessary as it had been before. Two days of distillation in this manner reduced the PPO concentration in the scintillator from 1.5 g/L to 1.33 g/L.

When the testing of the pseudocumene-PPO scintillator in the CTF was complete, the collaboration decided to use the facility to test other scintillator mixtures. The first such mixture was to be a pseudocumene-PPO-bis-MSB solution. The scintillator purification plant was used to prepurify the bis-MSB which was added to the existing scintillator in the containment vessel to produce the desired mixture. A concentration of 20 mg/L of bis-MSB was desired, so a total of 100 g of bis-MSB were required. This was purified by making a concentrated bis-MSB solution in approximately 50 L of pseudocumene-PPO scintillator and water extracting the concentrated solution.

Modifications were again made to the plant to allow this operation. The ineffective water coalescer was removed from the plant to make room for two 100 L

Figure 3.19. Removal of bottoms from evaporator drum. In this process, the valve to the vacuum pump from the condensate drum is first closed. The pressure inside the distillation unit is then raised by opening the control valve on the bleed nitrogen briefly. The valves between the sample flask and the vacuum pump are then opened. The last valves to be opened are those between the evaporator drum and the sample flask. When these valves are opened, the bottoms contents are drawn into the sample flask. The valves through the sample flask are then closed, and the vacuum pump is reconnected to the condensate drum. The control system quickly reestablishes system pressure at the desired value, and distillation continues.

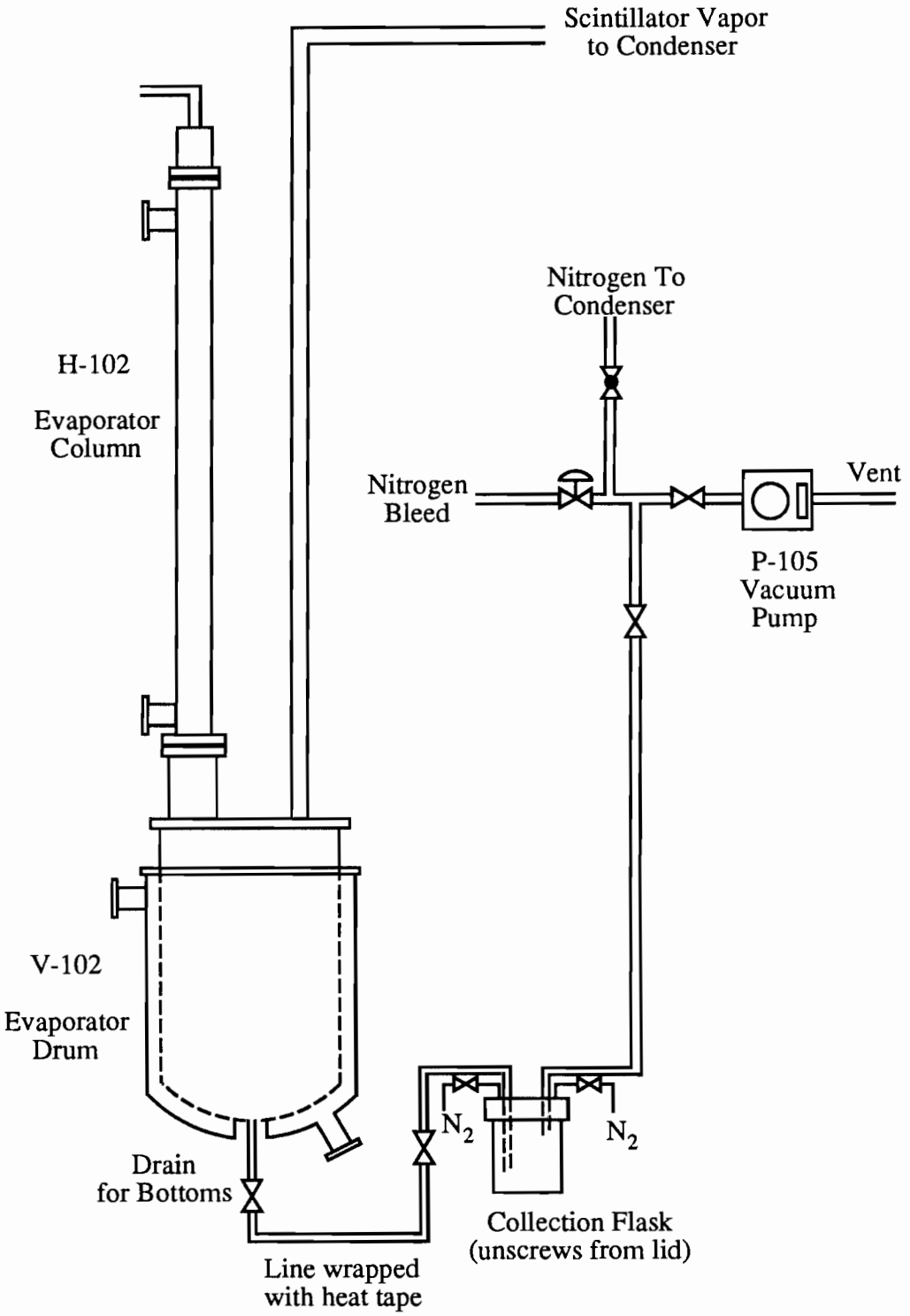
Scintillator Vapor
to Condenser
Nitrogen To
Condenser
H-102
Evaporator
Column
Nitrogen
Bleed
Vent
P-105
Vacuum
Pump
V-102
Evaporator
Drum
N_2
N_2
Drain
for Bottoms
Collection Flask
(unscrews from lid)
Line wrapped
with heat tape

Figure 3.19.

electropolished stainless steel tanks. The pump first used for off-line distillation was replumbed. Piping was added to allow circulation of liquid from one of the 100 L tanks, through the water extraction column, and into the other 100 L tank. This allowed the water extraction to be operated in a batch mode which could provide a more rapid purification than a procedure using one well-mixed tank. The piping connections made for this operation are shown in Figure 3.20. Three batch extractions in the standing water extraction mode were performed to prepurify the bis-MSB. Scintillator from the scintillator containment vessel was then contacted with the concentrated bis-MSB solution to introduce the second fluor into the detector. The new scintillator mixture was circulated through the water extraction portion of the purification plant for several cycles to ensure good mixing of the bis-MSB, but no water extraction or nitrogen stripping took place at this time.

The bis-MSB scintillator was studied for three months. It was then displaced with high-purity water. The water was replaced with a pure pseudocumene scintillator in order to study light propagation in the pure solvent. Pseudocumene was available from a storage barracks in 55 gallon drums. Preliminary tests indicated the presence of a low concentration of an optical impurity in this pseudocumene. Because of this, the pseudocumene was distilled using the purification plant as it replaced water in the scintillator containment vessel in August 1996. The filling and distillation procedures went quite smoothly, and the containment vessel was filled with pure pseudocumene in one week. Distillation did not remove a significant amount of the optical impurity, but this did not preclude light propagation measurements using the solvent. Residual PPO was present in the pseudocumene at a level of 0.2 ppm. This was attributed to PPO which remained on the surface of the nylon vessel when the pseudocumene-PPO-bis-MSB scintillator was removed.

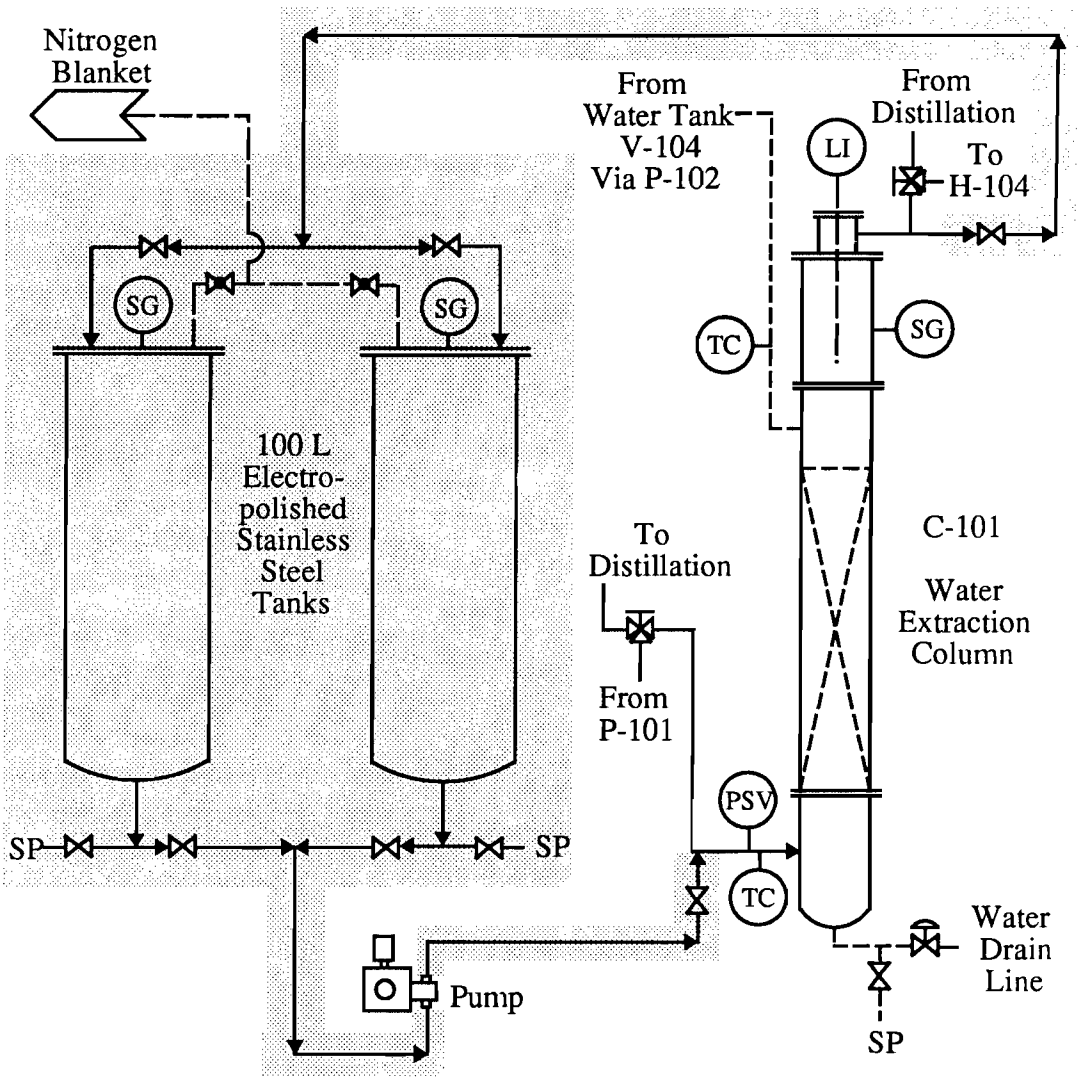

Figure 3.20. Plant modification to allow prepurification of bis-MSB. Changes in the plant necessary to implement the prepurification of concentrated bis-MSB solutions by water extraction are indicated here by a dotted background. Two 100 L electropolished stainless steel tanks, valves, and piping were added to the plant. The pump used in this procedure was originally used in off-line distillation, and its previous connections were removed or modified for this new duty. The scintillator is pumped out of the bottom of one tank, circulates through the water extraction column, and flows into the top of the other tank.

Operations with the scintillator purification system concluded with the distillation of the pure pseudocumene. An upgrade of the plant is planned to allow its use for fluor prepurification in Borexino. Although some problems were encountered, the purification system was very successful overall, as indicated by its removal of several impurities.

F. Results of Purification

1. Maintenance of Optical Properties

The effectiveness of the purification system for the removal of radioactive contaminants received most of the attention in the CTF trials. Its performance in maintaining the scintillator optical properties is also crucial to the success of the Borexino experiment. No problems with the optical properties of the scintillator were observed during the life of the CTF. This provides a qualitative measure of the effectiveness of the purification system in preserving the scintillator optical properties. Some measurements are also available to provide a quantitative look at the system's performance.

The nitrogen stripping column was quite crucial in preserving the optical clarity of the scintillator because it removed the water introduced into it by water extraction. The effectiveness of the nitrogen stripping column for water removal was measured during the water extraction operations. Scintillator samples were taken both before and after the stripping column. When the sample from before the nitrogen stripping column was cooled from 14 °C to 13 °C, water droplets formed in it. The sample which had been contacted with nitrogen was cooled to 0 °C, and no formation of water drops was observed. This indicates the effectiveness of nitrogen stripping for removing water from the scintillator.

The optical properties of the scintillator were monitored carefully during distillation because of the possibility that distillation could reduce the fluor content of the scintillator and reduce its light output. Scintillator samples taken during the distillation showed that the fluor concentration was maintained constant to within 1%. These measurements proved that distillation could be operated without adversely affecting the scintillator composition. Later operation of the distillation plant to intentionally remove some of the PPO fluor showed that concerns about fluor removal during distillation were valid. Improper operation of the distillation unit can significantly change the fluor concentration in the scintillator.

The optical purity of the scintillator was also examined by making attenuation length and fluorescence measurements. During distillation, the optical attenuation length of the scintillator at 420 nm was monitored. It remained at 7.5 m throughout the procedure. The Perugia group of the Borexino collaboration recorded absorption and emission spectra for scintillator taken from the CTF following purification operations.[11] They compared this spectrum with one measured for a high purity laboratory sample. The sample from the CTF did show evidence of a small fluorescent impurity, but the identity of this contaminant was not discovered.

The effectiveness of distillation for removing an optical impurity was tested during the introduction of pure pseudocumene into the scintillator containment vessel. The pseudocumene was shown to contain a small amount of an unknown impurity by laboratory measurements. It was distilled once as it passed from the storage drums to the scintillator containment vessel. Unfortunately, tests of the pseudocumene after distillation showed no abatement of the contaminant.

The overall performance of the purification system in maintaining the optical properties of the scintillator was satisfactory. Although it failed to remove a contaminant from the pure pseudocumene, the plant did not degrade the scintillator

optical properties. The distillation operation was shown to be safe for the scintillator composition if it was performed carefully. The scintillator remained in a good condition for a period of almost two years, and it showed no signs of degradation. These results indicate that there should be little concern over maintaining the optical properties of the scintillator in Borexino.

2. Removal of Radioactive Contaminants

The performance of the purification plant in the removal of radioactive contaminants was studied extensively. Prior to any purification operations, measurements were made of the uranium, thorium, and ^{14}C backgrounds after allowing time for the decay of radon introduced into the CTF during the filling procedure.[12]

The uranium background was determined by assuming equilibrium in the uranium decay chain and measuring the rate of $^{214}Bi - ^{214}Po$ coincidence events. ^{214}Bi and ^{214}Po are daughters of uranium and radon. A $^{214}Bi - ^{214}Po$ coincidence event occurs when a β-event with an energy of 0.9 – 2.7 MeV is followed by an α-event with an equivalent energy of 0.8 MeV with a mean time delay of 236 μs. Coincidence events are easily detected by the CTF electronics. The $^{214}Bi - ^{214}Po$ coincidence rate was fit to an exponential decay plus a constant. The exponential decayed with a mean lifetime of 5.48 ± 0.07 days, which compares quite well with the mean life of radon of 5.51 days. The constant was found to be 1.44 ± 0.44 counts per day, and this corresponds to $4.9 \pm 1.5 \times 10^{-16}$ grams of ^{238}U per gram of scintillator.

The thorium concentration was measured by examining the $^{212}Bi - ^{212}Po$ coincidence rate (432 ns mean time), and it was found to be $1.8 +1.6/-1.1 \times 10^{-16}$ grams of ^{232}Th per gram of scintillator. The amount of ^{14}C was determined by fitting the known shape of the ^{14}C spectrum to the experimental spectrum in the CTF over

the energy range from 50 – 150 keV.[13] Using this method, the ^{14}C:^{12}C ratio was found to be $1.94 \pm 0.09 \times 10^{-18}$. These values provide a reference point against which to measure the performance of the purification system.

The purification performance can also be gauged by examining the total number of events taking place in the detector before and after processing. The events of most concern are those which take place in the neutrino window, the energy range from 0.250 – 0.800 MeV. Prior to purification, approximately 2500 events per day occurred inside the detector in this energy range. Using the positional reconstruction techniques discussed in Chapter 2, these events were separated into external background, internal background, and surface events. Surface events are events due to activity in the nylon membrane of the scintillator containment vessel. Of the 2500 events per day, 480 were identified as internal background, and 370 were attributed to surface activity. The purification plant is effective only for the reduction of internal background.

The first purification procedure to be tested was nitrogen stripping. Nitrogen stripping was designed to remove radioactive gaseous contaminants from the scintillator. As mentioned in Section 3.E, the scintillator was contaminated with radon during the initial filling procedure. After the filling, the radon level was approximately 12000 events per day, as measured by ^{214}Bi – ^{214}Po coincidences. The radon contamination was attributed to air leakage during the filling.

Air exposure also introduces other contaminants such as ^{85}Kr to the scintillator. After the radon had decayed to less than 10 events per day, ^{85}Kr activity in the scintillator could also be detected. ^{85}Kr can be detected by an event coincidence technique similar to that used for radon. While most ^{85}Kr decays directly to ^{85}Rb in one step, 0.43% of the ^{85}Kr atoms first decay to an metastable excited state of ^{85}Rb ($^{85}Rb^*$) by emission of a 0.173 MeV β. The metastable rubidium relaxes to its stable

state with emission of a 0.514 MeV γ-ray. The $^{85}Rb^{*}$ has a mean life of 1.46 μs, and this coincidence is easily detectable in the CTF. Prior to purification, 1.3 ± 0.2 coincidence events per day of this type were observed. This corresponded to a total ^{85}Kr background of 300 events per day, of which 185 have energies in the neutrino window. Exposure to 4 L of air could have produced this level of contamination.

Nitrogen stripping was carried out for three cycles at flow rates of 30 L/hr of scintillator and 2.5 m^3/hr of nitrogen. The radon rate increased during this stripping from 2 events per day to 200 events per day. Nearly 4 events per day from the ^{220}Rn isotope in the thorium decay chain (^{220}Rn is known as thoron) were also detected. This indicated a radon source or leak somewhere in the purification system. The ^{85}Kr level was reduced by the stripping. The number of $^{85}Kr - ^{85}Rb^{*}$ coincidence events decreased to 0.24 ± 0.11 events per day, corresponding to a total of 56 ^{85}Kr decays, 34 of which were in the neutrino window. After correcting for the radon introduced during the stripping, the overall internal background in the scintillator decreased from 479 ± 77 events per day to 265 ± 74 events per day. This reduction is slightly greater than can be attributed to ^{85}Kr removal alone, and is probably due to abatement of other gas contaminants such as ^{39}Ar.

Because the radon increase during the stripping was accompanied by a thoron increase, but not by a ^{85}Kr increase, an air leak could be ruled out as the cause of the radon contamination. This made an emanation source the likely origin of the radon. As discussed in the previous section, radon emanation tests on different sections of the plant were negative, and the radon source was determined to be in the liquid nitrogen tank. By maintaining the liquid nitrogen level near the top of the tank, the radon rate in the CTF could be kept to less than 50 events per day. This indicated that the radon source was probably dirt near the midpoint of the nitrogen tank.

The effectiveness of water extraction for removing radioactive impurities was also examined. Water extraction was carried out for five cycles with a scintillator flow rate of 30 L/hr. The first two cycles were in a standing water extraction mode, while the last three were operated in a counter-current mode with a water flow rate of 5 L/hr. During the extraction, the radon rate in the scintillator varied between 200 and 400 events per day and the thoron rate ranged from 4 to 6 events per day. The ^{85}Kr rate remained constant. These data again indicate an emanation source in the liquid nitrogen tank from which the stripping nitrogen is obtained.

Radon introduced during the extraction was allowed to decay for one month before the background level in the scintillator was analyzed to determine the effectiveness of water extraction. This analysis showed that the internal background in the scintillator had been reduced to approximately 50 events per day. The reduction of one contaminant, ^{210}Po, was especially dramatic. ^{210}Po is a daughter of radon, and its level in the scintillator will accumulate after a high radon exposure such as that experienced during the initial filling. Figure 3.21 shows the energy spectrum of events in the neutrino window and at slightly higher energies before and after water extraction. ^{210}Po decays by emission of a 5.3 MeV α, but because of the quenching factor for α's in the scintillator (discussed in Chapter 4) it is detected at 0.395 MeV in the CTF. The removal of the ^{210}Po peak at 0.395 MeV can be clearly seen in Figure 3.21. ^{210}Bi is another radon daughter that should be present in the scintillator along with ^{210}Po. ^{210}Bi decays by emission of β's with a range of energies. Because there is not a single peak in the energy spectrum associated with the ^{210}Bi, its removal is not as easy to demonstrate as the removal of the ^{210}Po.

Distillation was the final purification operation to be analyzed for its effect on radioactive contamination. Distillation was run for three cycles with a scintillator flow rate of 12 L/hr. During this processing, the radon level increased to between

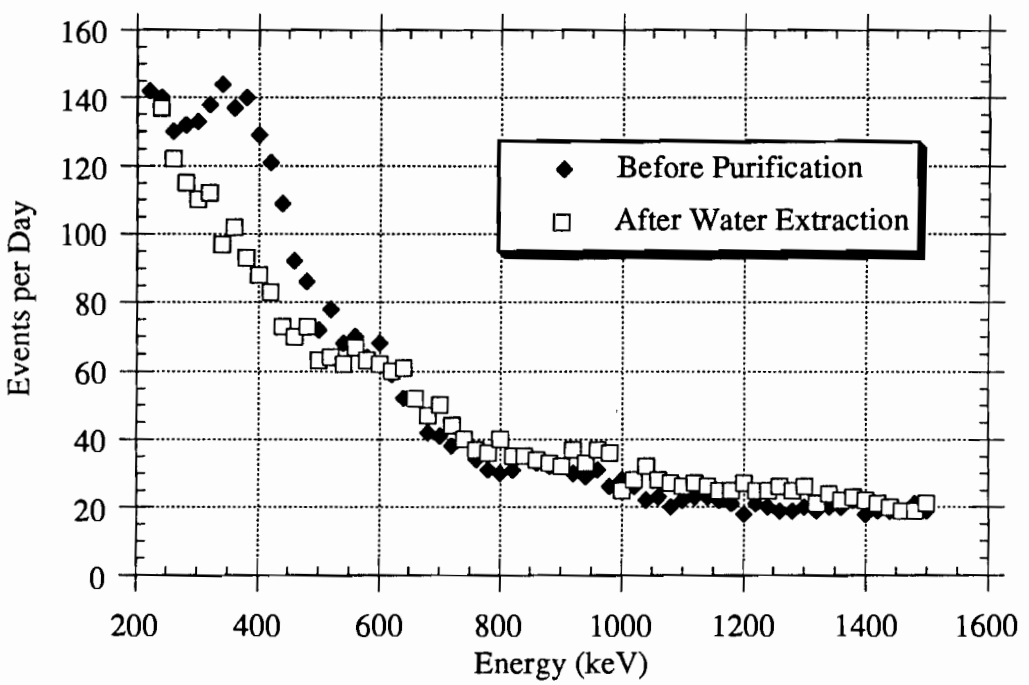

Figure 3.21. Removal of ^{210}Po by water extraction. This plot shows the energy spectrum of events in the CTF before and after water extraction. The energies shown are those in and slightly above the neutrino window. Water extraction clearly removed the peak 0.395 MeV, which has been attributed to ^{210}Po. From Benziger et al.[2]

1000 and 2000 events per day and showed large fluctuations of unknown origin. The thoron rate was approximately 5 events per day. The coincidence events due to ^{85}Kr increased from 0.2 ± 0.2 events per day to 0.45 ± 0.2 events/day during the first five days. This level then returned to 0.2 ± 0.2 events per day by the end of the distillation processing. The initial jumps in the radon and ^{85}Kr levels are consistent with a small spike of air contamination at the beginning of distillation. The decline in krypton and the continued high levels of radon indicate continued emanation from the nitrogen tank.

The internal background in the scintillator improved slightly as a result of distillation. This can be seen in Table 3.2, which lists the number of background events at various stages during the purification. The distillation produced less reduction in impurity levels than did water extraction, but distillation began when the backgrounds were already much lower. An examination of Table 3.2 shows that the errors in the internal background at the end of purification are equal to or larger than the quoted background values. These errors are due to leakage of external background events into the detector, making them difficult to distinguish from internal background. An internal background of essentially zero is consistent with the data at the end of purification.

Distillation was also used to remove PPO from the scintillator in an attempt to determine if it was the major cause of ^{14}C contamination in the detector. The PPO was successfully removed at a level of 12%. The results were inconclusive. A reduction of approximately 7% in low energy events was observed in the detector following the removal of PPO. This could be attributed to ^{14}C reduction, but it also consistent with reduced light production in the scintillator due to the reduction in fluor concentration. Because both effects are of the same magnitude, it has been impossible

Table 3.2. Backgrounds in the CTF during purification operations. The number of events/day in the neutrino window (0.250 – 0.800 MeV) at various stages in the purification process are listed below. The events listed under ^{210}Po include all the events under the peak at 0.395 MeV, which includes ^{85}Kr, ^{210}Po, and ^{210}Bi events although the majority are due to ^{210}Po. Data from Benziger et al.[2]

Time Period	Total Background (events per day)	Total Internal Background (events per day)	^{85}Kr (events per day)	^{210}Po (events per day)
Initial Filling	2596 ± 216	479 ± 77	185 ± 34	335 ± 57
After Nitrogen Stripping	2325 ± 222	285 ± 72	25 ± 25	265 ± 62
After Water Extraction	2074 ± 194	< 40 ± 65	25 ± 25	< 40
During Distillation			50 ± 25	0
After Distillation	2005 ± 192	<35 ± 67	< 25 ± 25	0

to rule out either one and make a definite statement regarding the ^{14}C level in the fluor.

The uranium and thorium levels calculated for the scintillator after the initial filling were not improved by purification, although the processing did reduce the number of internal background events in the scintillator. While the thorium level was at or below the limit of detectability in the CTF at both times, the uranium level was somewhat higher. Because the uranium concentration was determined by measuring the decay of radon daughters, a constant radon source in the detector could cause an erroneous measurement. The existence of such a source is supported by the fact that while the uranium and thorium concentrations in the scintillator should be quite similar due to the chemical similarities between the two elements, the uranium level in the scintillator was measured to be much higher than that of thorium.

Two potential sources for radon in the scintillator are emanation from the nylon membrane due to uranium contained in it and diffusion of radon from the shielding water through the nylon. Radon levels in the shielding water were 10 – 20 times higher than expected in the design of the experiment. Recent measurements by Cadonati[8] on the diffusion of radon in nylon indicate that the 25 mBq/m^3 of radon in the shielding water could diffuse into the scintillator at a rate sufficient to account for the entire background in the scintillator originally attributed to uranium. Radon emanation from the permatex lining of the shielding water tank is suspected to be the cause of the relatively high radon levels in the shielding water. (The CTF water plant can produce water with a radon content of less than 10 mBq/m^3 before it enters the shielding water tank.). These results are quite encouraging with respect to scintillator purity, because many of these sources of radon background will be avoided in the design of Borexino.

The overall results of the scintillator purification to remove radioactive contaminants are quite encouraging. The nitrogen stripping, water extraction, and distillation operations were all shown to have the ability to reduce radioactive background in the scintillator. These operations are promising for use in Borexino, and analysis of the CTF data indicate that the purity goals of Borexino can be met if problems with radon contamination can be overcome.

3. Mixing in the Scintillator Containment Vessel

In all the purification operations, the background reduction with each cycle was less than exponential. This can be explained in two ways: incomplete removal of the contaminant with each pass through purification or incomplete mixing in the scintillator containment vessel. If the mixing in the containment vessel is imperfect and scintillator flows through it in a plug flow manner, the purification obtained with each cycle will be greater than that observed when perfect mixing occurs. If the mixing is such that processed scintillator is more likely to be reprocessed by the system than unprocessed scintillator, less purification will take place. (This could occur if scintillator returning to the top of the containment vessel follows a flow path taking it toward the outlet at the bottom.)

Laboratory measurements which attempted to scale the CTF behavior to a 20 cm diameter sphere indicated that perfect mixing would occur. CTF results with PPO removal and bis-MSB addition did not reflect this. Approximately 15% of the scintillator volume was processed to remove 12% of the PPO from it. At the end of this removal, scintillator exiting the containment vessel still contained the original level of PPO. This indicated that good mixing was not taking place, but seems to support a plug flow behavior which would actually improve purification performance. Scintillator mixing upon addition of bis-MSB also went slowly, and several cycles of circulation were required to mix the scintillator completely. Perfect mixing certainly

does not occur in the scintillator containment vessel of the CTF, but this may not explain the slower than expected scintillator purification. Incomplete contaminant removal with each pass through the purification plant also must be considered as the cause of this less than ideal performance.

G. Lessons from the CTF Scintillator Purification Plant

Overall, the scintillator purification system was quite successful. The optical properties of the scintillator were maintained over a period of almost two years. The plant also showed that contaminants could be removed from the scintillator to make it extremely radiopure, although the purities required for Borexino could not quite be demonstrated due to the existence of other backgrounds. Many of the design features used in this plant will also be used in the purification plant for Borexino. The choice of construction materials was validated by the CTF purification results; no contamination problems originated from the electropolished stainless steel or Teflon. The computer control system performed flawlessly, and allowed the plant to be operated safely 24 hours a day.

The greatest problem with the purification plant was the contamination of the stripping nitrogen with radon, and this must be corrected for Borexino. This problem can be solved by obtaining a new tank to supply the boil-off nitrogen; the new tank must be cleaned to the same standards as the rest of the plant. Such a tank has been built, and now must be tested to see if the contamination has been eliminated.

In addition to showing that purification of the scintillator was a viable strategy, the CTF purification plant also served as a learning experience. The lessons learned during its operation should improve the performance of the plant for Borexino when it is constructed. The plant must be vacuum tight, not simply liquid tight, in order to ensure that the scintillator cannot be contaminated from radon in the air. This requires

the use of appropriate gaskets in the system. The VCR, Swagelok, Teflon-encapsulated viton, and Teflon-taped pipe thread seals all performed well. The Teflon sandwich gaskets were not reliable and will be replaced in the next plant. The Topline™ connections were also found to be problematic. Although they sealed to vacuum when tight, the Teflon gaskets in them flowed, and they began to leak over a period of months.

The piping design for the Borexino plant can also be optimized based on CTF experience. Valves to isolate each vessel in the plant should be provided to allow individual cleaning of the vessels. Dead volumes in the piping must be reduced to an absolute minimum, because these areas are very difficult to clean adequately. The plant must be designed with cleaning procedures in mind, and the cleaning mechanisms should be included as an integral part of the plant. In the CTF plant it took a great deal of time to provide the utilities necessary for an effective cleaning.

While the instrumentation in the CTF plant worked well, additional information, especially that which could have been provided by a flow meter in the scintillator piping, would have been useful. Implementation of the Borexino plant would also be facilitated by contracting the installation of electric power and instrument signal cables to a commercial firm. Although this was done quite effectively by the Princeton group, it took a significant amount of time due to manpower limitations.

Results from the CTF purification also provided information on backgrounds in the experiment. The only backgrounds which were specifically identified were ^{222}Rn, ^{220}Rn, ^{85}Kr, and ^{210}Po. Three of these four were identified through the use of delayed coincidence techniques which the CTF was very powerful in providing. The CTF plant was effective in removing the ^{85}Kr and ^{210}Po backgrounds, and would have removed radon as well if the stripping nitrogen had not been contaminated. Other

small unidentified backgrounds were also removed. The importance of minimizing exposure to air was reinforced by CTF operations. Air exposure introduced radon and krypton contamination which had to be removed by purification. It was found that allowing the radon to decay is not sufficient to achieve the necessary purity in the scintillator because of the accumulation of radon daughters. The radon daughters are a source of additional activity, and they must be removed by purification. The ubiquity of radon was not fully appreciated before the CTF was constructed, and many radon sources found in the CTF will be avoided by appropriate design strategies in Borexino. The most notable of these strategies will be the use of a stainless steel sphere to contain the scintillator and a pseudocumene buffer. This will eliminate the problem of radon diffusion from the shielding water.

The results from the CTF, in which the purification plant played an integral part, allow the Borexino collaboration to proceed with some confidence toward the design and construction of Borexino. The CTF has shown, at least to the lowest level possible without the construction of Borexino, that a liquid scintillator has the necessary radiopurity for the larger experiment. The purification plant demonstrated that the scintillator can be processed without contaminating it and that impurities introduced by improper handling can be removed.

References

1. Borexino Collaboration. "A Large Scale Low Background Liquid Scintillation Detector: The Counting Test Facility at Gran Sasso", *Nucl. Inst. and Meth. A* , in press.

2. J.B. Benziger, F.P. Calaprice, M.C. Chen, N. Darnton, M.C. Johnson, F. Loeser, and R.B. Vogelaar, "Purification System for a Low-Background Liquid Scintillation Detector", in preparation.

3. Benziger, J. B.; Calaprice, F. P.; Chen, M. C.; Eisenstein, R. A.; Vogelaar, R. B. NSF Borexino Proposal, Princeton, 1996.

4. Vogelaar, R. B.; Benziger, J. B.; Calaprice, F.; Darnton, N. *Nucl. Inst. Meth. A* **1996**, *372*, 59.

5. Hines, A.L.; Ghosh, T.K.; Loyalka, S.K.; Warder, R.C. *Indoor Air Quality and Control*; PTR Prentice Hall: Englewood Cliffs, New Jersey, 1993; Chapter 1.

6. Wojcik, M., University of Krakow, private communication (manuscript in preparation).

7. Sandler, S.I. *Chemical and Engineering Thermodynamics*; John Wiley & Sons: New York, 1989; p 439.

8. Cadonati, L. *Bull. Am. Phys. Soc.* **1997**, *42*, 1633.

9. *CRC Handbook of Chemistry and Physics*; Lide, D. R., Ed.; CRC Press: Boca Raton, 1991; p 5-60 – 5-63.

10. Balata, M. *Nucl. Inst. and Meth. A* **1996**, *370*, 605.

11. Elisei, F.; Masetti, F.; Mazzucato, U. Borexino Project - Report N. 10, January 29, 1996; Perugia.

12. Borexino Collaboration. "Ultra-low Background Measurements in a Large Volume Underground Experiment", *Astroparticle Phys.*, in press.

13. Borexino Collaboration. "Measurement of the ^{14}C Abundance in a Low-Background Liquid Scintillator, *Phys. Lett. B*, in press.

CHAPTER 4: PROCESSES AFFECTING LIGHT PROPAGATION IN LIQUID SCINTILLATORS

A liquid scintillation detector measures incident radiation through detection of the emitted scintillation light. The incident radiation excites the scintillator components which then relax to their ground state and sometimes emit light in the process. The emitted light is detected with devices such as photo-multiplier tubes (PMTs). Organic liquid scintillators normally consist of an aromatic solvent and one or more fluors. Because the bulk of the scintillator consists of the solvent, most of the incident radiation will excite this component. Most solvent species have a rather low efficiency for turning their excitation energy into light, and the fluor(s) are added to improve this efficiency. The fluor molecules have a much higher efficiency for producing light from their excitation energy. In a properly designed scintillator, the solvent efficiently transfers its energy to the fluor, which emits the detected light. Unfortunately, not all the light emitted by the fluor is detected. The study of light propagation in a liquid scintillation detector is concerned with light production and the journey of the emitted photons from their point of emission until their detection at a PMT. The study of this subject is very important in predicting and understanding the behavior of large-scale scintillation detectors such as the CTF and Borexino.

There are several processes which can occur during the production and transport of photons in an organic scintillator. This chapter provides a background on many of these processes and reviews some relevant literature on the subject. Liquid scintillation detectors have been used since the early 1900's, and there is a large amount of literature in the field. Although scintillators in general are considered, this review stresses those aspects most important to detectors like the CTF. Scintillation parameters are reported for benzene and some of its alkyl derivatives. These derivatives, including toluene (methylbenzene), p-xylene (1,4-dimethylbenzene), and

mesitylene (1,3,5-trimethylbenzene), are of interest because of their similarity to pseudocumene, the CTF solvent. Some scintillation parameters for pseudocumene are also considered here. Parameters are listed for the fluors PPO, bis-MSB, and p-terphenyl because of their use in the CTF, and to illustrate the differences between solvent and fluor performance.

Because the entire scintillation process is driven by the behavior of the excited states of the π-electrons in aromatic molecules, the structure of these states is examined. The excitation of electrons to those states by ionizing and photon radiation incident upon the scintillator is also considered. A preview of the transitions among electronic energy levels is presented, and some nomenclature is introduced. Transitions between energy levels accompany absorption of light, emission of light, energy transfer from solvent to fluor(s), and quenching of emission. Light can also be scattered elastically in the scintillator through Rayleigh scattering, and the mechanism of this scattering is reviewed. Other effects, including the reflection and refraction of light at the scintillator-water interface and the reflection of light from the glass of the PMTs, can also affect the path of light in the detector.

A. Π-electron Excited States: The Perimeter Free Electron Orbital Model

The electronic energy levels of aromatic molecules are often treated theoretically by the perimeter free electron orbital (PFEO) model.[1,2] The model is usually applied to cata-condensed hydrocarbons, defined as aromatic molecules in which no carbon atom belongs to more than two rings. In this model, the π-electrons are assumed to belong to the whole molecule and have the characteristics of the "free" electrons in metals and semiconductors. The π-orbitals are treated as a one-dimensional loop around the molecular perimeter. Approximating the perimeter as a

circle of circumference p, the orbital wavefunction ψ must satisfy the boundary condition

$$\psi(x) = \psi(x + p) \qquad (4.1)$$

where x is measured along the perimeter. Solution of the Schrödinger equation gives the eigenfunctions ψ_q and eigenvalues E_q for the π-orbitals. Because the electron has a spin of $\pm$ 1/2 and can move either clockwise or counterclockwise around the perimeter, all the energy levels except for E_0, the lowest, are doubly degenerate.

The parameter q in the eigenvector and eigenvalue notation is the orbital ring quantum number. It is a measure of angular momentum which describes the number of nodes of the wavefunction. This number no longer describes angular momentum when the circular perimeter is distorted to conform to a molecular perimeter and a periodic potential due to the carbon atoms in the molecule is added, but it remains a good quantum number because it describes the number of nodes. In an n-ringed molecule, the highest filled level in the ground state corresponds to q = n. In the PFEO model nomenclature, the electron shells for which q = n - 1, n, n + 1, and n + 2 are represented by e, f, g, and h. A total ring quantum number Q is given by the algebraic sum of the individual q's of the electrons. In PFEO nomenclature, the letters A, B, and C are used to describe states with Q = 0, 1, and 2 while K, L, and M describe states with Q = 2n, 2n + 1, and 2n + 2. If a constant potential around the perimeter is assumed, each state excluding the A state is doubly degenerate. If a periodic potential due to the carbon atoms is added, this degeneracy is removed, and each state splits into two components represented with subscripts a and b which differ in the position of the nodes relative to the molecule.

The ground state of the system is represented by ^1A, and has the configuration f^4, Q = 0, and electron spins paired. If an electron is excited from f to g ($\Delta q = 1$) then the configuration becomes f^3g and $Q = (n + 1) \pm n = 1$ or 2n + 1. The excited state is

either singlet or triplet depending on whether or not there is a spin reversal in the transition. Because of this, there are eight possible states corresponding to the f^3g configuration: ^1B_a, ^1B_b, ^1L_a, ^1L_b, ^3B_a, ^3B_b, ^3L_a, and ^3L_b. The 1 and 3 superscripts refer to singlet and triplet states, respectively. Other higher states can be formed with $\Delta q = 2$ transitions, but they will not be considered here.

Although the PFEO model is applicable to larger aromatic compounds, it will be considered here only for benzene because pseudocumene is an alkyl benzene used in the CTF. No PFEO model calculations have been found for pseudocumene or PPO, the CTF scintillator components. In benzene, the triplet state ^3L_a is the lowest excited state. The lowest excited singlet state is ^1L_b, followed by ^1L_a and ^1B (in benzene the ^1B_a and ^1B_b states are degenerate and represented by ^1B). The triplet states ^3L_b and ^3B (the triplet B state is also degenerate) lie at higher energies than the ^3L_a state. The relative positions of these energy levels are shown in Figure 4.1a. Figure 4.1b indicates the pairing and spins of the π-electrons in the ground state and in the first excited singlet and triplet states. Pseudocumene has the same order of excited states as benzene does, and these energies have been measured for some singlet states. The energies of the ^1L_b, ^1L_a, and ^1B states in pseudocumene are 38000 cm^{-1}, 46700 cm^{-1}, and 51300 cm^{-1}, respectively, above ground level.[3]

Selection rules based on electron spin and symmetry can be used to predict which transitions will be the strongest. A transition is forbidden if the spin of the electron in the initial and final states differs; a singlet to triplet transition is not allowed and is referred to as spin-forbidden. The intensity of the transition from ^1A to ^3L_a is only 10^{-8} that of the spin-allowed ^1A to ^1L_b transition. There is a finite amount of the forbidden transition due to spin-orbit interaction which couples the eigenfunctions of the singlet and triplet states. Transitions are forbidden by symmetry considerations if the initial and final states have the same symmetry. In the PFEO

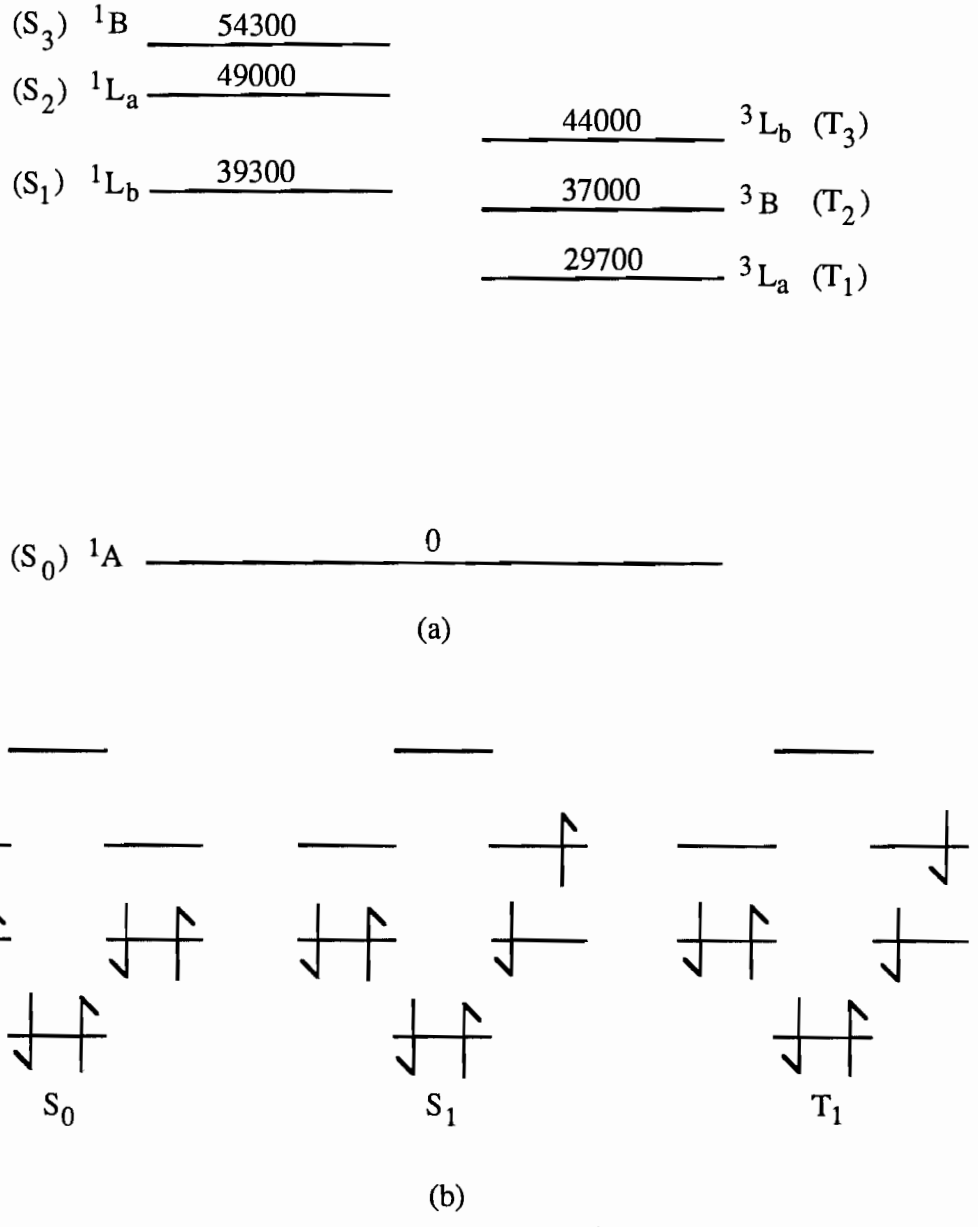

Figure 4.1. Excited electronic energy levels of benzene. a) The energies of the first three singlet and the first three triplet electronic states are shown for benzene. Units are in cm^{-1} above the energy of the ground state. Data from Birks.[1] b) The arrangement of the π-electrons in benzene are shown for the ground state and the first singlet and triplet states. The electron spins are paired in the singlet state and they are unpaired in the triplet.

model, the ^1A state has symmetry similar to the ^1L_b and ^1L_a states, while that of the ^1B state is different. The transitions to the former two states from the ground state are symmetry-forbidden and that to the latter is symmetry-allowed. Experimental measurements have shown that the intensity of the transition to the ^1L_b state is reduced by a factor of $10^2 - 10^3$ from that to the ^1B state, while that to the ^1L_a state is reduced by a factor of 10. Although they are forbidden by symmetry, these transitions occur because of molecular vibrations which modify the symmetry of the pure electronic states.

In addition to labeling the excited electronic states in terms of the PFEO model nomenclature, Figure 3.1 also identifies the excited states using another convention. This is the S_0, S_1, S_2, S_3, T_1, T_2, and T_3 scheme, where S_0 is the ground state, S_1 is the first excited state with paired electron spins, S_2 is the second excited state with paired electron spins, T_1 is the first excited state with unpaired electron spins, and so forth. The S states are known as the singlet manifold and the T states are known as the triplet manifold. The S and T designations are used more extensively in this review than the PFEO model nomenclature.

B. Excitation of Scintillator by Ionizing Radiation

A scintillation detector is designed to receive excitation energy from a source of ionizing radiation and convert this energy into light. Many events occur when ionizing radiation (electron, proton, α-particle, γ-ray, etc.) passes through the scintillator. As the radiation travels through the scintillator, it imparts energy to the scintillator molecules. Most of this energy is in the form of kinetic energy of the scintillator molecules and cannot be detected. Ions, electronically excited molecules, free radicals, and secondary electrons (ejected from their molecule through interaction with the ionizing radiation) are all formed along the track of the ionizing radiation.

The secondary electrons form tracks of their own in the scintillator. Interactions occur between the ions, free radicals, excited molecules, and ground state molecules along the track, and result in the nonradiative decay of many excited molecules. Some of the electronically excited molecules do retain their excitation energy, and other electronically excited molecules are formed from the recombination of ions in the scintillator. This electronic excitation energy is the cause of light emission from the scintillator.

The efficiency of the conversion of the energy of the incident ionizing radiation to electronic excitation energy in the scintillator depends upon the type of radiation. The scintillation efficiency is defined as the ratio of the amount of energy contained in the photons emitted by the scintillator to the initial energy of the incident radiation. For an electron, a scintillation efficiency of approximately 5% is obtained.[4] Assuming that most of the electronic excitation energy of the scintillator is emitted in the form of photons (see later sections of this chapter), this means that only slightly more than 5% of an incident electron's energy is converted to electronic excitation energy in the scintillator. The distribution of this electronic excitation energy has been measured for β-particle excitation. Most of the excited molecules, 87.1%, are in the S_3 state,[3] with 12.6% in S_2, and 0.3% in S_1. Because almost all fluorescence comes from S_1, most of the energy must be converted to this state before emission occurs. The scintillation efficiency varies somewhat with the energy of the electron; higher energies exhibit a slightly higher efficiency. The scintillation efficiency for an α-particle is about an order of magnitude lower, as confirmed by measurements of Borexino collaborators.[5] They found that the light yield for electrons in the CTF scintillator was 10,000 photons per MeV, while the light output from α-particles was quenched by a factor of nearly 10. (The quenching factor depended slightly on the energy of the α-particle.) As a general rule, higher specific ionization (the amount of

ionization caused in the scintillator per unit length of radiation track) corresponds to lower scintillation efficiency.

The timing characteristics of the resulting fluorescence emission also depend on the incident radiation. With their higher specific ionization, α-particles excite more scintillator molecules into triplet states than does β-radiation. If two triplet state molecules diffuse near each other and interact, this can result in the formation of a molecule in an excited singlet state. Fluorescence emission occurs, but it is delayed by the time required for the diffusion process. These delayed photons cause a measurable tail in the light emission, as seen in Figure 1.8. This phenomenon is used for α-β discrimination in the CTF. Actual emission from the triplet states (phosphorescence) would occur on an even longer time scale and it is not observed in liquid scintillators.

Other types of ionizing radiation in addition to α- and β-particles also interact with scintillators. One of these is γ-radiation. γ-Rays normally interact with the scintillator by scattering off electrons in the liquid. Because scintillator excitation is caused by these scattered electrons, scintillation from γ-ray interaction closely resembles that from a β-particle. In Borexino, an important source of scintillation will be neutrinos. Neutrinos scatter off electrons in the scintillator, and neutrino events resemble β events in timing.

The processes which result in the conversion of a fraction of the energy of the incident radiation into electronic excitation energy in the scintillator are quite complicated and are not completely understood. It has been established that the spectrum of light emitted from a scintillator is the same when it is excited by ionizing radiation as when light photons in the ultra-violet region of the spectrum cause the excitation.[6] (The energy of light in the ultra-violet region corresponds to the energy of the electronic transitions in aromatic molecules.) The scintillation efficiency and the

timing characteristics do depend upon the mode of excitation, and appropriate radiation sources must be used in order to determine these properties of a scintillator. Many studies of light propagation in scintillators have been performed using ultra-violet excitation because of the simplicity of using photon sources and because the processes by which photon excitation takes place are well-understood. Because the laboratory studies for this thesis were concerned mainly with what happened to the light after its initial emission, ultra-violet excitation was utilized in them. Radioactive excitation was employed in experiments which used the CTF to study light propagation, but the CTF experiments were designed to determine what happened to the light after its initial emission and not to probe the processes of scintillator excitation by ionizing radiation.

C. Introduction to Photophysical Processes in Aromatic Molecules

The optical properties of the organic molecules under consideration in this work are largely determined by the energy levels of their π-electrons. Figure 4.2 presents an energy level diagram for the π-electrons of a generic aromatic molecule. The figure shows some transitions between the various singlet and triplet energy levels. The transitions shown in Figure 4.2 will be described here briefly, and those of importance in the CTF will be covered in more detail in later sections. The nomenclature introduced here corresponds to that of Birks.[1]

The processes occurring in the electronic energy level transitions shown in Figure 4.2 can be divided into three categories: radiative excitation (absorption), radiative relaxation (luminescence), and nonradiative. The processes mentioned in the following paragraphs refer to transitions labeled by small Roman numerals in Figure 4.2. The excitation transitions in Figure 4.2 are assumed to be caused by photon absorption, whether the source of the photon is a light source in a laboratory

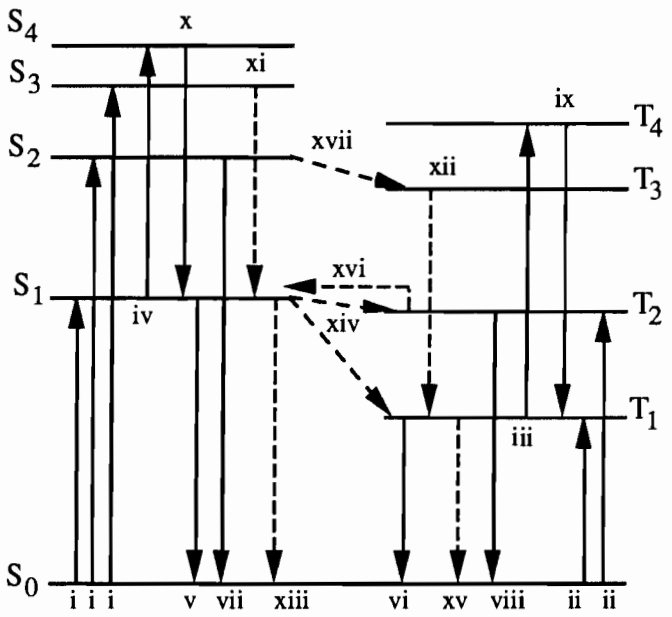

Figure 4.2. Transitions between energy levels. The diagram shows various transitions which can occur between the electronic energy levels of an aromatic molecule. The small Roman numerals identify transitions which are discussed in the text. The solid lines indicate radiative transitions, and the dashed lines indicate nonradiative transitions. From Birks.[1]

experiment or the emission of another scintillator molecule. It should be remembered that these same transitions are caused by interactions with ionizing radiation, the source of the initial excitation in an operating scintillation detector.

Excitation transitions between states with the same multiplicity include S_0 to S_1 (i) and S_0 to $S_{p\ (p>1)}$ (i) transitions. These transitions correspond to the main electronic absorption spectrum. S_1 to S_p (iv) and T_1 to $T_{q\ (q>1)}$ (iii) transitions are also spin-allowed. They originate from excited states, however, and can only be observed under special conditions involving intense light sources. Because of this, they do not play a role in light propagation in the CTF. The S_0 to T_1 (ii) and S_0 to T_q (ii) transitions are spin-forbidden, as described in Section 4.A, and are unlikely to occur due to photon excitation. Excitement into the triplet states is more common with ionizing radiation.

Luminescence is the release of energy from the molecule in the form of a photon. Luminescence transitions which are spin-allowed are known as fluorescence, while those which are forbidden are known as phosphorescence. The radiative S_1 to S_0 (v), S_p to S_0 (vii), S_p to S_1 (x), and T_q to T_1 (ix) transitions are all examples of fluorescence. S_1 to S_0 fluorescence is by far the most common, and it is considered to be the source of all light emission in the CTF. Emission due to the S_p to S_0 transition has been detected from some molecules, but is difficult to observe because the wavelength of the emitted light lies in the absorption band of the emitting molecule and it is quickly reabsorbed. The T_q to T_1 radiative transition has also been observed under special conditions for a few molecules, but it is an uncommon phenomenon. The S_p to S_1 emission has never been observed, but it is a plausible process. Phosphorescence occurs in the radiative T_1 to S_0 (vi) and T_q to S_0 (viii) processes. The T_1 to S_0 is more common and almost all observed phosphorescence is attributed to it. The T_q to S_0 emission is very improbable. In a scintillation detector such as the

CTF, phosphorescence is not a factor in the detected light. Phosphorescence occurs on a long time scale due to the forbidden nature of the transition, and the molecules in a liquid scintillator relax by other means before it takes place.

Radiationless transitions which are spin-allowed are known as internal conversions. They include the S_2 to S_1 (xi), S_p to S_{p-1} (xi), T_2 to T_1 (xii), T_q to T_{q-1} (xii), and S_1 to S_0 (xiii) processes. The S_2 to S_1 and S_p to S_{p-1} conversions usually occur rapidly before fluorescence can occur, and this is the reason little emission is seen from higher singlet states. The radiationless S_1 to S_0 transition is conversion to the ground state, and it is in direct competition with S_1 to S_0 fluorescence. Radiationless transitions which result in a change in electron spin are called intersystem crossings. They include the S_1 to T_1 (xiv), S_1 to T_q (xiv), T_1 to S_0 (xv), and S_p to T_q (xvii) processes. The intersystem crossing from T_1 or T_2 to S_1 (xvi) may occur if the T_1 or T_2 state is thermally activated.

A notation also exists for referring to the various excitation states of the molecules in a scintillator. A solvent molecule in the ground state is labeled ^1M. The solvent in the first excited singlet state (S_1) is $^1M^*$, and in any higher singlet state it is $^1M^{**}$. A similar convention is followed for the triplet solvent states; a T_1 state is represented by $^3M^*$. The solute is denoted by Y. The solute in the ground state is ^1Y, and $^1Y^*$ represents the solute in its first excited singlet state. If a second solute is present, it is represented as Z. An excited solvent molecule can react with an unexcited molecule of the same species to form an excited dimer, $^1D^*$. These dimers are dissociated in the ground state. Some impurities in the scintillator can cause quenching of fluorescence, and they are labeled as Q.

A systematic method is also used for representing the rate constants of the photophysical processes. The symbol k stands for a rate parameter, and a subscript indicates the process. When two subscript letters are present, the first indicates the

result of the process and the second its origin. When only one subscript letter is written, the rate is for the sum of all processes originating in the state indicated by the subscript. The subscript notation is listed below:

m = $^1M^*$	d = $^1D^*$	q = quencher molecule
g = ground state	y (or z) = fluor	p = phosphorescence
t = $^3M^*$	f = fluorescence	i = internal quenching
h = $^1M^{**}$	k = $^3M^{**}$	

D. Excitation of Aromatic Molecules by Photon Radiation

Radiation is absorbed by aromatic molecules when the energy of the radiation corresponds to the energy of a transition in the molecule. The molecular energy is composed of three components: electronic, vibrational, and rotational. Electronic energy levels are spaced by 1 – 6 eV, vibrational levels are spaced by an average of 0.1 eV, and rotational levels are approximately 0.001 eV apart. The vibrational and rotational transitions correspond to absorption of light in the infrared region. (In this thesis, photon radiation is referred to as light.) Electronic transitions are induced by light in the ultraviolet region, and these transitions are the ones of interest in aromatic scintillators.

Although the energies of vibrational transitions are much lower than that of the ultraviolet light being considered here, they do affect its absorption. This effect is illustrated in Figure 4.3, where absorption of light causes a transition from the lowest vibrational state of S_0 to various vibrational states in S_1. The frequency of radiation which induces the transition is determined by the vibrational level of the final state. Because these transitions result in changes in both the electronic and vibrational energy levels, they are called vibronic transitions. Similar transitions occur to the S_2 and higher states. Excitation into the triplet states can occur, but this is rare because

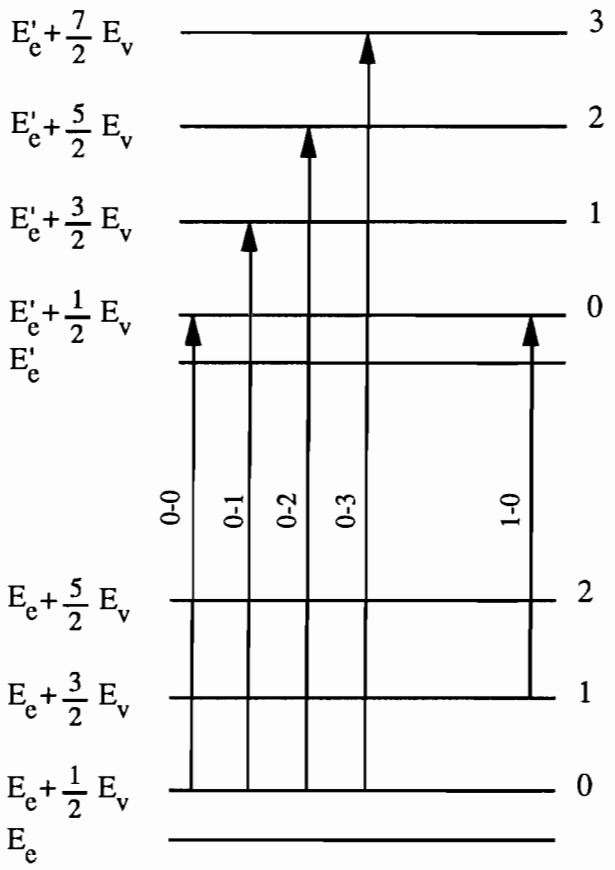

Figure 4.3. Vibronic transitions in absorption. The diagram shows vibronic transitions from the ground electronic state (at energy E_e)to various vibrational levels in the first excited electronic state (at energy E'_e). Most absorption takes place from the 0 vibrational level in the ground state, but absorption from other levels can also occur, resulting in hot bands in the absorption spectrum. From Birks.[1]

those transitions are spin-forbidden. The transitions mentioned above took place from the ground level vibrational state in S_0. Transitions also take place from other vibrational levels in S_0, as shown in Figure 4.3. Transitions from higher vibrational levels are less common because 99% of the molecules are in the lowest vibrational state at room temperature. (This is calculated from the Boltzmann distribution with $\Delta E = 0.1$ eV). Absorption from the first excited vibrational state can give rise to a feature in absorption spectra known as the hot band.

The vibronic transitions are denoted by the vibrational levels between which they occur. The transition from the lowest vibrational state in S_0 to the first excited vibrational state in S_1 is a 0-1 transition, and one from the first excited vibrational level of S_0 to the ground vibrational state of S_1 is labeled 1-0. The lowest energy transition from the ground vibrational level in S_0 is the 0-0 transition. This transition is forbidden in some molecules, such as benzene, due to symmetry.

In the gas phase absorption spectra of aromatic molecules, the individual vibronic transitions can be identified. The 0-0, 0-1, 0-2, etc. transitions give sharp peaks in the spectrum. In the liquid phase, these sharp peaks are not seen because of vibronic coupling between the states, and normally only a broad peak is observed. An absorption spectrum for pseudocumene is shown in Figure 4.4. The features near 270 nm are due to S_0 (^1A) to S_1 (^1L_b) transitions. The shoulder at 215 nm can be assigned to S_0 to S_2 (^1L_a) transitions, and the peak at 195 nm to S_0 to S_3 (^1B) absorption. It is clear that the allowed ^1A to ^1B transition is more intense than the other two symmetry-forbidden transitions. (In pseudocumene, as in benzene, the ^1L_b and ^1L_a states have the same symmetry as the ^1A state. Symmetry-based selection rules forbid transitions between states with the same symmetry. The ^1B state exhibits a different symmetry, and transitions from ^1A to ^1B are therefore symmetry-allowed.)

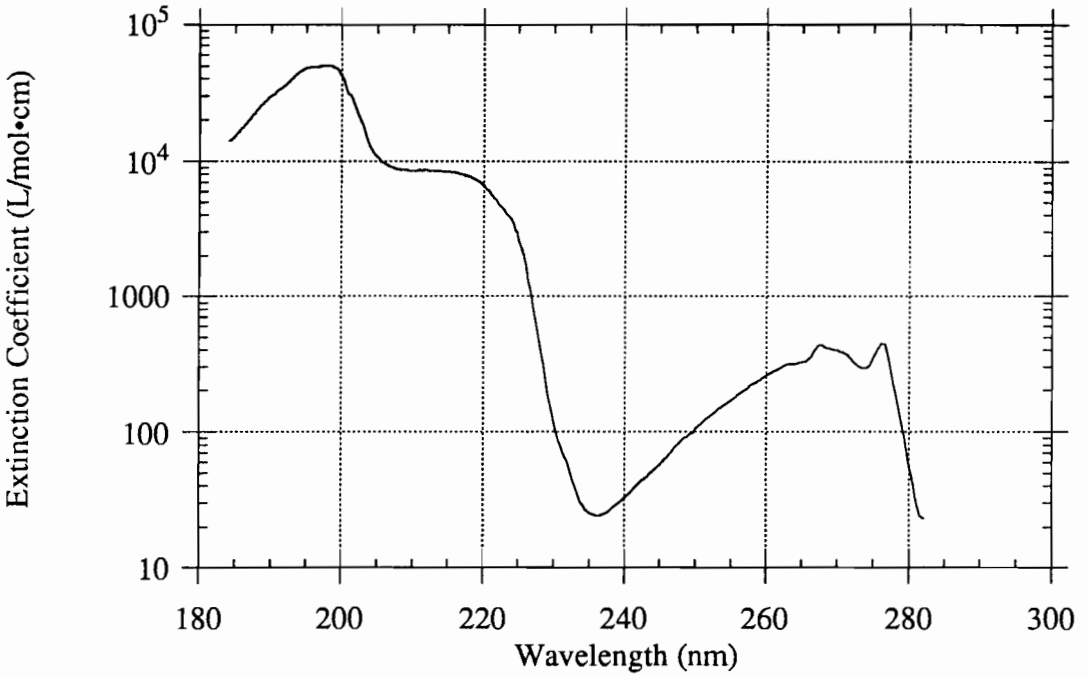

Figure 4.4. Absorption spectrum of pseudocumene. Pseudocumene absorption is shown in terms of the molar decadic extinction coefficient. The extinction coefficient is plotted on a logarithmic scale. Data from Perkampus.[7]

In Figure 4.4, the intensity of the transitions is shown by the parameter ε. This is the molar decadic extinction coefficient. It is commonly used in absorption spectroscopy to express the intensity of an absorption transition. From Beer's law, it is known that the intensity of light passing through an absorbing medium can be represented by an exponential decay of the initial intensity of the light entering the medium. The decay rate depends on the molecular cross section for absorption of light, the density of absorbing molecules, and the distance through the medium. Beer's law is often expressed in the form

$$I = I_0 \, 10^{-\varepsilon c d} \qquad (4.2)$$

I is the intensity of light transmitted through the medium. I_0 is the intensity of light entering the medium, ε is the molar decadic extinction coefficient (L/mol•cm), c is the concentration of absorbing molecules (mol/L), and d is the distance through the medium (cm).

Absorption of light by the scintillator molecules plays a critical role in light propagation in a scintillation detector. The extinction coefficients provide a measure of how strongly light of different wavelengths is absorbed by the scintillator. Wavelengths which are strongly absorbed travel only a short distance in the detector before the absorption occurs. Wavelengths which are more weakly absorbed travel greater distances and have a higher probability of escaping from the scintillator to reach the phototubes surrounding it. Absorption of photons creates excited scintillator molecules which cannot be distinguished from those excited by ionizing radiation. The absorption in the detector depends on the concentrations of the scintillator components as well as their extinction coefficients. The solvent concentration is fixed in a liquid scintillator, but the fluor concentration can be varied in order to optimize performance. Lower fluor concentrations result in less absorption of fluorescence, but the efficiency of energy transfer from the solvent also decreases as the fluor becomes

more dilute (see Section 4.H). The extinction coefficients measured for light absorption are quite useful for predicting the behavior of light in a large-scale detector. These coefficients are very accurate in the main absorption bands where the absorption is intense. Some care must be taken when the extinction coefficients at wavelengths outside these bands are used, because competing effects from other mechanisms during their measurement can render them misleading.

E. Relaxation of Aromatic Molecules

Once it is excited, an aromatic molecule eventually returns to the ground state. This is achieved through a series of radiative and nonradiative processes. For a scintillator, the useful transitions are those which result in the emission of light. For years, the empirically derived Kasha's Rule[8] was believed to apply to almost all aromatic molecules. It stated that all the emission of light from a molecule occurs from the lowest excited states of each multiplicity, the S_1 and T_1 states. Because in most practical scintillators only fluorescence is produced, it means that all the light is produced from S_1. For this to occur, the higher excited states have to convert their energy efficiently to the lower state. An emission spectrum is produced as molecules in S_1 relax to various vibrational levels of the ground electronic state. A high conversion efficiency is also implied by Vavilov's Law,[8] another empirical statement about fluorescence, which says that the quantum efficiency of a molecule is independent of the excitation wavelength as long as the exciting light has as much energy as the lowest energy absorption band of the molecule. Quantum efficiency is defined as the ratio of the number of photons emitted by a molecule to the number absorbed. Higher energy radiation excites the molecule into the S_2, S_3, and higher states, as seen in Figure 4.4. If Vavilov's Law accurately describes scintillator behavior, the conversion efficiency from the higher singlet states to S_1 must be 100%.

More recent research has found that neither of these empirical statements is entirely true.[8] Azulene was always known to be an exception to Kasha's rule because it emitted S_2 to S_0 fluorescence. Benzene, toluene, p-xylene, and mesitylene have since been found to exhibit S_2 to S_0 fluorescence, and p-xylene and mesitylene have even shown S_3 to S_0 emission. This fluorescence is very difficult to observe. The wavelengths of light emitted in these transitions also correspond to strong absorption transitions, and the light is absorbed quickly before it can travel far in the liquid. The quantum yields for these processes are 10^{-5} that of S_1 to S_0 fluorescence. Kasha's Rule is not completely accurate, but it still serves as an excellent description of the origin of fluorescence emission. In scintillator studies, all fluorescence is considered to come from S_1.

Although some older work confirmed Vavilov's Law,[9] violations of it have been found by later researchers.[8,10,11,12] The quantum yields of several scintillator solvents, including benzene, toluene, p-xylene, mesitylene, and pseudocumene, were observed to decrease as the excitation wavelength was varied from 250 nm (excitation into S_1) to 190 nm (excitation into S_3). Horrocks[3] hypothesizes that pseudocumene has a higher conversion efficiency from the upper singlet states to S_1 than the other solvents because it produced a higher scintillation yield when excited with β-particles under similar conditions.

While the yield of excitation energy transfer from higher singlet states to S_1 is not unity, this yield is still quite high. The conversion to S_1 is very important in the scintillation process because only 0.3% of the solvent molecules excited by a β-particle are initially in the S_1 state.[3] The energy of an excited molecule consists of three parts: electronic (E_e'), zero-point vibrational ($1/2\ E_v'$) and vibrational (nE_v'). In this formulation, n is the vibrational level, harmonic oscillator energies are assumed for the vibration, and the rotational energy is ignored. Excess vibrational energy in an

electronic state is usually dissipated in 10^{-12} to 10^{-13} s through interactions with neighboring molecules.[1] This loss of vibrational energy takes place much faster than does fluorescence emission, which takes approximately 10^{-7} s. A molecule in S_2 will quickly relax vibrationally to have energy $E_e'' + 1/2\ E_v''$. It can then undergo an isoenergetic radiationless electronic transition to S_1 where the energy is $E_e' + 1/2\ E_v' + nE_v'$ and n is the vibrational level in which the molecule has the same energy it had initially. The molecule then relaxes to its lowest vibrational level in S_1. Similar transitions occur from other higher singlet states. The rate of conversion from higher singlet states[1] has been estimated at 10^{12} s^{-1}. The rate of fluorescence emission from these states can be estimated from the intensity with which they absorb light, and values of 10^8 s^{-1} for $\varepsilon = 10^4$ and 10^9 s^{-1} for $\varepsilon = 10^5$ have been calculated.[1] Given the relative values of these rate constants, it is not surprising that the higher singlet states convert to S_1 before they emit fluorescence.

The vast majority of fluorescence emission originates in the lowest vibrational level of S_1 due to the rapid nature of vibrational relaxation compared to fluorescence. The fluorescence spectrum is produced because the molecule emits different frequencies of light from S_1 depending on the vibrational level in the S_0 state to which it relaxes. These different transitions can be seen in Figure 4.5. As the absorption spectrum of a molecule provides information on the vibrational structure of the S_1 state, the fluorescence spectrum represents the vibrational structure of the S_0 state. At room temperature, enough molecules are in the first excited vibrational level of S_1 that they contribute to the fluorescence spectrum.[8] This emission is at the blue end of the spectrum, and it can be hard to observe because it lies under the S_0 to S_1 absorption band. The fluorescence emission spectrum of pseudocumene is shown in Figure 4.6.

A comparison of Figure 4.4 with Figure 4.6 will show that fluorescence from pseudocumene occurs at longer wavelengths than the absorption does. The difference

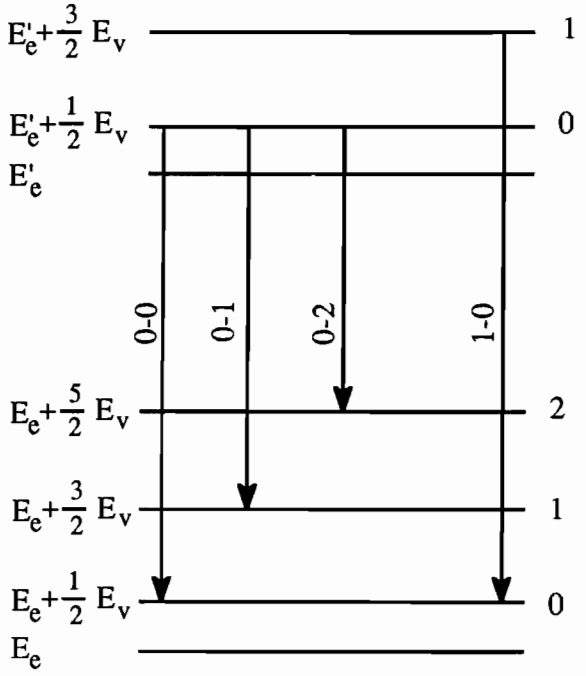

Figure 4.5. Vibronic transitions in fluorescence. The diagram shows vibronic transitions from the first excited electronic state (at energy E'_e) to various vibrational levels in the ground electronic state (at energy E_e). Most fluorescence takes place from the 0 vibrational level in S_1, but emission from other levels can also occur. From Birks.[1]

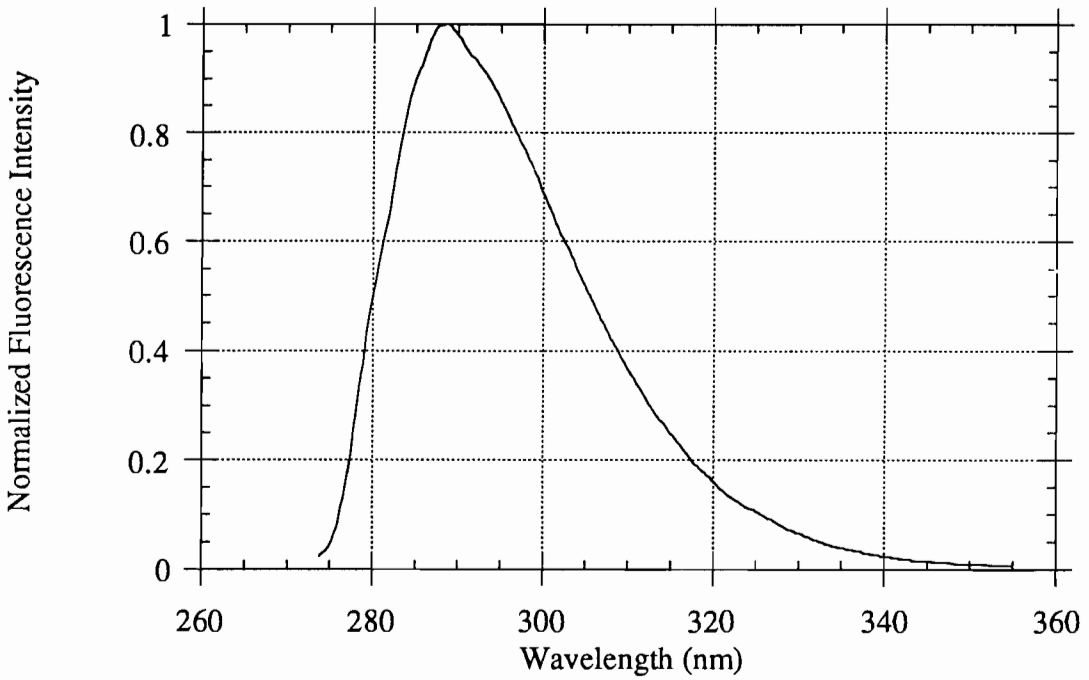

Figure 4.6. Fluorescence spectrum of pseudocumene. Normalized fluorescence from pseudocumene is shown in the figure. Data from Berlman.[2]

in energy between the absorption maximum of S_1 and the fluorescence maximum is knownas the Stokes shift. One reason for this difference is that absorption takes place mostly from the zero-point vibrational level of S_0 to various vibrational levels in S_1, while fluorescence takes place from the zero-point vibrational level of S_1 to various vibrational levels in S_0. The only transition which overlaps is the 0-0 transition. The Stokes shift is also caused by the separation of the Franck-Condon maxima for the two spectra.

The Franck-Condon principle states that because the time required for an electronic transition is negligible compared to that of nuclear motion, the most probable electronic transitions are those that result in no change in nuclear coordinates. This corresponds to a vertical transition on a potential energy diagram, as shown in Figure 4.7. This diagram is for a diatomic molecule where the abscissa is the interatomic distance. A similar diagram can represent a polyatomic molecule if a nuclear configuration coordinate Q, which no longer represents a simple interatomic distance, replaces r on the abscissa . If the nuclear configurations of the ground state and excited state differ, as shown in Figure 4.7, the most probable transitions from the zero-point vibrational ground state by absorption and the zero-point vibrational excited state by fluorescence will have different energies. The energies of the absorption and fluorescence maxima will differ, and the Stokes shift results.

Unfortunately for scintillator performance, fluorescence, which occurs with rate k_{fm}, is not the only process that can take place from S_1. Radiationless transitions with a rate k_{im} are also possible. These radiationless transitions involve conversion from S_1 to the triplet manifold (rate k_{tm}) or to the ground state (rate k_{gm}), where $k_{im} = k_{tm} + k_{gm}$. All these rate parameters have units of s^{-1}. It is difficult to separate these rate constants, although it can be done through a study of the triplet states of the molecule. The rate of intersystem crossing, k_{tm}, has an Arrhenius temperature

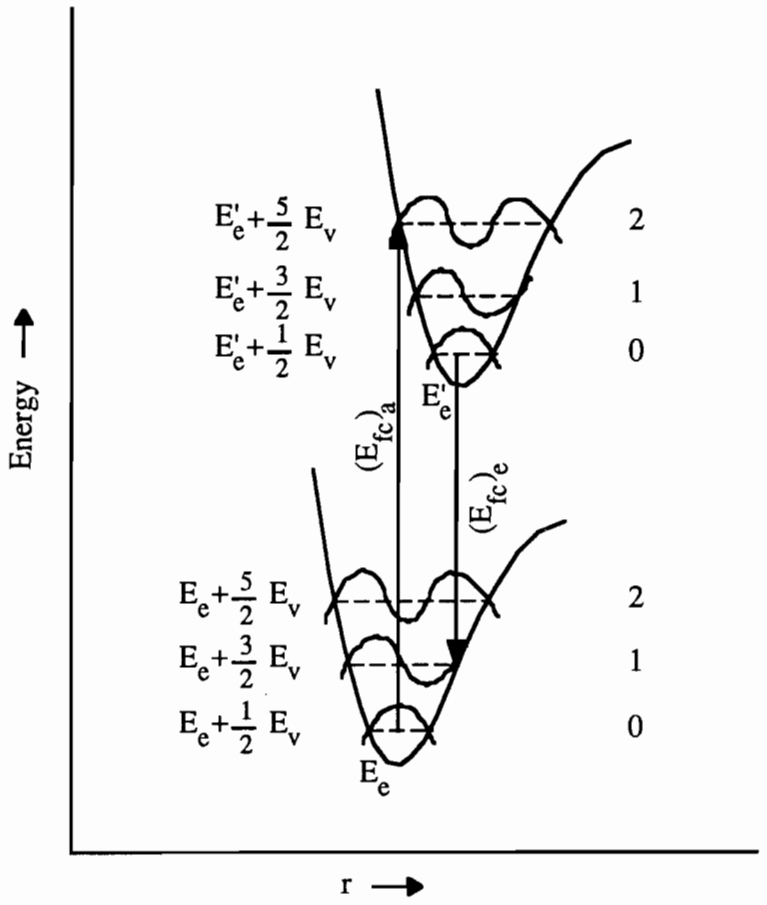

Figure 4.7. Stokes shift caused by a difference in Franck-Condon maxima. Schematic potential energy diagram of a diatomic molecule, showing vibrational wavefunctions of ground (at energy E_e) and excited (at energy E'_e) electronic states. $(E_{fc})_a$, Franck-Condon maximum in absorption; $(E_{fc})_e$ Franck-Condon maximum in emission. From Birks.[1]

dependence.[1] Birks has written that k_{gm} is independent of temperature,[1] but other research indicates that it may also have an Arrhenius dependence.[13]

The S_1 to S_0, S_1 to T_2, and S_1 to T_1 radiationless transitions occur in an isoenergetic manner like that for the transitions to S_1 from the higher singlet states. Most of the intersystem crossing transitions take place into the T_2 state because its energy is closer to that of S_1. Internal conversion can then occur to T_1. Intersystem crossing has a much lower rate than internal conversion in the singlet manifold because the transition is spin-forbidden. The S_1 to S_0 internal conversion has a lower rate than those from the higher singlet states to S_1 because the energy gap which exists between S_1 and S_0 is larger than those among the higher singlet states and between them and S_1. While it is difficult to obtain independent values for k_{gm} and k_{tm}, their sum, k_{im}, is easily determined by measuring the fluorescence quantum efficiency of the molecule.

The time behavior of an aromatic molecule in S_1 is often modeled through the use of kinetic equations. The rate equation for a solvent molecule excited with a δ-pulse at t = 0 in the absence of fluor molecules can be written

$$\frac{d[^1M^*]}{dt} = -(k_{fm} + k_{im})[^1M^*] \qquad (4.3)$$

where k_{fm} is the rate of radiative transition and k_{im} is the rate of nonradiative transition. Both have units of s^{-1}. Sometimes the parameter $k_m = k_{fm} + k_{im}$ is used instead. The preceding equation can be solved to give an exponential decay form for $^1M^*$.

$$[^1M^*] = [^1M^*]_0 \exp\{-(k_{fm} + k_{im})\, t\} \qquad (4.4)$$

Here $[^1M^*]_0$ is the number of initially excited solvent molecules. The decay time of the molecule is defined as $\tau_m = 1/(k_{fm} + k_{im}) = 1/k_m$. The fluorescence quantum efficiency is defined as the ratio of the number of molecules which fluoresce to the total number of excited molecules. The quantum efficiency, q_{fm}, can be expressed as

$k_{fm}/(k_{fm} + k_{im})$ or as k_{fm}/k_m. The reciprocal of the radiative transition rate, $(1/k_{fm})$, is called the radiative decay time, τ_{fm}, and q_{fm} can be expressed as τ_m/τ_{fm}. The expressions in eqs 4.3 and 4.4 also apply to a solute species excited with a δ-pulse.

A number of fluorescence parameters have been introduced in the preceding paragraphs. Literature values of these parameters are listed in Table 4.1 for benzene and related molecules, as well as for some fluors. It should be noted that k_{fm} and k_{im} are calculated directly from the measured τ_m and q_{fm} values. Separate k_{gm} and k_{tm} values are reported for benzene, and these were calculated by determining the phosphorescence quantum efficiency as well as τ_m and q_{fm}. A large difference can be seen between the solvents and the fluors in their lifetimes and quantum yields. The short lifetimes of the fluors reduce the ability of other processes to compete with fluorescence and are a major factor in the high quantum yields of these molecules. The fluors also exhibit a much larger Stokes shift than the solvents, which is useful because it reduces the self-absorption of fluorescence in the scintillator. Pseudocumene and p-xylene have higher quantum efficiencies than the other solvents, and they have been found to give higher light yields when used in scintillators. It should be noted that the quantum yields of Berlman[2] in Table 4.1 have been criticized by Birks,[1,14] and are generally considered to be too high. The fluorescence decay times listed in Table 4.1 are all based on experimental measurements, but theoretical expressions also exist to calculate the fluorescence radiative lifetime τ_{fm} based on the spectral data.[1,15]

Phosphorescence, or emission from T_1, has not been considered in this section in any detail because it does not play a role in a scintillator such as the CTF. This is because phosphorescence occurs on a very long time scale and with a very low quantum efficiency. The long time scale means that the light is not emitted in the 500 ns window required by the CTF data collection system, while the low quantum

Table 4.1. Fluorescence parameters. Parameters are listed for some alkyl benzene solvents and some fluors. The τ_m and q_{fm} values have been measured experimentally, and the k_{im} and k_{fm} values are calculated from them.

	τ_m (ns)	q_{fm}	k_{fm} (10^6 s^{-1})	k_{im} (10^6 s^{-1})
Benzene	29.0[a]	0.07[a]	2.0[b]	32.5[b]
		0.10[c]		
	33.6[d]	0.04[d]	1.1[d]	29[d]
		0.07[e]		
Toluene		0.24[c]	4.2[b]	22.1[b]
	35.2[d]		4.0[d]	24[d]
		0.23[e]		
p-Xylene		0.40[c]	11.1[b]	22.3[b]
		0.24[e]		
	33.3[d]	0.22[d]	6.6[d]	33[d]
Mesitylene		0.19[c]	3.9[b]	23.6[b]
		0.14[e]		
	38.3[d]	0.09[d]	2.3[d]	24[d]
Pseudocumene		0.28[d]	10.3[d]	26[d]
		0.31[e]	12.6[b]	24.2[b]
	27.2[c]	0.41[c]		
PPO	1.4[a]	1.00[a]		
bis-MSB	1.4[a]	0.94[a]		
p-Terphenyl	1.2[a]	0.93[a]		

[a] Berlman, I. B. *Handbook of Fluorescence of Aromatic Molecules*; Academic: New York, 1971.

[b] Birks, J. B. *Photophysics of Aromatic Molecules*; Wiley-Interscience: London, 1970.

[c] Birks, J. B.; Braga, C. L.; Lumb, M. D. *Brit. J. Appl. Phys.* **1964**, *15*, 399.

[d] Froehlich, P. M.; Morrison, H. A. *J. Phys. Chem.* **1972**, *76*, 3566.

[e] Berenfel'd, V. M.; Krongauz, V. A. *Theor. Exp. Chem. USSR*, **1967**, *3*, 63.

efficiency means that most of the triplet molecules lose their excitation energy in some other way before phosphorescence occurs. The triplet lifetimes of benzene and some alkyl derivatives are given in Table 4.2. The rate parameter for phosphorescence of benzene, k_{pt}, was measured as 0.034 s^{-1} and was independent of temperature.[1] Because the triplet lifetime of benzene at 77 K is 7 s, the yield of triplet molecules which phosphoresce at this temperature is only 0.24. The rate of radiationless intersystem crossing to S_0 increases with temperature while k_{pt} remains constant, so this yield decreases with temperature. For this reason, all the studies of benzene phosphorescence have been performed under cryogenic conditions and no phosphorescence has been observed at room temperatures. It is to be expected that the solvents and fluors in the CTF behave in a similar manner.

The fact that phosphorescence can be ignored in the CTF does not imply that triplet states in the scintillator are not important. Triplet states can be formed due to direct excitation by incident radiation or by intersystem crossing from excited singlet molecules. Two triplet state molecules can interact to produce an excited molecule in the singlet state and another in the ground state. The singlet molecule can then fluoresce, but this will be delayed by the time it took for the two triplet molecules to diffuse near each other and react. Fluorescence due to triplet-triplet association is called P-type delayed fluorescence, and it adds a long lifetime component to the scintillation decay. Because α-particles produce more triplet molecules than β's or γs, the delayed component is larger for α excitation. This makes α-β separation by pulse shape discrimination possible.

The fluorescence parameters discussed in this section are important in determining the behavior of the scintillation detector. The contrast between the τ_m and q_{fm} values of typical solvents and typical fluors illustrates the importance of efficient energy transfer from the solvent to the fluor in determining detector performance. The

Table 4.2. Phosphorescence decay times.

	t_{pt} (s)
Benzene	7 (77 K)[a]
	16 (4 K)[a]
Toluene	3.5 (77 K)[b]
p-Xylene	4.7 (77 K)[b]
Mesitylene	4.1 (77 K)[b]

[a] Birks, J. B. *Photophysics of Aromatic Molecules*; Wiley-Interscience: London, 1970.

[b] Froehlich, P. M.; Morrison, H. A. *J. Phys. Chem.* **1972**, *76*, 3566.

higher quantum yield and shorter decay time of the fluor are necessary for efficient detection of ionizing radiation. The fluorescence parameters are also relevant in light propagation. If a fluorescent photon is absorbed in the scintillator, the probability of reemission and its timing characteristics are determined by the q_{fm} and τ_m of the absorbing molecule. The absorption and reemission of photons in the scintillator is considered further in Section 4.I.

In the discussion of fluorescence thus far, only the intramolecular processes of fluorescence, internal conversion, and intersystem crossing have been considered in the relaxation from the S_1 state. There are also several other processes involving interactions with other molecules that can result in a return to the S_0 state. These include impurity quenching, concentration quenching, and energy transfer. In impurity quenching, another species present in the scintillator besides the solvent and fluor(s) interacts with an excited molecule and quenches it, causing it to return to the ground state without emitting radiation. The quenching molecule also emits no fluorescence. Concentration quenching is the result of the formation of dimers, complexes of one excited molecule and one ground state molecule of the same species. Dimers have a lower quantum yield and a different fluorescence emission than an individual excited molecule. Energy transfer occurs when a solvent molecule passes its excitation energy to a fluor and returns to the ground state. This transfer is highly desirable in working scintillators. These processes change the quantum yield and decay time in the scintillator from the molecular parameters τ_m and q_{fm} to the solution parameters τ and Φ_{fm}. The bimolecular processes and their effects on quantum yield and decay time will be considered in the following sections. The text above refers specifically to solvent molecules, but fluor molecules undergo the same effects, although they can only transfer energy to other fluors and not back to the solvent. The absorption of light in the scintillator and its subsequent reemission can

also affect quantum yield and timing parameters, and this will be considered in more detail as well.

F. Impurity Quenching

Some types of molecules cause quenching of fluorescence; these molecules increase the likelihood that an excited solvent or fluor molecule will relax without emitting a photon. There are three main categories of quenchers: molecules with unpaired electrons, molecules containing heavy atoms, and molecules with unshared pairs of electrons. Molecular oxygen and nitric oxide have unpaired electrons in their ground states. They can form charge-transfer complexes with the excited aromatic molecules. Many spin-allowed transitions are available in these complexes through which the complex can relax without emitting a photon, and the fluorescence is quenched. O_2 and NO also increase the rate of intersystem crossing to the triplet manifold. Molecules containing heavy atoms such as chlorine and bromine serve as quenchers because the heavy atoms have greater spin-orbit coupling than the lighter atoms normally found in scintillator components. The greater spin-orbit coupling facilitates intersystem crossing to triplet states in the excited molecules and a subsequent reduction of fluorescence. Examples of this type of quencher are carbon tetrachloride and bromobenzene. The third class of quenchers consists of molecules containing an unshared pair of electrons. Some of these molecules, such as aniline, pyridine, and carbonyl compounds, have π-n^* transitions as their lowest excited state. These states do not fluoresce, and any energy transfer to them results in quenching.

The rate equation for decay of an aromatic solvent excited with a δ-pulse at t=0 in the presence of a quencher can be written

$$\frac{d[^1M^*]}{dt} = -(k_{fm} + k_{im})[^1M^*] - k_{qm}[Q][^1M^*] \qquad (4.5)$$

Here k_{qm} is the quenching rate parameter with units of L/mol•s and [Q] is the molar concentration of the quencher. A collisional mechanism is assumed in most quenching reactions. For a diffusion-controlled process, the rate parameter k_{qm} can be expressed as

$$k_{qm} = 4\pi N' p_{qm} (D + \Lambda) R_{qm} \left(1 + \frac{p_{qm} R_{qm}}{\sqrt{\pi (D + \Lambda) t}} \right) \qquad (4.6)$$

Here R_{qm} is the distance in cm at which the encounter occurs (often assumed to be the sum of the molecular radii of the quencher and the fluorescent molecule), N' is Avogadro's number per millimole (10^{-3} N), D is the sum of the diffusion coefficients of the quencher and the fluorescent molecule in cm^2/s ($D_q + D_m$), Λ is the solvent excitation migration parameter in cm^2/s (this parameter will be covered in detail in Section 4.H), and p_{qm} is the probability of quenching per collision. The transient second term in eq 4.6 becomes small for most liquid scintillators on the ns time scale. It has been estimated that neglecting this term causes an error of 5 – 10% for a normal liquid scintillator.[16] This term is usually dropped, and k_{qm} is assumed to be a time-independent parameter..

If k_{qm} is independent of time, eq 4.5 can be solved to obtain

$$[^1M^*] = [^1M^*]_0 \exp \{-(k_m + k_{qm}[Q])t\} \qquad (4.7)$$

Expressions for the decay time and quantum yield of the scintillator can be derived, and they can be related to the molecular parameters τ_m and q_{fm}.

$$\tau = \frac{1}{k_{fm} + k_{im} + k_{qm}[Q]} = \frac{\tau_m}{1 + \tau_m k_{qm}[Q]} \qquad (4.8)$$

$$\Phi_{fm} = \frac{k_{fm}}{k_{fm} + k_{im} + k_{qm}[Q]} = \frac{q_{fm}}{1 + \tau_m k_{qm}[Q]} \qquad (4.9)$$

When these equations are valid, the ratio of the solution quantum yield to the molecular quantum yield can be expressed as

$$\frac{\Phi_{fm}}{q_{fm}} = \frac{1}{1 + k[Q]} \qquad (4.10)$$

where k is the Stern-Volmer constant. In this case $k = \tau_m q_{fm}$. This form was first developed by Stern and Volmer to model gas-phase quenching in 1919.[1] Although eq 4.10 neglects the transient term in eq 4.6 and does not fit the data well in all cases, it is often used to describe impurity quenching. Stern-Volmer kinetics is also applied to energy transfer in scintillators, as discussed in Section 4.H.

Many studies of quenching have been carried out and quenching rate parameters have been measured. Some of these parameters for quenching in common solvents are listed in Table 4.3. Several of these investigations occurred concurrently with determination of energy transfer parameters. In a series of studies, Chikkur and co-workers measured the product $p_{qm}R_{qm}$ for some quenchers. By assuming that R_{qm} was the sum of the molecular radii, p_{qm} was determined to be approximately 0.2 for bromobenzene.[17] For aniline[18] a much lower value of 0.05 was found. The quenching probability increased as the viscosity of the solution increased,[19] showing an increased chance of quenching as the quencher spent more time in the vicinity of the excited molecule.

Some recent calculations have considered quenching caused by electron transfer.[20,21] Work at a picosecond time scale has found that Stern-Volmer kinetics is not obeyed in this time regime due to static quenching.[22] Static quenching occurs when fluorescer-quencher pairs are close enough that upon excitation they react at a rate determined by an intrinsic reaction rate, not a rate governed by diffusion. The effect of these considerations for a scintillation detector such as the CTF should be minimal because it does not have the time resolution necessary to observe them.

The studies of impurity quenching discussed above are quite useful because they provide some insight into the energy transfer which takes place in a scintillation detector. Impurity quenching should not be a major concern in the CTF because of the

Table 4.3. Quenching parameters. Measured k_{qm} values for various quenchers in alkyl benzene solvents. Units (10^{10} M^{-1} s^{-1}). From Birks.[1]

Quencher	Benzene	Toluene	p-Xylene	Mesitylene
O_2	5.5	5.7	6.5	5.4
	5.9	5.6	6.2	
CBr_4		5.5		
Biacetyl	3.4	5.5	6.1	

extremely pure scintillator which is used; a scintillator solution which meets the radiopurity requirements of the CTF is unlikely to contain any impurity quenchers at a concentration high enough for them to have a noticeable effect. The quenchers examined here do reinforce the need to maintain the scintillator in an oxygen-free status so that the light output is not reduced. The possibility of intentionally adding a quencher to the pseudocumene buffer in Borexino was mentioned briefly in Section 2.B. If this measure is taken, the subject of impurity quenching will become much more important to the Borexino collaboration.

G. Excimers and Concentration Quenching

Excited solvent molecules can also interact with other molecules of the same species. In some cases, the excitation energy may be transferred from one molecule to another by a dipole-dipole resonance mechanism as discussed for energy transfer in Section 4.H. In other encounters, the molecules form an excimer, an excited state dimer of an excited aromatic molecule and an unexcited molecule of the same species. The concentration of excimers is governed by the equilibrium reaction

$$^1M^* + {}^1M \leftrightarrow {}^1D^* \qquad (4.11)$$

where ^1M is the single molecule and $^1D^*$ is the dimer. The rate of the forward reaction is $k_{dm}[^1M][^1M^*]$ and that of the reverse reaction $k_{md}[^1D^*]$; k_{dm} has units of L/mol•s and k_{md} has units of s^{-1}. These dimers are called excimers because they do not exist in the ground state; if $^1D^*$ loses its excitation energy, the two molecules in the dimer dissociate. As with an excited monomer, an excimer can relax by fluorescence with rate constant k_{fd} or by radiationless transitions with rate constant k_{id}. These radiationless transitions include intersystem crossing to form a molecule in the $^3M^*$ state and a ground state molecule (rate constant k_{td}) and internal conversion to two ground state ^1M molecules (rate constant k_{gd}). The constants k_{td} and k_{gd} sum to k_{id}.

All the dimer dissociation rate parameters have units of s^{-1}. An energy level diagram showing excimer formation and some excimer transitions is shown in Figure 4.8.

The excimer has a different fluorescence emission spectrum and a lower fluorescence yield than the monomer for the aromatic species used in the CTF. Formation of excimers decreases the quantum yield of the solution. Because excimers are more likely to form as the concentration of the aromatic molecule increases, this reduction of quantum yield is known as concentration quenching. The rate equation for $[^1M^*]$ can be written as

$$\frac{d[^1M^*]}{dt} = k_{md}[^1D^*] - (k_m + k_{dm}[^1M])\,[^1M^*] \tag{4.12}$$

when excimer formation occurs and excitation is by a δ-pulse at $t = 0$. The rate equation for excimer concentration $[^1D^*]$ is

$$\frac{d[^1D^*]}{dt} = k_{dm}[^1M][^1M^*] - (k_d + k_{md})\,[^1D^*] \tag{4.13}$$

Here $k_m = k_{fm} + k_{im}$ and $k_d = k_{fd} + k_{id}$. These equations can be solved to give the fluorescence response functions of the excited monomer and the excimer.

At "high" temperatures, where

$$k_{dm}[^1M],\ k_{md} \gg k_m,\ k_d \tag{4.14}$$

an equilibrium constant K_e with units of L/mol can be defined for eq 4.11 as

$$K_e = \frac{k_{dm}}{k_{md}} = \frac{[^1D^*]}{[^1M]\,[^1M^*]} \tag{4.15}$$

Eq 4.14 is satisfied for each species above a critical temperature which depends on the excimer binding energy and the solvent viscosity. For the compounds used in the CTF, this critical temperature is below room temperature, so eq 4.14 is always satisfied. The equilibrium constant K_e is temperature dependent, and by measuring this temperature dependence, a binding energy for the excimer can be determined.

Excimer formation changes the scintillator quantum yield and decay time. Its effect is to add a $k_{dm}[^1M]$ term to the denominator in eqs 4.8 and 4.9. The addition of

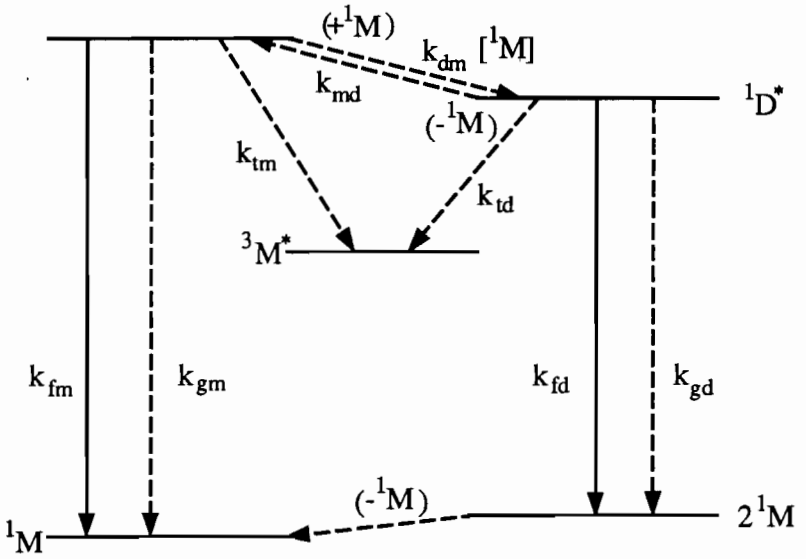

Figure 4.8. Excimer formation and transitions. Energy level diagram showing some of the transitions an excimer can undergo. Radiative transitions are indicated by solid lines and nonradiative transitions by dashed lines. From Birks.[1]

this term is only strictly correct when excimer formation is a diffusion controlled process and k_{dm} is not time-dependent. The assumption that these restrictions are met has validity similar to those made in deriving Stern-Volmer kinetics for impurity quenching.

Excimers do exhibit fluorescence with a rate k_{fd}. This excimer fluorescence is red-shifted from the fluorescence produced by the monomer (as expected from the relative energies of $^1M^*$ and $^1D^*$ in Figure 4.8), and it is usually in the shape of a broad, structureless band. Excimer fluorescence is often of low intensity because the quantum efficiency of the excimer is lower than that of the excited monomer. An excimer is more likely to undergo radiationless relaxation than an excited monomer because k_{fd} is smaller than k_{fm}. More time is allowed for other relaxation processes to compete before fluorescence occurs. Because of this, excimer formation causes concentration quenching. As the concentration of an aromatic species increases, the formation of excimers is more likely, and the quantum yield of the scintillator is reduced.

Not all aromatic molecules have the same probability for excimer formation. Birks and Christophorou[23] have found that the likelihood of excimer formation is enhanced for molecules in which the S_1 state is of the ^1L_b type and is adjacent to a ^1L_a state with a larger transition intensity. These criteria are satisfied by the species of interest in the CTF, and concentration quenching should be noticeable for these compounds.

Excimer formation has been studied in several experiments. Pyrene was one of the first compounds for which excimer fluorescence was found; it forms excimers at relatively low concentrations.[24] Neat solutions of benzene and some of its methylated derivatives were also examined for excimer fluorescence.[25] Benzene exhibits a great deal of excimer fluorescence. The amount of excimer formation tends to decrease as

methyl groups are added to the benzene ring in toluene, p-xylene, and mesitylene. Toluene still shows a large amount of excimer fluorescence, especially at low temperatures (as low as –76 °C). No excimer fluorescence was measured for p-xylene, although it does exhibit concentration quenching, indicating that some excimers form. Mesitylene also produces little excimer fluorescence, and none above 0 °C. In a study of energy transfer, excimers were important for toluene, but of little importance for mesitylene.[26] Measured parameters for excimer formation in benzene and its derivatives are listed in Table 4.4.

Excimer fluorescence from pseudocumene has not been studied in the literature. Because of the similarity of pseudocumene to p-xylene and mesitylene, it is reasonable to assume that its excimer formation behavior will resemble that of the other two species. Based on the studies reported in the previous paragraph, this means that it will produce no excimer fluorescence under conditions present in the CTF. Concentration quenching is likely to be observed for pseudocumene. Fast energy transfer in the CTF scintillator from pseudocumene to PPO (see Section 4.H) makes the effect of concentration quenching in the solvent negligible in the detector.

Excimer formation of PPO has been studied. Berlman[27] found that PPO forms excimers at a concentration of 100 g/L. Excimer fluorescence was seen at this concentration. The PPO excimer had a lifetime of 14 ns and a lower quantum yield than PPO in the excited monomer form. No excimer formation was seen at a concentration of 1 g/L and no significant difference was found between the quantum yield at this concentration and that measured in very dilute solutions. Birks et al.[28] also examined PPO for excimer formation. At 10^{-1} M, excimer formation was seen, but none was observed at 10^{-2} M (2 g/L). This indicates that formation of PPO dimers is unlikely to be of importance at the CTF concentration of 1.5 g/L and that concentration quenching in the detector will be negligible.

Table 4.4. Excimer parameters. Measured parameters for excimer formation and fluorescence in alkyl benzene solvents. From Birks et al.[10]

	Benzene	Toluene	p-Xylene	Mesitylene
q_{fd}	0.03	0.05		0.02
K_e (M^{-1})	0.121	0.055		0.018
k_{md} (10^9 s^{-1})	6.5	9.2	24	22
k_{dm} (10^{10} M^{-1} s^{-1})	7.8	5.1	4.9	3.9
m†	0.43	0.63	0.86	0.89

† m is the fraction of excited molecules in the $^1M^*$ state.

H. Energy Transfer in Scintillators

Most practical liquid scintillators consist of an aromatic solvent and one or more additional fluorescent compounds known as fluors. The aromatic solvent constitutes the bulk of the scintillator mass, and it is the component which is excited by ionizing radiation. A scintillator consisting of only an aromatic solvent does not perform well. As seen in Table 4.1, the quantum efficiency of organic solvents commonly used in scintillators is quite low. These low quantum efficiencies mean that a great deal of the electronic excitation energy is lost through nonradiative relaxation instead of being released as fluorescence. When it does occur, there are many undesirable features of direct emission from the aromatic solvent. The emission wavelengths of most solvents are below 300 nm, a region of low sensitivity for photo-multiplier tubes. The solvent normally has a small Stokes shift, and the high concentration of the solvent results in the absorption of much of the emitted light.

To improve the performance of the scintillator, other species of aromatic molecules known as fluors are added to the solvent to form the scintillator mixture. These molecules have a S_1 state with a lower energy than the S_1 state of the solvent, and receive the excitation energy from the solvent. The fluors have high quantum yields (usually greater then 70%) and emit at longer wavelengths where photo-tubes are more sensitive. They exhibit less self-absorption of fluorescence than the solvent because of their lower concentration and larger Stokes shift. Sometimes a second fluor is added to the mixture to further shift the wavelength of the emitted light away from the solvent absorption bands.

The use of fluors greatly increases the efficiency of liquid scintillation detectors. In order for the fluor to be of use, the electronic excitation energy must be transferred from the solvent to the fluor. Figure 4.9 shows an energy level diagram of a solvent and two fluors. An excited solvent molecule can decay to the ground state

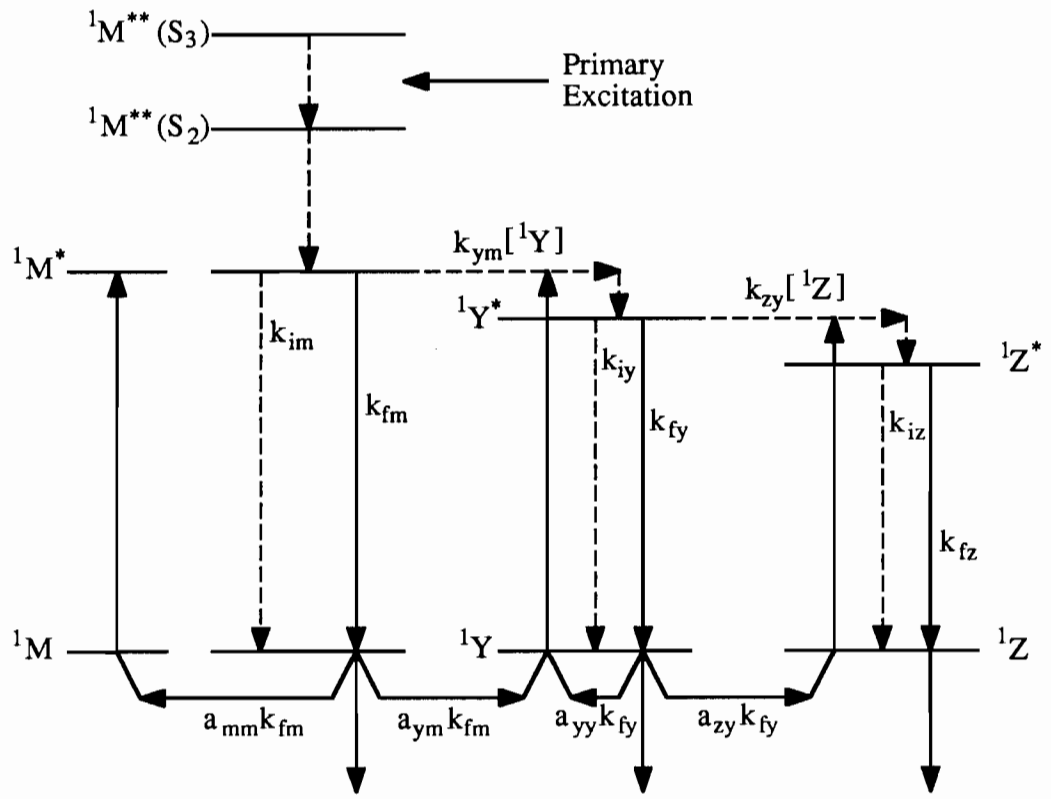

Figure 4.9. Solvent-fluor energy transfer. Energy level diagram showing energy transfer from a solvent to two fluors. Radiative transitions are indicated by solid lines, while non-radiative transitions are denoted by dashed lines. Not shown here are absorption of fluor fluorescence by the solvent, absorption of fluorescence of fluor Y by fluor Z, and direct transfer from solvent to fluor Z (radiative and non-radiative). If only one fluor is present in the scintillator, the transitions to fluor Z can be ignored. From Birks.[29]

nonradiatively, decay by emission of a photon, transfer its energy to another solvent molecule, or transfer its energy nonradiatively to a fluor molecule. If the solvent emits a photon, this can by absorbed by another solvent molecule or a fluor molecule. This absorption results in the excitation of the absorbing molecule, and the process is known as radiative energy transfer. The first fluor can relax nonradiatively or by emission of a photon following its excitation. It can also transfer energy nonradiatively to another molecule of its own species or to the second fluor, but this is unlikely at the fluor concentrations normally used. Transfer back to the solvent is impossible because the S_1 state of the fluor is lower in energy than that of the solvent. The second fluor can also relax nonradiatively or by emission of a photon, but it can only transfer energy to other molecules of the same species because its S_1 state is below that of the other two components.

The mechanism of radiative energy transfer from the solvent is straightforward. The solvent emits a photon, and it is absorbed by the fluor. Radiative transfer between the solvent and the fluor is undesirable for two reasons. Two major advantages gained through use of a fluor are high quantum efficiency and short decay time. Both of these are lost if the energy transfer occurs radiatively because the solvent emits light with its own quantum yield and decay time. Effective nonradiative transfer results in almost complete transfer of the electronic excitation energy to the fluor in a short time, so that the fluor quantum yield and decay time dominate the process. For this reason, liquid scintillators are designed to facilitate nonradiative energy transfer. Radiative transfer between two fluors is often acceptable, due to the second fluor's use as a wavelength shifter and not as a means to obtain higher efficiency and better time resolution.

In studies of solvent-solute energy transfer, the important value is f_{ym}, the fraction of the solvent excitation energy which is transferred to the solute. This can be defined in terms of rate parameters as

$$f_{ym} = \frac{k_{ym}[^1Y]}{k_m + k_{ym}[^1Y]} \tag{4.16}$$

Here k_{ym} is the transfer rate parameter with units L/mol•s. The parameter f_{ym} is essentially a quantum yield for energy transfer. If a quencher is present or excimer formation is important, the relevant terms would appear in the denominator of eq 4.16. If k_{ym} is a constant, then eq 4.16 can be rearranged to show that a plot of $[^1Y]/f_{ym}$ vs. $[^1Y]$ will have a slope of k_{ym}. This provides an easy way of calculating k_{ym}, but the procedure is not useful when k_{ym} is a function of time. Three methods[30] are commonly used for experimental determination of k_{ym}: measurement of the decay time of the scintillator solution knowing the molecular decay times of the solvent and fluor, measurement of the change in light output from the solvent upon addition of the fluor, and measurement of the ratio of the light output of the fluor when the solvent is excited to the light output of the fluor when it is excited directly.

Because nonradiative energy transfer is critical to the performance of liquid scintillators, it has been studied in great detail. Förster was the first to study nonradiative transfer.[31] He studied transfer from a species of "donor" molecules to a species of "acceptor" molecules under conditions where diffusion was unimportant. The donors correspond to the solvent in a liquid scintillator, while the acceptors are fluor molecules. There are two major differences between the conditions of his study and those which exist in a liquid scintillator such as the CTF. In Förster's study, the excited donors were surrounded by an inert matrix, not other molecules of the same species as with a scintillator solvent. Diffusion is important in a liquid solution, and it must be taken into account.

Förster modeled the energy transfer as a electric dipole-dipole resonance process. He developed a distance dependent rate constant k'_{ym}, where

$$k'_{ym} = \frac{1}{\tau_m}\left(\frac{R_0}{r}\right)^6 \qquad (4.17)$$

Here r is the separation distance between the donor and the acceptor and R_0 is the critical transfer distance at which energy transfer and deactivation by fluorescence or internal quenching are of equal probability. R_0 depends on the overlap of the donor fluorescence spectrum and the acceptor absorption spectrum, the quantum yield of the donor, the refractive index of the medium, and the lifetime of the donor in the absence of the acceptor.

As donor decay progresses under the conditions considered by Förster, regions of the medium become depleted of excited molecules, and the distance at which the transfer takes place changes. Because k'_{ym} is dependent on separation, this results in a time dependent rate constant. The rate of decay of the concentration of donor molecules depends on time to the one-half power. Energy transfer which exhibits this time dependence is said to follow Förster kinetics.

Additional research has been done on the resonance transfer of energy in scintillators.[32,33] Dexter[34] extended the dipole-dipole resonance of Förster to include electric dipole-quadrupole interaction between donors and acceptors in a solid matrix. This interaction has a r^{-8} dependence as opposed to the r^{-6} dependence in eq 4.17. The concept can be extended to quadrupole-quadrupole interactions, which have a r^{-10} dependence, and others of higher order. These higher order multipole interactions can become important when dipole-dipole interactions are forbidden by symmetry, as they are between benzene molecules.

Energy transfer mechanisms other than resonance have also been investigated. The electron exchange interaction has received the most study.[35,36,37,38,39] It depends

exponentially on separation distance and is only important when the molecules are relatively close.

The applicability of Förster kinetics to situations where diffusion is unimportant has been confirmed by experimental data. Bennett[40] found that these equations accurately described transfer between donors and acceptors embedded in a plastic film. They also describe the transfer in solutions where the viscosity is high enough to reduce the diffusivities of the molecules enough so that the condition $R_0 \gg \sqrt{2D\tau_m}$ is satisfied.[41,42,43,44] In studies where $R_0 \ll \sqrt{2D\tau_m}$ Förster kinetics has failed to accurately describe the rate of energy transfer.[41,42,43,45] This is not surprising, because the assumptions under which the rate equations were derived are invalid when the donor and acceptor molecules can diffuse freely.

Yokota and Tanimoto[46] were the first to theoretically treat the effect of diffusion on energy transfer by dipole-dipole interaction between donors and acceptors in an inert solvent. The influence of diffusion on resonance energy transfer was also studied by other researchers.[47,48,49,50,51] When the effect of diffusion dominates that of dipole-dipole resonance transfer, the following expression for k_{ym} is valid.

$$k_{ym}(t) = 4\pi D r_{ad}\left(1 + \frac{r_{ad}}{\sqrt{\pi D t}}\right) \qquad (4.18)$$

Here r_{ad} is the sum of the radii of the donor and the acceptor (cm) and D is the sum of their molecular diffusivities (cm^2/s). Experimental data have confirmed this theoretical model.[45] Analogs of eq 4.17 were also developed for higher order multipole-multipole interactions.

Birks and Georghiou[41] considered the effect of diffusion on energy transport between donors and acceptors in an inert medium in a series of experiments. They studied energy transfer between the same donor-acceptor pair in six solvents with viscosities ranging from 0.4 cp to 64.6 cp. They defined a parameter $\bar{r}$ as the distance

of mean molecular diffusion during the $^1M^*$ lifetime where $\bar{r} = \sqrt{2D\tau_m}$. Results indicated that for $\bar{r} < R_0$, Förster kinetics was applicable. In the lowest viscosity solvents, an equation similar to eq 4.18 was used for the transfer parameter. It was derived from diffusion theory as the rate of a diffusion controlled collision process. A parameter p_{ym} was included as the reaction probability per collision. Birks and Kuchela[52] studied energy transfer between two fluors in a liquid solution. At low concentrations radiative transport competed with nonradiative transfer, but as concentration was increased, the nonradiative mechanism dominated and indicated dipole-dipole transfer.

Voltz and co-workers[53,54] also used an equation similar to eq 4.18. Instead of r_{ad}, they used R_0 with a reaction probability per collision of 0.5 because R_0 is defined as the distance at which the energy transfer probability is 0.5. This approach has been criticized[1] because it gives transfer rates which are too large.

The second term in eq 4.18 is often considered negligible, and this is valid when

$$t^{1/2} \gg \frac{R_0}{\sqrt{\pi D}} \tag{4.19}$$

If the second term is negligible, the transfer rate becomes independent of time and the following differential equations for donor and acceptor concentration can be written for δ-pulse excitation at t = 0.

$$\frac{d[^1M^*]}{dt} = -(k_m + k_{ym}[^1Y]\,)\,[^1M^*] \tag{4.20}$$

$$\frac{d[^1Y^*]}{dt} = k_{ym}[^1Y][^1M^*] - k_y\,[^1Y^*] \tag{4.21}$$

These can be easily solved to obtain the donor and acceptor fluorescence emission, i_m and i_{ym}, as functions of time.

$$i_m(t) = k_{fm}[^1M^*]_0 \exp\{\,-(k_m + k_{ym}[^1Y])\,t\,\} \tag{4.22}$$

$$i_{ym}(t) = \frac{k_{fy}\, k_{ym}[^1Y][^1M^*]_0}{k_m - k_y}\{\exp(-k_y t) - \exp(-(k_m + k_{ym}[^1Y])\, t)\} \quad (4.23)$$

When the transfer rate can be considered time independent, the system follows Stern-Volmer kinetics. This occurs when the rate of statistical mixing exceeds the energy transfer rate and when $R_0 \ll \sqrt{2D\tau_m}$. Stern-Volmer kinetics is often assumed in the analysis of energy transfer data because of the simplicity of the resulting equations, and it often models the data well in low viscosity solutions.[42] Where Stern-Volmer kinetics is applicable, the decay time and quantum yield of the solvent can be expressed in a manner similar to that of eqs 4.8 and 4.9. The $k_{qm}[Q]$ terms in the denominators of these equations are replaced by $k_{ym}[Y]$. If efficient energy transfer is occurring, it is the decay time and quantum yield of the fluor which are important in determining the behavior of a scintillator.

Sipp and Voltz[55,56,57] have considered the effect of diffusion on energy transfer by the electron exchange interaction as well as by dipole-dipole resonance in the transfer of energy from donors to acceptors in an inert solvent. The exchange interaction takes place on a much shorter time scale and at a much closer interaction distance than dipole-dipole resonance. This close proximity can be reached in a highly diffusive medium before transfer occurs by other means.[58]

Experimental results have shown that by considering only the dipole-dipole resonance and diffusion mechanisms, energy transfer from donors to acceptors can be successfully modeled in an inert solvent.[59] When the solvent is the donor species, as in the CTF scintillator, additional transfer mechanisms must be considered. When the entire solvent consists of donor molecules, transfer occurs more rapidly then predicted by equations such as eq 4.18 using measured diffusion coefficients. The more rapid transfer has been attributed to solvent-solvent energy migration. The form of eq 4.18 must be modified to include a parameter Λ, with units of cm^2/s, which accounts for the

energy migration. Many researchers have investigated the effects of solvent-solvent interaction using a transfer rate of the form

$$k_{ym} = 4\pi N' (D + \Lambda) R_{eff} \left(1 + \frac{R_{eff}}{\sqrt{(D + \Lambda) t}} \right) \qquad (4.24)$$

Here R_{eff} is the distance at which the transfer occurs (cm), D is the sum of the molecular diffusivities of the donor and the acceptor (cm^2/s), and N' is Avogadro's number (molecules per millimole). In most studies, the transient second term is ignored. Some experimental k_{ym} and Λ values are listed in Tables 4.5 and 4.6.

There is considerable disagreement among researchers over the mechanisms of solvent-solvent energy migration and solvent-fluor energy transfer. Birks and Conte[60] consider the transfer range to be r_{ad}, the sum of the radii of the solvent and the fluor. They feel that energy transfer is primarily a collisional process and they attribute the solvent-solvent energy migration to collisional processes involving the formation and dissociation of excimers. Voltz et al.[53] equate R_{eff} to $R_0/2$, because they believe that energy transfer is primarily due to dipole-dipole interactions. They also ascribe solvent-solvent migration to dipole-dipole interactions. Birks et al.[61] propose a model in which R_{eff} is three times the molecular radius. This work proposes that the excitation energy is delocalized in the solvent as a result of excimer formation and dissociation. Chalzel[62] reviewed the proposals mentioned above and performed calculations which showed that dipole-dipole interactions were the most important means of energy transfer. Other researchers consider R_{eff} an adjustable parameter to be fit by experimental data.[17,18,19,63,64,65,66] In experiments with a concentrated donor, R_{eff} was found to be similar to the sum of the molecular radii of the donor and acceptor. When the donor was diluted in an inert solvent, R_{eff} became closer to $R_0/2$. In a neat donor solution, solvent-solvent transfer may allow the excitation to move rapidly through the solvent and cause most of the energy transfer to take place at short

Table 4.5. Energy transfer parameters. Measured k_{ym} values for PPO and p-terphenyl in alkyl benzene solvents. Units (10^{10} M^{-1} s^{-1}). From Birks.[1]

Fluor	Benzene	Toluene	p-Xylene	Mesitylene
PPO	4.9	5.2	6.1	5.1
	4.7	5.1	6.2	
p-terphenyl	4.6	6.0		
	5.4	5.0	4.7	

Table 4.6. Energy migration parameters. Measured Λ values in alkyl benzene solvents. Units (10^{-5} cm^2 s^{-1}).

	Λ	Reference
Benzene	3.4	a
	4 ± 1	b
	6.8	c
Toluene	4 ± 1	b
	7.5	c
p-Xylene	4 ± 1	b
	9.9	c
Mesitylene	4 ± 1	b
	7.3	c

[a] Birks, J. B.; Braga, C. L.; Lumb, M. D. *Brit. J. Appl. Phys.* **1964**, *15*, 399.

[b] Voltz, R.; Laustriat, G.; Coche, A. *J. Chim. Phys.* **1966**, *63*, 1253.

[c] Birks, J. B.; Conte, J. C. *Proc. Roy. Soc. A* **1968**, *303*, 85.

range. When the donor is diluted, donor-donor transfer is less efficient, and longer range dipole-dipole interactions have a chance to compete.

There has been a great deal of study on energy transfer from solvent to fluor, but there is still no consensus on the mechanism by which it occurs. Although the exact mechanism is in dispute, some conclusions important to the functioning of the CTF are well-established. In a liquid scintillator where the solvent is the donor and a fluor is the acceptor, diffusion and solvent-solvent energy migration allow the use of Stern-Volmer kinetics to model the transfer process.

Regardless of the exact mechanism by which it occurs, energy transfer is crucial to the performance of a liquid scintillation detector. In order to obtain a significant light output, the solvent excitation energy must be efficiently transferred to the fluor. As shown by eq 4.16, the efficiency of energy transfer increases as the concentration of the fluor rises. Eq 4.16 also indicates that an efficiency of 1.0 is approached asymptotically. Once the fluor concentration reaches a certain level, additional fluor only increases the transfer efficiency slightly, but it continues to cause additional light absorption in the scintillator. Because of this, the amount of fluor in the scintillator must be optimized. Transfer efficiencies of over 95% can be achieved without introducing unacceptable levels of light absorption due to the fluor in the scintillator. A fluor concentration of approximately 1 – 5 g/L is usually sufficient to obtain this level of transfer. At this concentration of fluor, transfer of energy from the solvent to the fluor takes place almost entirely by the nonradiative mechanisms discussed in this section. Other mechanisms, such as radiative transfer, do not have to be taken into consideration.

I. Radiative Migration and Transfer

Although radiative transfer from solvent to fluor is not important in the CTF, other radiative processes play a major role in determining its behavior. Photons emitted in a scintillation detector by the solvent or a solute may be absorbed by scintillator components before they escape from the detector. When a photon is absorbed by the species which emitted it, the process is known as radiative migration. When it is absorbed by a different species the process is defined as radiative transfer. The absorbing molecule becomes excited upon absorption, and it can then emit a photon of its own. The radiative migration or transfer continues until a photon escapes from the scintillator or an excited molecule relaxes by a nonradiative transition. The mechanism by which the radiative processes occur is quite simple; it is excitation of molecules by photon absorption followed by their relaxation. The effects of radiative processes on scintillator behavior are difficult to model due to the many variables involved: the geometry of the scintillator, the direction of photon emission, and the wavelength of the photon.

Birks[1] considered the effects of radiative processes on scintillator behavior. He defined a parameter a_{ab} as the probability of absorption of an emitted photon in the scintillator. The probability of photon escape is $1 - a_{ab}$. The probability a_{ab} is calculated from

$$a_{ab}\, q_{fm} = \int_0^\infty F(\bar{\nu}) \{1 - 10^{-\varepsilon(\bar{\nu})[^1M]x}\}\, d\bar{\nu} \qquad (4.25)$$

where $\varepsilon(\bar{\nu})$ is the absorption spectrum expressed as the molar decadic extinction coefficient, $[^1M]$ is the concentration of the aromatic species, $F(\bar{\nu})$ is the fluorescence spectrum, and x is the thickness of scintillator through which the fluorescence must travel before it escapes. If an absorbed photon is reemitted with quantum efficiency q_{fm} (the same quantum efficiency as for the initial fluorescence), the effect of the

absorption on the measured quantum yield and the decay time can be calculated. The measured quantum yield Φ_{fm} is related to q_{fm} by

$$\Phi_{fm} = q_{fm} (1 - a_{ab}) [1 + a_{ab} q_{fm} + (a_{ab} q_{fm})^2 + ...] \qquad (4.26)$$

where the terms in the brackets correspond to escape after 1, 2, 3, ... emissions. The measured fluorescence lifetime, τ, is equal to the molecular lifetime, τ_m, divided by $(1 - a_{ab} q_{fm})$.

Only one aromatic species is present to emit and absorb photons in the equations above, but the inclusion of a fluor is straightforward. For absorption of solvent emission by the fluor, the absorption spectrum of the fluor and its concentration, $[^1Y]$, replace the respective solvent quantities in eq 4.25. For fluor absorption of fluor emission, the solvent fluorescence spectrum is also replaced with that of the fluor. Birks[67] carried out this analysis for traps in a scintillator crystal, which behave similarly to fluors in a liquid scintillator.

The equations above are derived based on the assumption that a_{ab} is constant for each reemission step. This requires that all the parameters in eq 4.25 remain the same for each reemission. The absorption spectrum and the concentration do not change from one emission to the next. The path length through the scintillator could easily change, and this is examined by other authors. Changes in the fluorescence spectrum and the molecular quantum yield must also be considered. In the literature, it is assumed that the emission spectrum does not change as photons are absorbed and reemitted. If a molecule absorbs a photon of a wavelength in the tail of its absorption spectrum, the photon wavelength is likely to have come from the middle of the molecule's emission spectrum. There is no reason to assume that the emission spectrum and quantum yield for emission following absorption in the tail of the absorption spectrum will be the same as that following absorption in the main absorption band. The emission behavior following long wavelength absorption is a

crucial question for modeling the CTF and Borexino, and it has not been considered in the literature.

Other researchers have studied the effect of absorption and reemission on the timing of the fluorescence response from a scintillator. Sipp and Miehe[68] found that self-absorption of fluorescence was a major effect and worsened the time resolution of a scintillation counter as cell dimensions were increased from 0.2 cm to 5 cm. Baumann et al.[69] modeled the absorption and reemission of photons in a manner similar to that of Birks. They derived expressions for the time decay of the scintillator after various number of emission steps. The fluorescence response after the initial excitation with a δ-pulse at t = 0 is

$$i_0(t) = \frac{[^1M^*]_0}{\tau_m} \exp(-t/\tau_m) \tag{4.27}$$

The rate of fluorescence after one absorption and reemission step is

$$i_1(t) = \frac{a_{ab}\, q_{fm}[^1M^*]_0}{\tau_m^2}\, t \exp(-t/\tau_m) \tag{4.28}$$

and after n reemissions it becomes

$$i_n(t) = \frac{a_{ab}^n\, q_{fm}^n[^1M^*]_0}{\tau_m^{n+1}\, n!}\, t^n \exp(-t/\tau_m) \tag{4.29}$$

Baumann et al. also measured decay times of Rhodamine 6G at low concentrations and found that the decay time was slightly dependent on the fluorescence wavelength. While the shorter wavelengths were well-fit with one exponential, the longer wavelengths required two or three exponential terms to obtain a good fit. They claim that reemission changes the absolute values of the decay parameters, but does not affect the wavelength dependence. Wiorkowski and Hartmann[70] developed similar expressions for fluorescence rates after n absorption and reemission steps for atomic fluorescence, but they included the effect of different

a_{ab} values for each step. A Monte Carlo code was used to calculate the a_{ab} values. Their assumptions included Beer's law absorption, isotropic emission, and an identical reemission spectrum at each step. Hammond[71] also treats self-absorption of fluorescence, and develops equations similar to those of Birks for excitation at the center of a sphere. He also examines a different geometry of a slab of scintillator solution through which the fluorescence must pass.

The fluorescence spectrum can change drastically between the point of emission and detection because of absorption. The short wavelengths are preferentially absorbed, as can be seen from the absorption spectrum of any fluorescent molecule; the absorption and fluorescence spectrums overlap more at the short wavelength end of the emission spectrum. This preferential absorption causes the fluorescence spectrum to change with concentration as absorption becomes more significant. This effect has been observed in the literature.[28] D'Ambrosio et al.[72] calculated the effect of absorption on the emission of a scintillator-doped polystyrene fiber using the absorption spectrum of the scintillator and Beer's law. They then measured the light yield at various lengths along the fiber at distances up to 40 mm. The calculated values were in good agreement with the experimental results, indicating that measured extinction coefficients can be used to predict absorption in a larger scintillator.

The most rigorous treatment of radiative processes in a scintillator has been carried out by Martinho and co-workers.[73,74] They initially considered only one species of fluorescing molecule in the scintillator, and developed an exact expression for the probability of absorption after each emission step. The probability of absorption after the nth emission, α_n, was calculated from the integration of $\alpha_n'(\lambda)$ which was calculated from the integration of $\alpha_n''(\lambda,\Omega)$.

$$\alpha_n''(\lambda,\Omega) = \int\int \{1 - 10^{-\varepsilon(\lambda)[^1M]r'(r,\Omega)}\}\, f_n(r)\, dr\, dr' \qquad (4.30)$$

Here $f_n(r)$ is the normalized distribution of nth generation excited donors and $r'(r,\Omega)$ is the path length of photons emitted nth generation donors in direction Ω,

$$\alpha_n'(\lambda) = \int \alpha_n''(\lambda,\Omega)\, d\Omega \qquad (4.31)$$

and

$$\alpha_n = \int_0^\infty \alpha_n'(\lambda)\, F(\lambda)\, d\lambda \qquad (4.32)$$

where $F(\lambda)$ is the normalized fluorescence spectrum of the molecule. In eq 4.32, it is assumed that the fluorescence spectrum is the same for each generation of emission. By making the assumption that $F_n(\lambda)$ is independent of n, the authors imply a rapid thermal equilibration in the excited state. Rapid thermal equilibration prior to emission allows for an emission spectrum independent of the excitation wavelength if the overlap of the fluorescence and absorption spectra is due to absorption hot bands. Monte Carlo methods were suggested for calculating the α_n's. They also developed decay kinetics for n absorption and reemission steps. These are similar to those of Baumann et al., but they are calculated for a finite pulse excitation rather than excitation by a δ-pulse.

Some decay measurements were reported for 9,10-diphenylanthracene.[73] In order to fit the data, the decay kinetics mentioned above were combined with a geometry factor for the experiment and an escape probability $S_n(\lambda)$ for each generation of emission. These equations can be reduced to those of Birks by assuming that the escape and absorption probabilities are not a function of the generation of emission, but it was found that these dependences are necessary to correctly fit the data. Results indicated that the decay time increased at longer wavelengths. This is attributed to longer wavelengths arriving from deeper in the fluorescence cell at later times, while shorter wavelengths were absorbed and could not escape from the cell when they originated deep inside it. The authors later extended their treatment to

include a donor-acceptor system interacting through radiative and nonradiative transfer. They found that at low acceptor concentrations (below 5×10^{-3} M), radiative transfer was important and should not be neglected in energy transport models.

The main effect of radiative processes on the behavior of the CTF is expected to be in the propagation of light emitted by the PPO fluor. As discussed in Section 4.H, the amount of light emitted by pseudocumene will be very small due to nonradiative transfer to PPO. Light emitted by PPO is likely to experience radiative processes before it exits the scintillator. The study of these processes is an area in which the behavior of a large-scale detector such as the CTF differs significantly from that of smaller experiments. In small experiments, the effect of absorption in the long wavelength tail of the spectrum is negligible. This absorption is critical in the CTF, however, due to the large distances which photons must travel through the CTF scintillator. Based on the mechanisms discussed in this section, the PPO emission could be affected by pseudocumene or PPO absorption. This is undoubtedly true for emission wavelengths in the main PPO absorption band. Other mechanisms which may become more important than absorption in the tails of the pseudocumene and PPO extinction coefficient curves are discussed in Sections 4.J and 5.D.

J. Rayleigh Scattering of Light

Light passing through a scintillation detector is affected by absorption and reemission from solvent and fluor molecules. This process is known as inelastic scattering and it was discussed in Section 4.I. It involves a change in frequency of the photon and it takes place on a time scale of the decay time of the scintillator molecules: approximately 10^{-8} s. Light can also be scattered elastically without a change in frequency. Elastic scattering takes place on a time scale of 10^{-15} s, the

vibration frequency of the light. This type of scattering is of great importance in a scintillation detector the size of the CTF or Borexino.

Elastic scattering occurs via the Rayleigh mechanism. Photons passing through a medium create induced dipoles from the particles in the medium. This is generally applied to small particulates in a liquid or to gas molecules, but it is equally valid for the liquid molecules themselves. The induced dipoles will oscillate and radiate electromagnetic energy. In a perfectly homogenous medium, the radiation from these oscillators will cancel out due to destructive interference caused by phase differences between the emissions. In a real liquid, there are microscopic density fluctuations that destroy the perfect symmetry of the oscillators. Some of the radiation will escape, causing Rayleigh scattering.

Hirschfelder et al.[75] develop the theory of Rayleigh scattering to obtain an expression for its intensity. The ratio of the intensity of the scattered light to that of the incident light can be written as

$$\frac{I}{I_0} \propto \frac{N\alpha^2 (\varepsilon_d + 2)^2}{\lambda^4} [1 + \cos^2 \theta] \qquad (4.33)$$

In eq 4.33, N is the number of scattering molecules, α is the polarizability of the molecules, ε_d is the dielectric constant of the medium, λ is the wavelength of the scattered light, and θ is the angle between the incident and scattered directions. Due to assumptions about molecular correlation made in the derivation, eq 4.33 does not give quantitative predictions for scattering in a liquid as it does for a gas. The dependence of the amount of scattering on the various parameters in eq 4.33 does hold for the liquid. Because of the dependence on N, the amount of Rayleigh scattering depends linearly on the molar density ρ_m of the liquid. Other equations, similar to eq 4.33, describing Rayleigh scattering in liquids have been derived by other researchers.[76,77,78]

Experimental measurements of Rayleigh scattering have been reported for many liquids. These measurements are usually expressed in terms of the Rayleigh ratio, or R_θ, where θ is the angle between the direction of the incident light and the direction in which the scattered light is detected. R_θ is the energy scattered per steradian by a unit volume in direction θ when the medium is illuminated with unpolarized light of unit intensity. An extinction coefficient ε based on scattering can be calculated from R_θ.

$$\varepsilon = \frac{(16/3)\,\pi\,(\log e)\,P_\theta}{[1 + \cos^2\theta]\,C} \tag{4.34}$$

Here C is the molar concentration of the liquid.

In most scattering measurements reported in the literature, the scattered light is measured at 90° from the incident beam and R_{90} values are given. Table 4.7 lists R_{90} and polarizability data for several liquids. The polarizabilities of pseudocumene and phenylxylylethane (PXE) are calculated based on a correlation given by Israelachvili.[79] Scattering values have been reported for benzene at two wavelengths. Values are reported for the R_{90} of water at four wavelengths, as shown in Table 4.8.

Some comparisons can be made between elastic scattering theory as expressed in eq 4.33 and the available experimental data. If the water scattering values are fitted with a power function, the fit has a λ dependence of –4.48. This is close to the theoretical value of –4. The small discrepancy could be due to the slight wavelength dependence of α and ε_d.

At a given wavelength, the scattering should vary with the quantity $\alpha^2\rho_m$ of the various liquids. Some $\alpha^2\rho_m$ values for liquids are shown in Table 4.9, and comparisons can be made among the amounts of scattering they exhibit at 546 nm. Cyclohexane does not follow the expected pattern. It has an $\alpha^2\rho_m$ similar to that of

Table 4.7. Scattering and polarizability data for liquids. The α values for pseudocumene and PXE are based on a correlation. All other values were measured experimentally.

	R_{90} (10^{-6} cm^{-1}) @ 546 nm[a]	α (10^{-24} cm^3)
Benzene	15.8	10.32 - 10.74[b]
	46.5 @ 436 nm	
Toluene	18.4	12.26 - 12.3[b]
Cyclohexane	4.56	10.87 - 11.0[b]
Water	1.05	1.45[b]
Mesitylene		15.5 - 16.1[b]
Pseudocumene		15.7[c]
PXE		25.2[c]

[a] Kerker, M. *The Scattering of Light and Other Electromagnetic Radiation*; Academic: New York, 1969.

[b] *CRC Handbook of Chemistry and Physics*; Weast, R. C., Ed.; CRC: Boca Raton, Florida, 1989; p E-70.

[c] Israelachvili, J. N. *Intermoleclar and Surface Forces*; Academic: London, 1985; p 54.

Table 4.8: R_{90} values for water. From Krant and Dandliker.[80]

λ (nm)	R_{90} (10^{-6} cm)
365	6.80
405	4.05
436	2.89
546	1.05

Table 4.9. $\alpha^2\rho_m$ values for liquids. The listed values are calculated based on the densities of the species and the polarizabilities listed in Table 4.7.

	ρ(g/cm^3)	MW(g/mol)	ρ_m (mol/cm^3)	$\alpha^2\rho_m$(10^{-50} mol•cm^3)
Water	1.00	18	5.6×10^{-2}	11.7
Cyclohexane	0.78	84	9.3×10^{-3}	111
Benzene	0.88	78	1.1×10^{-2}	119
Toluene	0.87	92	9.5×10^{-3}	144
Mesitylene	0.865	120	7.2×10^{-3}	180
Pseudocumene	0.876	120	7.3×10^{-3}	182
PXE	0.985	196	5.0×10^{-3}	319

benzene, but exhibits much less scattering. The difference in scattering between water and benzene (and also toluene) is not as quite as large as one would expect from the difference in polarizabilities. For benzene and water, $(\alpha^2\rho_m)_{benzene}/(\alpha^2\rho_m)_{water} = 10$ while $R_{90,benzene}/R_{90,water} = 15$. For benzene and toluene, $(\alpha^2\rho_m)_{toluene}/(\alpha^2\rho_m)_{benzene} = 1.21$ and $R_{90,toluene}/R_{90,benzene} = 1.16$. The $\alpha^2\rho_m$ values predict the trends in scattering behavior, but they are not quantitative.

Rayleigh scattering is important in a large-scale scintillator because it can change the direction of photon travel without causing absorption. This scattering degrades the positional resolution obtainable in the CTF just as inelastic scattering does. The amount of incident light which is scattered elastically in a 1 cm path length is very small, and experiments to measure such scattering must be performed carefully. This scattering becomes significant when the path length is 1 m or more, as in the CTF and Borexino. The importance of elastic scattering in light propagation in a large-scale detector is one of the most crucial differences between a detector of this size and a smaller instrument.

K. Conclusions

Several mechanisms which affect light propagation in a liquid scintillation detector were discussed in this chapter. All of them play a role in the behavior of the CTF and Borexino. The scintillator solvent in these detectors is initially excited by ionizing radiation. The transfer of excitation energy takes place nonradiatively, as discussed in Section 4.H. Concentration quenching due to excimer formation is not important for the components and concentrations used in the CTF. Impurity quenching also plays a minimal role, although this role will increase if a quencher is used in the pseudocumene buffer of Borexino.

The absorption parameters of Section 4.D and the fluorescence parameters (emission spectrum, quantum yield, and decay time) of Section 4.E are crucial in determining the behavior of a large scintillation detector. Because these parameters are normally measured using small samples, the challenge is to understand how to apply the small-scale results in order to correctly predict the large-scale behavior.

The two effects which dominate large-scale detector behavior (although they are relatively unimportant at smaller scales) are radiative migration of excitation energy by absorption and reemission of fluorescence as described in Section 4.I and elastic Rayleigh scattering of light as discussed in Section 4.J. The relative magnitudes of the effects of these processes are discussed in this thesis, as are experimental techniques designed to measure their influence on light propagation.

References

1. Birks, J. B. *Photophysics of Aromatic Molecules*; Wiley-Interscience: London, 1970.

2. Berlman, I. B. *Handbook of Fluorescence of Aromatic Molecules*; Academic: New York, 1971.

3. Horrocks, D. L. *J. Chem. Phys.* **1970**, *52*, 1566.

4. Horrocks, D. L. In *Liquid Scintillation Counting;* Crook, M. A.; Johnson, P., Eds.; Heyden: London, 1974; Vol. 3, p 3.

5. Ranucci, G. *Nucl. Inst. Meth. A* **1993**, *335*, 121.

6. Birks, J. B.; Braga, C. L.; Lumb, M. D. *Brit. J. Appl. Phys.* **1964**, *15*, 399.

7. Perkampus, H. H. *UV-VIS Atlas of Organic Compounds*, 2nd ed.; VCH Verlagsgesellschaft: Weinheim, 1992; Part 2.

8. Birks, J. B. *J. Res. Nat. Bur. Stnds. A* **1976**, *80*, 389.

9. Cohen, S. G.; Weinreb, A. *Proc. Phys. Soc.* **1956**, *B69*, 593.

10. Birks, J. B.; Conte, J. C.; Walker, G. *J. Phys. B (Proc. Phys. Soc.)* **1968**, *1*, 934.

11. Laor, U.; Weinreb, A. *J. Chem. Phys.* **1965**, *43*, 1565.

12. Braun, C. L.; Kato, S.; Lipsky, S. *J. Chem. Phys.* **1963**, *39*, 1645.

13. Burgdorff, C.; Löhmannsröben, H. G. *J. Lumin.* **1994**, *59*, 201.

14. Birks, J. B. *J. Lumin.* **1974**, *9*, 311.

15. Bolton, J. R.; Archer, M. D. *J. Phys. Chem.* **1991**, *95*, 8453.

16. Ware, W. R. *J. Phys. Chem.* **1962**, *66*, 455.

17. Umarjee, D. M.; Chikkur, G. C. *Phys. Lett. A* **1985**, *112*, 57.

18. Umarjee, D. M.; Chikkur, G. C. *Phys. Lett. A* **1987**, *123*, 23.

19. Hanagodimath, S. M.; Chikkur, G. C.; Gadaginamath, G. S. *Chem. Phys.* **1990**, *148*, 347.

20. Murata, S.; Tachiya, M. *Chem. Phys. Lett.* **1992**, *194*, 347.

21. Murata, S.; Nishimura, M.; Matsuzaki, S. Y.; Tachiya, M. *Chem. Phys. Lett.* **1994**, *219*, 200.

22. Eads, D. D.; Dismer, B. G.; Fleming, G. R. *J. Chem. Phys.* **1990**, *93*, 1136.

23. Birks, J. B.; Christophorou, L. G. *Proc. Roy. Soc. A* **1963**, *274*, 552.

24. Birks, J. B.; Dyson, D. J.; Munro, I. H. *Proc. Roy. Soc. A* **1963**, *275*, 575.

25. Birks, J. B.; Braga, C. L.; Lumb, M. D. *Proc. Roy. Soc. A* **1965**, *283*, 83.

26. Sasson, R.; Weinreb, A. *J. Lumin.* **1991**, *48*, 239.

27. Berlman, I. B. *J. Chem. Phys.* **1961**, *34*, 1083.

28. Birks, J. B.; Geake, J. E.; Lumb, M. D. *Brit. J. Appl. Phys.* **1963**, *14*, 141.

29. Birks, J. B. *The Theory and Practice of Scintillation Counting*, Pergamon: Oxford, 1964.

30. Berlman, I. B. *J. Chem. Phys.* **1960**, *33*, 1124.

31. Förster, T. *Ann. Physik.* **1948**, *2*, 55.

32. Birks, J. B. *J. Phys. B (Proc. Phys. Soc.)* **1968**, *1*, 946.

33. Mikhelashvili, M. S.; Mikhaeli, A. M. *Chem. Phys. Lett.* **1991**, *185*, 347.

34. Dexter, J. L. *Chem. Phys.* **1953**, *21*, 836.

35. Inokuti, M.; Hirayama, F. *J. Chem. Phys.* **1965**, *43*, 1978.

36. Burshtein, A. I. *Soviet Phys. JETP* **1972**, *35*, 382.

37. Haan, S. W.; Zwanzig, R. *J. Chem. Phys.* **1978**, *68*, 1879.

38. Gochanour, C. R.; Andersen, H. C.; Fayer, M. D. *J. Chem. Phys.* **1979**, *70*, 4254.

39. Loring, R. F.; Andersen, H. C.; Fayer, M. D. *J. Chem. Phys.* **1982**, *76*, 2015.

40. Bennett, R. G. *J. Chem. Phys.* **1964**, *41*, 3037.

41. Birks, J. B.; Georghiou, S. *J. Phys. B (Proc. Phys. Soc.)* **1968**, *1*, 958.

42. Pandey, K. K. *Chem. Phys.* **1992**, *165*, 123.

43. Kaschke, M.; Vogler, K. *Laser Chem.* **1988**, *8*, 19.

44. Porter, G.; Treadwell, C. J. *Chem. Phys. Lett.* **1978**, *56*, 278.

45. Butler, P. R.; Pilling, M. J. *Chem. Phys.* **1979**, *41*, 239.

46. Yokota, M.; Tanimoto, O. *J. Phys. Soc. Jpn.* **1967**, *22*, 779.

47. Steinberg, I. Z.; Katchalski, E. *J. Chem. Phys.* **1968**, *48*, 2404.

48. Gösele, U.; Hauser, M.; Klein, U. K. A.; Frey, R. *Chem. Phys. Lett.* **1975**, *34*, 519.

49. Klein, U. K. A.; Frey, R.; Hauser, M.; Gösele, U. *Chem. Phys. Lett.* **1976**, *41*, 139.

50. Gösele, U. *Spectroscopy Lett.* **1978**, *11*, 445.

51. Allinger, K.; Blumen, A. *J. Chem. Phys.* **1980**, *72*, 4608.

52. Birks, J. B.; Kuchela, K. N. *Proc. Phys. Soc.* **1961**, *77*, 1083.

53. Voltz, R.; Laustriat, G.; Coche, A. *J. Chim. Phys.* **1966**, *63*, 1253.

54. Voltz, R.; Klein, J.; Heisel, F.; Lami, H.; Laustriat, G.; Coche, A. *J. Chim. Phys.* **1966**, *63*, 1259.

55. Sipp, B.; Voltz, R. *J. Chem. Phys.* **1983**, *79*, 434.

56. Sipp, B.; Voltz, R. *J. Lumin.* **1984**, *31*, 609.

57. Sipp, B.; Voltz, R. *J. Chem. Phys.* **1985**, *83*, 157.

58. Bandyopadhyay, T.; Rao, K. V. S. *Chem. Phys.* **1992**, *167*, 131.

59. Jana, P.; Mallik, G. K.; Ganguly, T.; Bannerjee, S. B. *Bull. Chem. Soc. Jpn.* **1992**, *65*, 2196.

60. Birks, J. B.; Conte, J. C. *Proc. Roy. Soc. A* **1968**, *303*, 85.

61. Birks, J. B.; Najjar, H. Y.; Lumb, M. D. *J. Phys. B: Atom. Molec. Phys.* **1971**, *4*, 1516.

62. Chalzel, A. *J. Chem. Phys.* **1977**, *67*, 4735.

63. Mathad, R. D.; Umakantha, N. *Phys. Lett.* **1985**, *108A*, 167.

64. Mathad, R. D.; Chikkur, G. C.; Umakantha, N. *J. Chem. Phys.* **1986**, *84*, 2187.

65. Hanagodimath, S.M.; Chikkur, G. C.; Gadaginamath, G. S. *Pramana - J. Phys.* **1991**, *37*, 153.

66. Hanagodimath, S.M.; Gadaginamath, G. S.; Chikkur, G. C. *Acta Physica Pol. A* **1992**, *81*, 361.

67. Birks, J. B. *Mol. Cryst. Liq. Cryst.* **1974**, *28*, 117.

68. Sipp, B.; Miehe, J. A. *Nucl. Inst. and Meth.* **1974**, *114*, 255.

69. Baumann, J.; Calzaferri, G.; Hugentabler, T. *Chem. Phys. Lett.* **1985**, *116*, 66.

70. Wiorkowski, P.; Hartmann, W. *Optics. Comm.* **1985**, *53*, 217.

71. Hammond, P. R. *J. Chem. Phys.* **1979**, *70*, 3884.

72. D'Ambrosio, C.; Leutz, H.; Tailhardat, S.; Taufer, M.; Deustruel, P.; Puertolas, D.; Güsten, H. *Nucl. Inst. and Meth. A* **1991**, *307*, 430.

73. Martinho, J. M. G.; Maçanita, A. L.; Berberan-Santos, M. N. *J. Chem. Phys.* **1989**, *90*, 53.

74. Martinho, J. M. G.; d'Oliveira, J. M. R. *J. Chem. Phys.* **1990**, *93*, 3127.

75. Hirschfelder, J. O.; Curtiss, C. F.; Byrd, R. B. *Molecular Theory of Gases and Liquids*; John Wiley & Sons: New York, 1954.

76. Kerker, M. *The Scattering of Light and Other Electromagnetic Radiation*; Academic: New York, 1969.

77. Coumou, D. J.; Mackor, E. L.; Hijmans, J. *Trans. Faraday Soc.* **1964**, *60*, 1539.

78. Parfitt, G. D.; Wood, J. A. *Trans. Faraday Soc.* **1968**, *64*, 805.

79. Israelachvili, J. N. *Intermoleclar and Surface Forces*; Academic: London, 1985; p 54.

80. Krant; Dandliker *J. Chem. Phys.* **1955**, *23*, 1544.

CHAPTER 5: OPTICAL PROPERTY MEASUREMENTS

The importance of understanding light propagation in a large-scale scintillation detector such as the Counting Test Facility (CTF) was discussed at the end of Section 2.C. Light propagation in the detector affects the reliability of positional reconstruction and α-β separation. Light propagation is also influenced by reflections, refraction, and scattering in other parts of the detector, but propagation in the scintillator plays a dominant role.

This chapter describes the measurement of several optical properties of the scintillator which play crucial roles in light propagation. The theory underlying this work was presented in Chapter 4. These measurements were made using small (approximately 3 cm^3) samples of scintillator. Measurement of scintillator optical properties on a larger scale using the CTF will be described in Chapter 6. Absorption and fluorescence spectra, quantum yields, and fluorescence decay times of several scintillator components, as well as elastic scattering in scintillator mixtures and the effects of impurity quenching on the scintillator are reported here. Three instruments were used to produce the measurements reported in this chapter: an absorption spectrophotometer, a luminescence spectrophotometer, and a fluorescence decay time measurement system. Application of these parameters to the prediction of the behavior of large scale scintillation detectors is also considered.

A. Absorption Measurements

In absorption spectroscopy, the amount of light transmitted through a sample is measured. Absorption spectrophotometers have a linear geometry, and any light which is lost from the source beam is counted as a loss in transmission. Because of this, the instruments cannot differentiate between light which is absorbed by the

sample and that which is scattered or reflected away from the source beam. When absorption of the sample is large, these other effects are negligible, but they can complicate the interpretation of the results when the sample absorbs very little light.

The absorption measurements described here were made using a Shimadzu UV-1201 single beam absorption spectrophotometer. A schematic diagram of this instrument is shown in Figure 5.1. The UV-1201 can perform measurements at wavelengths from 200 to 1200 nm. A software card was purchased for the spectrophotometer to enable it to measure absorption while scanning over a range of wavelengths. Absorption was measured for samples in quartz cuvettes with a 1 cm path length. The cuvettes held approximately 3 cm^3 of liquid. Prior to measuring the absorbance of a sample, the instrument was zeroed to correct for variations in source intensity and detector response with wavelength. The instrument produced its most reliable results when the measured absorbance was between 0.046 and 1.0. An absorbance of 0.046 corresponds to transmission of 90% of the incident light, while an absorbance of 1.0 corresponds to a transmission of 10%. When better data were unavailable, absorbances as low as 0.010 (corresponding to 97.7% transmission) were utilized.

The absorption spectra of several potential scintillator components were measured. The solvents pseudocumene and phenylxylylethane (PXE) were studied. The main absorption bands of these solvents absorb too strongly to allow measurements using the pure liquids in 1 cm cells. A series of volumetric dilutions of pseudocumene and PXE were made in cyclohexane to enable their absorption spectra in the main absorption region (approximately 250 – 290 nm) to be obtained. The dilutions were made in combinations of 25:1 and 10:1 steps. The solvents required dilution by a factor of nearly 10000 to bring their absorbance in the $S_0 \rightarrow S_1$ band (at approximately 270 nm for pseudocumene and PXE) below 1.0 with a 1 cm path

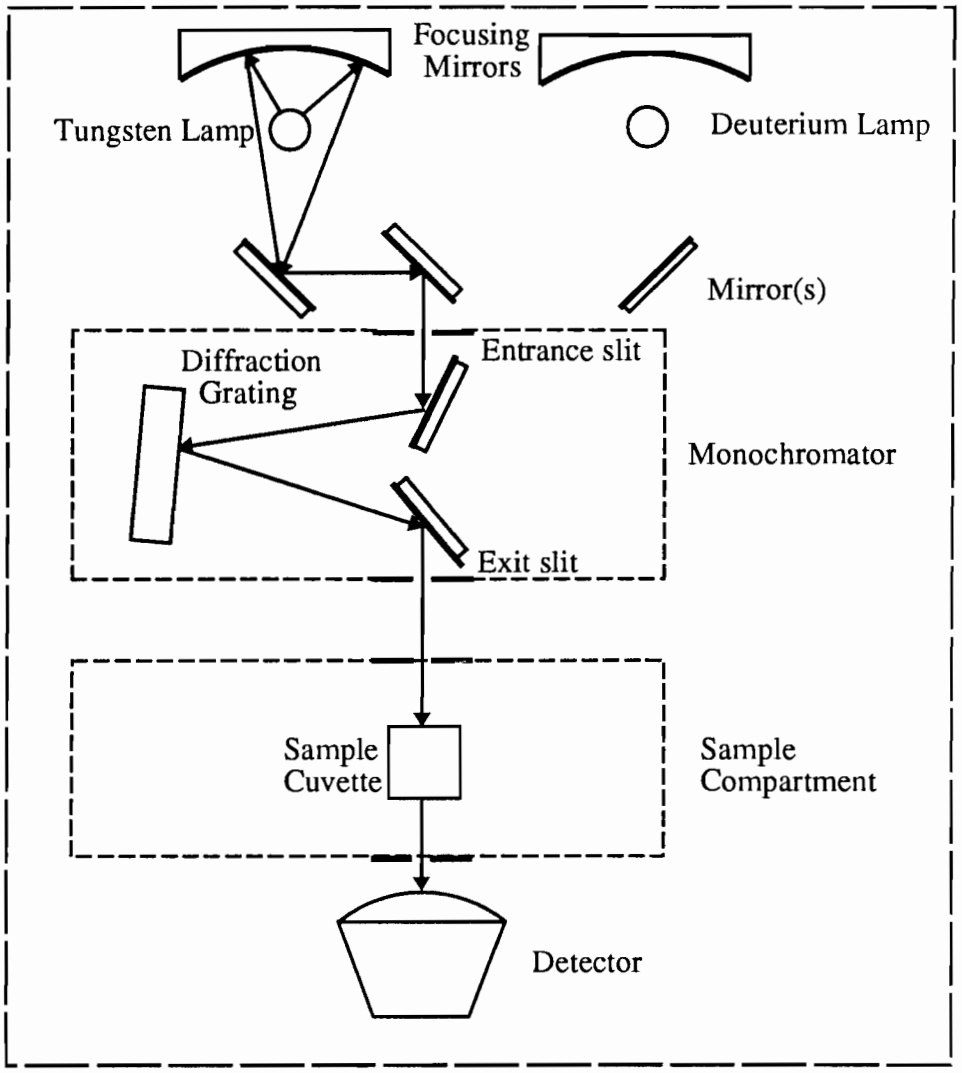

Figure 5.1. Schematic disagram of UV-1201. The UV-1201 is a single beam absorption spectrophotometer. The instrument contains two light sources: a deuterium lamp for wavelengths from 200 to 325 nm and a tungsten lamp for wavelengths from 329 to 1200 nm. Transmission of light through the sample is measured for a wavelength which is selected by a grating monochromator. The UV-1201 must be zeroed properly prior to the collection of absorption data in order for meaningful results to be obtained.

length. The accuracy of the reported extinction coefficients can not be any better than the accuracy of the dilutions; the dilutions were reliable to within ± 1%. The instrument was zeroed by using a cuvette containing cyclohexane when spectra were measured using the diluted solvent samples.

The pure solvents, pseudocumene and PXE, were used in the wavelength region above 290 nm. Data were obtained using the pure solvents at wavelengths where the absorbance was between 0.010 and 1.0. Reliable results were obtained for pseudocumene at wavelengths up to 325 nm and for PXE at up to 355 nm. Data at longer wavelengths, where the absorbance is less, can be obtained by using a more accurate instrument or a sample cell with a longer path length.

Selection of a fluid for zeroing the instrument is more difficult when the pure solvents are used as samples. Ideally, the blank should not absorb any light. Air has the desirable property of low absorption of ultra-violet light, but reflections are more severe when a cuvette contains air because of the large mismatch in refractive indices between air and quartz. A cuvette containing air shows more absorbance than does one containing water or cyclohexane. The inability to differentiate between absorbed and reflected or otherwise scattered light is an important limitation of absorption spectroscopy. The absorbance of water and cyclohexane was found to be identical down to 230 nm. At wavelengths below 230 nm, water displayed less absorbance. Because of this, the UV-1201 was zeroed by using a cuvette containing water for absorption measurements made with the neat solvents.

Absorption spectra were also measured for the fluors 2,5-diphenyloxazole (PPO) and bis-methylstyrylbenzene (bis-MSB). Spectra were acquired for solutions of the fluors in both pseudocumene and cyclohexane. Extremely dilute solutions were required to achieve an absorbance below 1.0 at the most strongly absorbing wavelengths. A PPO concentration of 5×10^{-5} g/L was used at 320 nm and a bis-MSB

concentration of 2×10^{-5} g/L was used at 345 nm. Concentrated fluor solutions were mixed by weight, and a dilution procedure was employed to obtain the desired concentration. The long wavelength absorption measurements for the fluors were limited by the their solubility in the solvents. The most concentrated solutions used in pseudocumene were 200 g/L of PPO and 40 g/L of bis-MSB. In cyclohexane, the most concentrated solutions were 1.56 g/L of PPO and 1 g/L of bis-MSB. The absorption spectra were almost identical in the two solvents. The UV-1201 was zeroed by using cuvettes containing neat pseudocumene and cyclohexane, respectively, before the fluor absorption measurements.

The absorption of other liquids and solutions was also studied. Water and cyclohexane were both examined, as were acidic aqueous solutions of quinine bisulfate (QBS). The quinine bisulfate was used as a luminescence standard in quantum yield measurements.

Treatment of the samples prior to the measurement of their absorption spectra was important. The effects of distillation, filtration, and nitrogen sparging on the optical clarity of pseudocumene have been discussed in Chapter 3. The nitrogen sparging operation is the most crucial for obtaining accurate results. As the scintillator samples are exposed to air, oxygen diffuses into the liquid. The oxygen forms a charge transfer complex with the organic molecules and this complex has a structureless absorption band.[1] Pseudocumene, PXE, and cyclohexane all exhibit increased absorbance in the presence of oxygen. The effect of oxygen on absorption is more significant at short wavelengths. Removal of oxygen from liquid organic samples has been reported in the literature.[2] It is accomplished by a freeze-thaw-pump technique or by nitrogen sparging with equal effectiveness.

In order to obtain accurate spectra, oxygen was removed from the liquids by nitrogen sparging. The sparging was accomplished by inserting syringe needles into

the cuvettes and bubbling bottled nitrogen through them. The sparging was performed in a glove box containing a nitrogen atmosphere. The cuvettes were capped with teflon stoppers before they were removed from the glove box and taken to the spectrophotometer. Tests indicated that no appreciable oxygen leakage into the sample occurred during the first hour following removal from the glove box. A sparging time of 10 minutes was found to be sufficient. Rotation of the cuvettes during sparging to ensure good mixing was necessary for complete oxygen removal. The samples used to zero the UV-1201 were also sparged to remove oxygen. Oxygen was found to have no effect on the absorption of water. It also had a negligible effect on the absorption by the fluors .

Absorption spectra measured for some scintillator components are shown in Figures 5.2 – 5.7. The absorption is shown in these plots in terms of an extinction coefficient. The graphs in Chapter 3 showed absorption in terms of attenuation length, but absorption spectra are commonly plotted using the molar decadic extinction coefficient. The UV-1201 reports data in terms of absorbance or percent transmission. Absorbance (A) is equal to the negative log (base 10) of the fraction of transmitted light. The molar decadic extinction coefficient (ε) is calculated from absorbance using

$$\varepsilon = \frac{A}{c\,l} \qquad (5.1)$$

Here c is the concentration of the absorbing molecule (mol/L) and l is the path length through the cuvette (cm).

The resolution of the UV-1201 is sufficient to discern spectral features with a width of 5 nm or more. It provides a wavelength accuracy of $\pm$ 0.5 nm in the absorption spectra. This resolution is lower than that of the instruments used to collect other absorption data which are shown for comparison in Figures 5.2 – 5.7. The peaks of the spectra measured using the UV-1201 are less sharp due to this lower resolution.

Figure 5.2 displays four absorption spectra for pseudocumene with the extinction coefficient plotted on a linear scale: one measured using the UV-1201, one measured by the Perugia group of the Borexino collaboration,[3] and two spectra from the literature.[4,5] The results agree well qualitatively. Results obtained with the UV-1201 consistently indicated more absorption at 270 nm than at 267 nm, while the other reported spectra show the opposite behavior. This is explained by the lower resolution of the UV-1201. The linear scale allows for easy comparison between the spectra in the first absorption band near 270 nm.

The same four absorption spectra for pseudocumene are shown again in Figure 5.3. In this figure, the extinction coefficient is plotted on a logarithmic scale. This allows a better view of the low absorbance region at wavelengths greater than 290 nm and the high absorbance region at wavelengths below 250 nm. A third spectrum from the literature[6] is also included in Figure 5.3. Eitel et. al measured pseudocumene absorption at long wavelengths. Their extinction coefficients are slightly higher than those reported by Perugia. The measurements made with the UV-1201 agree well with the literature data below 250 nm. They also reflect the qualitative trend found by the Perugia group at wavelengths of 290 – 325 nm. The UV-1201 extinction coefficients are slightly higher than the Perugia values at these wavelengths. This could be due to the use of a different blank or to inaccuracy in the UV-1201 at small absorbances. The Perugia group was able to report extinction coefficients at much longer wavelengths than was possible using the UV-1201 due to their possession of a more accurate spectrophotometer and cuvettes with longer path lengths of up to 10 cm. The reliability of their measurements is questionable at wavelengths longer than 450 nm, as indicated by the large fluctuations shown in the data in Figure 5.3.

Figure 5.4 displays two absorption spectra for PXE on a log scale. One of the spectra was produced using the UV-1201 and the other was measured by the Perugia

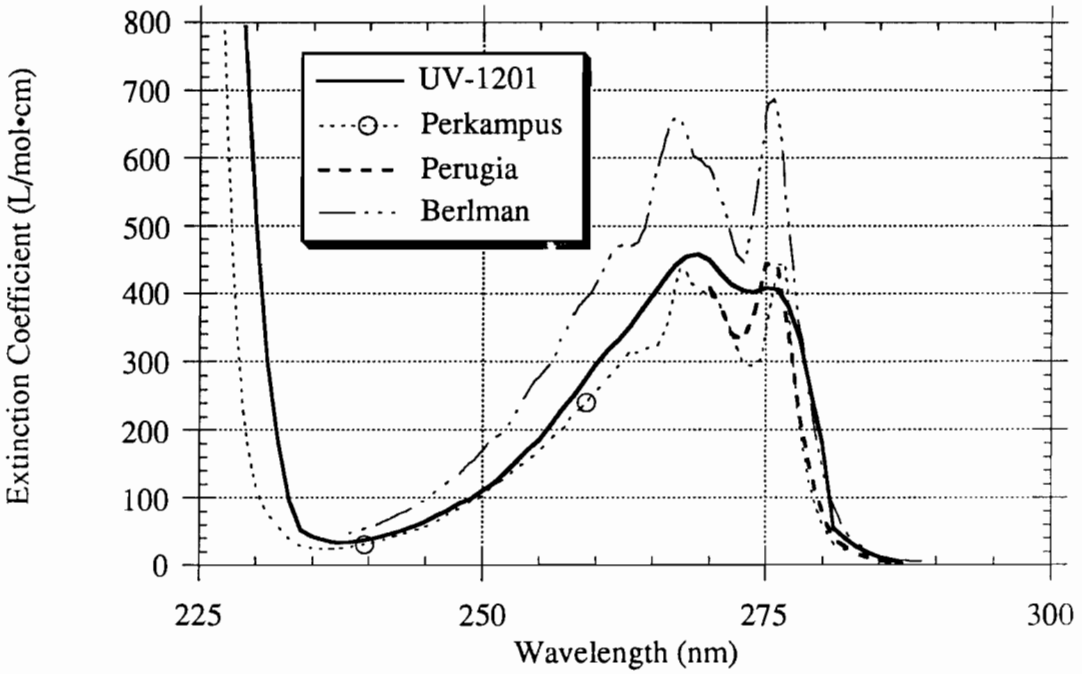

Figure 5.2. Absorption spectrum of pseudocumene (linear scale). The linear scale facilitates examination of pseudocumene absorption in the first absorption band near 270 nm. Data collected with the UV-1201 are shown as are data from Perugia,[3] Berlman,[4] and Perkampus.[5] The UV-1201 results were obtained in 1 cm cuvettes with concentrations ranging from pure pseudocumene (7.3 M) to 4.7×10^{-4} M pseudocumene in cyclohexane. The UV-1201 has a wavelength accuracy of ± 0.5 nm and a spectral resolution of 5 nm.

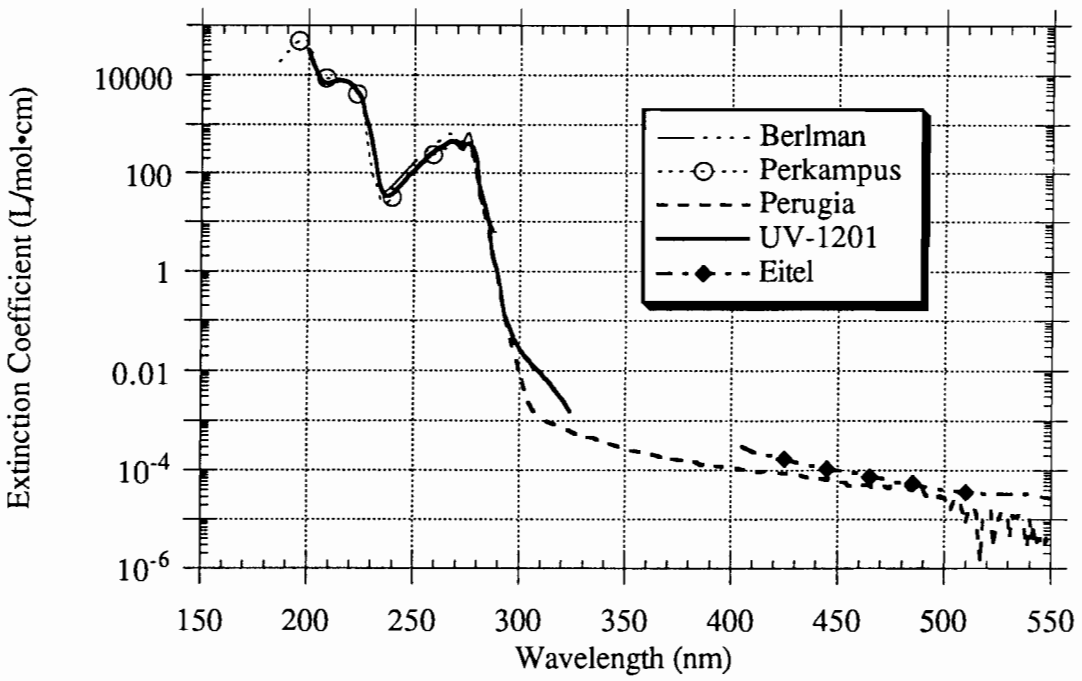

Figure 5.3. Absorption spectrum of pseudocumene (log scale). The log scale facilitates examination of pseudocumene absorption at long wavelengths. Data collected with the UV-1201 are shown along with data from Perugia,[3] Berlman,[4] Perkampus,[5] and Eitel.[6] The UV-1201 results were obtained in 1 cm cuvettes with concentrations ranging from pure pseudocumene (7.3 M) to 4.7×10^{-4} M pseudocumene in cyclohexane. The UV-1201 has a wavelength accuracy of $\pm$ 0.5 nm and a spectral resolution of 5 nm.

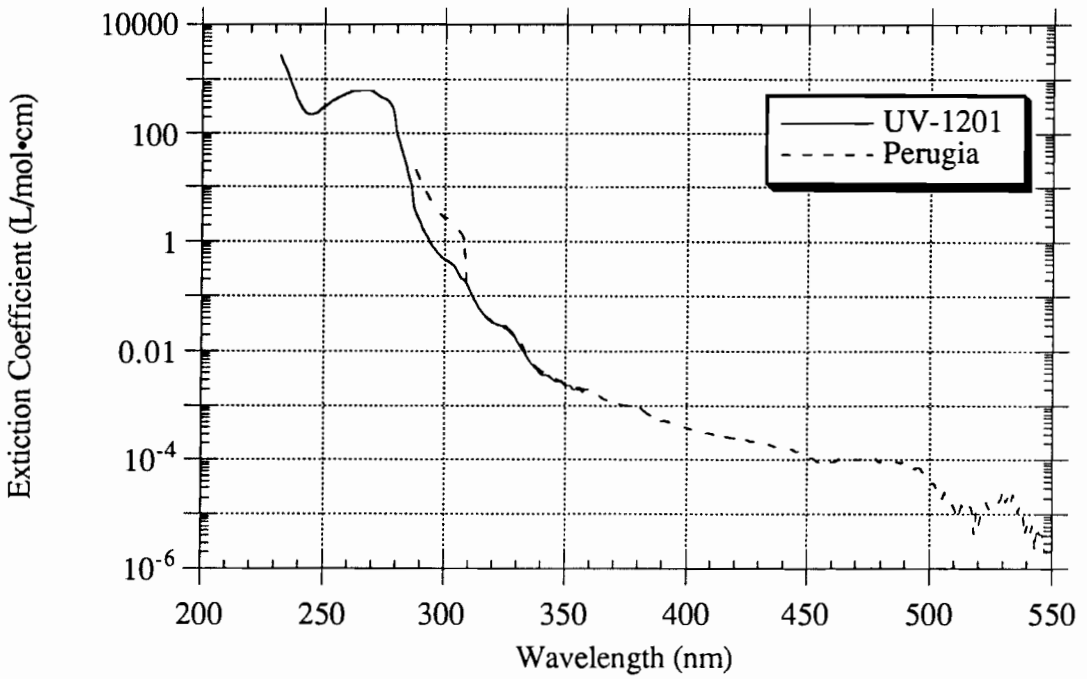

Figure 5.4. Absorption spectrum for PXE. This is a log scale plot of the extinction coefficient for PXE. Data obtained using the UV-1201 are shown along with data from Perugia.[7,8] The UV-1201 results were obtained in 1 cm cuvettes with concentrations ranging from pure PXE (5.0 M) to 3.2×10^{-4} M PXE in cyclohexane. The UV-1201 has a wavelength accuracy of $\pm$ 0.5 nm and a spectral resolution of 5 nm.

group.[7,8] No spectra for PXE were found in the literature. PXE absorbs in a wavelength region similar to that of pseudocumene. Its absorption peak is slightly red-shifted from that of pseudocumene and its absorption band has less structure.

Absorption spectra of the fluors PPO and bis-MSB are shown in Figures 5.5 – 5.7. PPO absorption is displayed on a linear scale in Figure 5.5 and on a log scale in Figure 5.6. The linear scale provides a better perspective of the main absorption band near 320 nm, while the log scale is more useful for showing loss of transmission at long wavelengths. Three spectra are plotted in both Figure 5.5 and Figure 5.6: one produced with the UV-1201, one from the Perugia group,[7] and one from Berlman.[4] The spectra show the same qualitative features. The Perugia data again extend to longer wavelengths than do those of the other two measurements. Absorption spectra for bis-MSB from the same three sources are shown in Figure 5.7. This figure is plotted on a log scale. Good qualitative agreement between the spectra can again be seen.

The absorption spectra in Figures 5.2 – 5.7 have displayed absorption in terms of the molar decadic extinction coefficient. Another way of representing this data is in terms of attenuation length. The attenuation length is the distance a photon of a given wavelength travels through a medium before its probability of loss of transmission in a linear geometry is $(1\text{-}e^{-1})$ or 62%. Attenuation lengths (a_L) can be calculated from extinction coefficient values by using

$$a_L = \frac{\log (e)}{\varepsilon c} \qquad (5.2)$$

Figure 5.8 shows attenuation lengths for photons traveling through pseudocumene and a 1.5 g/L solution of PPO. The PPO curve only accounts for loss of transmission by the fluor itself and does not include attenuation caused by the solvent in which the PPO is dissolved. A PPO concentration of 1.5 g/L is represented in Figure 5.8 because it is the concentration used in the CTF. Examination of the

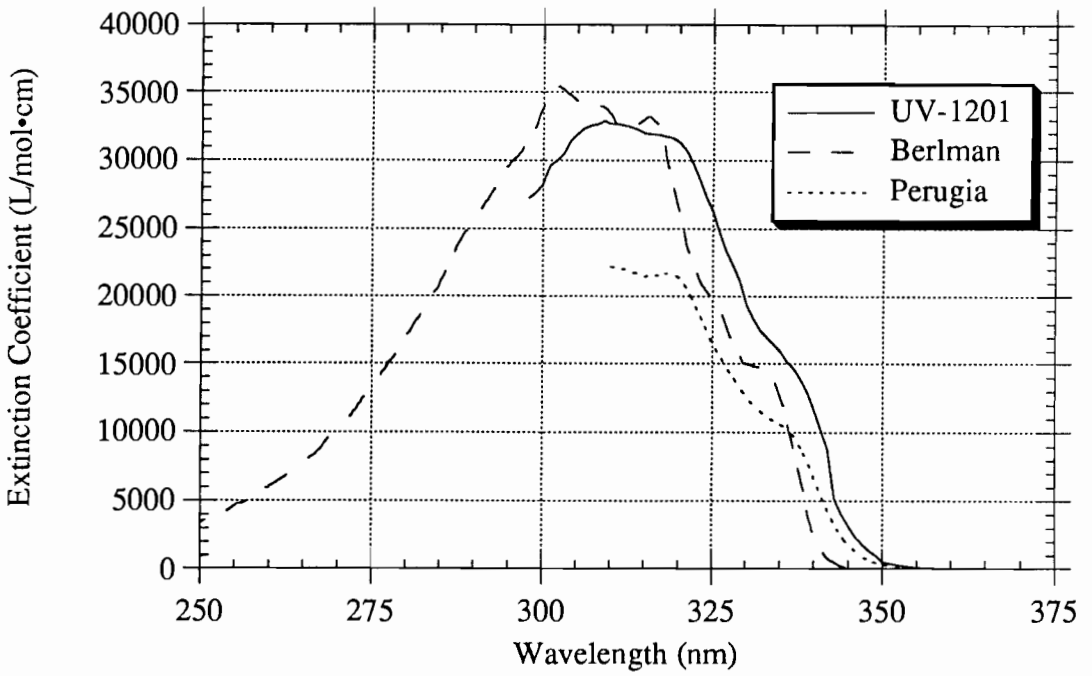

Figure 5.5. Absorption spectrum for PPO (linear scale). The extinction coefficient of PPO is shown on a linear scale to allow comparison of the different measurements over the first absorption band of PPO. Data from Perugia[7] and Berlman[4] are shown along with results from the UV-1201. The UV-1201 results were obtained in 1 cm cuvettes with concentrations ranging from 0.93 M to 9.0×10^{-7} M PPO in pseudocumene. The UV-1201 has a wavelength accuracy of $\pm$ 0.5 nm and a spectral resolution of 5 nm.

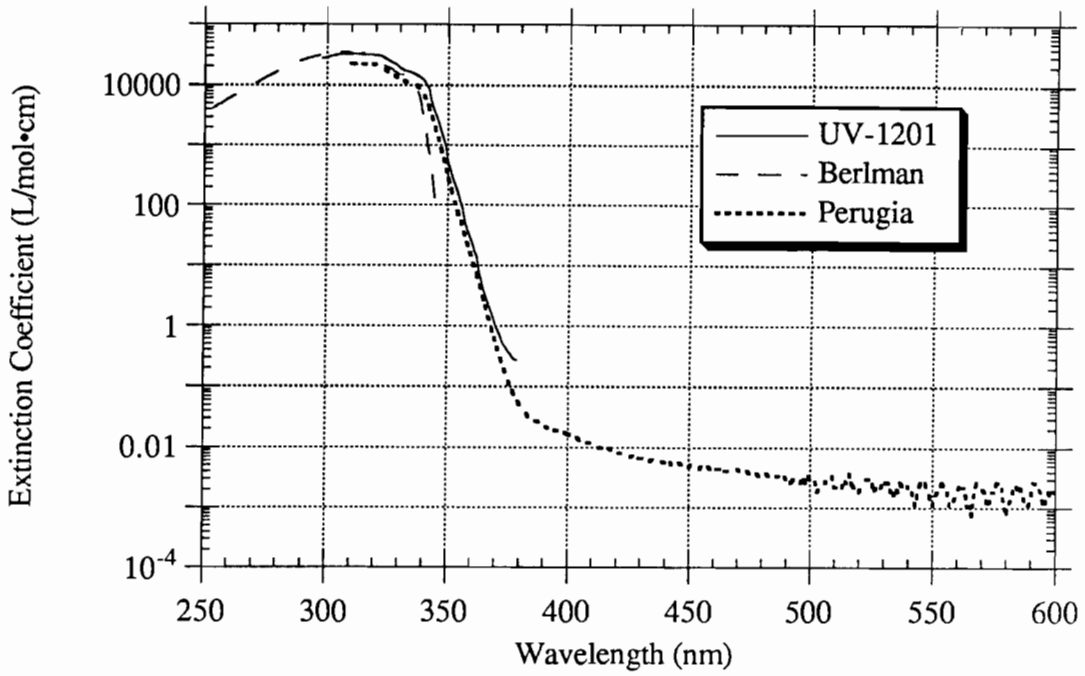

Figure 5.6. Absorption spectrum for PPO (log scale). The extinction coefficient of PPO is shown on a log scale in order to clearly show absorption values at long wavelengths. Data collected using the UV-1201 are shown along with data from Perugia[7] and Berlman.[4] The UV-1201 results were obtained in 1 cm cuvettes with concentrations ranging from 0.93 M to 9.0×10^{-7} M PPO in pseudocumene. The UV-1201 has a wavelength accuracy of ± 0.5 nm and a spectral resolution of 5 nm.

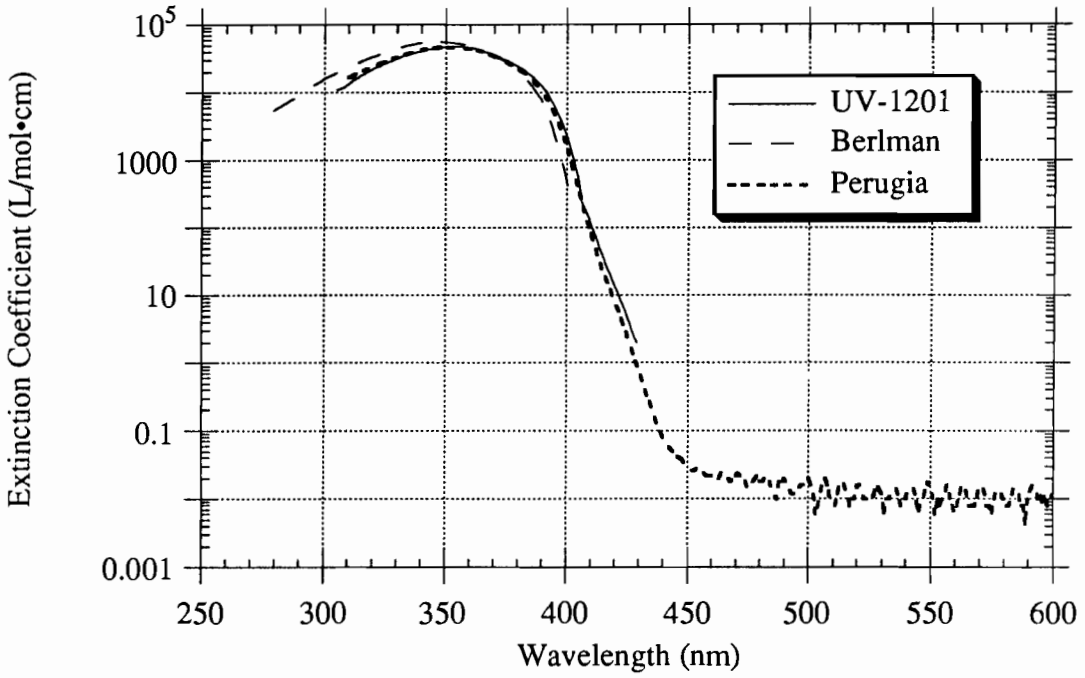

Figure 5.7. Absorption spectrum for bis-MSB. The extinction coefficient of bis-MSB is shown here on a log scale. Data collected using the UV-1201 are shown along with data from Perugia[7] and Berlman.[4] The UV-1201 results were obtained in 1 cm cuvettes with concentrations ranging from 5.0×10^{-3} M to 2.0×10^{-6} M bis-MSB in pseudocumene. The UV-1201 has a wavelength accuracy of $\pm$ 0.5 nm and a spectral resolution of 5 nm.

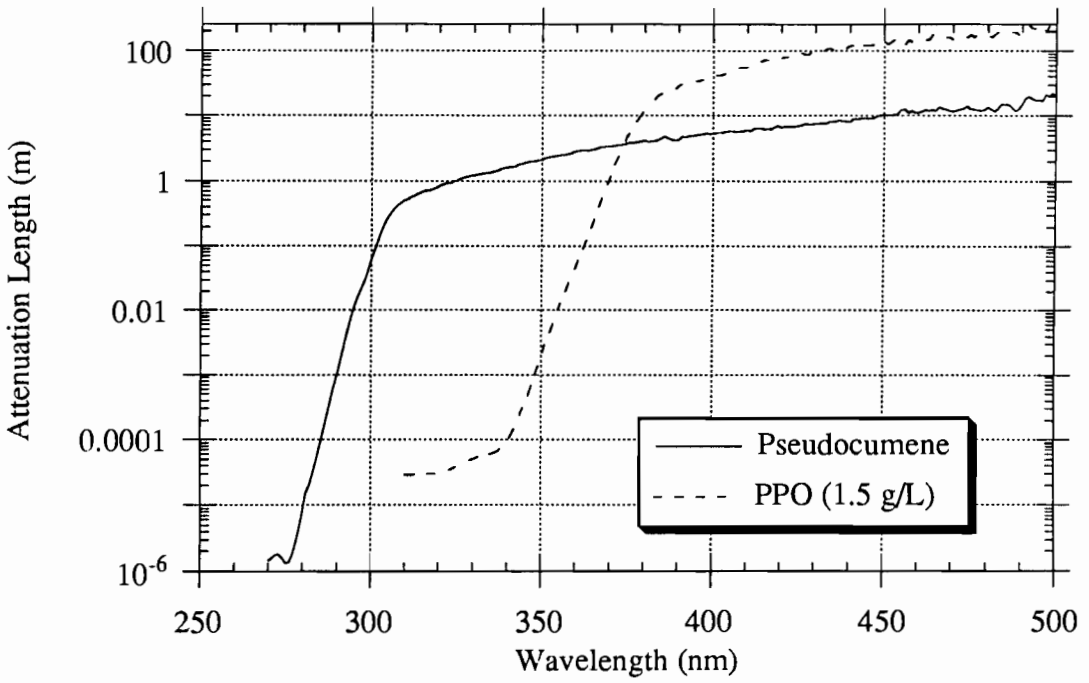

Figure 5.8. Attenuation length of light in pseudocumene and 1.5 g/L PPO solution. The loss of light transmission due to pseudocumene and PPO is shown here in terms of attenuation length. The PPO curve only represents loss of transmission due to the fluor at a concentration of 1.5 g/L. It does not include any contribution from the solvent in which the PPO is dissolved.

figure shows that in a scintillator containing 1.5 g/L of PPO in pseudocumene, PPO is the dominant cause of loss of light transmission at wavelengths below 350 nm. For light of wavelengths greater than 375 nm, pseudocumene has the most important influence. The two components have attenuation lengths of similar magnitude at wavelengths between 350 and 375 nm. Figure 5.8 shows that at wavelengths above 430 nm, the attenuation length becomes 8 m or longer. This is sufficient for a photon to escape from the CTF and Borexino.

The absorption measurements performed with the UV-1201 served to corroborate previous literature values and measurements by the Perugia group on the absorption of several scintillator components. The agreement of the values found here with previous work validated the experimental procedures that were developed, especially those for removal of oxygen from the samples. (The effect of oxygen removal for increasing the attenuation length in pseudocumene can be seen in Figure 3.5) The techniques developed were then applied to new compounds such as PXE and were used with confidence in studies on the effectiveness of various purification operations.

Before concluding this section on absorption measurements, it is important to emphasize what these measurements actually tell us. Absorption measurements only provide information on the loss of light transmission through a sample in a linear geometry. Because of geometrical limitations, the measurements cannot differentiate between light which is lost through absorption and that which is lost through reflections or scattering. Section 5.D will provide evidence that most of the loss of transmission indicated by the measurements in this section at long wavelengths (> 310 nm for pseudocumene, > 375 nm for PPO, and > 440 nm for bis-MSB) is due to elastic scattering and not to absorption. This has important consequences for light propagation in a large-scale scintillation detector.

B. Fluorescence Measurements

In luminescence spectroscopy, a sample is excited with a short pulse of light and any emission which comes from the sample upon its relaxation is monitored. During fluorescence spectroscopy, the sample is monitored for approximately 100 ns following the excitation pulse because fluorescence is a phenomenon with a short lifetime. In phosphorescence spectroscopy the sample is monitored for as long as several seconds to allow measurement of phosphorescence which has a much longer lifetime. Only fluorescence is of concern in Borexino, because the time scale on which phosphorescence takes place is too long to be useful in the experiment.

The fluorescence measurements reported here were made using a Perkin Elmer LS50 luminescence spectrophotometer. A schematic diagram[9] of this instrument is shown in Figure 5.9. The spectrophotometer is controlled through a personal computer interface. Excitation light is provided by a xenon flash tube which produces a short pulse of intense light over the spectral range of the LS50. A small festoon lamp close to the source maintains an even triggering of the flash tube. The light from the xenon flash tube passes through a monochromator which selects the excitation wavelength. The excitation beam coming out of the monochromator impinges on the sample cuvette. A photomultiplier tube detector is positioned perpendicular to the excitation beam. Emission from the sample traveling in this direction passes through another monochromator to isolate the emission wavelength before the light reaches the detector. In this arrangement, the detector only covers a small solid angle of the sample, and most of the sample emission is lost. The 90° arrangement is one of several geometries possible for a luminescence spectrophotometer. Other types of instruments utilize front-face and transmission geometries. The sample cuvette holder of the LS50 contains mirrors behind the two sides of the cuvette which do not face the

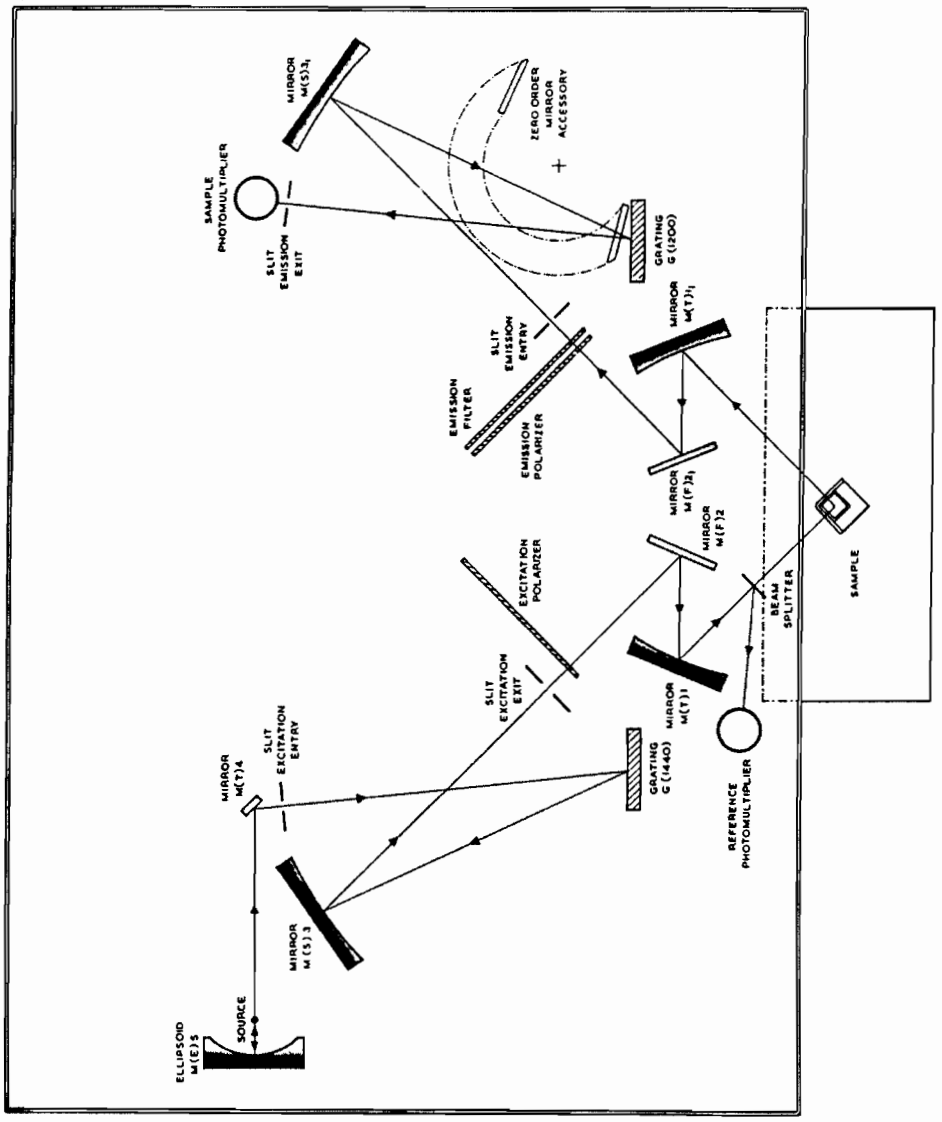

Figure 5.9. Schematic diagram of the Perkin Elmer LS50. This instrument is a luminescence spectrophotometer. It uses a xenon flash tube source, contains excitation and emission monochromators, and employs a phototube detector. The diagram is from the owner's manual.[9]

incoming excitation beam or the detector. These mirrors were covered with black felt to reduce the amount of stray light in the instrument.

Two types of spectra can be measured with the LS50: emission spectra and excitation spectra. An emission spectrum is obtained by maintaining the excitation monochromator at one wavelength and scanning the emission monochromator over a range of wavelengths. Emission spectra are the most commonly reported luminescence spectra. The choice of excitation wavelength has a large effect on the emission spectrum obtained. An excitation spectrum is obtained by scanning the excitation monochromator over a range of wavelengths while the emission monochromator is maintained at a constant wavelength, often chosen to be a peak in the emission spectrum. An excitation spectrum is closely related to an absorption spectrum because the wavelengths which are more strongly absorbed tend to result in more emission.

During spectrum acquisition one monochromator is scanned while the other remains at a fixed wavelength. Scanning takes place in wavelength increments of 0.5 nm. Several excitation pulses are sent at each wavelength during the scan, and the results are averaged to generate the reported detector response. The actual number of excitation pulses depends on the scanning speed. It ranges from 180 pulses per wavelength interval at a speed of 10 nm/s to 1 pulse per interval at a speed of 1500 nm/s.

The control software allows for variation in the slit widths of the monochromators. Slit width is chosen in terms of monochromator bandpass. The excitation monochromator slits can be adjusted from 2.5 to 15 nm, and the emission monochromator from 2.5 to 20 nm. Narrow slits allow good resolution to be obtained, but signal level is reduced. Wide slits result in a larger signal, but resolution suffers.

In general, the smallest slit setting which provided an acceptable signal was used to collect data.

1. Emission Spectra

Fluorescence spectra were measured for the scintillator components pseudocumene, PXE, PPO, and bis-MSB. The concentrations of the sample solutions containing these solvents and fluors were critical in obtaining meaningful results. The photo tube detector has a limited range of response. If the emission from the sample is too small, no signal above the background noise level is recorded by the photo tube. If the emission is too large, the photo tube saturates and the data are not useful quantitatively. As the excitation beam travels through the sample cuvette, some of the light in the beam is absorbed. The molecules absorbing this light are excited, and they can relax and emit light which is detected by the photo tube. Absorption of the excitation beam is expressed by Beer's law (see eq 4.2). As more light is absorbed, more molecules are excited, and the intensity of the emission increases.

A luminescence spectrophotometer like the LS50 with a 90° geometry provides the most accurate results when dilute samples are used. Although higher concentrations provide a more intense emission, they are undesirable for several reasons. If too much emission occurs, the photo tube becomes saturated, and the data are not useful. Higher concentrations also result in more self-absorption of fluorescence. This self-absorption usually occurs at the shorter wavelengths of the emission spectrum and can result in a distortion of the spectrum because the emission intensity at these wavelengths is reduced while that at the longer wavelengths remains unchanged. Best results are obtained when the absorbance for all the wavelengths in the emission spectrum is less than 0.01 (transmission of > 99%) over the path length of the sample cuvette.[2]

High sample concentrations are also undesirable because of what is known as the inner filter effect. The detector does not view the entire volume of the sample cuvette with the same efficiency. Optimum detection normally occurs from the center of the cuvette. If the absorption of the excitation beam in the cuvette is high, its intensity is not uniform over the entire cuvette. This does not cause distortion of the emission spectrum, but uniform illumination of the cuvette is necessary for quantitative measurements such as the determination of quantum yields. If the inner filter effect becomes important, the center of the cuvette receives less excitation light than the portion of the sample closer to the excitation source. The LS50 has a sample cuvette geometry similar to that shown in Figure 5.10.[2] Light can escape from the cuvette between points B and C, but it cannot reach the detector if it is emitted in other parts of the cell.

Parker[2] has derived a formula to correct the integrated emission intensity for the inner filter effect when the absorbance at the excitation wavelength is less than 0.2 (transmission > 63%). The formula is written

$$\frac{F_0}{F} = \frac{2.303\ D\ (d_2 - d_1)}{10^{-Dd_1} - 10^{-Dd_2}} \qquad (5.3)$$

where F_0 is the corrected intensity, F is the measured intensity, D is the sample optical density at the excitation wavelength in cm^{-1}, and d_1 and d_2 are the distances in cm as shown in Figure 5.10. The optical density of a sample is equal to the product of its molar decadic extinction coefficient at the excitation wavelength and the concentration of the absorbing molecule. The inner filter effect is unimportant when sample absorbance is less than 0.02 (transmission > 95.5%). In some cases, the inner filter effect is so severe that no emission can be seen. All the excitation light is absorbed within a very short region at the front face of the cuvette. No emission from this region can be seen by the detector, and no signal can be detected above the

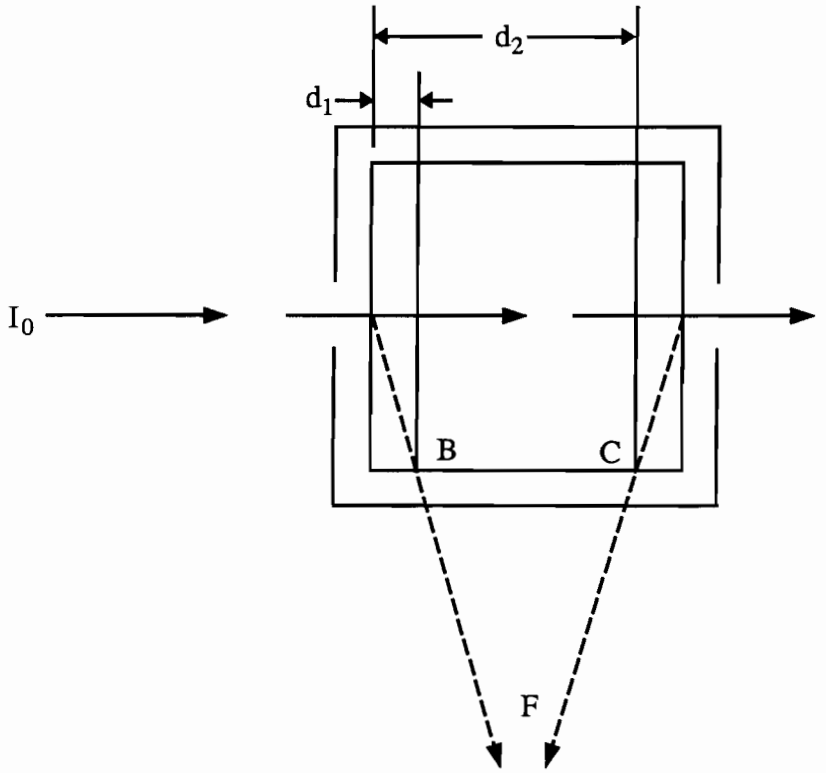

Figure 5.10. Inner filter effect caused by fluorescence sample cuvette geometry. The excitation beam of intensity I_0 enters the sample cuvette from the right. Fluorescence (F) escapes toward the detector. Light can escape from the cuvette between points B and C (at distances d_1 and d_2 from the entrance of the excitation beam). Emission which takes place in regions of the cuvette from which it cannot escape to the detector is lost. This gives rise to the inner filter effect. The effect is especially important for concentrated samples where most of the excitation beam is absorbed at distances less than d_1. The diagram is from Parker.[2]

background. Severe inner filter effects occur when using pure pseudocumene and PXE samples.

In order to avoid the detrimental effects of excessive absorption, dilute concentrations were used in the samples examined with the LS50. Because the samples absorb with different intensities as the excitation wavelength is changed, several different concentrations were utilized. The same concentrations were used for the fluorescence measurements as were used for the absorption measurements with the UV-1201.

Nitrogen sparging of the fluorescence spectroscopy samples was even more critical than for the absorption measurements. Dissolved oxygen has a large quenching effect on fluorescence of organic molecules. The spectra are altered more in intensity than in shape. The same sparging and cuvette sealing techniques were used for the fluorescence measurements as for the absorption work.

In order to report meaningful fluorescence emission spectra, it is necessary to account for parameters which vary between different spectrophotometers so that the spectra remain valid independent of the specific instrument on which they were recorded.[10] Variations can exist in the wavelength dependence of source intensity, monochromator efficiency, and detector sensitivity.

The LS50 has an internal calibration to adjust for variations in source intensity with time and wavelength. As shown in Figure 5.9, the excitation beam is split after it leaves the excitation monochromator. Most of the beam is used to excite the sample, but part of it is directed towards a reference phototube. The response of this phototube is used by the data collection software to correct the output signal for variations in excitation intensity. The effect of this internal calibration is evident in the noise signals at different excitation wavelengths. At short wavelengths such as 230 nm, the source intensity is much lower than at wavelengths near 400 nm. Random noise in the

detector phototube generates a larger signal at an excitation wavelength of 230 nm than at 400 nm because the output is adjusted for source intensity.

No internal calibration is provided for the variation in the efficiencies of the emission monochromator and phototube detector as a function of wavelength. A response curve is available from the phototube manufacturer, but this does not include the effects of the monochromator. The response of the LS50 was calibrated as a function of wavelength so that accurate spectra could be reported. Berlman[4] has reported spectra for many fluorescent organic compounds that have been corrected for instrumental response. By comparing the spectra measured using the LS50 to the corrected literature spectra, it was possible to develop a calibration curve. Solutions of quinine bisulfate[11,12,13] (QBS) in 0.1 N H_2SO_4, PPO in cyclohexane, and pseudocumene in cyclohexane were used to derive a calibration curve over the wavelength range of 270 – 550 nm. Details of this calibration are given in Appendix 5.I. The calibration curve for the LS50 is shown in Figure 5.11. The correction factor $S(\lambda)$ which is plotted in the figure can be expressed as

$$S(\lambda) = \frac{I_0(\lambda)}{I(\lambda)} \qquad (5.4)$$

where I is the intensity of the corrected spectrum and I_0 is the intensity measured with the LS50. Corrected spectra for other samples can be produced using this calibration curve.

Corrected fluorescence emission spectra recorded using the LS50 are shown in Figures 5.12 – 5.17. Figure 5.12 shows the normalized emission spectrum for pseudocumene in cyclohexane. Excitation was at 270 nm. A spectrum measured by the Perugia group[3] and one reported by Berlman[4] are shown for comparison. Good agreement is observed among the three emission curves. Figure 5.13 displays the normalized emission spectrum for PXE in cyclohexane following excitation at 270

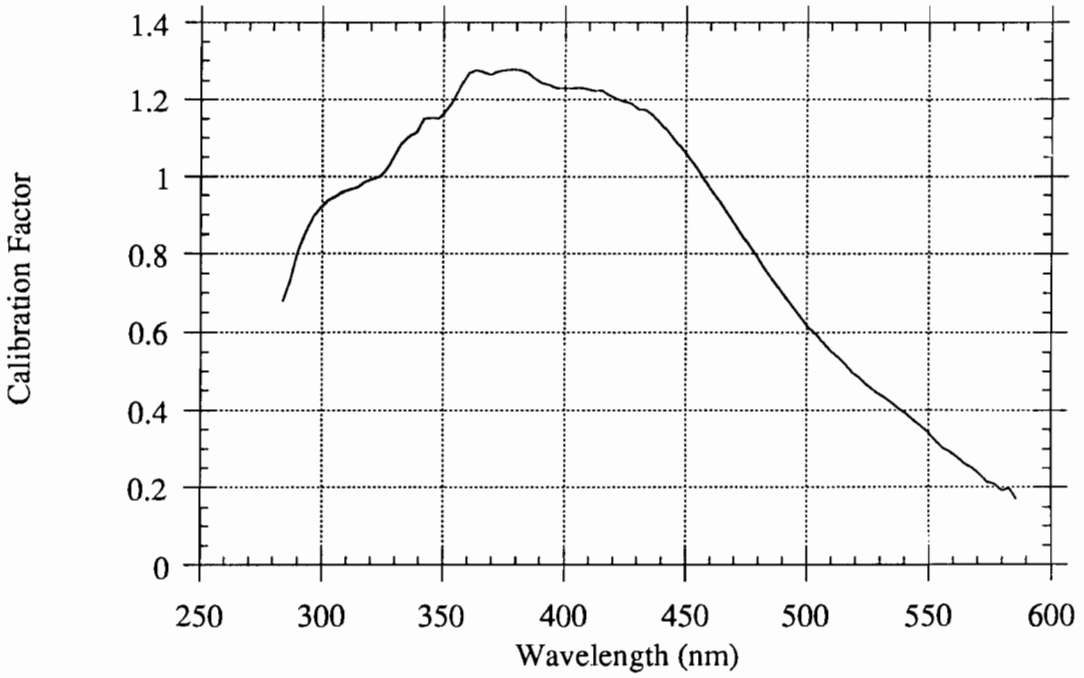

Figure 5.11. Calibration curve for the LS50. This figure shows the correction factor $S(\lambda)$, as defined in eq 5.4. The calibration curve was obtained by comparing corrected spectra of QBS, PPO, and pseudocumene in the literature[4,12] with spectra obtained using the LS50. See Appendix 5.I for more details on the calibration.

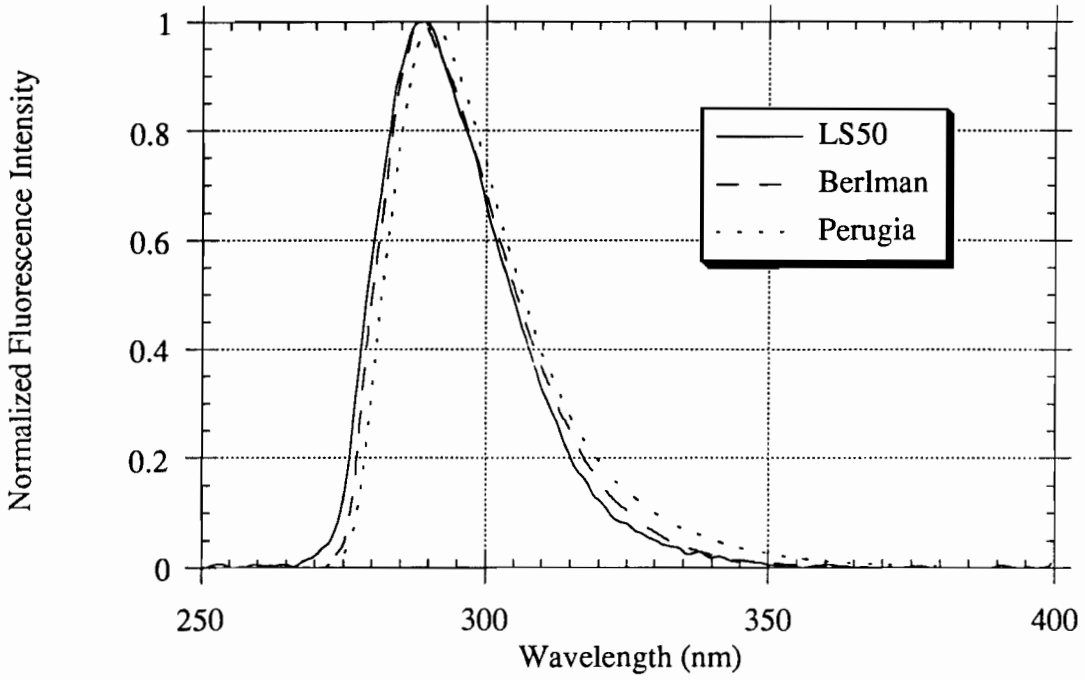

Figure 5.12. Emission spectrum of pseudocumene. The figure shows normalized emission spectra of pseudocumene as measured using the LS50 and as reported by Perugia[3] and Berlman.[4] In all cases, the emission spectrum was obtained from a dilute solution of pseudocumene in cyclohexane. The LS50 measurements were made using a 2.3×10^{-4} M solution of pseudocumene in cyclohexane. Excitation was at 270 nm, and a 1 cm cuvette was employed. The bandpass of the excitation monochromator was 5.0 nm and the bandpass of the emission monochromator was 2.5 nm.

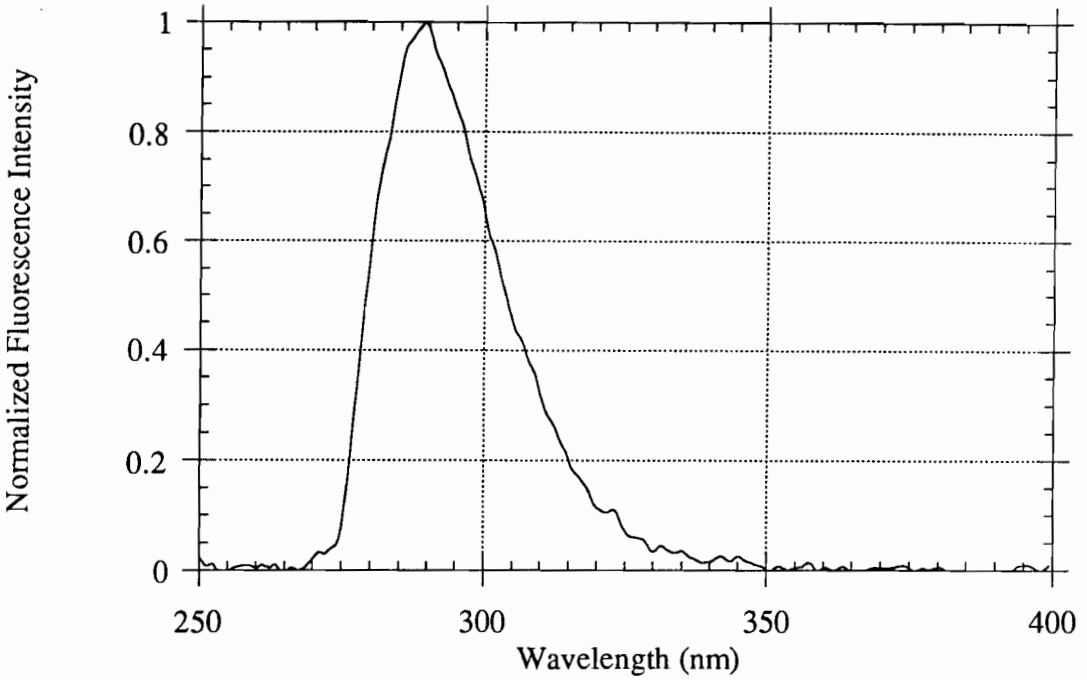

Figure 5.13. Emission spectrum of PXE. The figure shows a normalized emission spectrum of PXE as measured using the LS50. The emission spectrum was obtained from a dilute solution of PXE (3.2×10^{-4} M) in cyclohexane. Excitation was at 270 nm, and a 1 cm cuvette was employed. The bandpass of the excitation monochromator was 5.0 nm and the bandpass of the emission monochromator was 2.5 nm.

nm. PXE emission was studied at Perugia,[7,8] but no acceptable spectra were recorded because of fluorescent impurities in the PXE. The data in Figures 5.12 and 5.13 were collected with an excitation monochromator bandpass of 5.0 nm and an emission monochromator bandpass of 2.5 nm.

PPO emission spectra are plotted in Figures 5.14 and 5.15. In Figure 5.14, the PPO is in a cyclohexane solution; in Figure 5.15 it is in a pseudocumene solution. Excitation was at 320 nm in both cases. The spectrum taken with the cyclohexane solution shows more resolution. Resolution is lost in the pseudocumene solution due to vibronic coupling which occurs between the two aromatic species. A spectrum from Berlman[4] is shown in Figure 5.14, and data from the Perugia group[3] are included in Figure 5.15. In both figures, the LS50 results agree well with those from other sources. A bandpass of 2.5 nm for both the excitation and emission monochromators was used to obtain the LS50 data in Figures 5.14 and 5.15.

Figures 5.16 and 5.17 show emission spectra of bis-MSB dissolved in cyclohexane and pseudocumene, respectively. Excitation was at 345 nm. Data from Berlman[4] are shown in Figure 5.16 for comparison, and data from Perugia[7] are included in Figure 5.17. The Berlman and Perugia results again agree well with those recorded using the LS50. The data in Figures 5.16 and 5.17 were collected with an excitation and emission monochromator bandpass of 2.5 nm.

The spectra reported above were all measured using an excitation wavelength at the peak absorption of the compound under study. The effect of variation in the excitation wavelength was also studied. Wavelengths shorter than that of peak absorption resulted in no noticeable change in the emission spectra. The ability to excite the samples at shorter wavelengths was limited by the absorption bands of the solvents. A pseudocumene solvent limited the excitation wavelength to values of greater than 300 nm, while cyclohexane allowed excitation down to 230 nm.

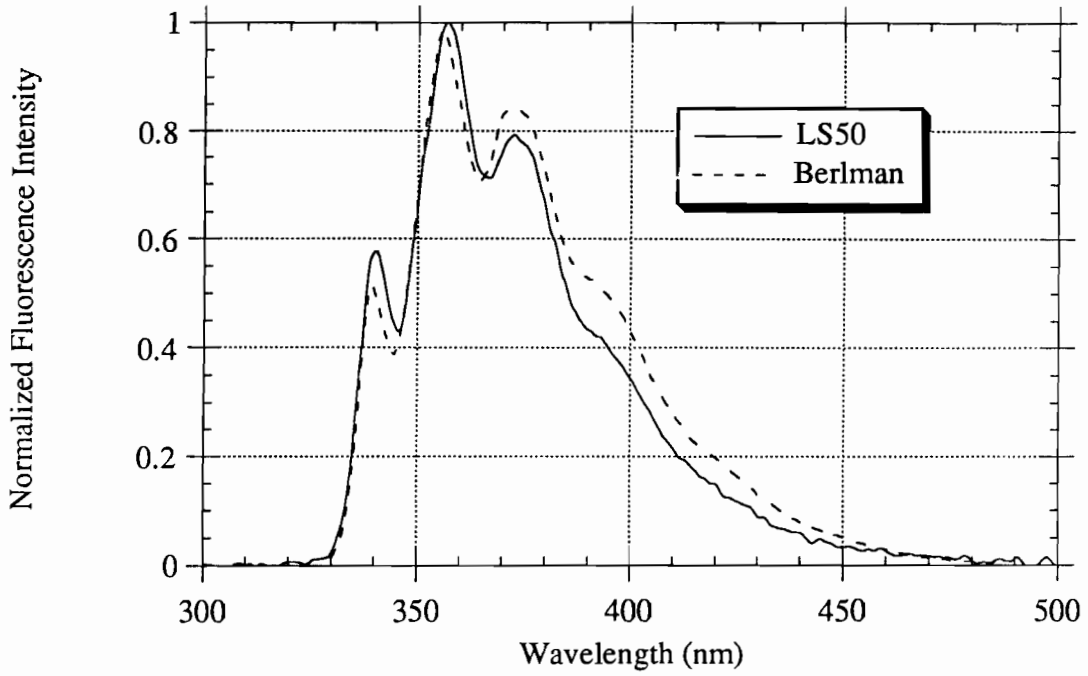

Figure 5.14. Emission spectrum of PPO in cyclohexane. The figure shows normalized emission spectra of PPO as measured using the LS50 and as reported by Berlman.[4] The emission spectra were obtained from dilute solutions of PPO in cyclohexane. The LS50 measurements were made using a 1.1×10^{-5} M solution of PPO in cyclohexane. Excitation was at 320 nm, and a 1 cm cuvette was employed. The bandpass of the excitation and emission monochromators was 2.5 nm.

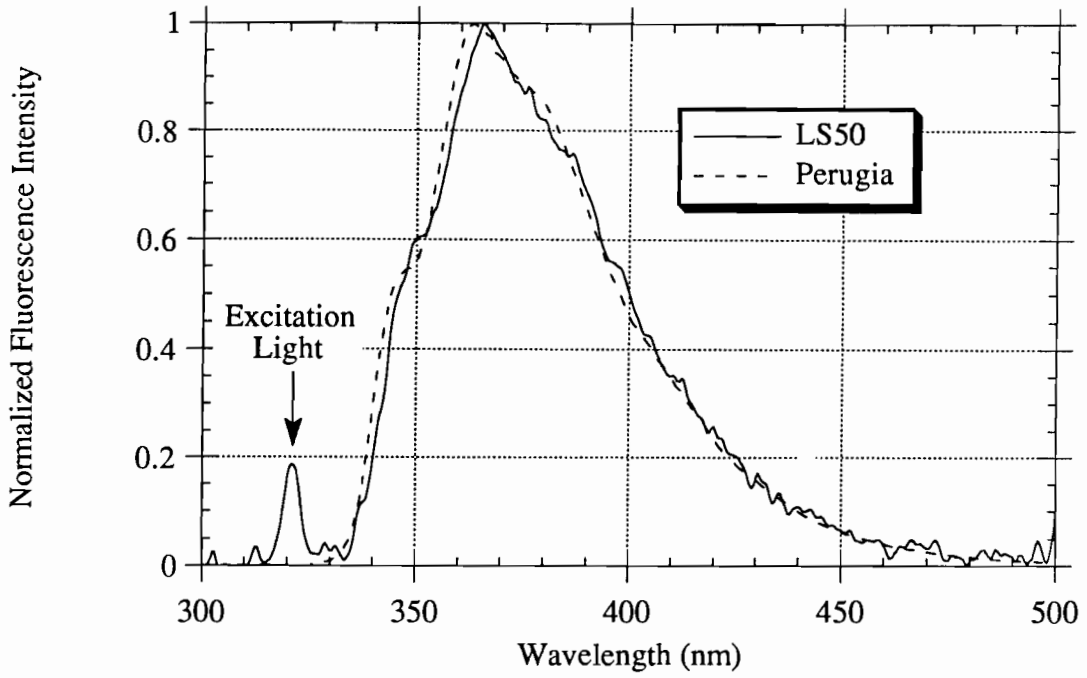

Figure 5.15. Emission spectrum of PPO in pseudocumene. The figure shows normalized emission spectra of PPO as measured using the LS50 and as reported by Perugia.[3] The emission spectra were obtained from dilute solutions of PPO in pseudocumene. Less resolution is seen in these spectra than in those of Figure 5.14. The resolution is decreased because there is greater vibronic coupling between PPO and pseudocumene than between PPO and cyclohexane. The LS50 measurements were made using a 4.7×10^{-6} M solution of PPO in pseudocumene. Excitation was at 320 nm, and a 1 cm cuvette was employed. The bandpass of the excitation and emission monochromators was 2.5 nm. The peak at 320 nm (marked with an arrow) is due to stray excitation light which escaped from the cuvette.

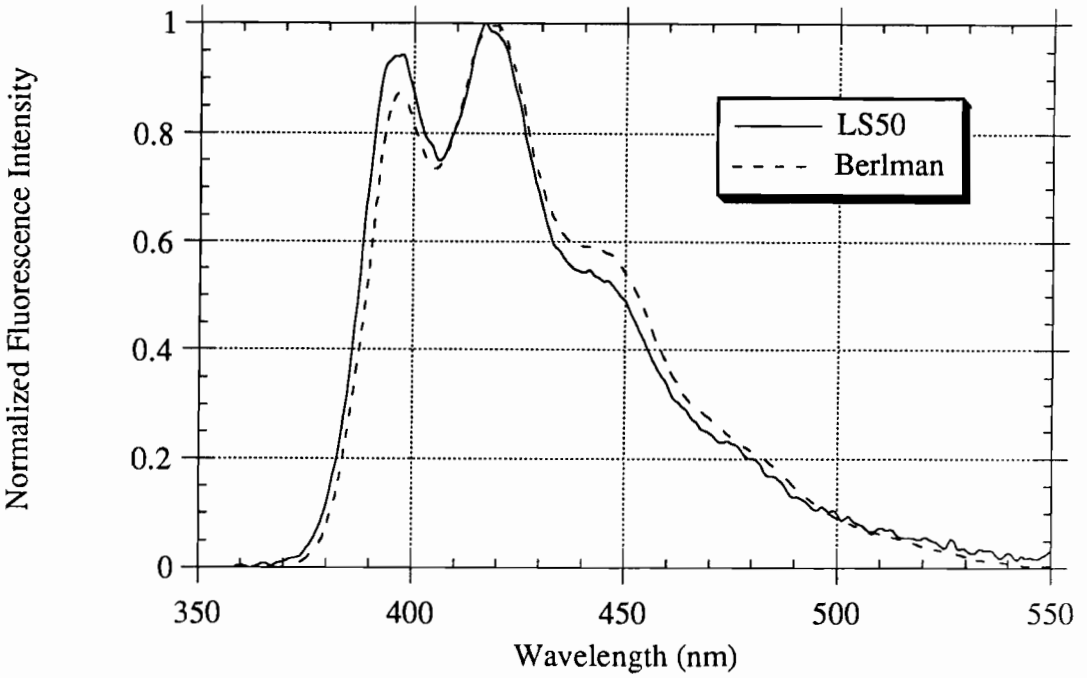

Figure 5.16. Emission spectrum of bis-MSB in cyclohexane. The figure shows normalized emission spectra of bis-MSB as measured using the LS50 and as reported by Berlman.[4] The emission spectra were obtained from dilute solutions of bis-MSB in cyclohexane. The LS50 measurements were made using a 5.2×10^{-6} M solution of bis-MSB in cyclohexane. Excitation was at 345 nm, and a 1 cm cuvette was employed. The bandpass of the excitation and emission monochromators was 2.5 nm.

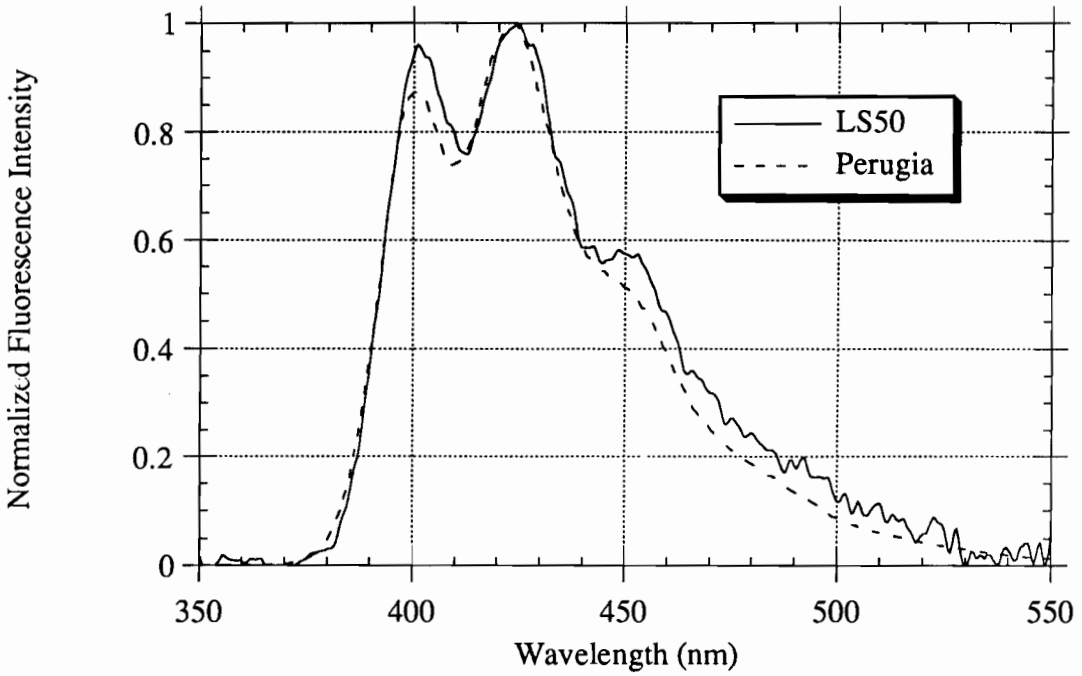

Figure 5.17. Emission spectrum of bis-MSB in pseudocumene. The figure shows normalized emission spectra of bis-MSB as measured using the LS50 and as reported by Perugia.[3] The emission spectra were obtained from dilute solutions of bis-MSB in pseudocumene. The LS50 measurements were made using a 2.0×10^{-6} M solution of bis-MSB in pseudocumene. Excitation was at 345 nm, and a 1 cm cuvette was employed. The bandpass of the excitation and emission monochromators was 2.5 nm.

Excitation at longer wavelengths also had no measurable effect when the wavelength was still within the main absorption band of the compound (up to 280 nm for pseudocumene, 350 nm for PPO, and 415 nm for bis-MSB).

It was of great interest to examine the fluorescence behavior of the compounds when the excitation wavelength was outside the main absorption band (at longer wavelengths) because of the applicability of this knowledge to the modeling of absorption-reemission scattering. The excitation of PPO at 360 nm is an example of a study of this kind. The results from these attempts were inconclusive. At the longer wavelengths, absorption is very small. A high concentration is necessary so that enough absorption takes place to produce a measurable emission signal. At high concentrations, self-absorption effects are large enough to eliminate any emission of wavelengths shorter than the excitation wavelength. In these tests, no emission below the excitation wavelength was observed, but it was not possible to determine whether this was because no emission occurred at these wavelengths or because the emission was produced and absorbed. A more sensitive instrument than the LS50 might allow the use of lower concentrations and eliminate the self-absorption problem.

2. Quenching Measurements

In Chapter 4, the ability of some compounds to quench the fluorescence emission of scintillators was discussed. Normally such quenching is undesirable, and quenchers played no role in the CTF. The intentional use of quenchers is under consideration for Borexino. Because of this, the effect of some quenchers on scintillation light output was studied using the LS50.

In Borexino, the scintillator containment vessel is to be surrounded by a pure pseudocumene buffer. Although neat pseudocumene is a very poor scintillator, there is some concern that light emission caused by events in the buffer will add an unacceptable background to the detector. In order to provide a margin of safety

against such a background, the addition of a quencher to the pseudocumene buffer is being considered. A quencher would induce almost all of the excited pseudocumene molecules to relax nonradiatively, and reduce buffer scintillation to a negligible amount.

Although more detailed quenching studies were carried out by other collaboration members,[14] some preliminary work in the field was done with the LS50. The quenching effects of several compounds were examined. These included pyridine, 1-picoline, acetone, bromobenzene, and di-pyridyl. The quenching effects of gaseous oxygen were also studied. In order to accurately judge the efficiency of the various quenchers, it was necessary to prepare solutions of them in pseudocumene; dilutions of pseudocumene in cyclohexane were not useful because the dilution added complications to the interpretation of the results.

An excitation wavelength of 290 nm was employed in the quencher studies. The pseudocumene samples were not excited at their absorption peak of 270 nm because excitation light of this wavelength did not penetrate far enough into the 1 cm cuvettes to cause a measurable emission signal. The use of 290 nm excitation allows an emission spectrum to be measured for pseudocumene samples. This wavelength is not in the main pseudocumene absorption band, and the long wavelength excitation may introduce complications which interfere with determination of the quenching activity. The pseudocumene solutions exhibited self-absorption of fluorescence, and the spectra recorded with pure pseudocumene were quite distorted from the actual pseudocumene emission spectrum. (Compare Figures 5.18 and 5.20 to see this distortion.) Despite these difficulties, the LS50 measurements were useful in establishing the relative quenching efficiencies of various compounds.

The emission spectrum of pure oxygen-free pseudocumene excited at 290 nm is shown in Figure 5.18 along with a spectrum from unsparged pseudocumene. The

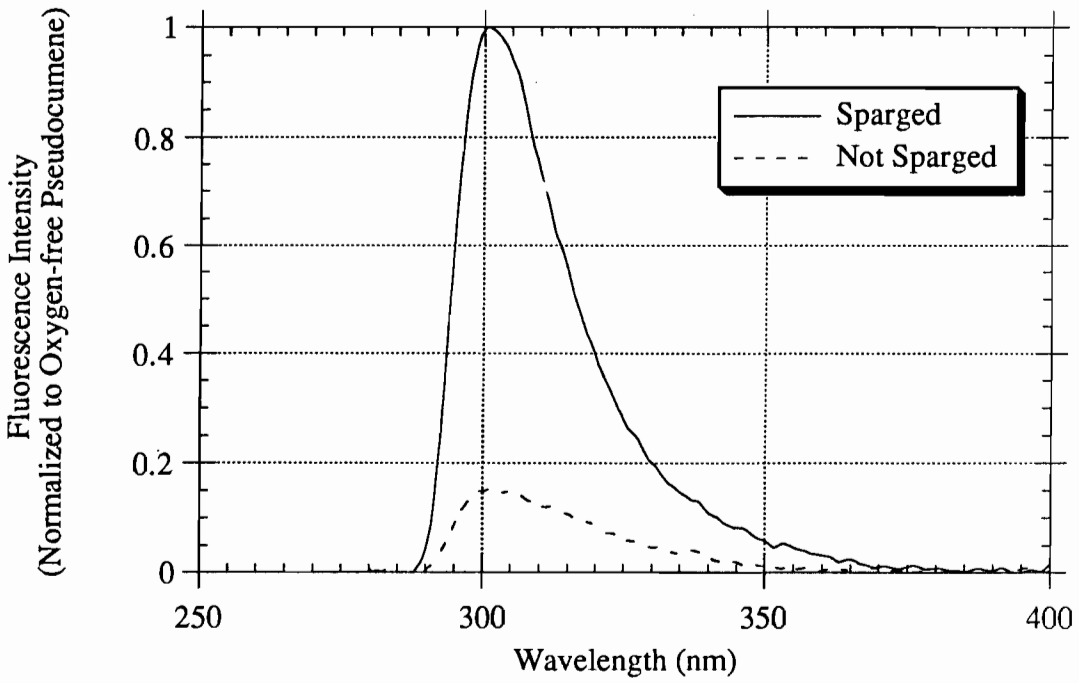

Figure 5.18. Neat pseudocumene emission spectra. Two emission spectra of pure pseudocumene are shown in the figure. One was recorded before nitrogen sparging and the other was recorded after sparging. Excitation was at 290 nm. The quenching effect of oxygen is very noticeable; the emission intensity is reduced by a factor of 5.5. The emission spectrum is distorted from that seen in Figure 5.12 due to self-absorption of fluorescence by the pseudocumene. The bandpass of the excitation and emission monochromators was 5.0 nm.

oxygen reduces the integrated emission intensity by a factor of approximately 5.5. Figure 5.19 shows spectra from sparged pseudocumene solutions containing 0.1, 0.3, and 0.5% of pyridine by volume. At these concentrations, the pyridine quencher reduces the integrated emission intensity by a factor of 4, 5, and 13, respectively. The other quenchers which were studied provided a quenching effect of similar magnitude when they were added to pseudocumene at the g/L level.

The quenching measurements made with the LS50 were adequate for establishing relative quenching efficiencies, but they were not useful for the determination of any quenching rate parameters because of the long wavelength excitation and the fluorescence self-absorption. Emission spectra of pseudocumene in cyclohexane following excitation at 270 nm are shown in Figure 5.20 before and after nitrogen sparging. The oxygen quenching reduces the integrated emission intensity by a factor of 2.4. This quenching factor agrees well with the oxygen quenching factor determined from decay time measurements (Section 5.C), but differs from that of 5.5 found when pure pseudocumene was excited at 290 nm. This discrepancy indicates that the measurements with 290 nm excitation are not quantitatively accurate, and that they should only be used to judge the relative effectiveness of different quencher candidates.

3. Quantum Yield Determinations

The LS50 was also used to determine the fluorescence quantum yields of several scintillator components. Quantum yields were determined for pseudocumene, PXE, PPO, and bis-MSB. The quantum yield of a species , as discussed in Chapter 4, is the ratio of the number of excited molecules of that species which relax by fluorescent emission to the total number of excited molecules. The accurate measurement of quantum yields is an exacting task. Relative quantum yield measurements are reported in this thesis. Corrected emission spectra were obtained

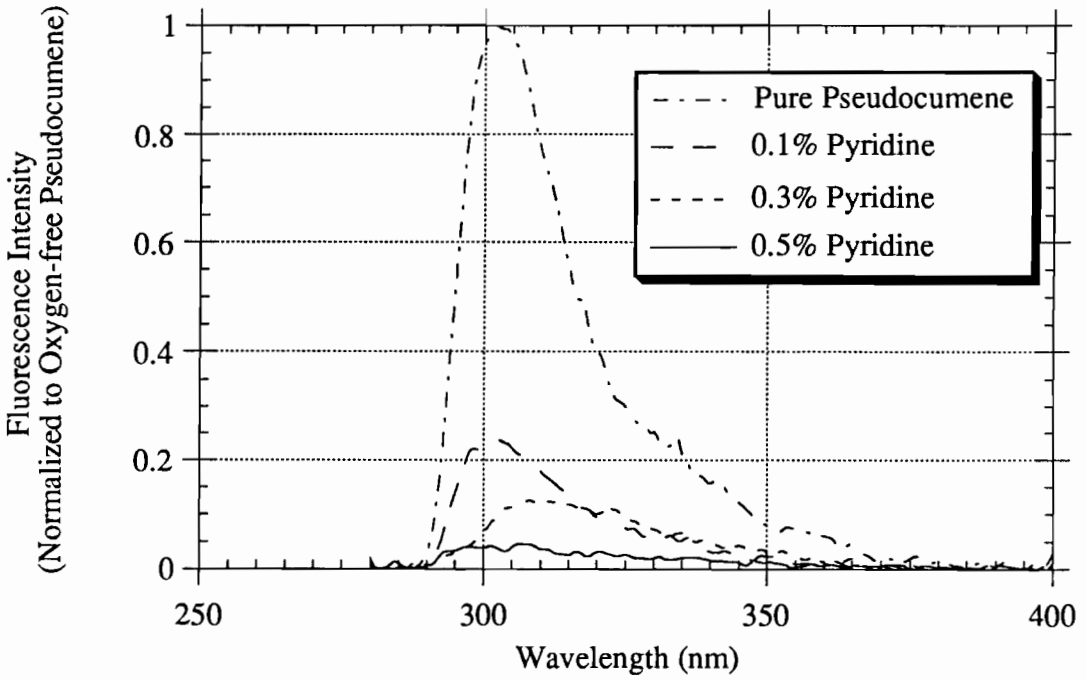

Figure 5.19. Quenching of pseudocumene by pyridine The spectra in this figure were recorded for neat pseudocumene with pyridine dissolved in it at a concentrations of 0.1, 0.3, and 0.5% (by volume). A spectrum from pure pseudocumene is included for reference. Excitation was at 290 nm. The pyridine reduces the pseudocumene emission intensity by factors of 4, 5, and 13, respectively. The bandpass of the excitation and emission monochromators was 5.0 nm.

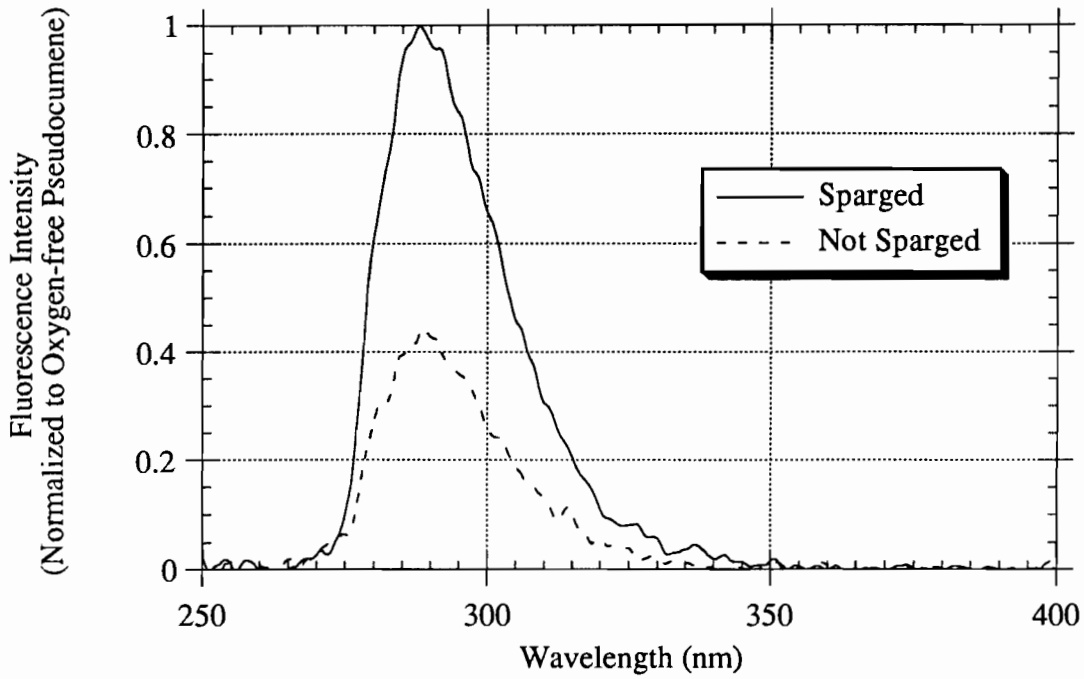

Figure 5.20. Oxygen quenching of pseudocumene. Emission spectra from a dilute solution of pseudocumene in cyclohexane (2.3×10^{-4} M) are shown here. One spectrum was recorded prior to nitrogen sparging and the other was recorded after sparging. Excitation was at 270 nm. The true pseudocumene emission spectrum is shown in this figure, and the oxygen quenching factor of 2.4 caused by equilibration of the sample with air is evident. The bandpass of the excitation and emission monochromators was 5.0 nm.

for the sample compounds of interest and a for standard with a known quantum yield using the same excitation wavelength. The quantum yield of the sample is related to the quantum yield of the standard by[2,15,16]

$$q = \frac{q_s D_s F}{D F_s}\left(\frac{n}{n_s}\right)^2 \qquad (5.5)$$

where q is the quantum yield of the sample, q_s is the quantum yield of the standard, D and D_s are the optical densities of the sample and the standard at the excitation wavelength in cm^{-1}, F and F_s are the integrated emission intensities of the sample and the standard, and n and n_s are the refractive indices of the sample and standard solutions. Previous research[17] has indicated that it is necessary to account for the refractive indices of the solutions because different refractive indices cause different changes in the direction of light at the cuvette surface. A larger sample refractive index results in greater bending of the emitted light as it leaves the cuvette, and less photons travel in the direction of the detector.

The use of dilute samples is desirable for quantum yield determinations because the self-absorption and concentration quenching which occur at higher concentrations can interfere with the measurement of the true molecular quantum yield. The LS50 is well suited for quantum yield measurements because it performs most accurately with dilute samples. The inner filter effect described earlier can also be important in quantum yield calculations. The formula given in eq 5.3 was used to calculate correction factors for the integrated emission intensities. The distances 0.1 cm and 0.9 cm were used for d_1 and d_2 in eq 5.3. The optical densities of the sample and the standard were measured with an absorption spectrophotometer just prior to the collection of the emission spectra.

Quinine bisulfate in an aqueous solution of 0.1 N H_2SO_4 was chosen as the fluorescence quantum yield standard. This compound was chosen for several reasons: Its quantum yield has been carefully measured and confirmed by several researchers.[11]

Its emission spectrum has been measured carefully; it is also used as a calibration standard for emission spectra. Quinine bisulfate is not quenched by oxygen, it does not exhibit much concentration quenching, and it is stable for long periods of time. It has a quantum yield of 0.51 at a concentration of 5×10^{-3} M, and the quantum yield increases to 0.55 at infinite dilution. Quinine bisulfate solutions with concentrations from 3.94×10^{-5} to 1.97×10^{-4} M were used here as quantum yield standards.

Several quantum yield results determined with data from the LS50 are listed in Table 5.1. The quantum yield of pseudocumene in a cyclohexane solution was calculated at excitation wavelengths of 230, 270, and 280 nm for samples containing oxygen and for samples which had been sparged. In all cases, the removal of oxygen increased the quantum yield by more than a factor of two. The quantum yields at excitation wavelengths of 270 and 280 nm are quite similar, while the yield following excitation at 230 nm is slightly lower. The quantum efficiency for emission decreases when singlet states above S_1 are excited.

Quantum yields were also determined for PXE in cyclohexane solution with excitation at 230, 270, and 280 nm. Oxygen removal again increased the quantum yield by more than a factor of 2. PXE has a slightly lower quantum efficiency than pseudocumene. The quantum efficiency of PXE remained almost constant as the excitation wavelength was changed.

Quantum yields were also measured for the fluors PPO and bis-MSB. Results for these fluors in pseudocumene and cyclohexane solutions are shown in Table 5.1. The quantum yields were measured both before and after sparging to remove oxygen. The PPO was excited at 320 nm and the bis-MSB at 345 nm. The absorption plots in Figures 5.5 – 5.7 show that the main absorption bands for these fluors extend to 250 nm or below. This makes it impossible to excite them in any other absorption band because of solvent absorption at the shorter wavelengths. No change in the emission

Table 5.1. Quantum yields of scintillator components. The quantum yields listed here are based on measurements using the LS50 instrument as described in the text. All results are based on comparison with a QBS quantum yield standard. The quantum yields both before and after nitrogen sparging to remove oxygen are listed here for four compounds. The solvent and excitation wavelength for each trial are also recorded.

Compound	Solvent	Excitation Wavelength (nm)	Quantum Yield (with O_2)	Quantum Yield (after sparging)
Pseudocumene	Cyclohexane	270	0.16	0.37
		280	0.17	0.38
		230	0.10	0.26
PXE	Cyclohexane	270	0.12	0.30
		280	0.11	0.27
		230	0.10	0.26
PPO	Cyclohexane	320	0.63	0.71
	Pseudocumene	320	0.68	0.80
bis-MSB	Cyclohexane	345	0.67	0.75
	Pseudocumene	345	0.61	0.65

spectrum of either compound was seen when the excitation wavelength was varied within the first absorption band. This indicates that the quantum yield of PPO is constant from 250 – 340 nm, and that of bis-MSB is constant from 250 – 400 nm. Oxygen removal makes less of a difference for the fluors than for the two solvents discussed previously. The fluors have a shorter decay time, providing less opportunity for quenching. The quantum efficiencies of the two fluors after sparging show a large variation upon change of solvent. PPO shows a higher quantum yield in pseudocumene than in cyclohexane, while bis-MSB displays the opposite trend. The quantum yield values in Table 5.1 should be considered accurate to within ± 15%.

The quantum yields measured here are in good agreement with other reported values. The Perugia group[18] found values of 0.80 for PPO, 0.75 for bis-MSB, and 0.35 for pseudocumene in deoxygenated solutions. Berlman[4] has reported higher quantum yields for all three compounds, but his results have been criticized by Birks[15,19] because he used the wrong quantum yield value for his standard. Other literature values[20,21,22] (see Chapter 4) are similar in magnitude to the Perugia results.

In the study of absorption-reemission scattering, it would be useful to know if the quantum yields of the scintillator components change at long excitation wavelengths. The measurements in Table 5.1 show that the quantum yields of pseudocumene and PXE do not change appreciably when the excitation changes from 270 to 280 nm. These wavelengths are both in the main absorption band, however, and no change in quantum yield would be expected. PPO and bis-MSB were also found to have a constant quantum yield within the main absorption band. As mentioned in Section 5.B.1, it was impossible to obtain emission spectra at the long wavelengths of interest. This precluded determination of the quantum yield at these longer wavelengths. A more sensitive spectrophotometer might make this determination possible.

C. Decay Time Measurements

Knowledge of the fluorescence decay times of the scintillator components is necessary for a good understanding of absorption-reemission scattering. An apparatus for measuring fluorescence decay times was assembled at Princeton. Excitation of the sample is provided by a dye laser pumped by a nitrogen laser. Fluorescence from the sample travels through a double monochromator and impinges on a multi-channel plate-photomultiplier tube (MCP-PMT). The output of the MCP-PMT is connected to a SCD5000 transient digitizer. The time responses of all the system components are less than 1 ns and allow a direct measurement of the fluorescence decay from the sample. The signal is averaged over many excitation cycles (100 – 1000) to reduce the noise in the data.

The nitrogen laser is a PTI Lasers, Inc., PL2300. It lases at 337.1 nm, produces a maximum average power of 56 mW, and has a maximum energy per pulse of 2.8 mJ. A laser pulse shape as recorded by the MCP-PMT is shown in Figure 5.21. From beginning to end, the pulse is approximately 4 ns long, with a full width at half maximum (FWHM) of close to 0.8 ns. This pulse was recorded by reflecting the laser beam towards (but not at) the monochromator slit and observing the pulse at a wavelength approximately 5 nm away from the laser wavelength. The full intensity of the laser pulse would damage the MCP-PMT.

The dye laser is a PTI Lasers, Inc., PL202 and it is pumped by the nitrogen laser. A schematic diagram[23] of the dye laser is shown in Figure 5.22. Two dye cuvettes are present in the dye laser: a lasing cuvette and an amplifier cuvette. The nitrogen laser beam is split as it enters the dye laser. One part of the beam excites the lasing cuvette which sits in a tunable laser cavity. This cavity can be tuned using a monochromator to select the wavelength at which the dye will lase. The light output from the lasing cuvette is reflected onto the amplifier cuvette. The other part of the

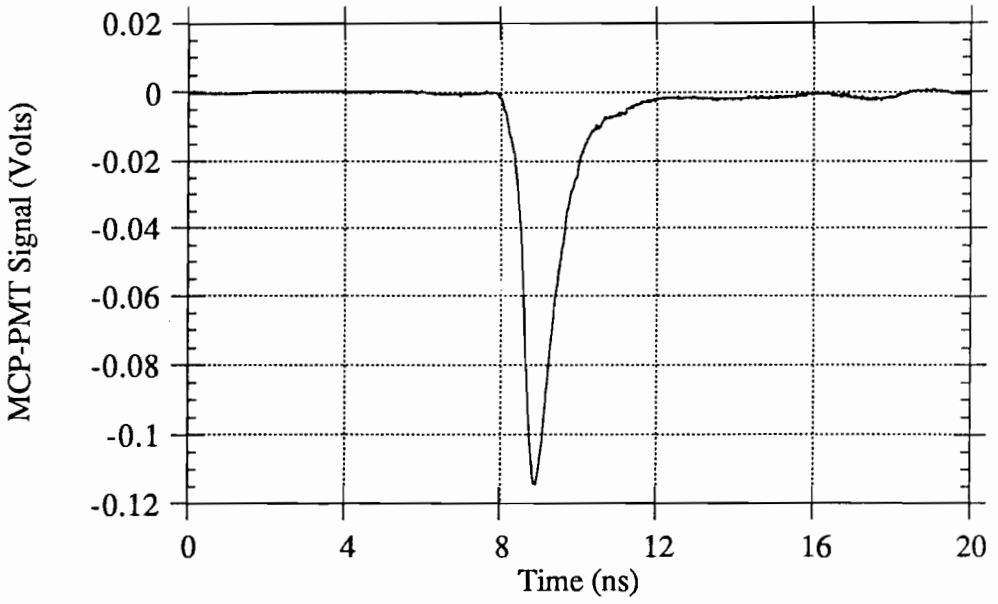

Figure 5.21. Laser pulse shape from the PL2300. This figure shows the time structure of the nitrogen laser pulse. It was recorded by reflecting the laser beam toward the slit of the double monochromator when the monochromator was set at a wavelength 5 nm from that of the light coming from the laser. Enough stray light made it through the monochromator to provide a signal to the MCP-PMT. The laser pulse has a FWHM of approximately 0.8 ns. There is a tail of the pulse which extends almost 4 ns past the time of the peak amplitude.

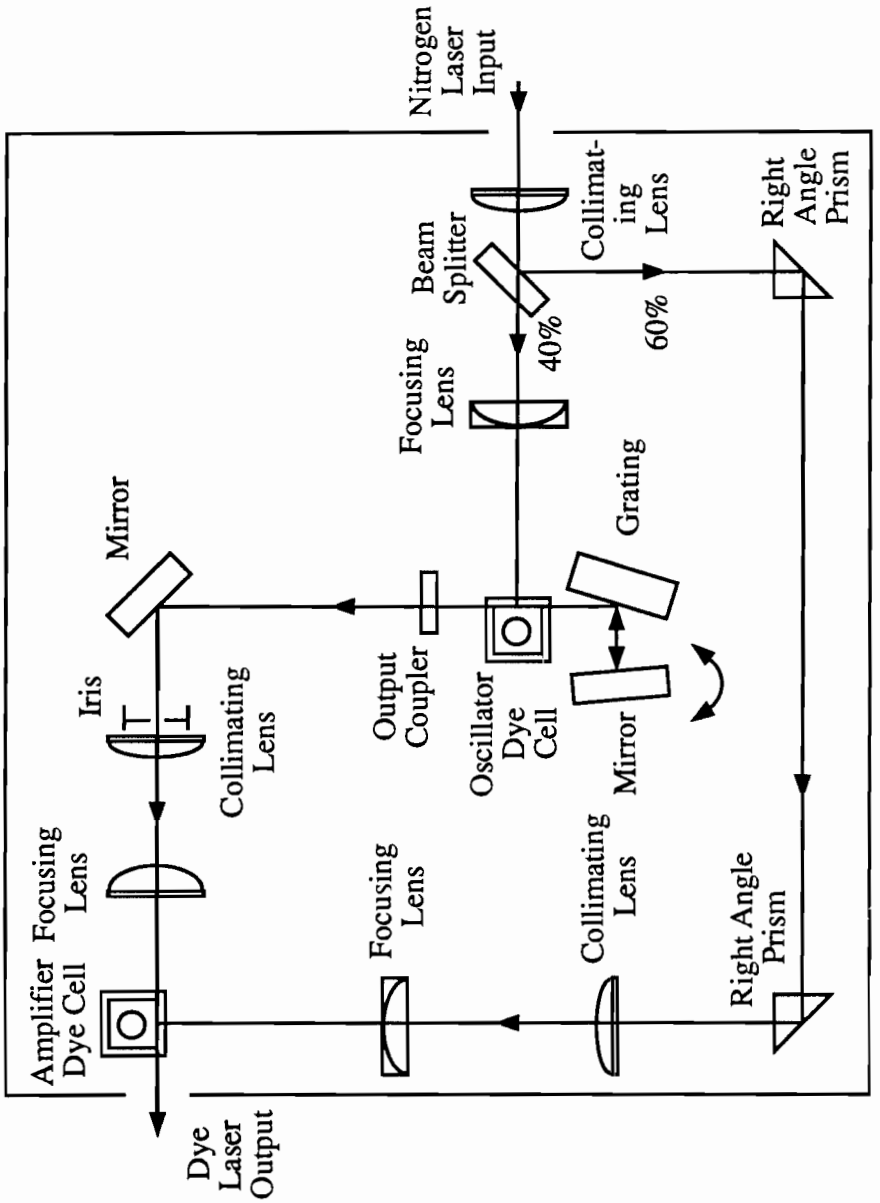

Figure 5.22. Schematic diagram of the PL202 dye laser. Light from a nitrogen laser pumps the fluorescent dye in the two cuvettes in this dye laser. One cuvette is the lasing cuvette, and the other serves as an amplifier. The wavelength of the light from the dye laser can be adjusted by rotating a mirror which directs the dye output towards a grating near the lasing cuvette.

nitrogen laser beam is also directed to this second cuvette. This cuvette serves to amplify the intensity of the dye laser pulse.

The laser dyes only lase over a small range of wavelengths, and this reduces the tunability of the system. In addition, the wavelength of light coming out of the dye laser is not always that which is set on the monochromator. In some cases, the dye continues to lase at the same wavelength regardless of the monochromator setting, until the setting is changed enough so that the dye does not lase at all. The actual wavelength of light from the dye laser must be determined by using the double monochromator and the MCP-PMT. The dye laser often emits polychromatic light, and wavelength spreads of 10 nm have been measured.

Almost all laser dyes emit light with a wavelength of 360 nm or longer. (They must emit at wavelengths longer than 337 nm in order to be pumped with a nitrogen laser.) In order to obtain shorter wavelengths, a frequency doubling crystal is used after the dye laser. Light at wavelengths from 276 to 293 nm have been obtained in this manner. A filter is placed after the doubling crystal to block the dye laser light which passes through the doubling crystal without being doubled. The configuration of the apparatus is shown in Figure 5.23.

A trigger signal for the SCD5000 was obtained from the laser pulses with the use of a light sensitive diode. In order to obtain this trigger signal, a small part of the laser pulse was scattered toward the diode. A delay cable was needed in the transmission of the MCP-PMT signal to the SCD5000. This was required so that the transient digitizer was ready to receive the MCP-PMT data when it arrived. The cable was approximately 30 feet long.

A mechanism was developed to remove oxygen from the samples. A syringe needle was inserted through a small hole drilled in the cuvette cap. This allowed nitrogen sparging of the sample as it sat in the laser beam line. After sparging, the

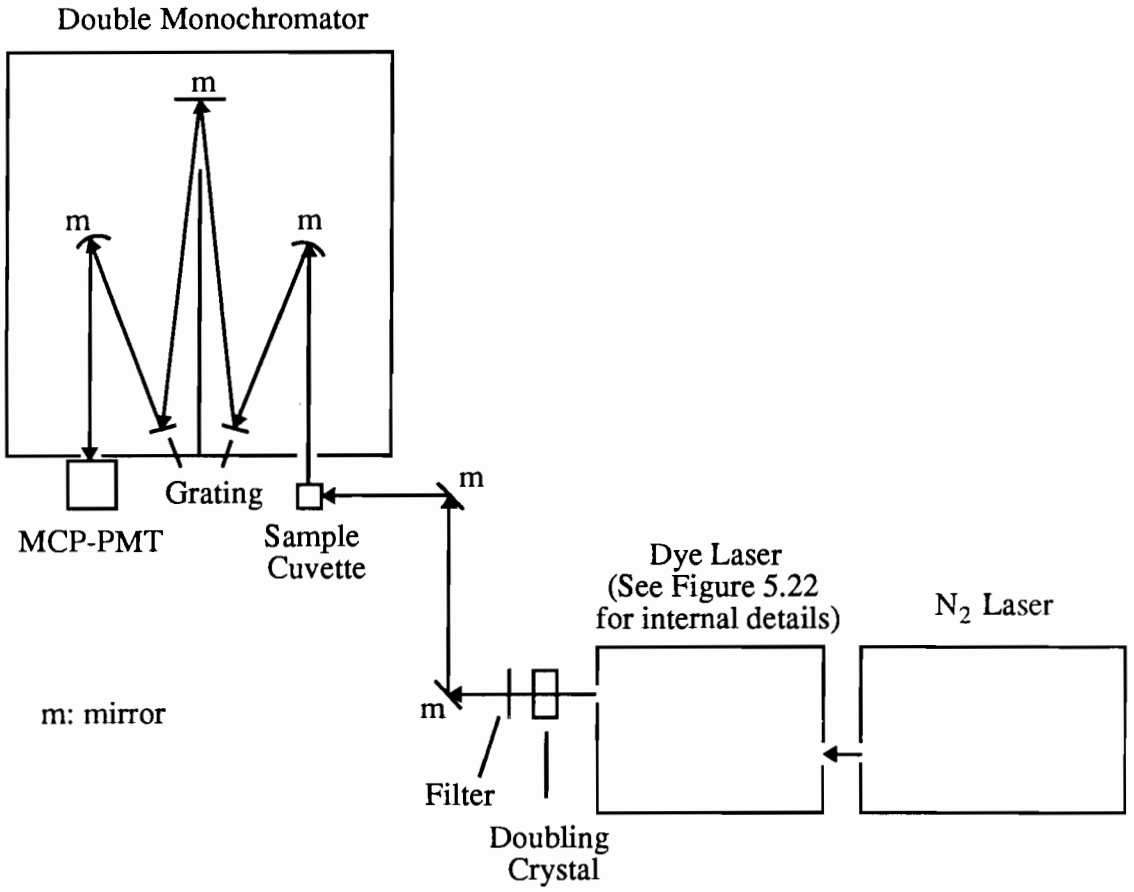

Figure 5.23. Apparatus for decay time measurement. The arrangement of the nitrogen laser, the dye laser, the sample cuvette, and the double monochromator during the decay time measurements is shown here.

needle was retracted from the liquid, but it was maintained in a position to purge the gas above the liquid in the cuvette. Effective oxygen removal was obtained within 10 minutes if the needle was maneuvered inside the cuvette during sparging to promote good mixing.

Fluorescence decay data were collected for several samples. Three different excitation wavelengths were used: 337.1 nm directly from the nitrogen laser, 292.5 nm from frequency doubled Rhodamine 6G emission, and 276.5 nm from frequency doubled Coumarin dye emission. Only one emission wavelength could be monitored per trial. The emission was usually monitored near the peak emission wavelength of the sample: 300 nm for pseudocumene and 365 nm for PPO. Additional trials were sometimes carried out at alternative emission wavelengths.

The decay curves were corrected for an electronic noise background. By recording a decay curve when the light path to the sample cuvette was blocked, a background curve was obtained. This was subtracted from the raw decay curve to obtain the true decay curve. A raw decay curve, a background curve, and the corrected decay curve can be seen in Figure 5.24 for a solution of 1.5 g/L of PPO in pseudocumene following excitation at 337 nm. The emission was monitored at 365 nm.

Pure pseudocumene was excited at 276.5 and 292.5 nm. The excitation light of 276.5 nm did not penetrate far into the cuvette, but an emission signal was obtained by aligning the front edge of the cuvette with the emission monochromator slit. The excitation beam of 292.5 nm penetrated through the whole cuvette. Nitrogen sparging had a large effect on the decay curves of the pseudocumene samples. Pseudocumene decay curves before and after sparging can be seen in Figure 5.25, and the increase in decay time after oxygen removal can be easily seen by visual inspection.

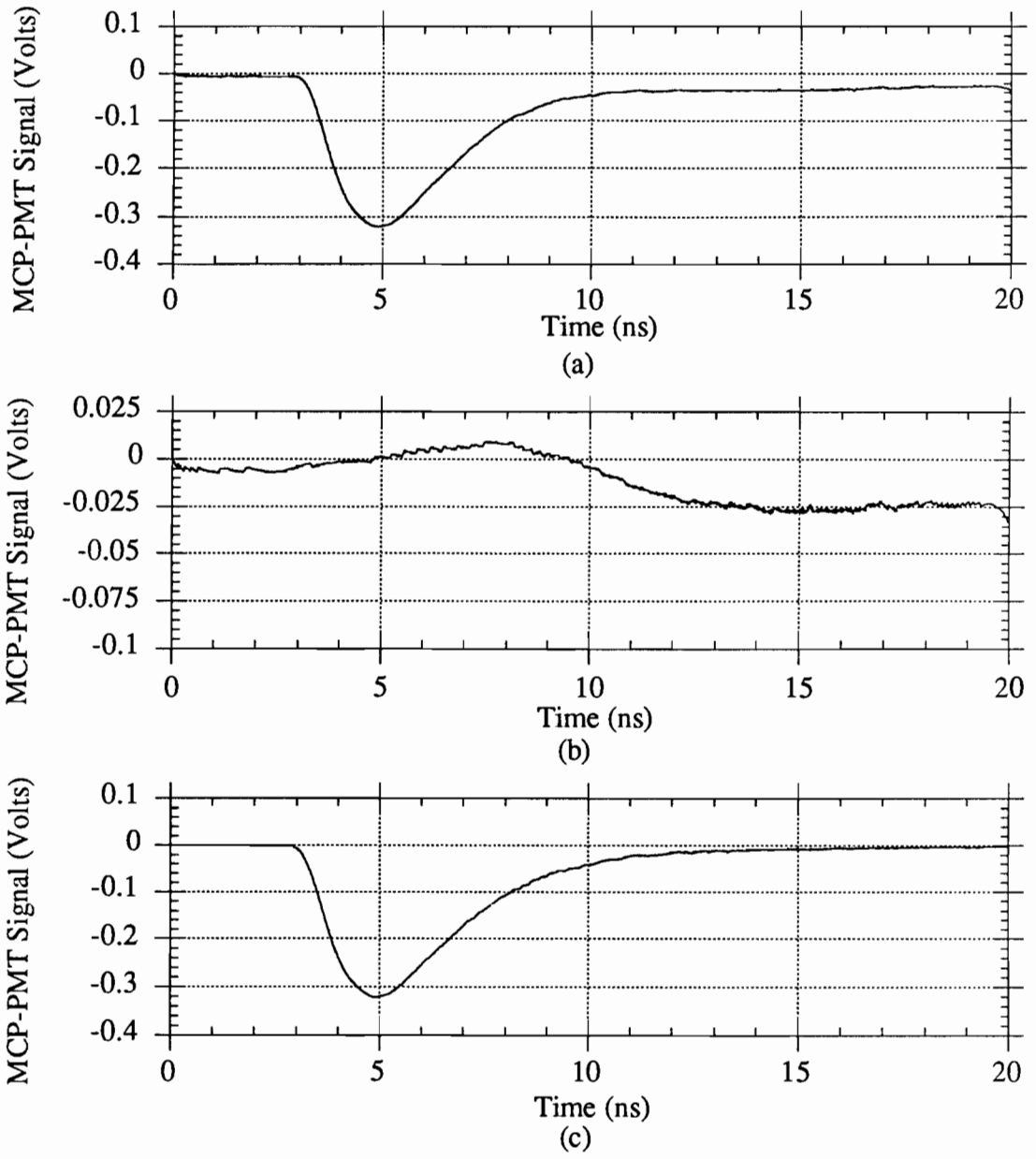

Figure 5.24. Raw decay curve, background curve, and corrected decay curve for PPO. a) A signal curve produced by the MCP-PMT following excitation of 1.5 g/L of PPO in pseudocumene at 276.5 nm. Emission was monitored at 365 nm. b) An electronic background curve recorded when no light reached the MCP-PMT. Note the change in the y-scale here. c) A corrected decay curve obtained by subtracting the background from the raw decay curve.

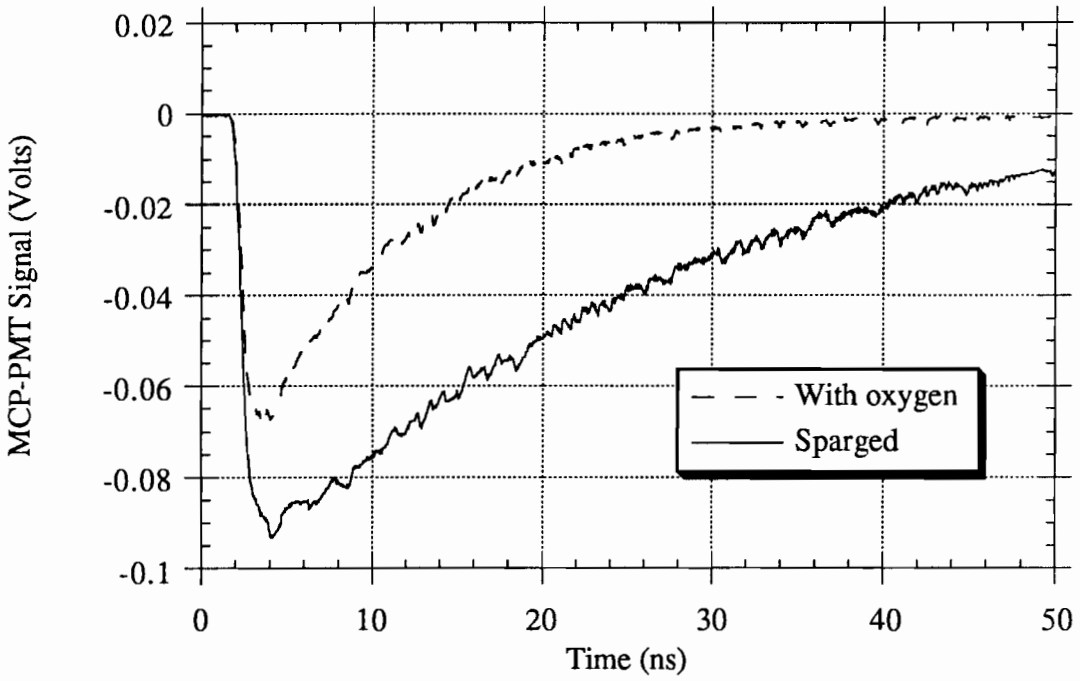

Figure 5.25. Fluorescence decay curves of pseudocumene. Fluorescence decay curves for neat pseudocumene before and after nitrogen sparging are shown here. The increase in the lifetime of the solvent after nitrogen sparging can be seen clearly. The fluorescence intensity is also smaller in the unsparged sample. These pseudocumene was excited at a wavelength of 276.5 nm and its emission was monitored at 300 nm.

In order to quantify the decay time results for pseudocumene, exponential decay functions were fitted to the corrected experimental decay curves. Only data points 4 ns or more after the emission peak were considered in the fitting procedure in order to avoid the tail of the laser pulse, which can be seen in Figure 5.21. The MatLab program was used to fit a double exponential function to the decay curves.

$$I(t) = -(A_1 e^{-t/\tau_1} + A_2 e^{-t/\tau_2}) \qquad (5.6)$$

I(t) is the emission intensity, A_1 and A_2 are amplitude parameters, and τ_1 and τ_2 are decay times. The negative sign appears in eq 5.6 because the MCP-PMT registers a negative voltage upon receiving photons. Because the fluorescence decay of pseudocumene is essentially mono-exponential, the best results were obtained when $A_1 >> A_2$. The decay time of the pseudocumene is then τ_1 . Measured pseudocumene decay data are shown in Figure 5.26 along with a fitted decay curve. Some pseudocumene decay times are listed in Table 5.2. Although there is some variation in the results, the average decay times are 9.4 ns in the presence of oxygen and 21.8 ns after nitrogen sparging.

Solutions of PPO in pseudocumene at a concentration of 1.5 g/L were excited at 337.1, 292.5 and 276.5 nm. The decay curves recorded following excitation at 292.5 and 337 nm were similar in appearance. This was expected, because the PPO in the mixture was being excited directly in both cases. (With 1.5 g/L of PPO and 292.5 nm excitation, 98.7% of the absorption is by PPO. At 337.1 nm, 99.9% of the absorption is by PPO.) When pseudocumene is excited, it must transfer its energy to the PPO before the fluor can emit light. An increase in the PPO decay time should be observed following excitation of the solvent. Such a change has been observed by the Perugia group.[18] They measured a change in the decay time of PPO from 1.7 ns following its direct excitation to 3.3 ns for excitation of pseudocumene in a solution containing 1.5 g/L of PPO in pseudocumene. When a 1.5 g/L solution of PPO in

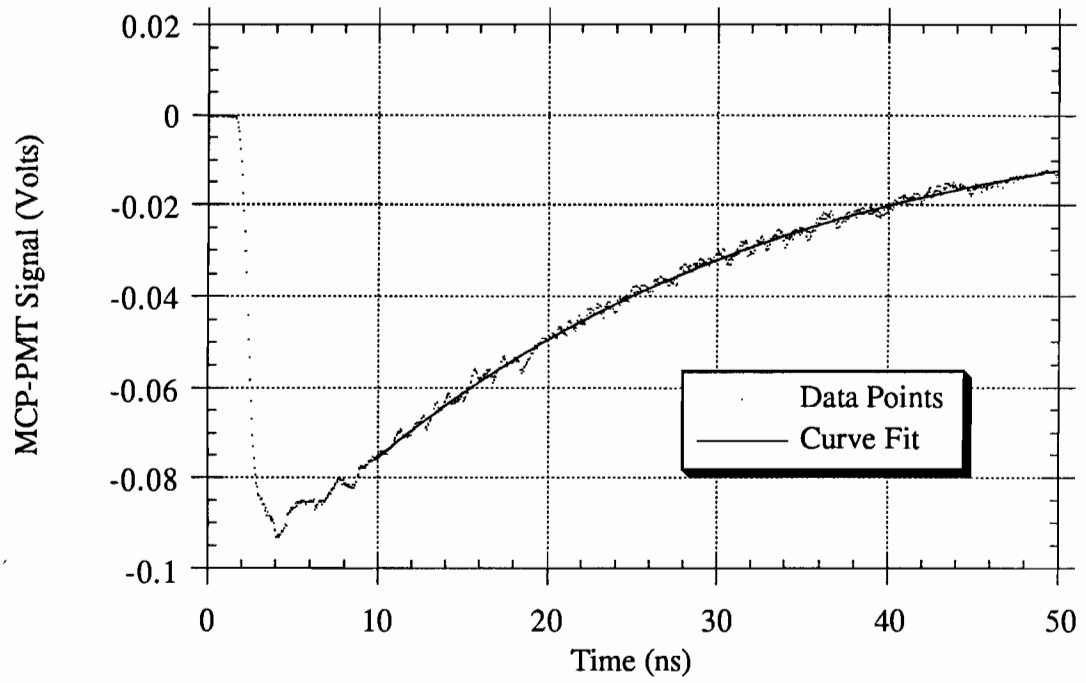

Figure 5.26. Pseudocumene fluorescence decay curve with fitted function. A fluorescence decay curve for neat pseudocumene after nitrogen sparging can be seen here. A function of the form of eq 5.6 has been fitted to the experimental data at times greater than 10 ns, and a plot of the function is included in the figure. The function parameters are: A_1=0.085, τ_1=20.5, A_2=0.0005, and τ_2=250. The pseudocumene was excited at 276.5 nm and its emission was monitored at 300 nm.

Table 5.2. Pseudocumene decay times. The decay times listed in this table were obtained by fitting eq 5.6 to the experimental decay data at times more than 4 ns after the emission peak. The decay time of the dominant exponential in eq 5.6 is reported here as the decay time for the pseudocumene.

Trial #	Excitation Wavelength (nm)	Sparging (Yes or No)	τ (ns)
79	276.5	No	11.3
88	276.5	No	10.2
102	276.5	No	8.5
104	276.5	No	8.7
106	276.5	Yes	20.5
107	276.5	Yes	20.5
108	276.5	Yes	19.4
109	276.5	Yes	26.9
114	276.5	Yes	19.8
116	292.5	No	8.4
121	292.5	Yes	23.8
122	292.5	Yes	19.2
123	292.5	Yes	21.6
124	292.5	Yes	22.5
125	292.5	Yes	22.0
128	292.5	Yes	21.8
129	292.5	Yes	25.0
130	292.5	Yes	21.0

pseudocumene is excited at 276.5 nm, 95% of the light is absorbed by pseudocumene. No visual difference was seen in this work between the decay curves recorded following excitation at 292.5 and 331 nm and those recorded after excitation at 276.5 nm. Visual inspection was also ineffective in identifying any change in the decay curves caused by the removal of oxygen from the solutions. It was necessary to analyze the decay curves mathematically in order to determine if any change in the decay time occurred.

The fitting procedure used for the pseudocumene decay curves was inadequate for PPO. When PPO decay curves were analyzed using the procedure described above, no difference was seen between direct excitation of PPO and excitation of pseudocumene followed by energy transfer to PPO. Because of the short decay time of PPO, rejection of data collected less than 4 ns after the emission peak caused the loss of too much information for a meaningful fit to be obtained. A new analysis procedure which folded the laser pulse shape into the fitting function was developed. This approach was much more computationally intensive, but it was successful in producing meaningful results. Analysis of the pseudocumene data using this technique produced the same results as the original procedure did. Measured decay data and a fitted decay function for PPO can be seen in Figure 5.27. PPO decay times under various conditions are listed in Table 5.3. The average decay time changes from about 1.78 ns for direct excitation of PPO to 2.45 ns following excitation of pseudocumene. No consistent effect is evident in Table 5.3 as a result of nitrogen sparging of PPO solutions.

The decay times measured here of 1.78 ns for PPO under direct excitation and 21.8 ns for deoxygenated pseudocumene agree well with values reported by Perugia[18] and in the literature.[4,20] The quenching effect of oxygen on pseudocumene, a reduction in decay time by a factor of 2.3, is similar to that found by the Perugia

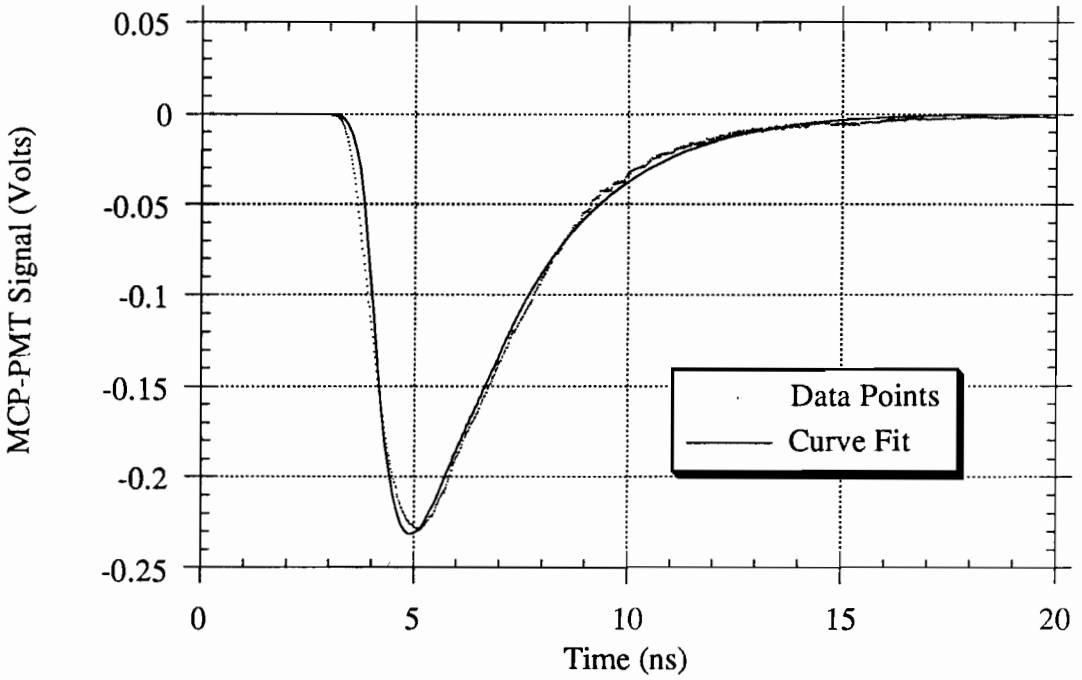

Figure 5.27. PPO decay curve with fitted function. A fluorescence decay curve for PPO at a nominal concentration of 1.5 g/L in pseudocumene can be seen here. A function of the form of eq 5.6 has been fitted to the experimental data by folding the laser pulse shape into the fitting procedure. The results of this fit are included in the figure. The function parameters are A_1=3.11, τ_1=2.57, A_2=–0.20, and τ_2=5.09. The laser pulse peak is at 4.77 ns (this an additional parameter in the new fitting procedure). The sample was excited at 276.5 nm and its emission was monitored at 365 nm.

Table 5.3. PPO decay times. The decay times listed here were calculated by using eq 5.6 and folding the laser pulse shape into the fitting routine. The time constant from the dominant exponential term is used as the PPO decay time.

Trial #	Excitation Wavelength (nm)	Sparging (Yes or No)	τ (ns)
21	337.1	No	1.70
55	292.5	No	1.70
56	292.5	No	1.80
60	292.5	Yes	1.83
61	292.5	Yes	1.74
75	292.5	No	1.89
83	276.5	Yes	2.51
85	276.5	No	2.35
86	276.5	Yes	2.82
133	276.5	Yes	2.57
142	276.5	Yes	1.98

group. This factor also agrees well with the reduction in pseudocumene quantum yield due to oxygen of 2.1 reported in section 5.B.3. The decay time of PPO following excitation of the pseudocumene solvent was not as long as that measured in Perugia, but an increase in the PPO decay time was seen when the solvent was excited. The decay time measurements were not sensitive enough to show a longer PPO lifetime after nitrogen sparging. This is because the effect of oxygen on PPO is small, as shown by the quantum yield measurements in Section 5.B.3.

Decay times at longer emission wavelengths were considered. When decay curves were obtained for emission wavelengths above that of peak emission, no change in lifetime was seen. Excitation of the samples at longer wavelengths was also attempted. Use of a different dye can produce excitation light at longer wavelengths (near 400 nm for excitation of PPO), but the low absorption and resulting weak fluorescence make such measurements extremely difficult. A monochromator with less accuracy, but which passes more light, would facilitate any measurements of this nature. Results on the variation of decay time with excitation wavelength were inconclusive.

D. Elastic Scattering Measurements

Two major types of scattering occur in the scintillator: absorption-reemission scattering and Rayleigh scattering. The absorption and fluorescence emission work described in Sections 5.A and 5.B is useful for characterizing absorption-reemission scattering. Specialized instruments do exist for the measurement of Rayleigh scattering in the scintillator, but it was possible to use the LS50 luminescence spectrophotometer for this purpose. During the elastic Rayleigh scattering measurements, the operation of the LS50 was modified slightly from that described in Section 5.B. To measure elastic scattering the excitation and emission

monochromators were set to the same wavelength and scanned in unison. This produced a spectrum of the amount of excitation light which was scattered towards the phototube detector.

The wavelength response of the phototube detector and emission monochromator assembly was calibrated for the elastic scattering measurements by recording a synchronous scan with no cuvette in the LS50. A synchronous scan is one in which the excitation and emission monochromators are scanned simultaneously. The black felt described in Section 5.B was in position during the calibration scan. The calibration curve in Figure 5.28 was obtained using this method. This curve is qualitatively similar to the one in Figure 5.11 derived from Berlman's corrected emission spectra. Figure 5.28 contains an additional peak near 450 nm. The curve in Figure 5.28 was used to correct the elastic scattering data for variations in detection efficiency with wavelength.

The elastic scattering spectrum of pseudocumene from 300 - 550 nm is shown in Figure 5.29. The values at wavelengths below 320 nm are somewhat inaccurate because absorption is taking place at these wavelengths as well as elastic scattering. As expected from eq 4.32 describing Rayleigh scattering, the amount of elastically scattered light decreases as the wavelength increases. In Figure 5.29, the amount of scattering from pseudocumene is seen to increase slightly near 390 nm. This apparent increase is an artifact of the calibration procedure. No actual increase in scattering is observed here. The calibration is very effective at correcting the measured curves for variations in detector and emission monochromator efficiency at most wavelengths, but it fails in the region near 390 nm.

Elastic scattering measurements were also made for cyclohexane, benzene, toluene, and mesitylene. Results for these liquids are shown in Figure 5.30. The amount of light scattered increases in the order cyclohexane < benzene < toluene <

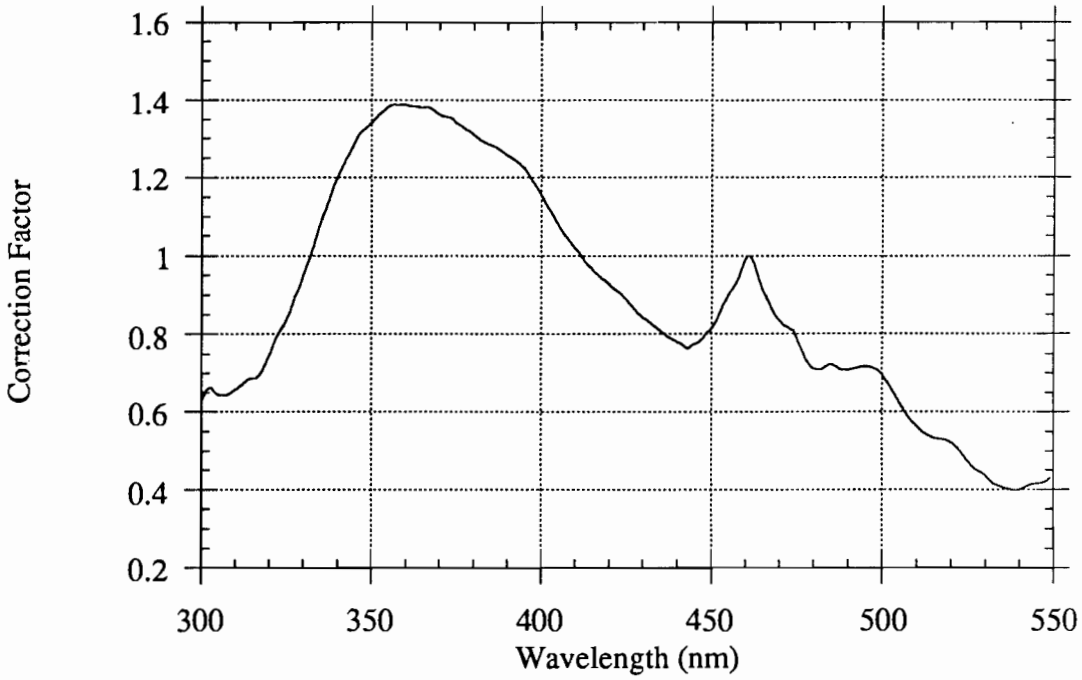

Figure 5.28. Calibration curve for LS50. This figure shows the correction S(λ) as calculated by recording a synchronous spectrum with the LS50 when no cuvette was in the instrument. This curve is similar to the one in Figure 5.11, but it does contain an additional peak near 450 nm. This curve is used to correct the elastic scattering data for variations in detector sensitivity and emission monochromator efficiency with wavelength.

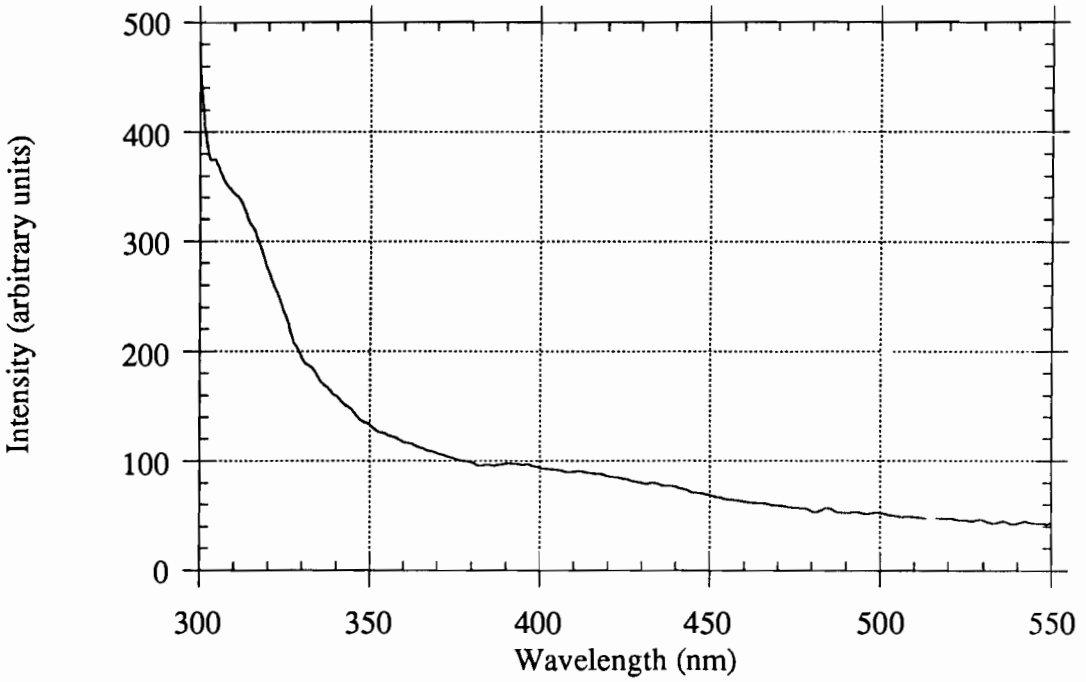

Figure 5.29. Elastic scattering from pseudocumene. The amount of light scattered elastically by pseudocumene is shown here as a function of wavelength. As predicted by the eq 4.32 governing Rayleigh scattering, the amount of light scattered decreases as the wavelength increases. The apparent increase in the amount of scattering at 390 nm is an artifact of the calibration procedure. These data were recorded during a synchronous scan of the LS50.

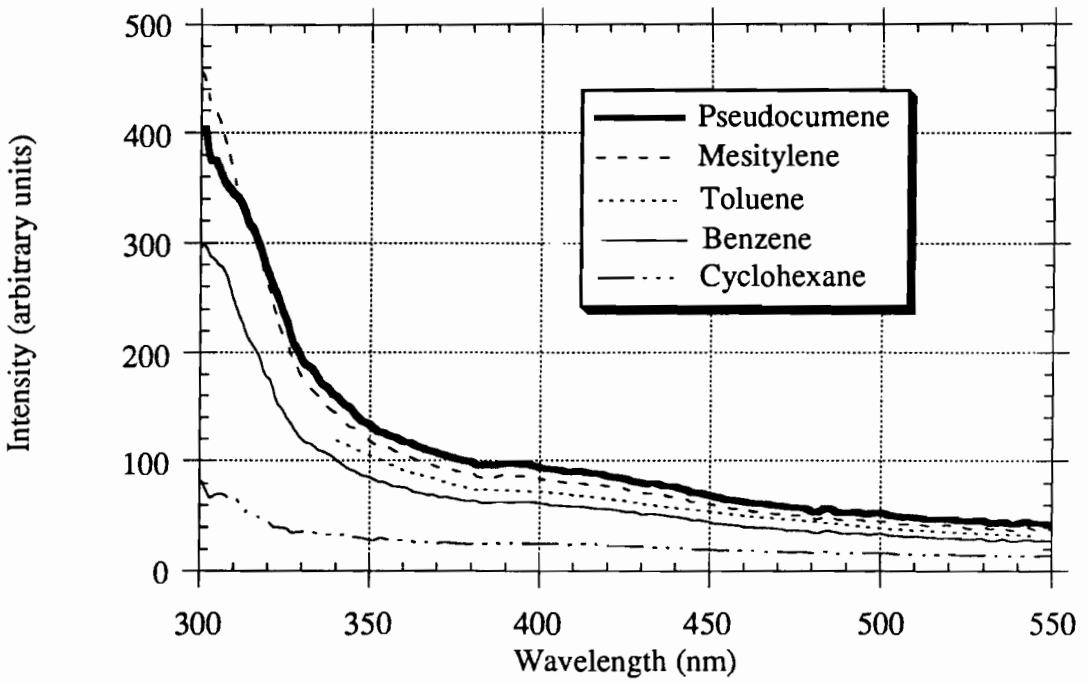

Figure 5.30. Elastic light scattering from organic liquids. In this figure, elastic scattering from several organic liquids is shown. Scattering increases in the order cyclohexane < benzene < toluene < mesitylene < pseudocumene. As in Figure 5.29, the increase in scattering at 390 nm for the liquids shown here is an artifact of the calibration.

mesitylene < pseudocumene. This trend can be predicted from the molecular polarizabilities and molar densities of the species. As discussed in Chapter 4, Rayleigh scattering varies with the product of the square of the molecular polarizability and the molar density. The cyclohexane results must be treated with caution. Cyclohexane scatters less light than the aromatic liquids. The scattering of the aromatic liquids was near the sensitivity limit of the LS50, and the cyclohexane data may be strongly influenced by background signals. PXE was also examined for elastic light scattering, and the results are shown in Figure 5.31. PXE scatters slightly less light than pseudocumene does.

Quantitative comparisons between the amount of light scattered at 436 nm by the different liquids are shown in Table 5.4. The $\alpha^2\rho_M$ values for the liquids are also shown so that predictions based on them can be compared to the measured results. Calculation of the $\alpha^2\rho_M$ values for the liquids is shown in Table 4.9. The relative amounts of scattering are described adequately in most cases by the $\alpha^2\rho_M$ dependence. This is especially true for the single ring aromatics benzene, toluene, mesitylene, and pseudocumene. Even among these similar molecules, mesitylene does not scatter as much light as would be expected from its $\alpha^2\rho_M$ value. Its polarizability and density are similar to that of pseudocumene, but it scatters less light.

The comparison based on $\alpha^2\rho_M$ values breaks down when more dissimilar molecules such as cyclohexane and PXE are considered. Cyclohexane[24] does not scatter as much light as would be expected from its $\alpha^2\rho_M$ value of 111×10^{-50} mol•cm^3. This is similar to the $\alpha^2\rho_M$ value of benzene, but cyclohexane scatters less than half as much light. Reports of cyclohexane scattering in the literature confirm that it scatters less light than benzene. PXE[25] has a very large $\alpha^2\rho_M$ value of 317×10^{-50} mol•cm^3,but it scatters less light than pseudocumene which has an $\alpha^2\rho_M$ value of 182×10^{-50} mol•cm^3. Molecular structure seems to be more important in

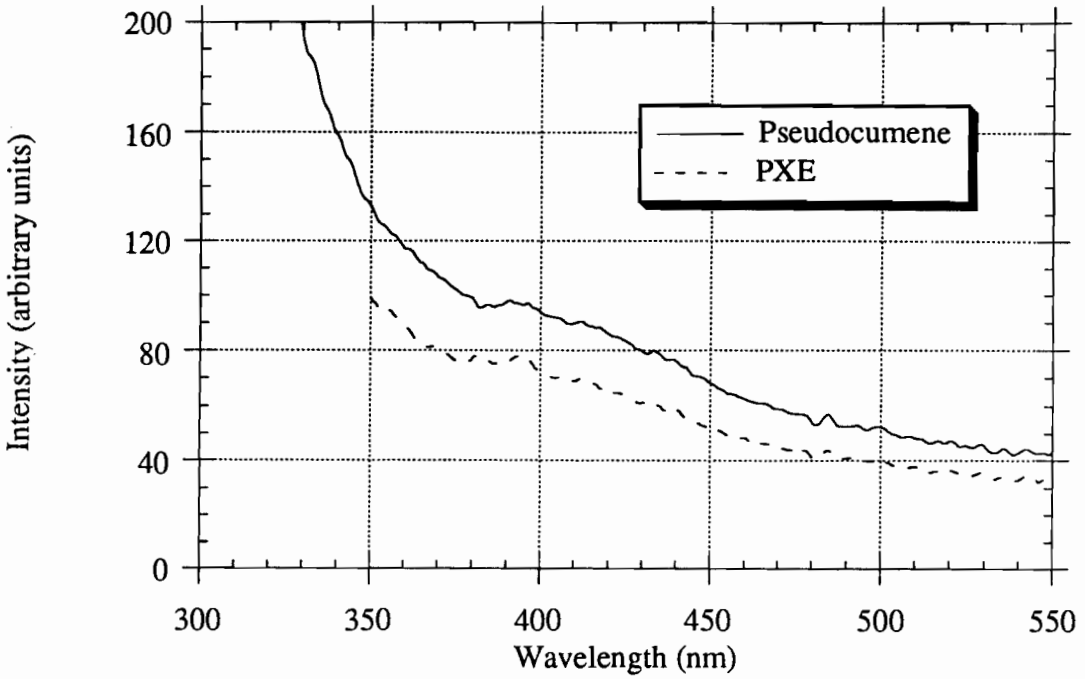

Figure 5.31. Elastic light scattering from PXE. Elastic scattering from PXE is shown in the figure. The scattering curve of pseudocumene is included for comparison. PXE scatters less light than pseudocumene. The increase in scattering at 390 nm for the two liquids is an artifact of the calibration procedure.

Table 5.4. Comparison of measured elastic scattering with $\alpha^2\rho_M$ predictions. The $\alpha^2\rho_M$ values are shown here to accurately predict the relative amounts of scattering exhibited by the alkylbenzenes. The comparison is not accurate between pseudocumene and dissimilar molecules such as cyclohexane and PXE.

Compound	$\alpha^2\rho_M$ (10^{-50} mol•cm^3)	Elastic Scattering @ 436 nm (arbitrary units)	$(\alpha^2\rho_M)_{PC}/(\alpha^2\rho_M)_{Compound}$	$(Scattering)_{PC}/(Scat.)_{Compound}$
Cyclohexane	111	21	1.64	3.67
Benzene	119	51	1.53	1.51
Toluene	144	58	1.26	1.33
Mesitylene	180	69	1.01	1.12
Pseudocumene	182	77		
PXE	317	59	.57	1.31

determining its scattering behavior than polarizability and molar density. Despite this, the $\alpha^2\rho_M$ values remain a good qualitative way to compare scattering among similar molecules such as the alkylbenzenes.

The pseudocumene elastic scattering data in Figure 5.29 were fitted with a power function and the wavelength dependence of the scattering was found to be –3.1. Although this is not quite the – 4 power predicted by eq 4.33 it is close enough to confirm the Rayleigh scattering mechanism. Other wavelength dependent parameters such as refractive index and molecular polarizability may be responsible for the difference between theory and experiment.

Scattering experiments were also conducted with water, but water did not scatter enough light to produce a signal above the background. Previous experiments[26] have shown that water scatters an order of magnitude less light than benzene. Because benzene scattering is near the limit of sensitivity of the LS50, the inability to measure scattering from water is not surprising.

The effect of oxygen on elastic scattering was also studied. The results reported above are all for deoxygenated samples. When oxygen was present, slightly less scattering took place at wavelengths below 350 nm. This can be attributed to absorption by oxygen complexes. When the oxygen is removed, there is less absorption, and more light penetrates into the cuvette where it can be scattered.

The effect of PPO on light scattering in pseudocumene is shown in Figure 5.32. No usable data were generated for wavelengths below 370 nm because PPO absorbs light at those wavelengths. Above 370 nm the PPO increases the amount of scattering slightly, but elastic scattering is dominated by the pseudocumene solvent.

The scattering results presented thus far have only been relative measurements. Although they are useful for showing that Rayleigh scattering is occurring in the scintillator solvent, they do not indicate the absolute amount of scattering which is

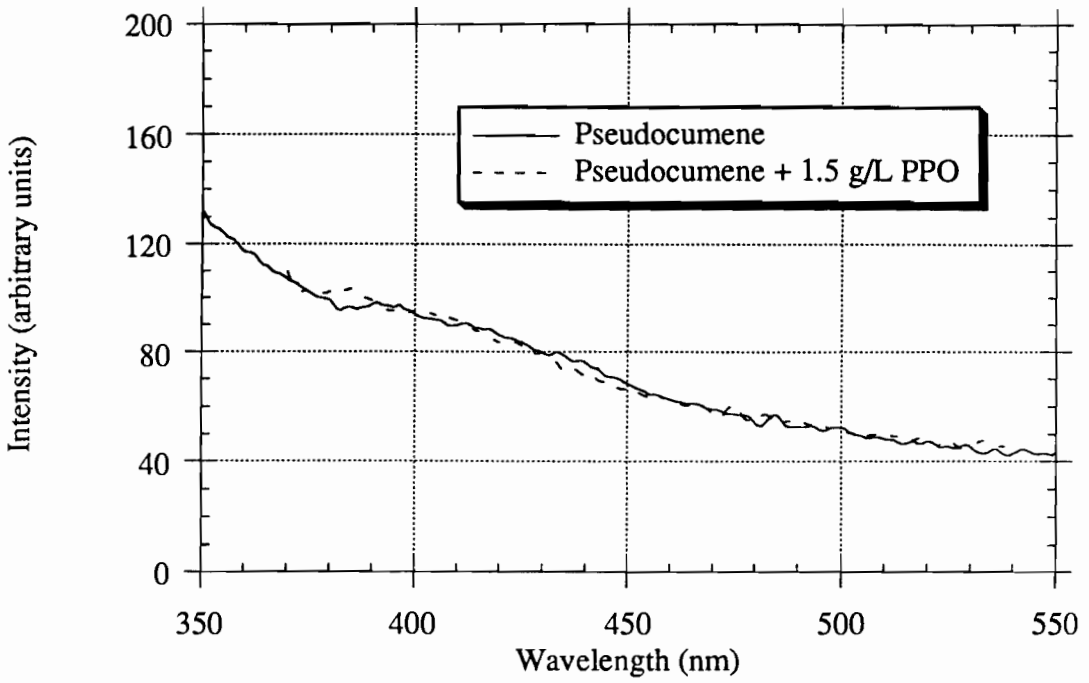

Figure 5.32. Elastic light scattering from PPO in pseudocumene. The amount of light scattered by a solution of 1.5 g/L of PPO in pseudocumene was measured using the LS50, and the results are shown in this figure. The scattering curve of pure pseudocumene is shown for comparison. The addition of PPO has a negligible effect on the amount of scattering. The increase in scattering seen at 390 nm is an artifact of the calibration procedure.

occurring. Absolute values were obtained by using benzene as a reference. Rayleigh scattering is commonly reported in terms of an R_{90} value, which indicates the amount of scattered light per steradian in a direction 90° from an incident beam of unit intensity. An R_{90} value has been reported for benzene[26] at a wavelength of 436 nm, where the LS50 received a large enough signal to make an accurate measurement possible. By relating this known R_{90} value to the photo tube detector output for benzene scattering at this wavelength, the LS50 results can be converted into absolute units. At 436 nm, an LS50 value of 51 (arbitrary units) corresponds to 46.3 cm^{-1}. The conversion factor is 0.91 arbitrary units per cm^{-1}.

The conversion of R_{90} values to scattering attenuation lengths is straightforward, as shown in eq 4.34. Scattering attenuation lengths calculated for pseudocumene in this manner are shown in Figure 5.33. Attenuation lengths for pseudocumene based on absorption results are also shown in the figure. At shorter wavelengths, near 300 nm, the absorption based attenuation lengths are shorter. This is expected because actual absorption occurs here and the scattering values are not very meaningful. From 350 – 450 nm, the two attenuation length curves approach each other and cross. Above 450 nm, the absorption measurements show attenuation lengths longer than the scattering measurements. This is physically impossible, and it can be attributed to inaccuracies in absorption measurements at very small absorbances. The inaccuracy of these measurements is indicated by the wide fluctuations in attenuation length values at these wavelengths, as the inaccuracy in the scattering measurements is reflected by wide fluctuations at short wavelengths.

The most significant result of these measurements is in the middle wavelength region of Figure 5.33, where both measurements are reasonably accurate. In this region, the two methods provide similar attenuation lengths. This is important because it shows that at these wavelengths, the light lost from a linear beam is due to

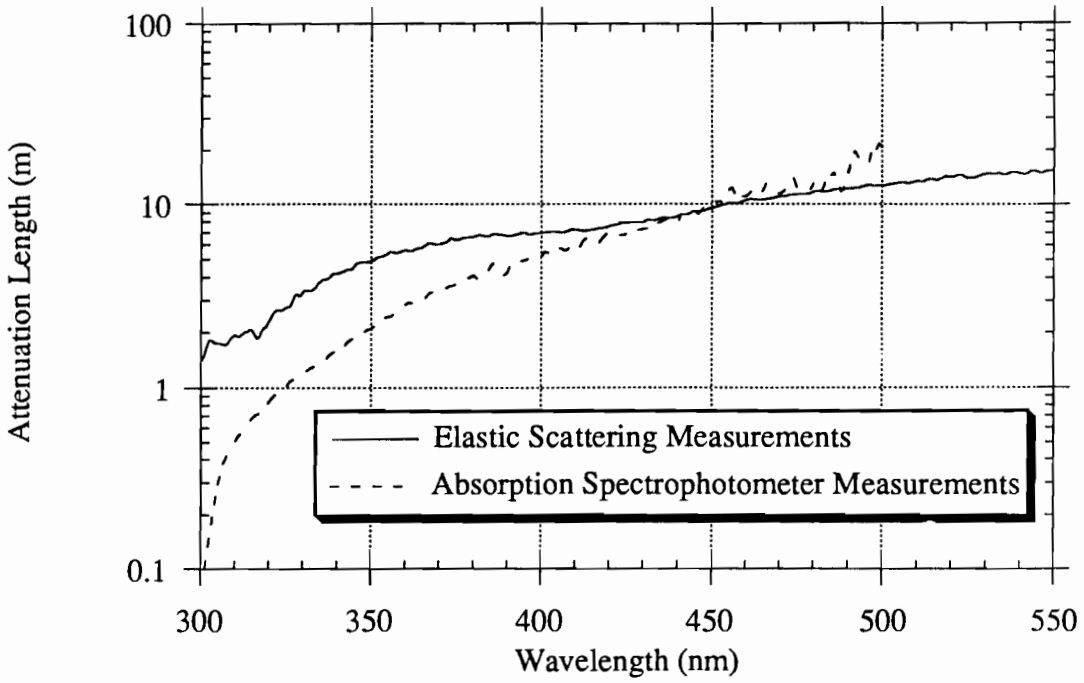

Figure 5.33. Attenuation lengths in pseudocumene from absorption and scattering. In this figure, attenuation lengths in pseudocumene calculated from absorption and scattering measurements are shown. The two methods agree closely at wavelengths above 350 nm. This indicates that most of the light lost at these wavelengths in an absorption spectrophotometer is due to elastic scattering and not to absorption.

elastic scattering, not absorption. Propagation of these wavelengths through the scintillator is governed by elastic scattering, in which there is no chance for loss of light, rather than absorption-reemission scattering, where there is such a chance. Results presented in this section and Section 5.B helped to redirect collaboration thinking about the propagation of light in the scintillation detector. Instead of the erroneous consideration of only the absorption and loss of light, scattering by absorption-reemission and elastic means are now accounted for in models of the propagation process.

Based on the results presented above, a second examination of Figure 5.8 is in order. The attenuation length curves shown there for pseudocumene and PPO can be divided into two parts. In the steep portions of the curves (280 – 310 nm for pseudocumene and 340 – 375 nm for PPO), absorption of light is occurring, and scattering is due mainly to absorption-reemission. In the flat parts of the curves (> 310 nm for pseudocumene and > 375 nm for PPO), absorption is negligible and scattering is elastic in nature. From this analysis, three regions of the figure can be clearly defined. Below 310 nm, light propagation is dominated by absorption-reemission caused by pseudocumene on a very short distance scale. This will occur simultaneously with transfer of energy from excited pseudocumene molecules to PPO. Between 310 and 370 nm, absorption/re-emission scattering by PPO will dominate at a length scale of 1 cm to 0.5 m. Above 370 nm, pseudocumene will again have the largest effect on light propagation, but at these wavelengths it will be through elastic scattering. This elastic scattering occurs on a length scale of 0.5 – 8 m. The elastic scattering measurements were of great importance in increasing our understanding of the light propagation in the CTF detector.

E. Prediction of Light Propagation in Large Scintillation Detectors

The optical property measurements described in the Sections 5.A to 5.D were made with the goal of using the results to predict light propagation in large scintillation detectors such as the CTF and Borexino. Despite the complexity of the light propagation in a liquid scintillator, attempts have been made to analyze this behavior analytically. The absorption of light initially emitted in the detector is easily modeled using Beer's law and the extinction coefficients discussed in Section 5.A. Based on the emission spectrum of PPO and the extinction coefficients for PPO and pseudocumene, it is possible to calculate what percentage of the light emitted during an event in the center of the CTF is absorbed or scattered at any given radius in the detector. In a scintillator of 1.5 g/L of PPO in pseudocumene, 15% of the light is absorbed at 1 cm, 26% is absorbed at 10 cm, 39% is absorbed at 0.5 m and 48% is absorbed at 1 m. Use of the convolution of emission and attenuation spectra to predict scattering in the detector is considered in more detail in Chapter 6. The does not give a complete picture of light propagation in the detector, however, because it cannot describe what happens to the light after its path is changed.

The effect of absorption on the shape of an emission curve can also be calculated analytically. The short wavelength photons are preferentially absorbed so the spectrum becomes red-shifted as the light travels farther through the scintillator. This effect has been calculated by Masetti et. al[18] for various concentrations of PPO in pseudocumene. While such calculations are quite valid in a linear geometry, their application to a spherical geometry is questionable because they do not take into account reemission of absorbed photons. D'Ambrosio et. al[27,28] performed similar calculations for the fluor PMP in toluene. Their experimental results in a linear geometry closely matched the theoretical predictions.

The effect of light propagation on scintillator decay time can also be modeled analytically. The effective decay time after n absorption and reemission steps was shown in eqs 4.27 – 4.29. While these equations are certainly accurate, they become difficult to apply in a large detector where photons are undergoing different numbers of scattering steps with different transit times between them. Elastic scattering is even more difficult to model analytically because it introduces no additional decay time, but only more transit time of a random amount.

While analytical solutions to parts of the propagation question are useful for gaining an understanding of the various processes, they are inadequate for any attempt at a complete model of the phenomenon. The random nature of many of the scattering processes make light propagation an ideal candidate for Monte Carlo simulation. Monte Carlo code has been used by the Borexino collaboration to predict light propagation in the CTF detector. The optical property measurements discussed above have been used to provide input data for the Monte Carlo model. The addition of absorption-reemission and elastic scattering to the simulations greatly increased their ability to reflect the actual behavior of the detector. The ultimate test of the simulations regarding light propagation was to collect experimental data involving light scattering, as described in Chapter 6, and to simulate these tests successfully with the computer codes, as discussed in Chapter 7. The optical property measurements of this chapter were essential in providing data for use in the Monte Carlo model.

In order for the simulation to produce correct results, the optical property measurements must be applied correctly in them. The absorption spectrophotometer measurements can be used at all wavelengths to model how far a photon of a given wavelength is likely to travel through the detector before being scattered as long as they are interpreted properly. In the steep portion of the attenuation curve, actual absorption is occurring. Here scattering takes place by absorption-reemission. In the

flat portion of the attenuation curve, scattering is due to the elastic Rayleigh mechanism.

Rayleigh scattering is relatively easy to treat in the simulation. The photon is assigned a new direction, the probability of which is determined by the $1 + \cos^2 \theta$ law of elastic scattering.

Treatment of absorption-reemission is more complicated. The simulation must correctly model photon behavior following absorption. The emission spectra, quantum yields, and decay times of the scintillator components have all been measured for excitation in the main absorption band. Much of the light emitted and re-absorbed in the scintillator is at the long wavelength end of this band, and it is not obvious that the same parameters apply there. Attempts to measure these parameters at long wavelengths have been described in this thesis, but no conclusive results have been obtained to indicate whether the parameters remain the same or if they change. The elastic scattering results in Section 5.D make the long wavelength measurements less critical. The elastic scattering results indicate that almost all the scattering at long wavelengths is elastic, and knowledge of fluorescence parameters at those wavelengths is not necessary. Because of this, the emission spectra, quantum yields, and decay times determined for the main absorption band can be used to model all absorption-reemission scattering in the simulation.

The important optical property values for correct simulation of light propagation in the detector are extinction coefficients at wavelengths in the main absorption band; elastic scattering attenuation lengths at longer wavelengths; and the fluorescence emission spectrum, quantum yield, and decay time following absorption of photons in the main absorption band. The measurement of these parameters has been described in this chapter. Attenuation length curves for pseudocumene and PPO (at the CTF concentration of 1.5 g/L) are shown in Figure 5.8. These curves show that

light propagation in the CTF will be dominated by absorption-reemission by PPO on a distance scale of less than 10 cm for wavelengths less than 360 nm. Wavelengths of light between 360 and 375 nm will be scattered by PPO absorption-reemission on a distance scale of 10 cm to 1 m. Propagation of wavelengths greater than 375 nm will be dominated by elastic scattering by pseudocumene on a distance scale of greater than 1 m. The emission spectrum of PPO in pseudocumene is shown in Figure 5.15. Pseudocumene has a quantum yield of 0.38 and PPO has one of 0.80. The decay time of pseudocumene is 21.8 ns and that of directly excited PPO is 1.8 ns. When the pseudocumene in a pseudocumene-PPO (1.5 g/L) scintillator is excited, the PPO decay time increases to approximately 3 ns.

F. Conclusions

In this chapter, the measurement of scintillator optical properties using small samples in commercial spectrophotometers was described. Values were obtained for decay times, quantum yields, and emission spectra of scintillator components. This work is summarized in Tables 5.1 – 5.3 and Figures 5.12 – 5.17. Attenuation spectra caused by absorption and elastic scattering were also measured. These data are reported in Figures 5.2 – 5.7 and 5.33. Comparison of the attenuation spectra showed that at wavelengths longer than the main absorption band, the apparent absorption recorded by absorption spectrophotometers is due to elastic scattering. This has important implications for light propagation in a scintillation detector because it means that light at these wavelengths cannot be absorbed and lost, but is only scattered elastically. Light propagation can be modeled by accounting for absorption and reemission of light by scintillator components at wavelengths in the main absorption band and allowing for elastic scattering of longer wavelengths.

The use of the small-scale parameters for predicting light propagation in a large scintillation detector was also considered. Convolution of emission and attenuation spectra and analytical expressions for scintillator decay time were shown to be valuable methods for approximating large scale light propagation. They were unable to make quantitative predictions, however. The use of Monte Carlo simulation was proposed as a more accurate means of utilizing small-scale parameters to predict the behavior of a large detector, and this use is considered in detail in Chapter 7.

References

1. Tsubomura, H.; Mulliken, R. S. *J. Am. Chem.Soc.* **1960**, *82*, 5966.
2. Parker, C.A. *Photoluminescence of Solutions*; Elsevier: Amsterdam, 1968.
3. Elisei, F.; Masetti, F.; Mazzucato, U. Borexino Project - Report N. 8, January 29, 1993; Perugia.
4. Berlman, I. B. *Handbook of Fluorescence of Aromatic Molecules*; Academic: New York, 1971.
5. Perkampus,. H. H. *UV-VIS Atlas of Organic Compounds*, 2nd ed.; VCH Verlagsgesellschaft: Weinheim, 1992; Part 2.
6. Eitel, K.; Gemmeke, H.; Maschuw, R.; Rapp, J.; Wolf, J. *Nuc. Inst. Meth. A.* **1994**, *340*, 346.
7. Elisei, F.; Masetti, F.; Mazzucato, U. Borexino Project - Report N. 10, January 29, 1996; Perugia.
8. Elisei, F.; Masetti, F.; Mazzucato, U. Borexino Project - Report N. 11, December 11, 1996; Perugia.
9. *The Model LS50 Luminescence Spectrometer User's Manual*; Perkin-Elmer: Beaconsfield, England, 1989.
10. Parker, C. A.; Rees, W. T. *Analyst (London)* **1960**, *85*, 587.
11. Melhuish, W. H. *J. Phys. Chem.* **1960**, *64*, 762.
12. Melhuish, W. H. *J. Phys. Chem.* **1961**, *65*, 229.
13. Melhuish, W. H. *J. Opt. Soc. Amer.* **1964**, *54*, 183.
14. Elisei, F.; Masetti, F.; Mazzucato, U. Borexino Project - Report N. 12, April 5, 1997; Perugia.
15. Birks, J. B. *J. Res. Nat. Bur. Std.* **1976**, *80A*, 389.
16. Lipsett, F. R. *Progr. Dielectrics.* **1967**, *7*, 217.
17. Demas, J. N.; Crosby, G. A. *J. Phys. Chem.* **1971**, *75*, 991.
18. Masetti, F.; Elisei, F.; Mazzucato, U. *J. Lumin.* **1996**, *68*, 15.
19. Birks, J. B. *J. Lumin.* **1974**, *9*, 311.
20. Birks, J. B.; Braga, C. L.; Lumb, M. D. *Brit. J. Appl. Phys.* **1964**, *15*, 399.
21. Froehlich, P. M.; Morrison, H. A. *J. Phys. Chem.* **1972**, *76*, 3566.

22. Berenfel'd, V. M.; Krongauz, V. A. *Theor. Exp. Chem. USSR.* **1967**, *3*, 63.

23. *PL202 Dye Laser Operating Manual*; PTI Lasers: London, Canada, 1987; p 11.

24. *CRC Handbook of Chemistry and Physics*; Weast, R. C., Ed.; CRC: Boca Raton, Florida, 1989; p E-70.

25. Israelachvili, J. N. *Intermolecular and Surface Forces*; Academic: London, 1985; p 54.

26. Kerker, M. *The Scattering of Light and Other Electromagnetic Radiation*; Academic: New York, 1969.

27. D'Ambrosio, C.; Leutz, H.; Tailhardat, S.; Taufer, M.; Destruel, P.; Puertolas, D.; Güsten, H. *Nuc. Inst. Meth. A* **1991**, *307*, 430.

28. D'Ambrosio, C.; Leutz, H.; Taufer, M.; Güsten, H. *Appl. Spectrosc.* **1991**, *45*, 484.

Appendix 5.I. Calibration Curve for Emission Spectra

As discussed in Section 5.B.1, a calibration curve was determined for the LS50 to account for variations in the efficiency of the emission monochromator and the sensitivity of the detector phototube with wavelength. This curve was calculated by comparing spectra generated by the LS50 for quinine bisulfate (QBS) in 0.1 N H_2SO_4, PPO in cyclohexane, and pseudocumene in cyclohexane with spectra for these compounds reported by Berlman which had been corrected for instrumental response. For the compounds of interest in the CTF (pseudocumene, PXE, PPO, and bis-MSB), it was necessary to measure fluorescence at wavelengths from 280 – 550 nm. Three standards as mentioned above were required to span this wavelength range. Berlman's spectra were only useful for calibration at wavelengths where the compounds had significant emission. QBS has significant emission over the range of 390 – 600 nm. PPO emits from 330 – 460 nm, and pseudocumene shows emission from 280 – 340 nm. In the region from 330 to 340 nm, neither PPO nor pseudocumene emits strongly.

The first step in the calibration was to compare each of the corrected spectra with that obtained for the same compound using the LS50. The LS50 spectra were normalized so that the emission peak had an intensity of 1 prior to this comparison. The corrected spectra were reported in this normalized fashion. A relative efficiency for the LS50 was calculated at each wavelength in the spectra. The relative efficiency was defined as the ratio of the normalized LS50 signal to the value of the corrected spectrum at that wavelength. The efficiencies were determined for each compound over the wavelength regions listed in the previous paragraph.

The three sets of relative efficiencies were then combined to form an overall calibration curve. The correction factor at 460 nm was chosen to be 1.0. The relative efficiencies over the QBS wavelengths were adjusted to reflect this arbitrary choice. The efficiencies at the PPO wavelengths were then adjusted so that PPO and QBS

gave the same correction factor at the wavelengths where they overlapped. The same procedure was used at the PPO-pseudocumene overlap region.

The curve in Figure 5.11 was produced using the calibration factors described in the previous paragraph. Before the curve was plotted, it was smoothed using a weighted least squared error routine in the KaleidaGraph program. This smoothing reduced the noise in the calibration curve and removed spurious structure from the emission curves which were corrected by using it.

The calibration curve used for elastic scattering corrections was also calculated with the correction factor at 460 nm equal to 1.0. This curve underwent the smoothing procedure as well.

CHAPTER 6: LIGHT SCATTERING MEASUREMENTS IN THE CTF

The optical property measurements described in Chapter 5 make it evident that light propagation in a large-scale scintillator should be governed by inelastic (absorption and reemission) and elastic scattering. In order to test the extrapolation of scattering measurements on small samples to long length scales, light scattering experiments in the Counting Test Facility (CTF) were performed. The experimental results were compared to simulated light scattering experiments to tune the simulation code so that it accurately represented light propagation in the detector.

A source consisting of a quartz vial filled with radon-spiked scintillator was inserted into the CTF. The decay of radon and its daughters inside the vial caused scintillation, and the light propagated into the CTF scintillator. The source vial used in these measurements was specially prepared so that light could only escape through a limited aperture; a portion of the vial's surface was darkened so that light could not pass through it. The phototubes facing the darkened side of the source vial only detect scattered photons. The ratio of the number of photons detected by directly illuminated phototubes to the number detected by those shielded from direct illumination is a measure of light scattering. (This measurement does not distinguish between inelastic scattering by absorption and reemission and elastic scattering.)

This chapter discusses several aspects of the light scattering measurements in the CTF, beginning with the preparation of the radon-spiked scintillator sources. The collection of the experimental data is then considered. Scattering measurements were made with three different scintillator mixtures in the scintillator containment vessel: 1.5 g/L of PPO in pseudocumene, 1.33 g/L of PPO and 20 mg/L of bis-MSB in pseudocumene, and pure pseudocumene. Analysis of the raw experimental data is described, and the amount of scattering in the various mixtures is quantified. The

distribution of photon arrival times at the phototubes is also affected by scattering, and this effect is shown for the three scintillator mixtures. The experimentally determined quantities of light scattered and timing distributions are compared with those generated by a Monte Carlo simulation in Chapter 7.

A. Preparation of Radon-Spiked Scintillator Sources

The sources consisted of scintillator spiked with ^{222}Rn contained in a quartz vial which could be inserted into the detector.[1] Radon offered several advantages as a radioactive source material, including the ease with which it could be detected. In the energy range of interest (0.2 – 1.0 MeV), the background rate in the CTF was approximately 2×10^{-2} Bq. Fortunately, in the ^{222}Rn decay sequence shown in Figure 6.1, there are time correlated events. In particular, the decay of ^{214}Bi followed by the decay of ^{214}Po with a mean lifetime of 236 μs was used to distinguish radon events. The endpoint energy of the ^{214}Bi β^- is 3.2 MeV and the equivalent electron energy of the ^{214}Po α is 0.8 MeV. Because the background coincidence rate was less than 10 events per day, a radon source with 0.1 Bq activity was sufficient for easy detection above the background in the CTF. The relatively short 3.8 day half-life of ^{222}Rn was also advantageous. This would allow its decay in the unfortunate case that a source contaminated the detector.

The sources were prepared in Hall C of the underground laboratories at the LNGS. The abundance of radon in the air (100 Bq/m^3) and water (10^4 Bq/m^3) of the laboratories provided a good source of radon. To prepare a source, radon was concentrated onto an activated charcoal trap. This radon was desorbed from the charcoal to a small amount of scintillator. The radon-spiked scintillator was then encapsulated in a quartz vial which could be inserted into the detector.

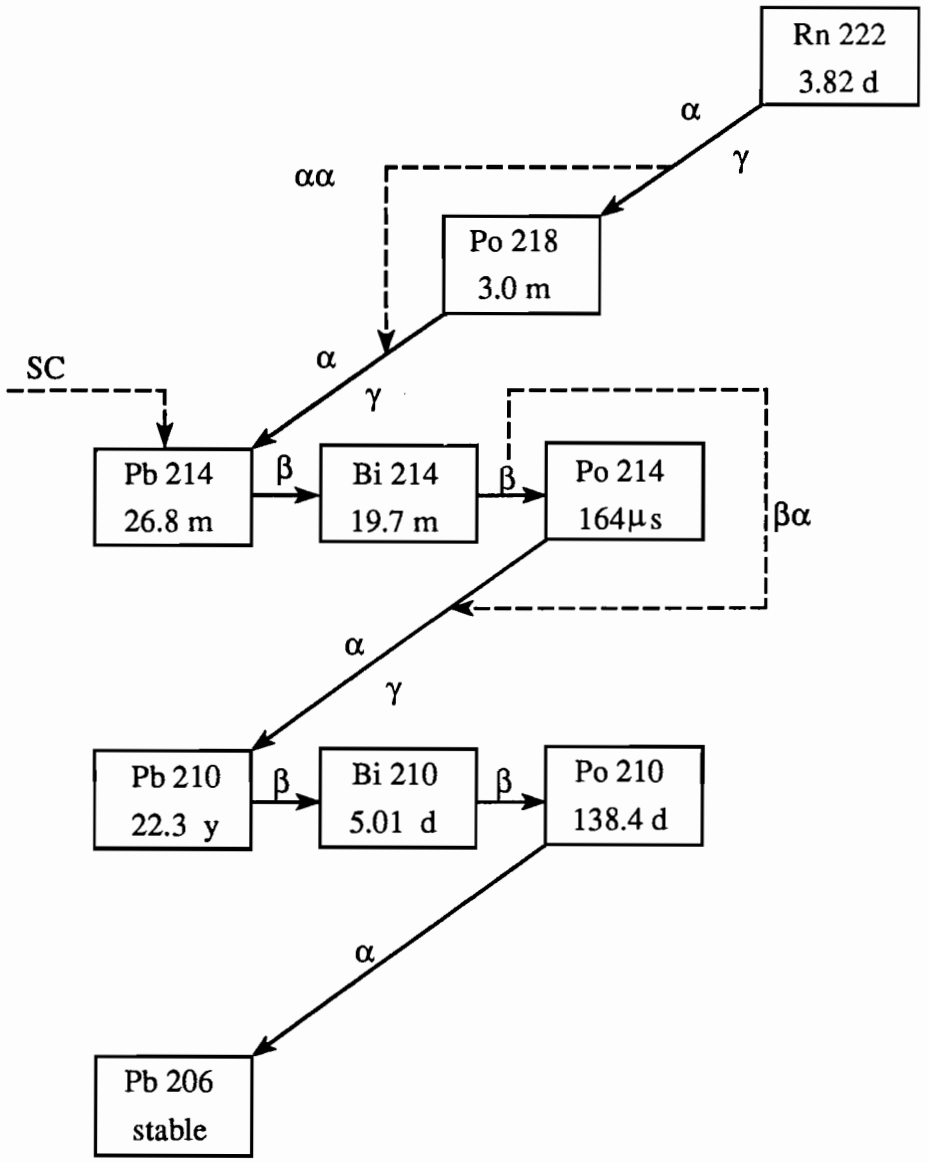

Figure 6.1. Decay chain of ^{222}Rn. The decay modes and half-lives of radon and its daughter nuclides are shown here. ^{222}Rn is detected in the CTF by monitoring the ^{214}Bi – ^{214}Po delayed coincidences.

The apparatus for trapping radon in charcoal is shown in Figure 6.2. Air containing radon is blown through the system by a small diaphragm pump. The air passes through a concentrated solution of NaOH which removes CO_2, through a Drierite column to remove water, and through a cryogenically cooled charcoal trap. The typical air flow rate varied from 100 to 500 cm^3/s.

The radon trapping procedure had to be carried out in a rather exacting manner. Water, carbon dioxide, and volatile organics are present in air at concentrations more than 10 orders of magnitude greater than radon, and these species are more effectively adsorbed on carbon adsorbents than radon.[2] In order to concentrate the radon, it was imperative that the water and carbon dioxide be reduced. Even after concentrating the radon it still had an insignificant partial pressure, so it required careful handling to transfer the radon into the scintillator without excessive dilution.

The radon trap was a stainless steel tube 1 cm in diameter and 12 cm long which was closed at one end and had a tee at the top. A 2 mm tube was fed through the tee to the bottom of the 1 cm tube. The annular region was filled with 5 g of charcoal (Cameron-Yakima, Inc. CYVCC Coconut Shell Carbon 8 × 30). The charcoal in the radon trap was prepared by pulling a vacuum on it with a mechanical pump while heating to 100 – 150 °C for approximately one-half hour. This pre-treatment of the charcoal was crucial to the final results. Heating in vacuum removed adsorbed water and carbon dioxide that collected on the charcoal from exposure to air. The presence of adsorbed water and CO_2 reduced the adsorption capacity of the charcoal for radon.

The CO_2 trap consisted of NaOH (75 g) in water (50 mL). This was a saturated solution at 20 °C with an excess of solid NaOH present in the bottom of the trap. Air was forced through a porous glass frit and immersed in the aqueous NaOH

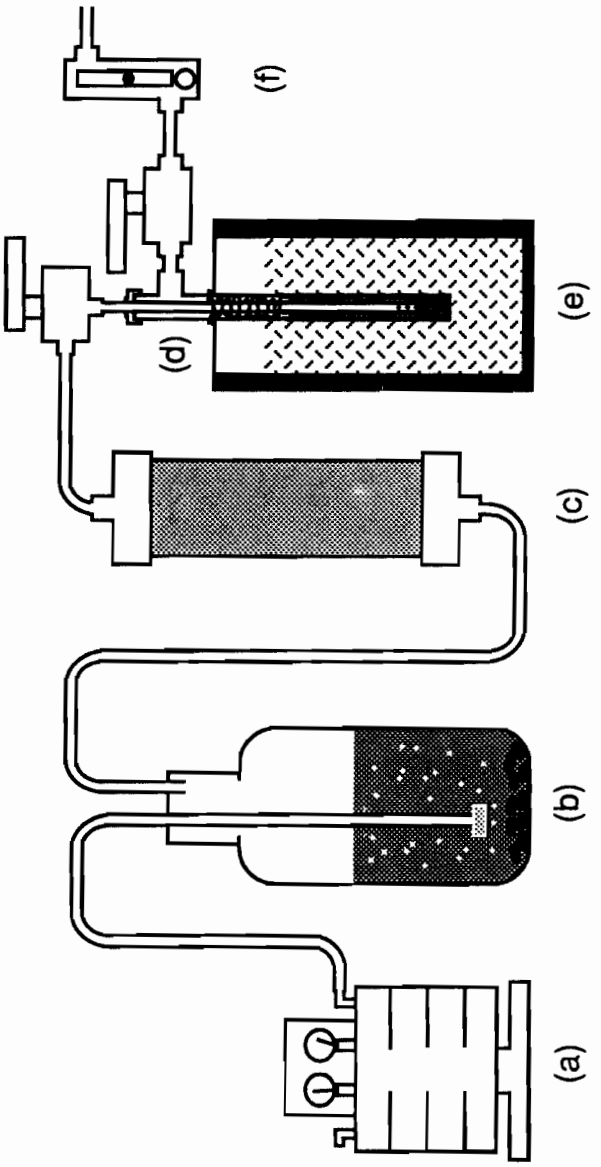

Figure 6.2. Radon trapping apparatus. The apparatus consists of a) a diaphragm pump, b) a CO_2 trap, c) a Drierite column, d) a charcoal trap surrounded by e) a cryogenic bath, and f) a flowmeter. It is used to concentrate radon in the underground air at LNGS so that scintillator can be spiked with radon for radioactive source tests in the CTF.

solution. This produced bubbles approximately 100 μm in diameter. Stoia measured the effectiveness of this technique for removing CO_2 from air.[3] At a flow rate of 80 cm^3/s the CO_2 level was reduced to approximately 60 ppm (from an ambient of 450 ppm) and the water vapor pressure was 6 mbar (from an ambient of 20 mbar or 20000 ppm) after sparging through the solution. At a flow rate of 160 cm^3/s the CO_2 level after sparging was approximately 175 ppm and the water vapor pressure was 8 mbar.

The Drierite column was filled with $CaSO_4$ pellets which adsorbed water from the air. The calcium sulfate contained a color additive that changed color when the pellets were saturated with water vapor. Flow through the system was halted when the front corresponding to water adsorption by the calcium sulfate reached three-quarters the length of the column. The Drierite column reduced the water vapor pressure to < 0.5 mbar, but did nothing to reduce the CO_2 level in the air.

The dry, "CO_2-free" air then passed into the radon trap. This trap consisted of charcoal which was cooled in a cryogenic bath. A temperature bath of frozen ethanol (–117 °C) was used to cool the trap. At this temperature radon (bp –62 °C) is trapped on the charcoal while nitrogen (bp –196 °C) and oxygen (bp –183 °C) are not. The CO_2 (sublimation pt –79 °C) and water removal steps were necessary because these gases would be trapped in charcoal at frozen ethanol temperatures and saturate the charcoal before an adequate amount of radon could be trapped. The air passed through a flowmeter after it left the charcoal trap and was returned to the atmosphere.

Normally air was passed through the system at a flow rate of 200 mL/s for nearly two hours . The Drierite was usually near exhaustion at this point. If 100% of the radon in the air was adsorbed on the charcoal, the charcoal would contain more than 100 Bq of radon activity. By replenishing the $CaSO_4$ in the Drierite column and the NaOH in the CO_2 trap, more air could be passed through the system. In one case, the air flow was continued for 12 hours, and a stronger source was produced.

The radon trapped in the charcoal was transferred into a sample of scintillator using the apparatus shown in Figure 6.3. The radon trap was detached from the air flow system, and connected to a flask containing approximately 50 mL of scintillator . The scintillator in the flask was identical to that which was present in the CTF. The scintillator was thoroughly sparged with nitrogen to remove any dissolved oxygen (dissolved oxygen quenched the fluorescence yield of the scintillator). The flask was attached to the air inlet side of the radon trap. A vacuum pump was attached to the air outlet from the trap, and the trap was evacuated while being maintained in the frozen ethanol bath at −117 °C. After evacuation, the charcoal trap was isolated, and the trap was removed from the ethanol bath and warmed using electric heat tape. A pressure gauge connected to the trap showed a rise in pressure as the heating caused radon (and CO_2 and water) to desorb from the charcoal. After heating, a small amount of helium was introduced into the trap through the valve where the vacuum pump had been connected. This helium increased the pressure in the trap; the valve between the trap and the scintillator flask was opened permitting gas to flow into the scintillator. The gas bubbled through a frit, exposing the scintillator to concentrated radon. The mass transfer rate of the desorbed radon from the gas phase into the liquid was low, and the helium carrier gas forced more gas through the scintillator, facilitating the radon transfer in a short period of time.

Even with the use of helium, this procedure had a rather low efficiency. It was estimated that at least 100 Bq of radon was trapped in the charcoal. This radon was extracted into 50 mL of scintillator. The partition coefficient of radon in the vapor to radon in the scintillator was estimated from the Ostwald coefficients of radon in pseudocumene and xylene of 11.5.[4,5] The vapor volume in the trap and above the scintillator was approximately 20 cm^3. If all the radon in the inlet air had been trapped on the charcoal, and equilibrium between gaseous radon and dissolved radon was

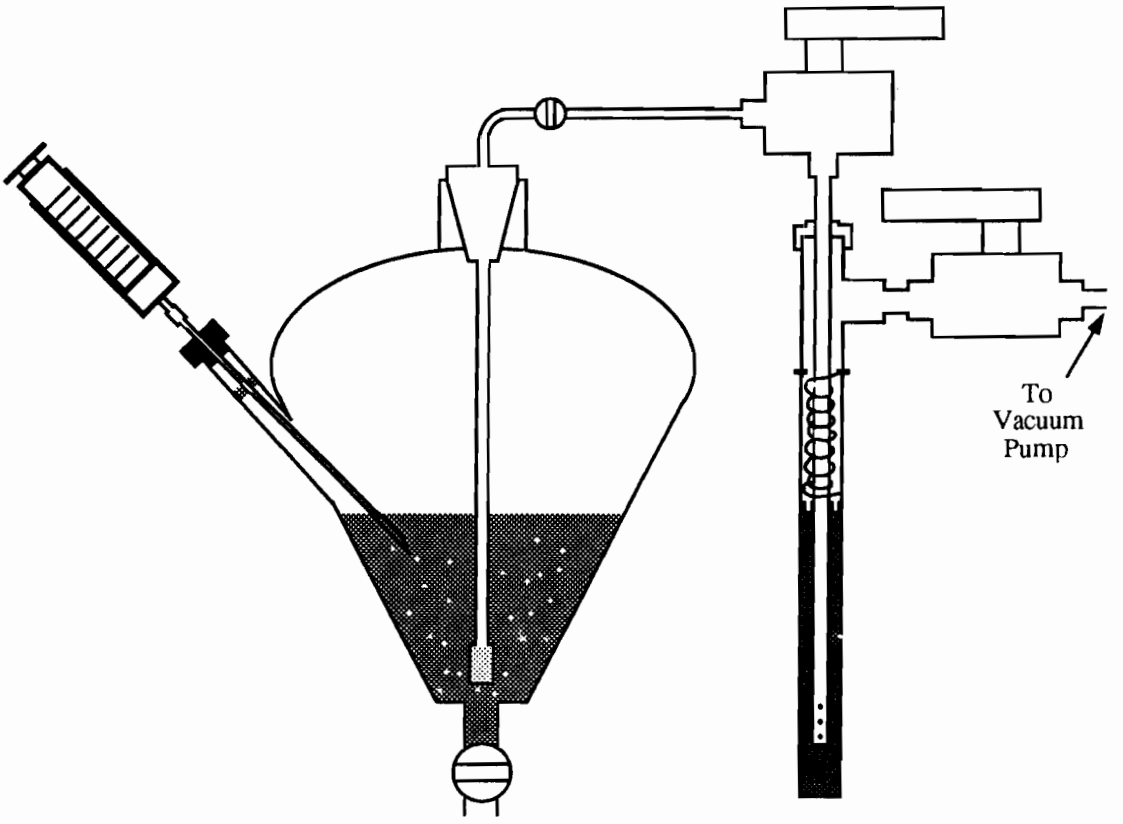

Figure 6.3. Transfer of radon to scintillator. This figure shows the separatory funnel used to transfer radon from the charcoal trap to the 50 mL scintillator sample in the funnel. The valve at the top of the separatory funnel is connected to the radon trap during transfer as shown in the figure. The syringe is used to remove radon-spiked scintillator from flask and to fill the sample vial. The syringe is not present during the transfer from the trap.

established, a source solution with a strength of 2 Bq/mL would have been obtained. The source solution typically had a strength of 0.5 Bq/mL, indicating an overall efficiency for radon collection and transfer of 25%.

The radon-spiked scintillator was transferred into a source vial for insertion into the detector. Selection and preparation of the source vials was important to reduce the risk of contamination of the detector. The source vials which were inserted into the CTF were made of quartz, which has a refractive index similar to that of the CTF scintillator. Some were made from Suprasil quartz which is more radiopure than natural quartz. The vials were cleaned by soaking in 10% nitric acid at 60 °C for several hours, rinsed with deionized water, and dried with nitrogen prior to use.

Several different shapes of quartz vial were used, with volumes between 1 and 5 mL. These vials and their dimensions are shown in Figure 6.4. Some of the vials had two threaded openings (Figure 6.4a). These vials were sealed with threaded Teflon or nylon caps and Teflon tape. Care had to be taken in order to tighten the caps enough so that they would seal, but not so much as to crack the caps. While these caps sealed the vial effectively, they also blocked light from exiting the ends of the source. Other vials were designed with only one end cap. A sealing mechanism consisting of a nylon snap-ring and a Teflon cap was also developed (Figure 6.4b), and some vials with one end cap were sealed in this manner. Some small spherical sources were also used (Figure 6.4c). These vials were sealed by placing a drop of epoxy in the narrow neck.

The vials shown in Figure 6.4 were used as omni-directional sources during the source testing. One vial was specially prepared for use as a limited aperture source to permit the study of light scattering in the CTF. A vial with two endcaps (Figure 6.4a) was modified by painting 170° of the its inside surface black with Permatex as shown in Figure 6.5. Light could only escape in the non-painted directions. Light was

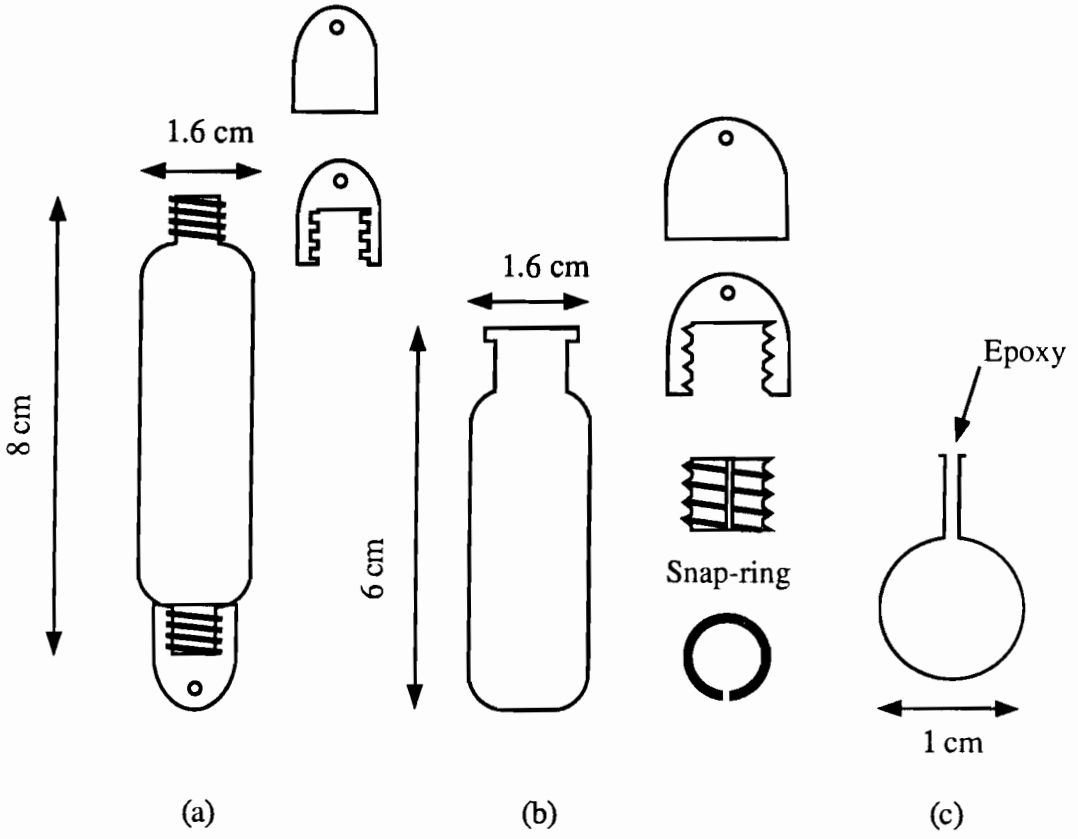

Figure 6.4. Quartz source vials and their dimensions. These source vials were used in omni-directional source tests in the CTF. The vial in a) is sealed with two Teflon end caps and Teflon tape. In b) the vial has only one end cap and is sealed with a Teflon cap and a nylon snap-ring. The small spherical vial in c) is sealed with a drop of epoxy.

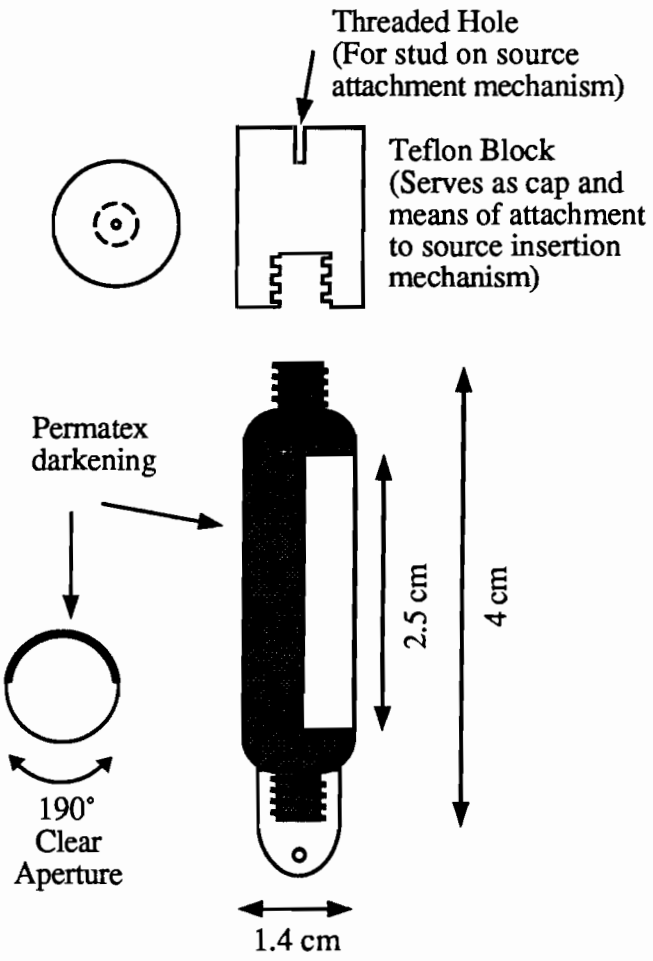

Figure 6.5. Permatex-painted limited aperture source. This source was designed to measure light scattering in the CTF. It consisted of a quartz vial with two end caps and the dimensions shown above. The vial was painted with Permatex over 170° of its interior surface to form a limited aperture for the escape of light. At the top and bottom of the source, it was painted over 360° to provide a well-defined geometry for the aperture in these regions.

also blocked to some extent by the endcaps, and the upper and lower portions of the vial were painted over 360° to provide a more regular geometry for this effect. The amount of light received by photo-multiplier tubes facing the clear side could be compared with the amount received by tubes facing the opaque side to make an estimate of the amount of light scattering in the detector.

A second type of limited aperture source was also developed. This source is shown in Figure 6.6, and consisted of a stainless steel jacket which was mounted to surround an omni-directional vial. Steel jackets with openings of 180°, 135°, and 90° were available to provide a limited aperture for escaping light. The steel jacket sources also blocked the emission of light from the top and bottom of the vial. Omni-directional sources sealed with a nylon snap-ring (Figure 6.4b) were used with the steel jackets to provide a complete source.

In the transfer of the radon-spiked scintillator to the vials, it was necessary to minimize oxygen contamination because oxygen diminishes the light yield of the scintillator. The scintillator in the flask in Figure 6.3 was sparged with nitrogen prior to radon transfer, and it was kept isolated from air after the sparging. Spiked scintillator was removed from the flask with a syringe through a septum and then injected into the source vials. The source vials were flushed with nitrogen prior to filling and the nitrogen flow was continued until moments before the vial was capped. The spiked scintillator could not be sparged for oxygen removal because this would also remove the radon. Although the procedures for avoiding oxygen contamination were improved as more sources were prepared, most showed some evidence of oxygen quenching. This was evidenced by the lower energy peak positions of the ^{214}Bi β's and the ^{214}Po α's as compared with their positions from events occurring in the free volume of the vessel. As a result of the scintillation quenching by oxygen, the sources were not used for an absolute energy calibration.

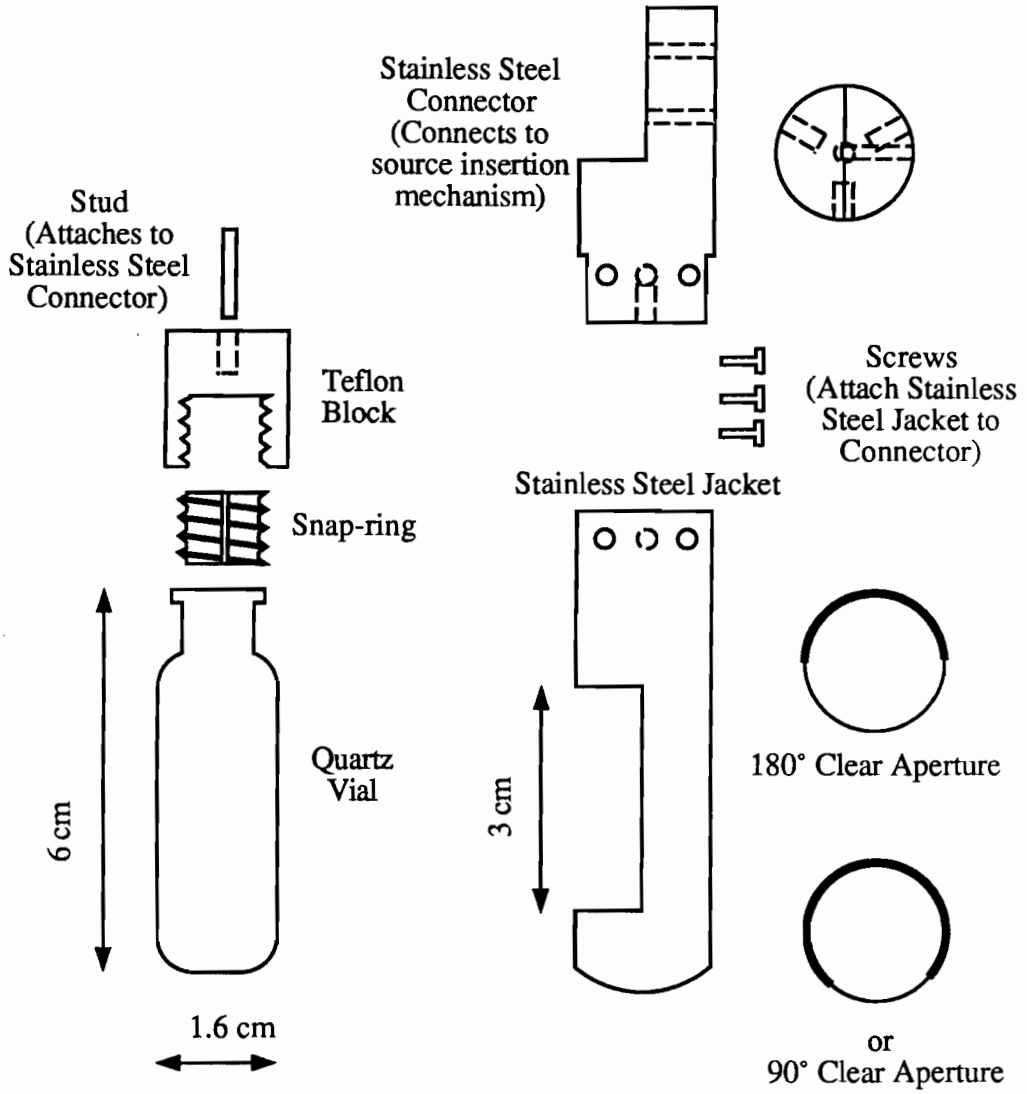

Figure 6.6. Stainless steel jacket limited aperture source. The dimensions of a source design for measuring light scattering in the CTF are shown here. Stainless steel jackets with apertures of 90°, 135°, and 180° were machined to create a limited aperture for light escape from a source vial. Quartz vials sealed with a nylon snap-ring and a Teflon cap (shown in Figure 6.4b) were used with the stainless steel jackets.

When sources were inserted into the CTF , they had high initial activity which decayed with a half-life of approximately 30 minutes. After a period of 3 – 4 hours, this activity diminished and a steady-state decay with a half-life of 3.8 days, characteristic of ^{222}Rn, was observed. The high initial activity was caused by ^{214}Pb which was externally deposited on the quartz vial, and especially on the Teflon caps, during atmospheric radon exposure.

B. Collection of Scattering Data Using Limited Aperture Sources

The light scattering measurements in the CTF were carried out as part of a larger program of source testing. The major portion of this testing was designed to measure the relative amount of light received by the phototubes from events at different locations in the detector and to measure a probability distribution function for photon arrival times at the phototubes. The source insertion equipment included apparatus that allowed positioning of a source virtually anywhere inside the scintillator containment vessel, but the light scattering experiments were all performed with the source at the nominal center of the containment vessel.

Sources were inserted into the CTF from the purification clean room on top of the shielding water tank. They passed through the plumbing by which scintillator is returned to the scintillator containment vessel. The plumbing-containment vessel assembly was clamped in place during source operations. The eye bolt (normally used as an attachment point for a counterbalance to the weight of the plumbing-containment vessel assembly) which can be seen at the top of the plumbing in the foreground of Figure 3.15 was removed, and the sources were inserted through this opening. A nitrogen purge flowed during source operations to prevent the entry of radon into the containment vessel. Nitrogen was introduced into the plumbing at a tee below the top opening, and it exited through this opening.

The sources were inserted into the scintillator containment vessel by using an apparatus made of stainless steel tubing. It consisted of eight 1 m sections. Each section was constructed of thin-walled one-half inch stainless steel tubing. The ends of each section were sealed with stainless steel plugs held in place by epoxy. Where the plugs protruded from the ends of the tube, they were machined to form tabs as seen in Figure 6.7. The tubing sections were connected by fitting their tabs together and joining them with two small screws. The first section, to which the source was attached, was pushed into the scintillator plumbing until approximately 20 cm of tubing was protruding from the eye bolt opening. A second section was then attached, and the process was repeated. The sectional nature of the apparatus was necessary because of height limitations imposed by the clean room ceiling.

The sources were attached to the insertion mechanism by a threaded stud. One end of the stud was threaded into a hole at the end of the insertion assembly, while the other end was threaded into a Teflon block. The Teflon block served as a cap for the source vial; it both sealed the vial and connected it to the insertion mechanism. Teflon blocks used for this purpose are shown in Figures 6.5 and 6.6, and the end of the source insertion apparatus to which the sources are attached is depicted in Figure 6.6.

Light scattering data were collected in the CTF by inserting the limited aperture sources described in Section 6.A into the center of the scintillator containment vessel. Phototubes which did not view the clear aperture of a source could only receive light if it was scattered inside the detector. The tubes which viewed the clear aperture could receive both direct and scattered light. In future discussions, phototubes facing the clear aperture of a source are referred to as front tubes, while those facing the opaque portion of a source are called rear tubes.

Data were collected with the limited aperture sources using the CTF data acquisition system. These data included both time-to-digital converter (TDC) and

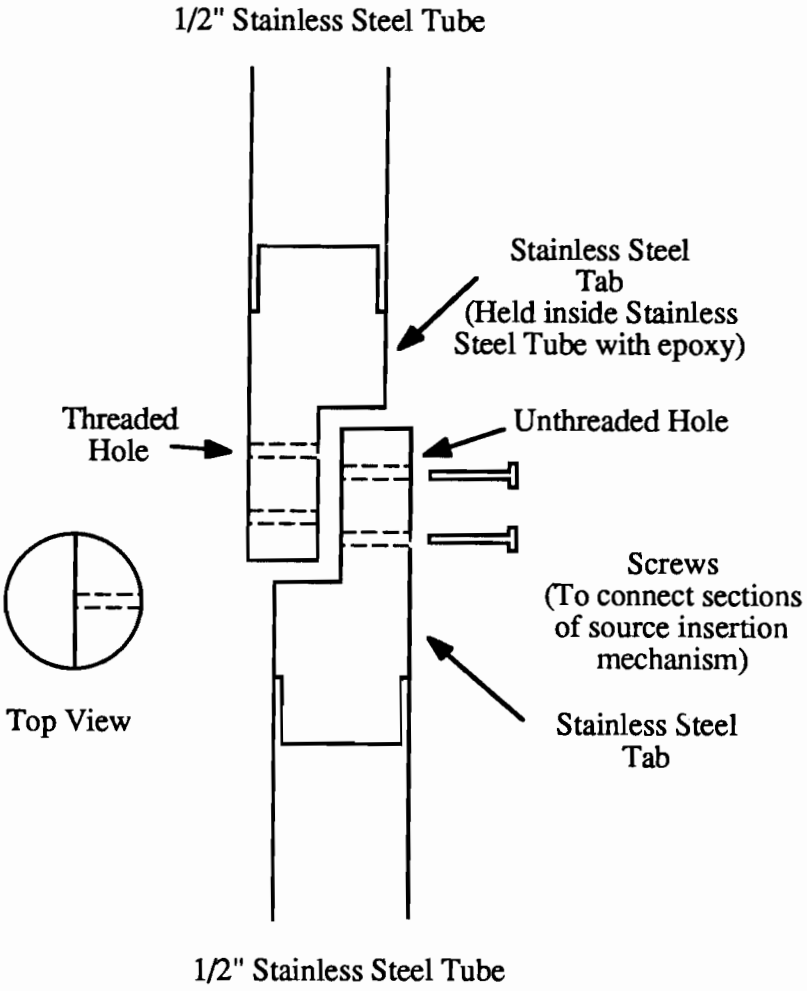

Figure 6.7. Source insertion apparatus. This apparatus consisted of eight 1 m sections of 1/2 in. stainless steel tubing. Stainless steel plugs were machined to form tabs and they were used to seal the ends of the tubing by holding them in place with epoxy. The sections were connected by using two screws through the tabs at their ends as shown in the figure.

analog-to-digital converter (ADC) information. The TDCs provide the relative times of arrival of the first photon at each channel. (As discussed in Chapter 2, some channels contain two phototubes, and other channels contain only one.) Because the TDCs only record the arrival time of the first photon, care must be taken in order to obtain accurate distributions of photon arrival times using data from them. Indiscriminant use of the TDC data results in a skewing of the arrival time distribution to earlier times, because only the first photon received by each channel is measured. To obtain accurate arrival time distributions, only channels which receive a single photon can be used. The ADCs provide information about the total integrated charge recorded by each channel. Based on a known calibration, the integrated charge can be converted to a number of photons. The ADC data are used to quantify the amount of scattering in the CTF, and to determine which channels received only one photon so their TDC information can be applied in determining the photon arrival time distributions.

The first scattering measurements in the CTF were made using the Permatex-painted limited aperture source. These measurements were made in a scintillator consisting of 1.5 g/L of PPO in pseudocumene. The radon-spiked scintillator inside the source was the same mixture. Prior to source insertion, the trigger in the data acquisition system was lowered to 4 tubes from the normal setting of 6 tubes. The threshold level was also lowered from –1.0 V to – 0.5 V. (See Chapter 2 for more discussion of these settings.) These adjustments were made because there was concern that initially blocking half the light output from the source with the Permatex would make it difficult to detect ^{214}Bi – ^{214}Po coincidence events in the CTF. No such difficulty was encountered with the data acquisition settings chosen, and a coincidence event rate of approximately 0.13 Hz was measured.

The first data to be examined during the initial limited aperture source trial were those from the TDCs. These data were studied on-line following the insertion of the source to determine whether coincidence events were being detected. Coincidence events were detected, and it was easy to see that some phototubes were receiving more light than others. During the first trial, the Permatex-painted limited aperture source was oriented so that the center of the aperture was facing in the –y direction. After operation in this alignment for 16 hours, the source was turned so that the aperture was centered along the –x axis. Data were collected in this configuration for 17 hours.

Figure 6.8 indicates the number of TDC hits received by each phototube for source alignment in the –y direction. The TDC data are not useful for quantifying the amount of scattering, but they can be used qualitatively to see if it occurring. Less than 100 phototubes are shown in Figure 6.8 because in February 1996, only 50 tubes were still in working condition; the other 50 tubes had malfunctioned. Phototube failures continued throughout the life of the CTF, and only 17 tubes remained active in June 1997.

The phototube numbering scheme shown in Figure 6.8 is taken from Manno,[6] and it is based on the numbering system designed for the CTF. A close examination of Figure 6.8 reveals that the phototubes near the –y axis received more TDC hits than the tubes along the +y axis for five of the six rings. In ring 2 the trend is reversed. This was the first evidence that the phototubes in ring 2 had been wired incorrectly. When the limited aperture source was oriented along the –x direction, the TDC behavior of ring 2 matched that of the other rings. This showed that ring 2 had been connected in a clockwise manner, while the other rings had been connected in a counterclockwise fashion. This is the reason for the clockwise numbering scheme for ring 2 in Figure 2.7. The incorrect wiring sequence was later confirmed by the data group of the collaboration.

Figure 6.8. TDC hits in a limited aperture source trial. The Permatex-painted limited aperture source was inserted into the center of the CTF and the center of its aperture was oriented along the –y axis. The number of TDC hits recorded by each active phototube during a trial of 16 hours are shown here. Both the source and the bulk scintillator solutions were 1.5 g/L of PPO in pseudocumene. The tubes in ring 2 show TDC opposite to that of the other five rings. (Ring 2 is the second ring from the center in the upper hemisphere. See Figure 2.4 for another view of the positions of the phototube rings.) They indicate more TDC hits for tubes facing the opaque side of the source than for tubes facing the clear aperture. This was evidence that the tubes in ring 2 were wired incorrectly.

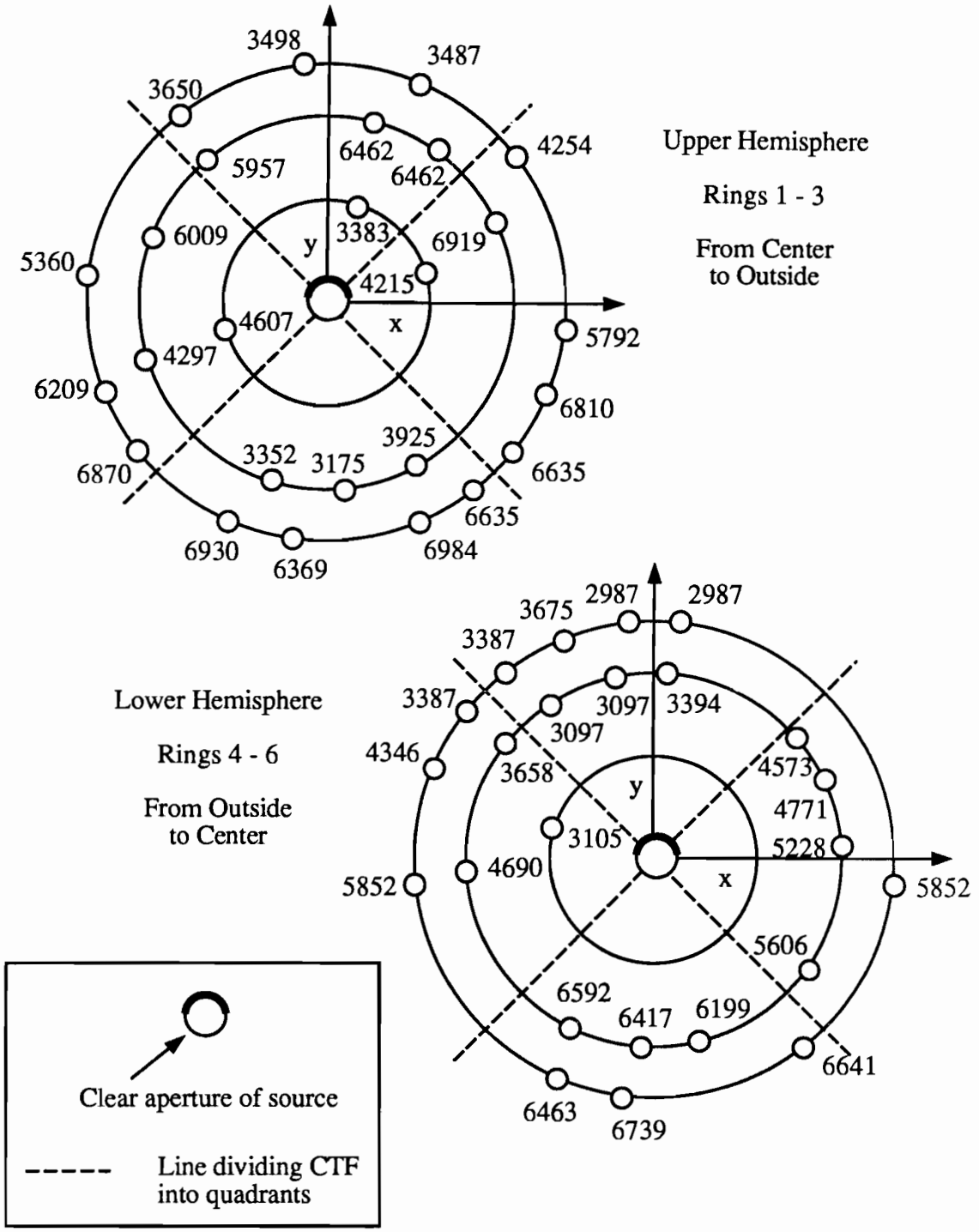
3498
3487
3650
4254
5957
6462
6462
6009
3383
6919
y
5360
4215
4607
x
5792
4297
6209
6810
3925
3352
3175
6635
6870
6635
6930
6984
6369
Upper Hemisphere
Rings 1 - 3
From Center
to Outside
Lower Hemisphere
Rings 4 - 6
From Outside
to Center
2987
2987
3675
3387
3387
3097
3394
3097
4346
3658
4573
y
4771
3105
5228
4690
x
5852
5852
5606
6592
6417
6199
6641
6463
6739
Clear aperture of source
Line dividing CTF
into quadrants

Figure 6.8.

The limited aperture source results provided important information to the collaboration even before they were analyzed to quantify the amount of scattering. When computer position reconstruction codes were modified to account for the correct positioning of all the phototubes, positional resolution improved slightly and a puzzling x-y asymmetry effect previously observed in the data disappeared. More quantitative scattering results are obtained through a more detailed analysis, as described in the next section.

A second set of limited aperture source trials were carried out with a scintillator mixture of 20 mg/L of bis-MSB and 1.33 g/L of PPO in pseudocumene. The steel jacket limited aperture source was used for these trials. An aperture of 180° was employed and the center of the clear aperture of the source was oriented along the –y, –x, +y, and +x axes. The coincidence rate was approximately 2 Hz throughout this set of measurements. The scintillator used inside the source vial was obtained from the scintillator containment vessel before it was spiked with radon to ensure that the two mixtures were identical.

A limited aperture source trial was also performed when the scintillator containment vessel contained pure pseudocumene. The steel jacket limited aperture source was used with an aperture of 180°. Data were collected with the center of the clear aperture of the source oriented in the –y direction. For this trial, the scintillator inside the source was not the same as that in the containment vessel. It was not possible to use a source containing pure pseudocumene because the pure solvent is not an efficient scintillator and its light output was not great enough to allow detection. The source vial was filled with a mixture of 1.5 g/L of PPO in pseudocumene, and a coincidence rate of 1 Hz was obtained.

C. Analysis of Scattering Data

Although a simple examination of the TDC data from the trials described in Section 6.B is sufficient to show that light scattering is occurring in the CTF, a more detailed analysis is necessary to quantify the amount of scattering and to determine the distribution of photon arrival times at the phototubes. Analysis was carried out on TDC and ADC data from the source trials described above which had been stored on magnetic tape. The Physics Analysis Workshop (PAW) software and FORTRAN computer code were used for data analysis.

The raw data tapes contain the ADC and TDC information of every channel for each event. The raw ADC data are in the form of integrated charge signals measured by the individual channels. Calibrations performed by the electronics group of the collaboration are available to convert this information into the number of photons received by a channel during an event. This calibration allowed the integrated number of photon hits received by each channel during a group of events to be calculated. Some phototubes are monitored on channels containing two phototubes. For these tubes, the number of photons received by the channel is divided by two, and that value is assigned to both phototubes.

Selecting the correct events for inclusion in the integration process is fundamental to the analysis. The source events are identified through the use of the $^{214}Bi - ^{214}Po$ coincidence which occurs with a mean lifetime of 236 μs. The data analysis for scattering is performed on the ^{214}Po α events, the group 2 events in these coincidences. The ^{214}Po α's are analyzed instead of the ^{214}Bi β's because they provide a much more accurate picture of scattering. The β's are accompanied by γ-emission; the γ's can escape from the quartz vial and cause scintillation in the main detector volume. If they produce light outside the source vial, it does not initially escape over a limited solid angle, and no scattering information is obtained. This effect was seen

in an examination of the data from the first limited aperture source trials. The TDC plots for group 1 events show much less difference between the amount of light received by tubes viewing the aperture and the amount received by those not viewing it than do the TDC plots for group 2 events. The steel jacket source minimizes the effect of β's penetrating the quartz vial, but group 2 events are also analyzed for trials using this source.

It is important to reject background events so that they are not included in the integrated photon totals. Two sources of potential background events are ^{214}Bi – ^{214}Po events in the bulk scintillator volume and accidental coincidences. Some radon was always present in the scintillator containment vessel and this radon causes ^{214}Bi – ^{214}Po coincidences to occur in the scintillator volume. These events produce a background which is spread evenly over the detector. It is accounted for by collecting data from the CTF immediately prior to insertion of a limited aperture source. The rate of coincidence events measured during this period is considered to be background, and the average number of photons received by each channel due to this background is subtracted when the integrated photon counts were determined. The relative durations of the background and source trials are accounted for in the background subtraction.

Because delayed coincidences are used to identify source events, accidental coincidences are a source of background events. An accidental coincidence occurs when two unrelated events occur within a certain time window. The CTF data acquisition system defines a group 2 event as one which occurs within 8 ms of the previous event. Because the ^{214}Bi – ^{214}Po coincidence occurs with a mean lifetime of 236 μs, only group 2 events which take place within 1 ms of the group 1 event are included in the scattering analysis. The 1 ms time window provides four mean lifetimes for ^{214}Po decay, and eliminates 88% of the accidental coincidences recorded by the data acquisition system. Accidental coincidences within the 1 ms time window

are accounted for by statistical analysis. Based on the singles rate in the CTF, the likelihood of two events occurring within 1 ms is calculated. The coincidence event rate resulting from these accidentals is then converted into a number of photons and subtracted from each channel. The accidental coincidence rate is approximately 7 per hour when the singles rate is 2 Hz. This rate is insignificant compared to the actual coincidence rate produced by the source.

Potential sources of light for the phototubes viewing the opaque side of the limited aperture source in addition to background were also considered. One source of non-scattered light to these tubes is direct emission from the source itself. The Permatex-painted source contained a small number of hairline cracks in the Permatex coating. Light escaping through these cracks travels directly to the phototubes viewing the opaque side of the source. The amount of light which escaped through these cracks was not quantified. It is assumed to be negligible, and it is not considered in the analysis. This assumption is validated by similar scattering results obtained with the steel jacket source, through which no light can leak.

Light can also escape from the source and travel directly to the phototubes viewing the opaque side of the source due to the geometry of the source itself. Figure 6.9 shows a two-dimensional representation of a limited aperture source with a 180° aperture in the CTF scintillator containment vessel. Front phototubes are defined as those in the 180° of the clear aperture, while rear phototubes are those in the 180° over which light is blocked. As indicated in Figure 6.9, a photon emitted in some locations inside the source can travel in a direction so that it escapes from the vial and reaches phototubes which are considered to be in the rear sector without being scattered. This effect was exaggerated for the Permatex-painted source because only 170°, rather than 180°, of the source surface was painted. The steel jacket source minimized this effect because the jacket which blocked light was mounted at a radius greater than that of the

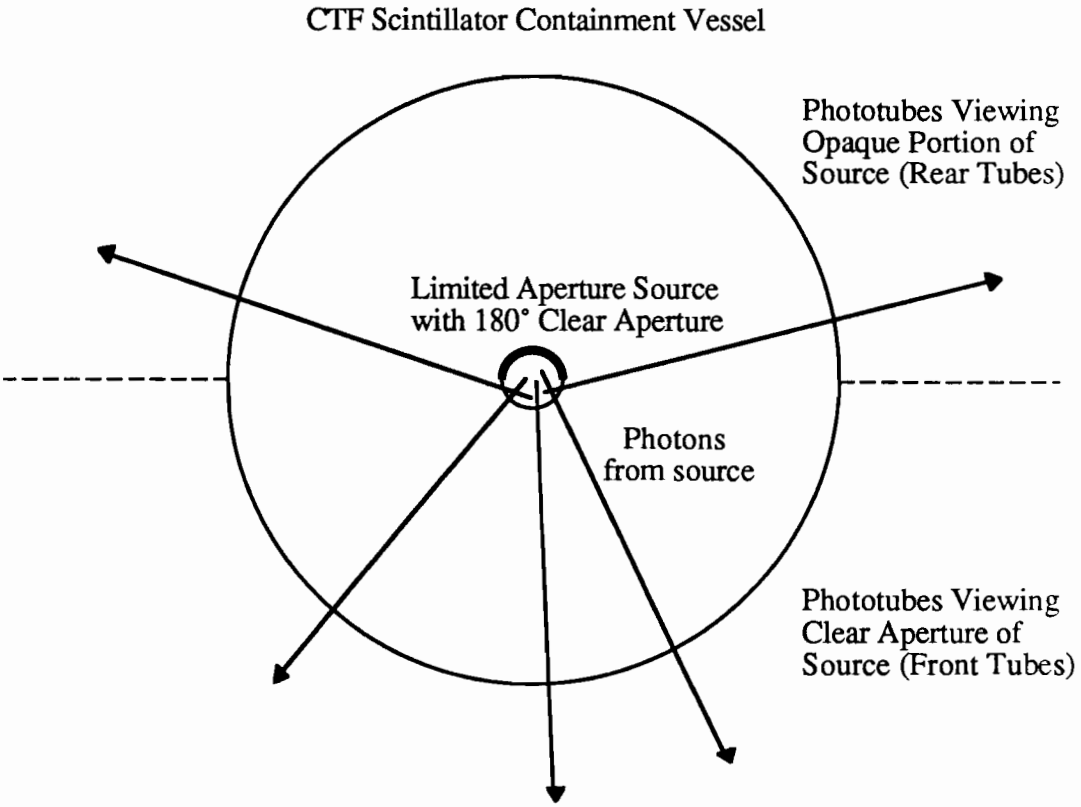

Figure 6.9. Escape of light from limited aperture source to rear phototubes. As seen in this diagram, some photons emitted inside a limited aperture source can travel directly to phototubes which view the opaque side of the source. The effect is shown here for a source with a 180° aperture.

source vial. A two-dimensional Monte Carlo was developed to determine how many photons escape from the source and travel directly to rear phototubes. The results of this Monte Carlo for a source with a 190° aperture are shown in Figure 6.10. A significant amount of light is received by the rear tubes at positions near the edge of the clear aperture, but the effect becomes minimal for tubes directly opposite the center of the aperture. Front tubes near the center of the aperture receive significantly more light than do those near its edge.

Not all the data channels in the CTF are used in the data analysis. The CTF is divided into quadrants. Only phototubes in the quadrant centered on the midpoint of the clear aperture and those in the quadrant directly opposite it are used. The use of the two opposite quadrants reduces the effect described in the previous paragraph to a level of less than 6%, as seen in Figure 6.10. There was some uncertainty (± 5°) in the orientation of the center of the clear aperture, and the effect of this on the results is negated by using data from only two quadrants.

The phototubes in rings 1 and 6 are not used in the data analysis. The geometry of the limited aperture sources blocks light traveling toward the top and bottom of the detector at all polar angles. Some light is received by phototubes in rings 1 and 6 during limited aperture source trials, but tubes in these rings always show less photon hits than tubes at similar polar angles in other rings. Because the path for light reaching these tubes is more complicated, they are not included in the analysis.

Photons received more than 20 ns after the beginning of an event are not used in the quantification of scattering. An examination of a TDC plot for a phototube viewing the opaque side of the source reveals a peak at 30 ns. This peak can be attributed to reflections off phototube glass of tubes viewing the clear aperture, as discussed in Section 6.E. Because this peak is not caused by scattering, but by

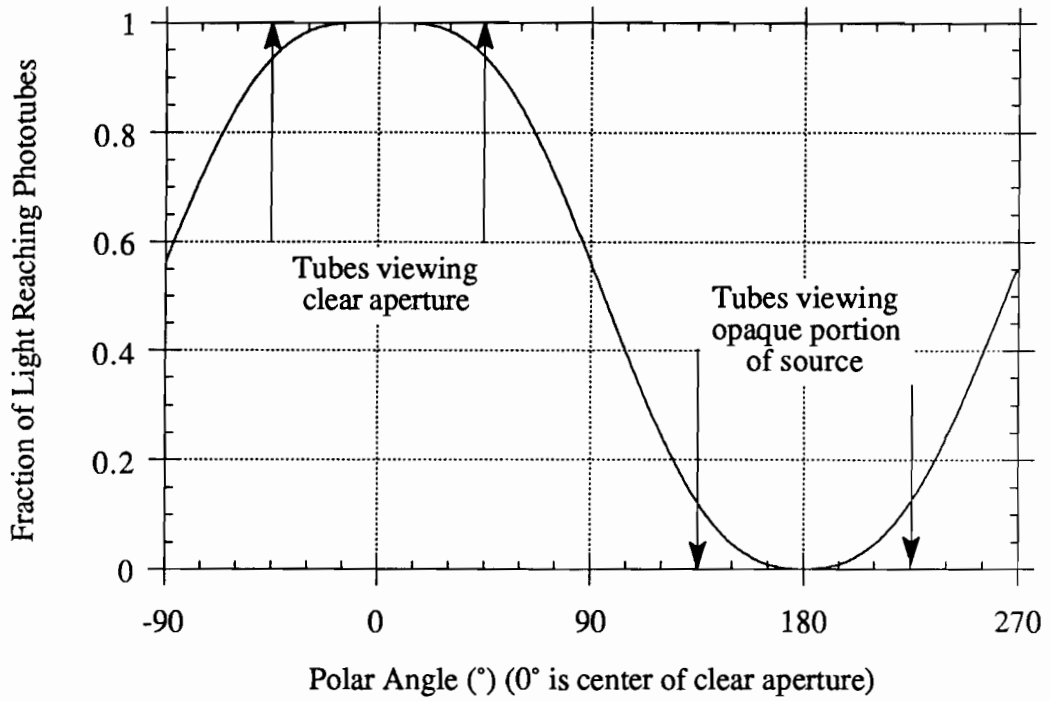

Figure 6.10. Light escape vs. polar angle. Monte Carlo results for light escape from a limited aperture source as a function of polar angle are shown here. The fraction of photons emitted inside the source which can reach phototubes at different polar angles is plotted. The center of a 190° clear aperture is oriented at 0° in this calculation. The fraction of light received by the phototubes changes significantly as a function of polar angle. By using data from only the two quadrants indicated by arrows in the figure (– 45° – 45° and 135° – 225°), the magnitude of this effect can be kept to less than 6%.

reflection, the scattering quantification is more accurate if these photons are omitted. It is only possible to omit reflected photons if they strike a channel which has not yet received any previous photons during that event. Once a channel has received one photon, the arrival time of other photons cannot be measured. The time cut of 20 ns is chosen because it results in complete removal of the 30 ns peak. This screening of reflected photons changes the integrated photon counts by less than 5%, and the inability to account for every reflected photon does not significantly affect the analysis.

The raw integrated photon counts must be adjusted for phototube efficiency. Trials with omni-directional sources indicate that some phototubes record more photon hits than others in situations when all should receive the same number. This variation may be due to differences in the efficiencies of the tubes themselves or to different collection efficiencies of their light cones. Figure 6.11 shows the number of photons received by each tube when an omni-directional source was placed in the center of the CTF for 15 hours. The source and bulk scintillator mixtures both consisted of 1.5 g/L of PPO in pseudocumene. The variation in phototube efficiency is evident in the figure because all the tubes should have received the same amount of light. In order to correct for this variation, a calibration factor is calculated for each channel. The calibration factor is determined by dividing the number of photons received by a tube by the average number of photon hits received. The raw integrated photon counts are then divided by these calibration factors to obtain counts for the final analysis. The calibration factors changed over time, and omni-directional source trials for the calibration were carried out immediately prior to the respective limited aperture source trials. Table 6.1 lists the relative phototube efficiencies calculated prior to each set of limited aperture source trials.

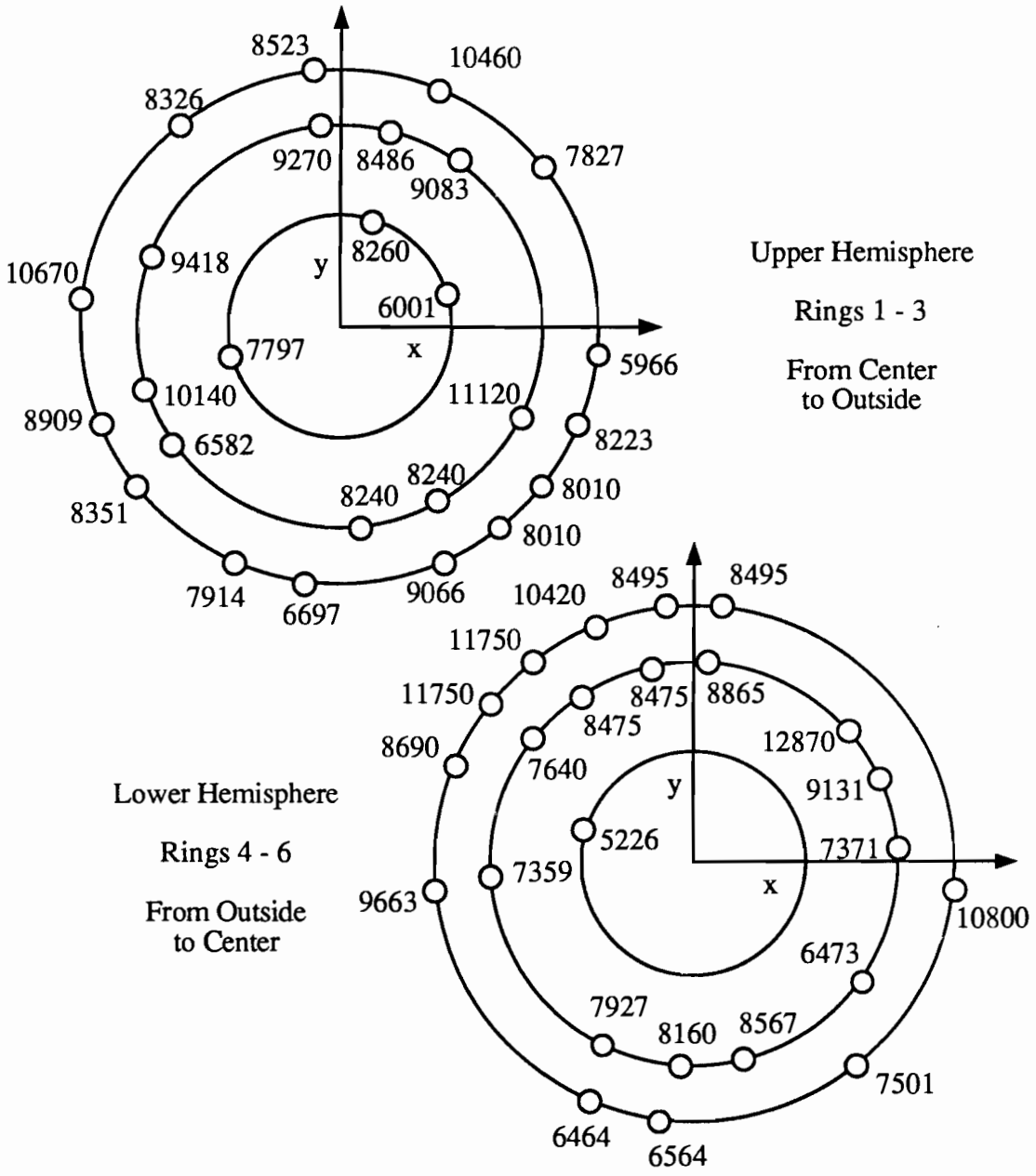

Figure 6.11. Photons received during omni-directional source trial. The number of photons received by each active phototube in the CTF when an omni-directional source was positioned at its center for 15 hours is shown here. Both source and bulk scintillator mixtures consisted of 1.5 g/L of PPO in pseudocumene.

Table 6.1. Phototube efficiencies. The relative efficiencies of the active phototubes in the CTF were calculated by examining the data from an omni-directional source trial collected prior to the limited aperture source trials with each scintillator mixture. Phototube efficiency was defined as the ratio of the number of photons received by a phototube to the average number received during that trial. A dash (-) in the table indicates that the tube has become inactive.

Tube Number	PC + PPO†	PC + PPO + bis-MSB†	Pure PC†
2	0.694	-	-
3	0.955	0.888	0.773
6	0.902	0.785	0.697
10	1.286	1.115	1.296
12	0.953	0.916	0.948
13	0.953	0.916	0.948
16	0.761	-	-
17	1.173	0.888	-
19	1.089	0.955	1.095
22	1.072	0.886	-
23	0.982	-	-
24	1.051	0.975	1.100
27	0.690	-	-
30	0.905	-	-
32	1.210	-	-
34	0.986	-	-
36	0.963	0.873	1.022
39	1.234	1.092	1.280
41	1.030	1.078	1.129
42	0.966	-	-
44	0.915	0.857	0.913
45	0.775	0.724	0.861
47	1.049	0.355	0.415
48	0.926	1.009	0.731
49	0.926	1.009	-
50	0.951	1.079	-
51	1.249	1.060	-
57	0.983	0.847	1.041
58	0.983	0.847	1.041
59	1.205	1.074	1.056
60	1.359	0.372	-
61	1.359	0.961	0.426
62	1.005	1.174	1.004

Tube Number	PC + PPO†	PC + PPO + bis-MSB†	Pure PC†
64	1.118	0.803	1.347
68	0.748	0.761	0.774
69	0.759	0.761	0.874
72	0.868	-	-
76	0.853	0.897	0.768
77	1.056	1.484	1.444
78	1.489	1.805	1.537
80	1.025	0.994	-
81	0.980	0.712	0.711
82	0.980	-	-
83	0.884	-	-
85	0.851	0.706	0.741
88	0.917	-	-
89	0.944	0.898	0.881
90	0.991	0.783	0.775
92	0.749	0.721	0.666
97	0.604	0.705	0.704

† The column headings refer to the following scintillator mixtures.

PC + PPO: 1.5 g/L of PPO in pseudocumene

PC + PPO + bis-MSB: 20 mg/L of bis-MSB and 1.33 g/L of PPO in pseudocumene

Pure PC: pure pseudocumene

The final photon counts for a limited aperture source trial in a scintillator of 1.5 g/L of PPO in pseudocumene are shown in Figure 6.12. The center of the aperture was oriented along the –y axis in this trial. The number of photon hits was averaged over the phototubes in the front and rear quadrants (one centered on the midpoint of the clear aperture and the other directly opposite from it). The scattering ratio is defined as the ratio of the average number of photon hits received in the rear quadrant to the average number received by phototubes in the front quadrant. This scattering ratio, r, can also be expressed in terms of the fraction of light scattered, s, and the fraction which travels directly to the phototubes, d.

$$r = \frac{\frac{1}{2}s}{d + \frac{1}{2}s} = \frac{\frac{1}{2}s}{1 - \frac{1}{2}s} \qquad (6.1)$$

The second part of eq 6.1 follows because the sum of the scattered light and the direct light is unity.

Eq 6.1 assumes isotropic scattering in the detector so that the front tubes receive half the scattered light and the rear tubes receive the other half. The assumption of isotropic scattering is valid for absorption-reemission because the excited molecules in a liquid solution radiate isotropically. Rayleigh scattering has a directional dependence of $1 + \cos^2 \theta$, where θ is the angle between the incident and scattered directions. The scattering of each individual photon is not isotropic. The effect of Rayleigh scattering in the CTF was investigated by numerically integrating the $1 + \cos^2 \theta$ distribution over regions of the detector. These calculations showed that because of the spherical symmetry of the CTF detector and the initial isotropic emission (although limited to approximately 2π steradians) of photons from the source, the overall elastic scattering of photons is isotropic when the phototubes are grouped in quadrants for analysis.

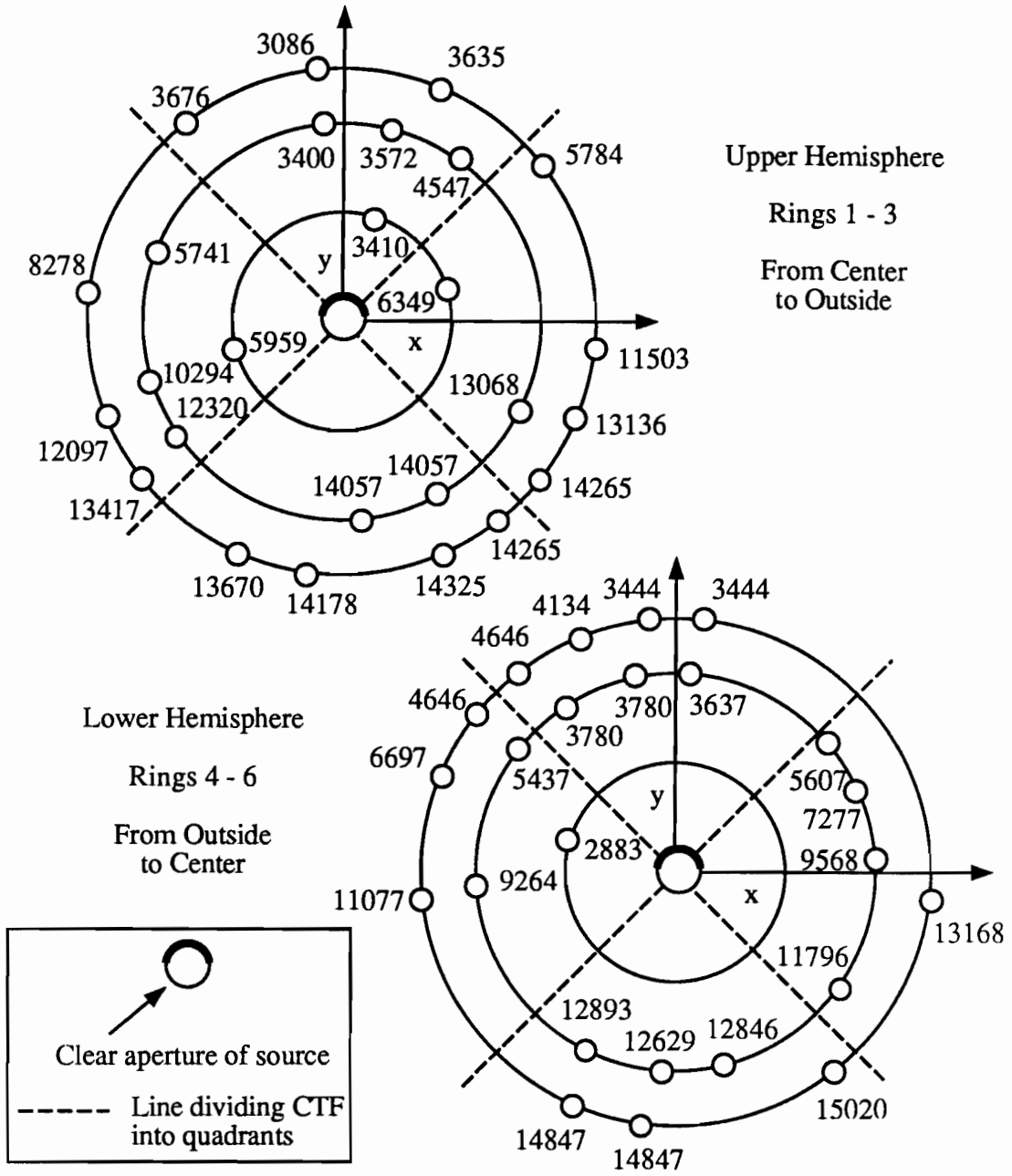

Figure 6.12. Final integrated photon counts for limited aperture source. These final integrated photon counts for each active CTF phototube were obtained for the source trial in which the Permatex-painted limited aperture source was inserted in the center of the CTF and the center of its aperture was oriented along the –y axis.

Eq 6.1 gives a quantitative result for the fraction of photons which are scattered at least once between their emission at the center of the scintillator containment vessel and their arrival at a phototube 3.3 m distant after traveling through at least 1 m of scintillator. Photons lost in the scintillator do not affect the result. This calculation does not provide any information about how many times the scattered photons are scattered or about the length scale on which the scattering occurs.

D. CTF Scattering Results

Data from the limited aperture source trials were analyzed using the techniques described in Section 6.C. Table 6.2 lists the ratio between the number of photons received by phototubes in the quadrant viewing the opaque side of the limited aperture source and the number of photons received by tubes viewing the clear aperture for each limited aperture source trial. The fraction of light scattered for each trial was calculated using eq 6.1, and these values are also listed in Table 6.2. The two trials with 1.5 g/L of PPO in pseudocumene produced quite similar values for the amount of scattering. The average fraction of light scattered in this mixture was 0.42 ± 0.04. Four trials were carried out for the bis-MSB scintillator. The scattering values determined in these trials vary over a wide range, and the error in the average result is rather large. The average fraction of light scattered was found to be 0.67 ± 0.09. Only one trial was carried out for the pure pseudocumene scintillator. The fraction of light scattered was found to be 0.20 ± 0.02.

Very little scattering is observed in the pure pseudocumene, a larger amount takes place in the scintillator with only the PPO fluor, and the most scattering occurs in the bis-MSB scintillator. The small amount of scattering measured in pure pseudocumene is not surprising. Light is emitted from the source with the PPO

Table 6.2. Light Scattering results measured in the CTF. Light scattering results are reported in two forms here: as the ratio of the number of photons received by tubes viewing the clear aperture to the number received by tubes viewing the opaque portion of the source and as the fraction of light scattered (calculated using eq 6.1).

	Ratio: Photons at Front Tubes to Photons at Back Tubes	Fraction of Light Scattered
PC + PPO†		
Trial 1 (-y)	0.266	0.420
Trial 2 (-x)	0.280	0.438
Average	0.27 ± 0.03	0.43 ± 0.04
PC + PPO + bis-MSB†		
Trial 1 (+y)	0.435	0.606
Trial 2 (+x)	0.684	0.812
Trial 3 (-y)	0.532	0.695
Trial 4 (-x)	0.404	0.575
Average	0.51 ± 0.11	0.67 ± 0.09
Pure PC†		
Trial 1 (-y)	0.11 ± 0.02	0.20 ± 0.03

† The nomenclature in the table refers to the following scintillator mixtures.

PC + PPO: 1.5 g/L of PPO in pseudocumene

PC + PPO + bis-MSB: 20 mg/L of bis-MSB and 1.33 g/L of PPO in pseudocumene

Pure PC: pure pseudocumene

emission spectrum. An examination of Figure 5.8 indicates that in pseudocumene the attenuation length for the shortest wavelengths (near 350 nm) in the PPO emission spectrum is 1.5 m. This increases to more than 7 m for emission wavelengths of 430 nm. The apparent attenuation in pseudocumene at all PPO emission wavelengths is due to elastic scattering, and no loss of light should be observed. Light emitted from PPO is expected to travel without much scattering through pseudocumene, and this was found to be the case.

It is possible to estimate the amount of scattering expected in a scintillator mixture by evaluating the convolution integral of the PPO emission spectrum and the scintillator mixture's attenuation spectrum (whether the attenuation is due to inelastic or elastic scattering). This method will not produce exact results because it cannot account for some effects such as multiple scattering steps, but it is useful to provide a qualitative understanding of the scattering process. This convolution integral was calculated for a PPO emission spectrum and a pure pseudocumene scintillator to reflect the limited aperture source trial with pure pseudocumene. Pseudocumene was treated as an elastically scattering medium over all PPO emission wavelengths. The calculation predicted that 24.5% of the light emitted by the source in the center of the vessel would be scattered before it traveled 1 m through the scintillator and escaped from the scintillator containment vessel. This result differs by 20% from the fraction of light scattered of 0.20 listed in Table 6.2.

The scintillator containing 1.5 g/L of PPO in pseudocumene scattered more light emitted from PPO than the pure pseudocumene did. This additional scattering is due to inelastic scattering (absorption-reemission) by PPO. Elastic scattering in the pseudocumene-PPO scintillator is almost entirely due to the solvent as seen by the relative attenuation lengths for PPO and pseudocumene at wavelengths above 375 nm

in Figure 5.8. It was not possible to use the limited aperture source ADC data to determine the length scale on which this scattering occurred.

Convolution of the PPO emission spectrum with the attenuation spectrums of pseudocumene and PPO can be used to obtain an estimate of the scattering expected in the CTF. In this calculation, pseudocumene was allowed to scatter elastically over all PPO emission wavelengths; PPO scattered inelastically from 300 – 375 nm and elastically at wavelengths above 375 nm. Evaluation of the convolution integral predicted that 48.4% of the light emitted from the source would be scattered before it escaped from the scintillator containment vessel. A similar evaluation showed that 12.6% of the light would be scattered within 0.5 cm. Because 0.5 cm is the average distance a photon must travel before leaving the source vial, scattering within this distance may not show up in the CTF results. The convolution results indicate that between 36 and 48% of the source light should be scattered in the CTF. This can be compared to the experimental result of 43%. The calculations also showed that almost all the scattering that takes place more than 10 cm from the source is due to elastic scattering by the pseudocumene, and the majority of the scattering that occurs within 10 cm of the source is due to absorption-reemission by the PPO.

The largest amount of scattering was observed in the scintillator containing 20 mg/L of bis-MSB and 1.33 g/L of PPO in pseudocumene. The bis-MSB is added to the scintillator as a wavelength shifter to red-shift the emitted photons so that they can travel through the medium with less attenuation. A scintillator containing 1.33 g/L of PPO and 20 mg/L of bis-MSB will initially emit light with a PPO spectrum. When bis-MSB is present at a concentration of 20 mg/L, energy transfer to bis-MSB from PPO takes place radiatively. Because the source is small, light emitted by PPO escapes from it and the energy transfer to bis-MSB can take place in the bulk scintillator. This shows up as scattering in the data analysis described above. If the

transfer of energy to bis-MSB takes place within 5 – 10 cm of the center of the source, it does not affect positional resolution and the bis-MSB serves its intended purpose. If the transfer does not take place within this distance, a higher concentration of bis-MSB is required for it to be an effective wavelength shifter.

Figure 6.13 shows the attenuation length (due to both absorption and elastic scattering) as a function of wavelength for bis-MSB at a concentration of 20 mg/L. Below 440 nm, bis-MSB shows absorption of light; above this wavelength the attenuation is due to elastic scattering by the fluor. With 20 mg/L of bis-MSB, the attenuation length of light in the PPO emission spectrum varies from 0.1 cm at 350 nm to 10 m at 430 nm. Radiative energy transfer from PPO to bis-MSB takes place over a wide range of distances. The shorter wavelength photons emitted from PPO are absorbed by bis-MSB inside the source vial, but the ones with long wavelengths are likely to escape from the CTF before energy transfer can take place. Photons emitted in the middle of the PPO spectrum will be absorbed by bis-MSB within 10 cm, and their wavelength is effectively red-shifted. The long wavelength photons which are not strongly absorbed by the bis-MSB are also weakly attenuated by the PPO and pseudocumene, and it is not necessary that they have their wavelength shifted in order to pass without attenuation through the scintillator. Data in addition to those provided by the ADC scattering results are needed to judge the effectiveness of bis-MSB addition to the scintillator.

The convolution integral described for the pure pseudocumene and pseudocumene-PPO scintillators can also be applied to the scintillator containing bis-MSB. For this analysis the PPO emission spectrum is used along with the attenuation spectra from pseudocumene, PPO, and bis-MSB. Pseudocumene scatters elastically at all PPO emission wavelengths, PPO scatters inelastically below 375 nm and elastically above this wavelength, and bis-MSB scatters inelastically below 440 nm and

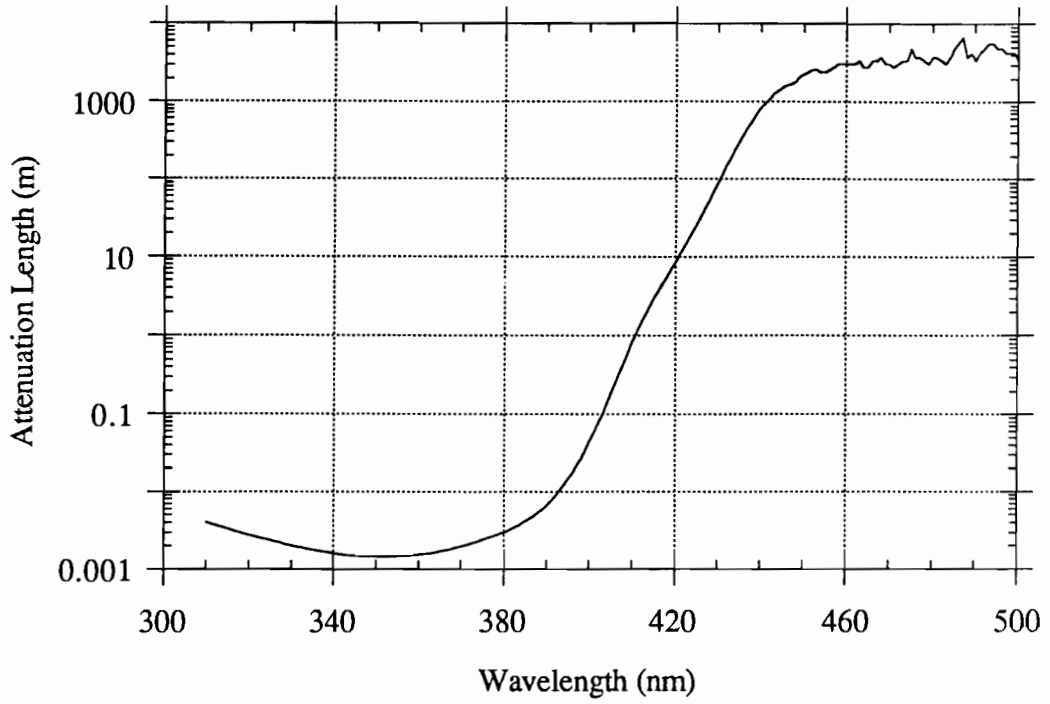

Figure 6.13. Attenuation length for 20 mg/L of bis-MSB. The fluor bis-MSB at a concentration of 20 mg/L attenuates light as a function of wavelength as shown in the plot. The attenuation lengths shown here do not include the effects of the solvent in which the fluor is dissolved. The attenuation is due to absorption at wavelengths below 440 nm and to elastic scattering at longer wavelengths.

elastically at longer wavelengths. This calculation predicts that 74.5% of the light emitted by the source will be scattered before it travels 1 m in the scintillator and escapes from the scintillator containment vessel. It also indicates that 49.6% of the light will be scattered within 0.5 cm, and 63.8% will be scattered within 10 cm. A large fraction of the light scattered within 0.5 cm (nominally inside the source) must be scattered again in order to obtain the experimental value of 67% for light scattering. The amount of scattering taking place within 10 cm reflects the effectiveness of bis-MSB as a wavelength shifter. Scattering within this distance will not reduce the positional resolution of the detector. Only 10% of the light is scattered between 10 cm and 1 m from the source. Most of the light which is not wavelength-shifted by the bis-MSB is of a sufficiently long wavelength to escape from the scintillator containment vessel without attenuation. Some of the scattering (12% of the total light) at distances less than 10 cm is due to PPO. Light reemitted by the PPO is likely to be scattered again by bis-MSB.

The light scattering results from the ADC analysis are very useful for comparing the relative amounts of scattering which occur in different scintillator mixtures. The calculations of the fractions of light scattered provide a quantitative picture of what is occurring in the scintillator. These quantitative results agree with qualitative descriptions which can be developed by examining the attenuation length curves of the different scintillator components. Convolution integrals of the PPO emission spectrum and the attenuation spectra of the scintillator mixtures are also useful in obtaining an understanding of the scattering process. The convolution calculations predict the same magnitudes of scattering as were found experimentally, although they do not agree exactly. These calculations also allow statements to be made about where the scattering occurs; the ADC results cannot provide such statements. Unfortunately, the convolution technique does not account for multiple

scattering steps inside the scintillator containment vessel. A more sophisticated technique is needed to allow consideration of this possibility. A mechanism for such an analysis is present in the Monte Carlo simulation of the CTF developed by the collaboration, as discussed in Chapter 7. The experimentally measured fractions of light scattered are useful as test cases for the Monte Carlo simulation. These measurements provide a benchmark with which the simulation results can be compared.

E. Photon Arrival Time Distributions

The scattering analysis considered in Sections 6.C and 6.D involved the use of ADC data from the limited aperture source trials. TDC data were also collected during these trials. The TDC information was used on-line to confirm that the limited aperture source was functioning as expected. Although it is not useful for determination of the fraction of light scattered, the TDC data can be employed in other ways to learn more about light propagation in the detector.

The TDCs record the arrival time of the first photon to reach each phototube. The data analysis system defines zero time as the beginning of an event. An event begins when a certain number of phototubes, defined by the trigger setting, receive a photon within 20 ns. Because some tubes receive photons before the event officially begins, negative arrival times are possible.

The TDC data from channels receiving more than one photon during an event are inaccurate. The TDCs record the arrival time of only the first photon. If channels receiving more than one photon are used, the arrival times of later photons are ignored. Because the shortest arrival time is counted, but the longer arrival times are not, the arrival time distribution is skewed towards shorter times. This problem is alleviated by only considering channels which have received a single photon during

the event. No arrival times are ignored with this procedure, and shorter arrival times are not favored. Many of the data from an event are discarded in this procedure, but the photon arrival time distributions obtained in this way are accurate.

The arrival time distributions presented here only contain TDC information from channels receiving a single photon. The channels receiving single photons are determined through analysis of the ADC data. Group 2 events from ^{214}Po α's are used in the TDC analysis, and events with a coincidence time of more than 1 ms are rejected to reduce the number of accidental coincidences. Only data from phototubes in rings 2 to 5 are used in the TDC analysis. Rings 1 and 6 are not used in order to avoid effects at the top and bottom of the detector caused by source end caps and the shape of the limited apertures.

The distribution of photon arrival times for an omni-directional source placed at the center of the scintillator containment vessel when the scintillator consisted of 1.5 g/L of PPO in pseudocumene is shown in Figure 6.14. The number of photons received as a function of time is summed over all the phototubes. The shape of the arrival time distribution is well-described from 0 to 20 ns by an exponential decay with a decay time of 5.8 ns. A similar study by other collaboration members found a decay time of 5.7 ns.[7] The photon arrival time distribution curves are fitted with exponential decays up to a time of only 20 ns because other effects in addition to the scintillator decay become important at longer times. The CTF measured decay time of 5.8 ns is longer than the scintillator decay time of 3.3 ns[8] measured for the same mixture in small-scale measurements. The lengthening of the decay time can be attributed to the scattering of light due to absorption-reemission in the scintillator. The reemission steps add additional decay time for photons which are scattered in this manner and increase the overall decay time.

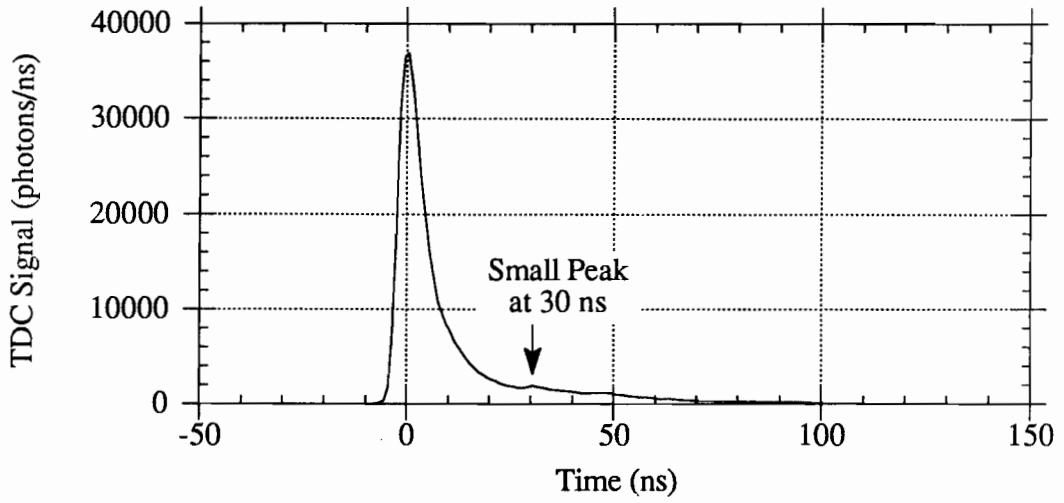

Figure 6.14. Photon arrival time distribution: omni-directional source in 1.5 g/L PPO-pseudocumene. This distribution was measured when an omni-directional source was inserted into the center of the CTF. Both source and bulk scintillators mixtures consisted of 1.5 g/L of PPO in pseudocumene. The decay time measured from 0 to 20 ns is 5.8 ns. There is a small peak at 30 ns caused by reflections from phototube glass.

The reemission steps do not increase the decay time in a purely exponential manner. They influence it as expressed in eqs 4.27 – 4.29, and the decay is expressed as $t^n e^{-\lambda t}$, where n is the number of re-emissions. The reemission steps decrease the quality of the fits obtained using a pure exponential to describe the observed decay curve. It is not possible to develop an analytical function to fit this non-exponential decay for two reasons: an unknown number of absorption-reemission steps takes place and there is an additional time delay in the photon arrivals caused by longer flight paths when the photons are not reemitted in their original direction. (This additional flight time is negligible if the scattering takes place on a short length scale.) Such an analytical function would also have to account for elastic scattering which adds time delays due to lengthened photon flight paths. Because many of the photons are not scattered, the exponential decay still fits the data relatively well, and it can be used for purposes of comparison. Accepting this approximation, scattering effectively increases the decay time observed in the CTF over that observed in small-scale measurements.

The effect of absorption-reemission on scintillator decay time is shown in Figure 6.15. Two decay curves are shown here for a scintillator with a small-scale decay time of 3 ns. A purely exponential decay is plotted, indicating the small-scale behavior. The second curve is calculated based on absorption-reemission timing behavior as expressed in eqs 4.26 – 4.28. The calculations were carried out for the case when 60% of the light was unscattered, 30% was absorbed and reemitted once, and 10% underwent two absorption-reemission steps. From Figure 6.15 it is clear that absorption-reemission lengthens the decay time of the scintillator. If the curve including inelastic scattering is forced to fit an exponential, a decay time of 4.2 ns is obtained. Absorption-reemission causes an increase in the effective decay time of the scintillator as observed in the CTF.

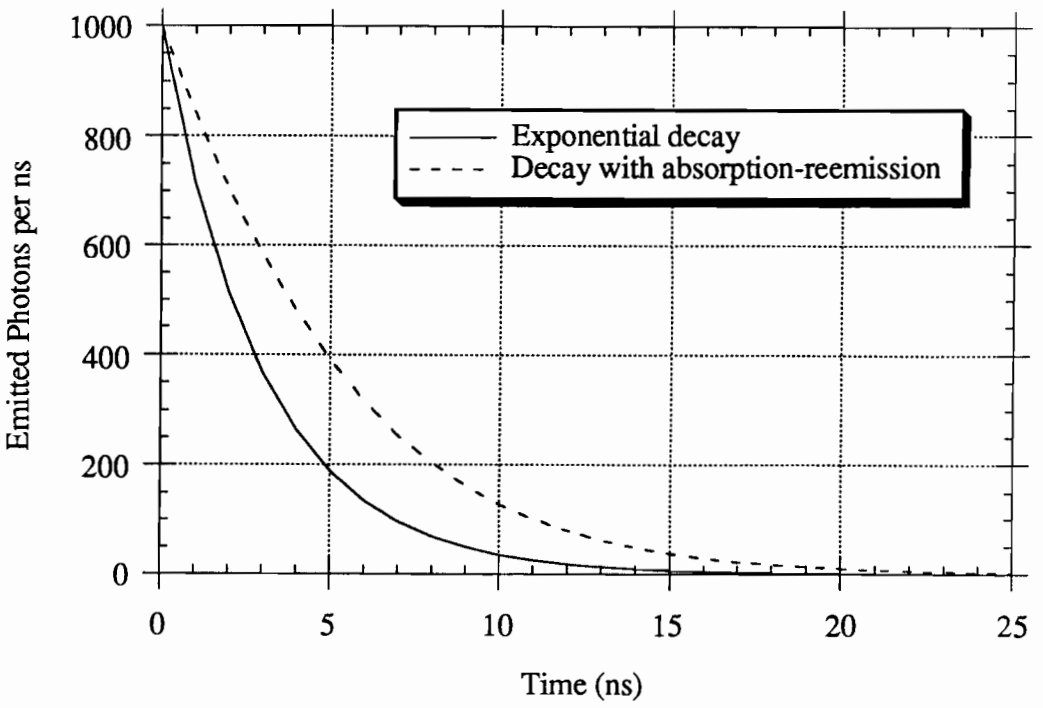

Figure 6.15. Effect of absorption-reemission on decay time. The effect of absorption-reemission on scintillator decay time was calculated for a scintillator with a decay time of 3 ns. The purely exponential decay of the scintillator is shown in the figure along with a decay in which 60% of the light is not scattered, 30% undergoes one absorption-reemission step, and 10% undergoes two inelastic scattering steps. The decay following absorption-reemission is treated as in eqs 4.26 – 4.28. The decay follows a $t^n e^{-\lambda t}$ pattern, where n is the number of reemission steps. The decay is slower when absorption-reemission is included. If the curve is forced to fit an exponential form, a decay time of 4.2 ns is obtained. This is greater than the scintillator decay time of 3 ns.

Figure 6.16 shows photon arrival times for an omni-directional source at the center of the CTF when the scintillator containment vessel contained 20 mg/L of bis-MSB and 1.33 g/L of PPO in pseudocumene. The source vial contained the same scintillator mixture as the containment vessel. The curve can again be fitted reasonably well by an exponential decay at times from 0 to 20 ns. In Figure 6.16 the decay time is 5.79 ns. Small-scale measurements indicated a decay time of 3.9 ns for a mixture of 20 mg/L of bis-MSB and 1.33 g/L of PPO in pseudocumene.[9] This value is greater than the decay time of the scintillator without bis-MSB (3.3 ns) because the bis-MSB decay time must be added to the PPO decay time due to the radiative energy transfer which takes place. The CTF decay time is again greater than the small-scale result because of scattering inside the detector.

A small peak at 30 ns can be seen in Figure 6.16; it is due to reflections off phototube glass on the opposite side of the detector from the receiving tube. The additional transit time after the reflection for travel through 2.3 m of water, 2 m of scintillator, and 2.3 m of water is 30.4 ns. A peak at 30 ns can also be seen in Figure 6.14, but it is less obvious in that photon arrival time distribution. The peak in Figure 6.14 has the same origin as the one in Figure 6.16.

The photon arrival time distribution was also measured for an omni-directional source in the center of the CTF when the scintillator containment vessel held pure pseudocumene. The source vial contained a mixture of 1.5 g/L of PPO in pseudocumene. The results are shown in Figure 6.17. An exponential decay fitted to the region of Figure 6.17 between 0 and 20 ns gives a decay time of 5.2 ns. This is shorter than the decay time found in Figure 6.14, although the same mixture was present inside the source in both cases. The decay time is shorter in Figure 6.17, and closer to that found in small-scale measurements, because less scattering occurs in the

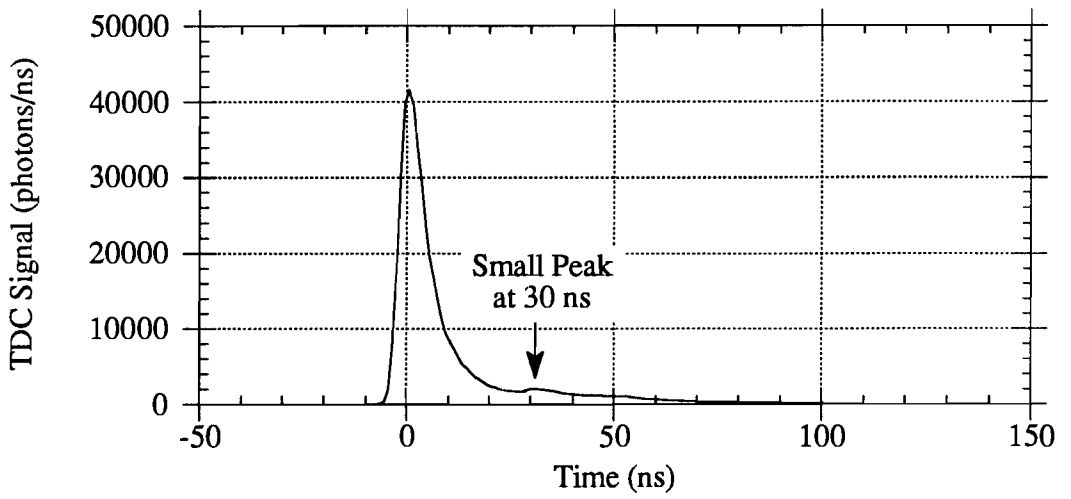

Figure 6.16. Photon arrival time distribution: omni-directional source in 20 mg/L bis-MSB-1.33 g/L PPO-pseudocumene. This distribution was measured when an omni-directional source was inserted into the center of the CTF. Both source and bulk scintillators mixtures consisted of 20 mg/L of bis-MSB and 1.33 g/L of PPO in pseudocumene. The decay time measured from 0 to 20 ns is 5.8 ns. A small peak at 30 ns due to reflections off phototube glass can be seen.

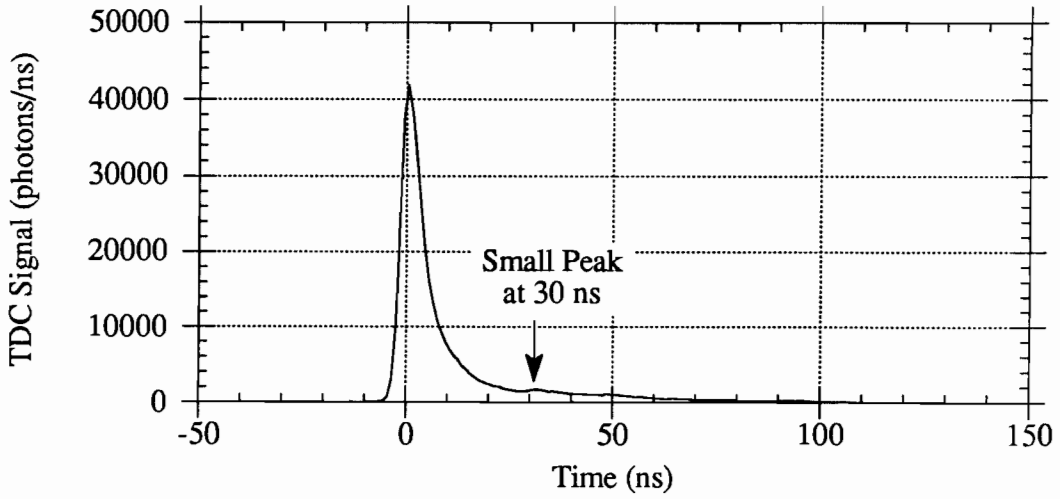

Figure 6.17. Photon arrival time distribution: omni-directional source in pure pseudocumene. This distribution was measured when an omni-directional source was inserted into the center of the CTF. The source vial contained a scintillator mixture consisting of 1.5 g/L of PPO in pseudocumene. The bulk scintillator was pure pseudocumene. The decay time measured from 0 to 20 ns is 5.2 ns. There is a small peak at 30 ns due to reflections off phototube glass.

pure pseudocumene than in the pseudocumene-PPO scintillator. A small peak can again be seen at approximately 30 ns.

Photon arrival time distributions were also measured using the limited aperture sources. Figure 6.18 shows two distributions obtained when the Permatex-painted source was located at the center of the CTF. Both the source vial and the CTF scintillator containment vessel held a mixture of 1.5 g/L of PPO in pseudocumene. Figure 6.18a shows the photon arrival time distribution for phototubes in the quadrant viewing the clear aperture. These tubes received both direct and scattered light. An exponential decay curve fitted between 0 and 20 ns indicates a decay time of 5.9 ns. This decay time is quite similar to that measured using the omni-directional source with the same source and bulk scintillator compositions. This similarity is expected because both direct and scattered light are received in both cases. One difference between Figures 6.15 and 6.18a is the lack of a peak at 30 ns in Figure 6.18a. A slow decay of a small portion of the received light can be observed at times greater than 20 ns, but there is no peak. Few reflections are seen off phototube glass on the opposite side of the CTF in this case because no photons are originally emitted in the opposite direction with the limited aperture source.

The structure seen in Figure 6.18b for phototubes in the rear quadrant is much different than that observed in the other photon arrival time distributions presented previously. These tubes receive only scattered light. An exponential-like decay is present from 0 to 20 ns, but a small shoulder in the curve can be seen at approximately 10 ns. The shoulder at 10 ns can be attributed to scattering at the nylon vessel. The extra transit time due to an additional path length of 2 m in the scintillator is 10 ns. Light scattering at the vessel occurs in the situations shown in Figures 6.14, 6.16, 6.17, and 6.18a as well, but the direct light component in these cases is enough to overwhelm the contribution of the nylon scattering.

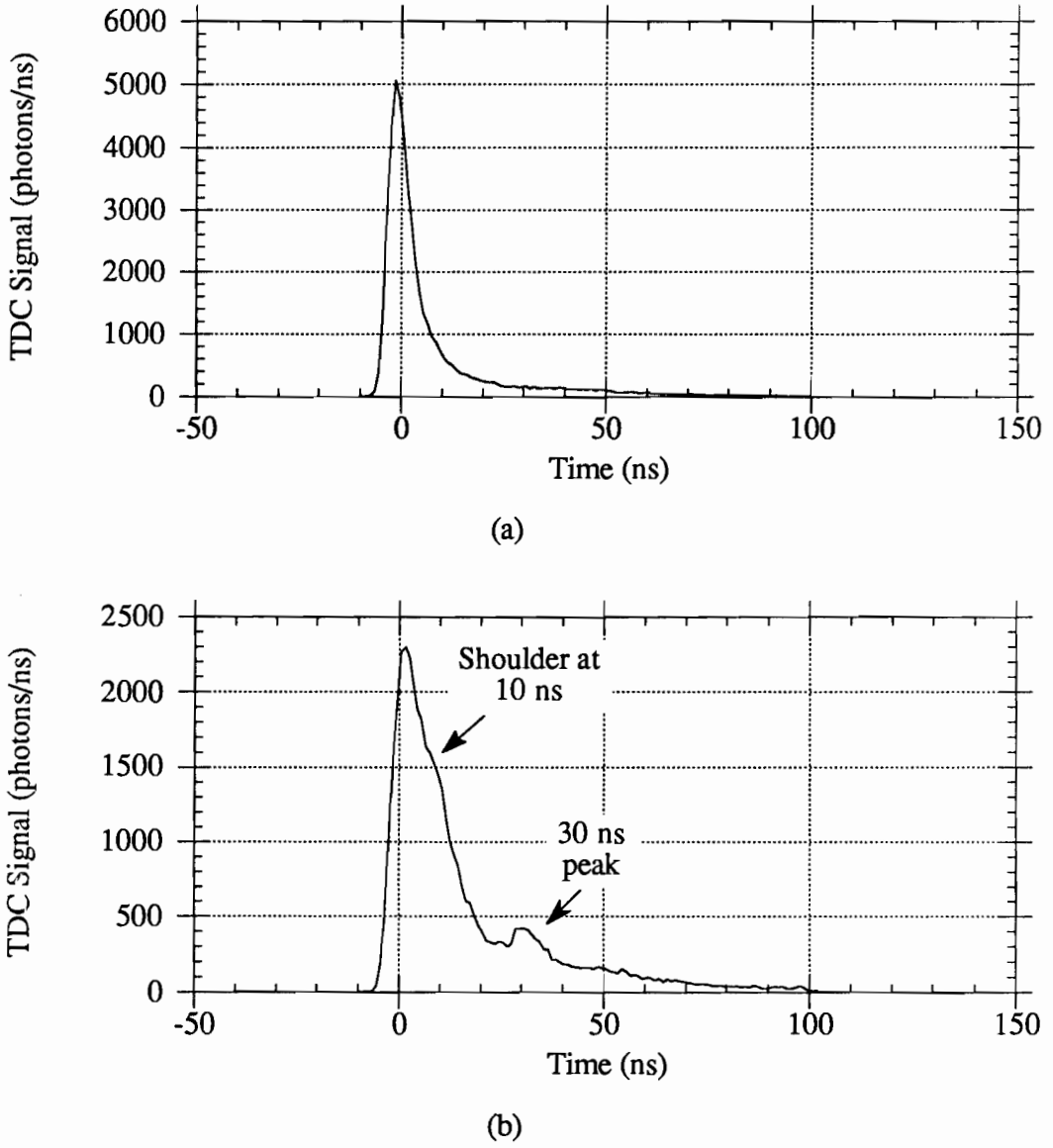

Figure 6.18. Photon arrival time distributions: limited aperture source in 1.5 g/L PPO-pseudocumene. These distributions are shown for a) tubes in the front quadrant and b) tubes in the rear quadrant for a limited aperture source located at the center of the CTF. Exponential fits from 0 to 20 ns result in decay times of a) 5.9 ns and b) 11.1 ns. In b) a shoulder at 10 ns due to scattering at the nylon vessel and a peak at 30 ns due to reflections from phototube glass can be seen.

Light scattering at the nylon vessel is an effect which has not been considered previously in this thesis. Although the work here has concentrated on the effect of the scintillator components on light propagation, it is obvious from the shoulder in Figure 6.18b that the nylon must also be considered. Attempts were made to measure the elastic scattering of nylon in air using the LS50. The experiments were similar to those described for organic liquids in Chapter 5. The nylon scattered too much light to allow the scattering to be quantified; the phototube detector in the LS50 was saturated by the elastic scattering. The measurements were examined qualitatively, and they showed that nylon scattering did not change significantly over the wavelength region from 300 to 500 nm. It is reasonable to expect that nylon elastic scattering obeys a λ^{-4} dependence.

The effect of the nylon membrane on light propagation was also studied by the Perugia group of the collaboration.[10] They imitated the conditions inside the CTF and exposed nylon strips to water on one side and a mixture of 1.5g/L of PPO in pseudocumene on the other. After nine months, they found that the transmittance of the nylon decreased, especially over the region of PPO absorption. Further analysis indicated that when excited, the nylon emitted light with a spectrum similar to that of PPO. The Perugia group concluded that the water swelled the polymer chains in the nylon and that PPO diffused into the membrane and remained there. It is likely that a similar diffusion occurred in the CTF.

The studies on light scattering by nylon described above must be used with caution in any attempts to describe the behavior of the nylon scintillator containment vessel in the CTF. These studies were carried out on nylon in air. More reflection occurs from a nylon-air interface than from nylon surrounded by water and pseudocumene; the liquids have refractive indices more similar to nylon than air does. This extraneous reflection is likely to overwhelm other effects the nylon may have.

Given this caveat, the studies indicate that propagation effects at the nylon vessel are likely to include elastic scattering which is relatively independent of wavelength and inelastic scattering which is most important over wavelengths where PPO absorbs.

The shoulder at 10 ns decreases the quality of an exponential fit over the 0 to 20 ns range, but an exponential decay time can still be obtained for purposes of comparison. A decay time of 11.1 ns was found in this manner. The overall decay time for the scattered light is longer than for the direct light because of the absorption-reemission steps. Longer photon flight paths could also introduce delays if the scattering occurred on a long enough distance scale. As discussed for the omni-directional sources, a pure exponential decay is not strictly valid for modeling the decay of the scattered light. An exponential is used, however, because of the difficulty in obtaining a more accurate analytical form which is still tractable.

The reflection peak at 30 ns is again present. Here it is more pronounced with respect to the main peak than in Figure 6.14. The amount of reflected light is the same in both cases, but there are less scattered photons in the main peak of Figure 6.18b than direct plus scattered photons in the main peak of Figure 6.14.

In Figure 6.19, photon arrival time distributions obtained with a 180° steel jacket limited aperture source located in the center of the CTF are shown. Both the source vial and the CTF contained a mixture consisting of 20 mg/L of bis-MSB and 1.33 g/L of PPO in pseudocumene. The distribution for tubes in the front quadrant is shown in Figure 6.19a. An exponential decay curve fitted from 0 to 20 ns yielded a decay time of 5.4 ns. This is similar to that found in Figure 6.16 for the omni-directional source when the source and bulk scintillators contained bis-MSB. A small peak at 30 ns is seen in Figure 6.19a. With bis-MSB in the scintillator, enough scattering takes place so that a noticeable number of reflections take place off the phototube glass of tubes originally blocked from receiving light.

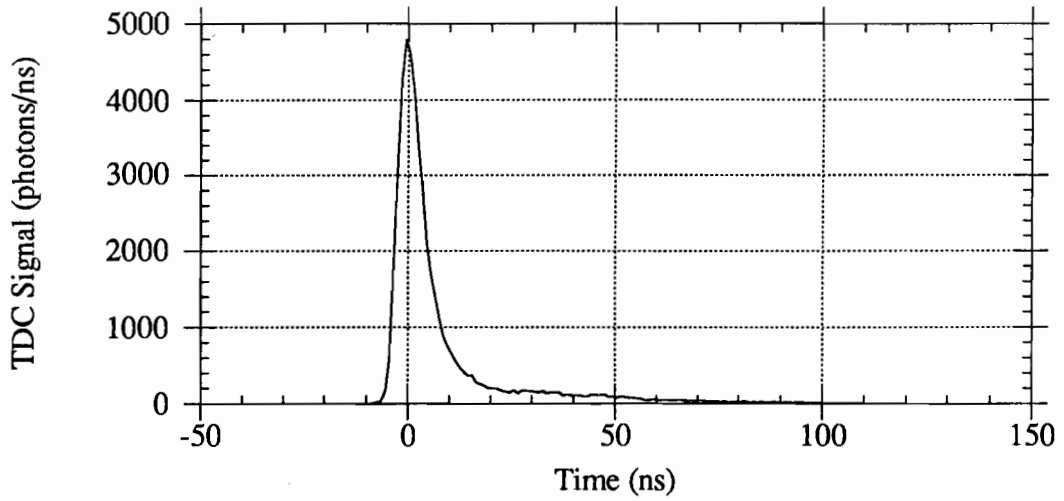

(a)

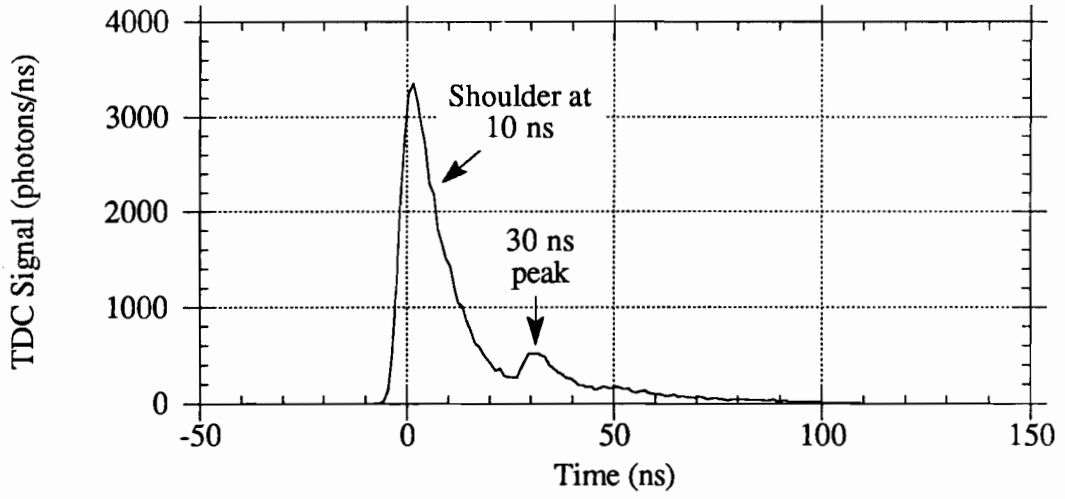

(b)

Figure 6.19. Photon arrival time distributions: limited aperture source in 20 mg/L bis-MSB-1.33 g/L PPO-pseudocumene. These distributions are shown for a) tubes in the front quadrant and b) tubes in the rear quadrant for a limited aperture source located at the center of the CTF. Exponential fits from 0 to 20 ns result in decay times of a) 5.4 ns and b) 8.5 ns. In b) a shoulder at 10 ns due to scattering at the nylon vessel and a peak at 30 ns due to reflections from phototube glass can be seen.

The photon arrival time distribution for tubes in the rear quadrant is seen in Figure 6.19b. A small shoulder is observed at 10 ns for the scattered light due to scattering at the nylon vessel. The curve can be fitted to an exponential from 0 to 20 ns, resulting in a decay time of 8.5 ns. This is longer than that found for the front quadrant, again indicating the time delay caused by reemission steps and longer flight paths. A prominent peak is again observed at 30 ns, as in Figure 6.18b.

Data were also recorded using a 180° steel jacket source filled with a mixture of 1.5 g/L of PPO in pseudocumene. It was inserted into the center of the CTF when the bulk scintillator was pure pseudocumene. Photon arrival time distributions for this configuration are shown in Figure 6.20. Figure 6.20a shows the distribution for tubes in the front quadrant. When fitted with an exponential over times from 0 to 20 ns, this curve gives a decay time of 4.4 ns. No peak at 30 ns is evident because of the small amount of scattered light available to reflect off the phototube glass of the tubes in the rear quadrant.

Results from tubes in the rear quadrant are seen in Figure 6.20b. A strange structure is evident in this curve. The arrival time distribution has a plateau-like feature from 0 to 10 ns before decaying in an exponential manner. The plateau is due to enhancement of the 10 ns peak. Scattering at the nylon vessel, which caused a shoulder in Figures 6.18b and 6.19b, results in a peak at 10 ns in Figure 20b. The 10 ns peak has become as large as the peak resulting from scattering in the scintillator containment vessel, and a plateau results. The 30 ns reflection peak is also more prominent in the pure pseudocumene scintillator than for the mixtures containing bis-MSB and PPO. The 10 ns and 30 ns peaks are emphasized in the pure pseudocumene scintillator because the same amount of light from PPO is scattered at the nylon vessel and reflected from the phototubes, while the amount of scattering occurring inside the vessel is reduced. An exponential fit to the decaying portion of the curve in Figure

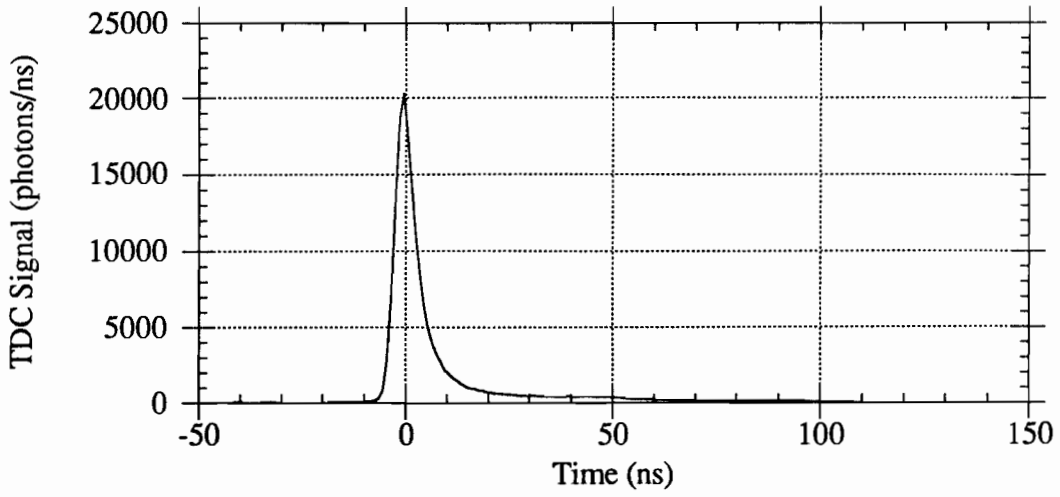

(a)

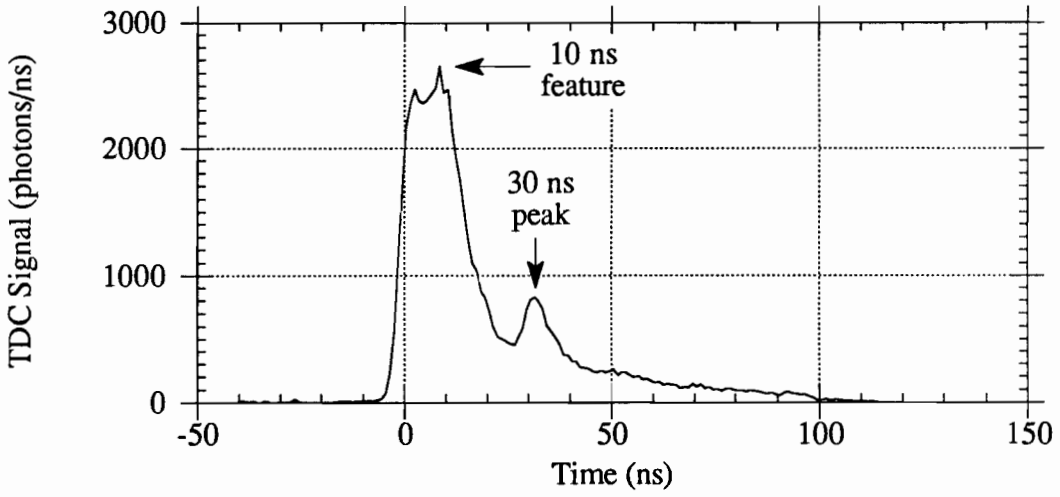

(b)

Figure 6.20. Photon arrival time distributions: limited aperture source in pure pseudocumene. These distributions are shown for a) tubes in the front quadrant and b) tubes in the rear quadrant for a limited aperture source located at the center of the CTF. Initial emission is from 1.5 g/L of PPO in pseudocumene. An exponential fit from a) 0 to 20 ns results in decay time 4.4 ns and b) 10 to 20 ns results in a decay time of 7.9 ns. In b) there are a feature at 10 ns due to scattering at the nylon vessel and a 30 ns phototube glass reflection peak.

6.20b from 10 to 20 ns yields a decay time of 7.9 ns. This indicates multiple reemission steps or lengthened photon flight paths.

The decay times fit to the photon arrival time distributions in this section indicate that scattering is occurring in the CTF. The decay time for omni-directional sources and tubes in the front quadrant during limited aperture source trials exhibit an increase over that found in small-scale measurements. The tubes in the rear quadrant during limited aperture source trials show even longer decay times.

The photon arrival time distributions are not only useful for the information they provide about light scattering in the CTF, but they have additional application in testing the Monte Carlo simulation developed to model the CTF. The simulation can predict arrival time distributions for various scintillator mixtures and source configurations, and it is described in Chapter 7. The ability of the Monte Carlo to reproduce the results measured experimentally aids in confirming that a correct understanding of light propagation in the detector is expressed in it.

F. Conclusions

The limited aperture source techniques described in this chapter were very useful for the measurement of light scattering in the CTF. These measurements were useful qualitatively and served as proof that scattering did occur inside the detector. Two types of scattering results were obtained in these studies for three scintillator mixtures: the fraction of light initially emitted in the center of the CTF which was scattered before reaching the phototubes and the arrival time distributions of these photons. These trials were important because they provided a chance to gain a more intuitive understanding of light scattering.

Although the scattering experiments described here provided a great deal of valuable information about light propagation in the detector, they were unable to

answer some important questions. These experiments showed that a significant amount of light emitted in the center of the detector is scattered before it reaches the phototubes in practical scintillators containing PPO and bis-MSB. In order to gauge the effect of this scattering on positional resolution in the detector, it is necessary to know the length scale at which the scattering occurs. Scattering at short distances less than the inherent positional resolution of the detector will not have a degrading effect, but scattering at longer distances will impair this resolution. The experiments described here were not very helpful in elucidating the length scale of scattering.

The evaluation of convolution integrals of the scintillator emission and attenuation spectra were considered as a means to model light scattering in the CTF. Results from this method were presented in Section 6.D. They modeled the experimental behavior well qualitatively and provided some measure of the light scale over which scattering occurred. The convolution results did not agree exactly with the experimental results because of their inability to account for multiple scattering steps.

A more sophisticated technique for predicting light scattering in the CTF is available in the Monte Carlo simulation developed by the collaboration. The ability of the Monte Carlo to correctly produce the results measured experimentally for fraction of light scattered and photon arrival time distributions serves as a test of the accuracy of the code in modeling light propagation in the detector. The simulation can also provide information about length scale on which scattering occurs. Studies with this simulation are described in Chapter 7.

References

1. Johnson, M.C.; Benziger, J.B.; Stoia, C.; Calaprice, F.; Chen, M.C.; Darnton, N.; Loeser, F.; Vogelaar, R.B. "Preparation of Radioactive Radon Sources for Use in a Low Background Detector", *Nuc. Inst. Meth A*, in press.

2. Hassan, N.M.; Hines, A.L.; Ghosh, T.K.; Loyalka, S.K. *Sep. Sci. Technol.* **1995**, *30*, 565.

3. Stoia, C., Princeton University, private communication.

4. Wojcik, M., University of Krakow, private communication (manuscript in preparation).

5. Gerrard, W. In *Gas Solubilities: Widespread Applications*; Pergamon Press: Oxford, 1980.

6. Manno, I. "Event Reconstruction in the CTF", Milan, 1995.

7. Manno, I.; Ranucci, G. "Simulation of Absorption-Reemission Processes in CTF", Milan, 1996.

8. Elisei, F.; Masetti, F.; Mazzucato, U. Borexino Project - Report N. 8, January 29, 1993; Perugia.

9. Elisei, F., University of Perugia, private communication.

10. Elisei, F.; Masetti, F.; Mazzucato, U. Borexino Project - Report N. 12, April 5, 1997; Perugia.

CHAPTER 7: MONTE CARLO SIMULATION OF LIGHT SCATTERING

Monte Carlo simulations have been developed by the collaboration to predict the behavior of the Counting Test Facility (CTF) and Borexino detectors. These simulations are quite detailed and they were used extensively in the design of the detectors. The simulation codes are used to generate estimates of the amount of shielding needed for the detectors to reduce the background to an acceptable level. Purity requirements for materials used in the detectors can also be studied. They allow calculation of background and neutrino event rates. The α-β separation and positional resolution that can be achieved in the detectors are also predicted by these simulations. The accuracy of these estimates depends upon the use of the correct physics in the codes, as well as correct data for the physical parameters. Because of the importance of the Monte Carlo codes in the design of the experiment and in the interpretation of data collected in it, it is important that their results be as reliable as possible.

The light scattering studies described in this thesis were very useful for examining the ability of the simulations to correctly model light propagation in the detector. The codes were designed to include all the physics felt to be important in light propagation. Parameters obtained from small-scale measurements such as those discussed in Chapter 5 were used in the simulations. The Monte Carlo codes were used to simulate a limited aperture source in the CTF. The simulated fractions of light scattered and photon arrival time distributions were compared with those measured experimentally. The ability of the simulations to accurately reproduce the experimental results confirmed that the appropriate physics and correct parameter values were being used. Because the Monte Carlo codes successfully scaled light propagation behavior from small-scale measurements to the CTF scale, the collaboration is confident that similar codes can accurately predict light propagation in Borexino.

In addition to confirming the validity of the simulations, use of the computer codes to study light scattering allows us to learn more about the scattering. The Monte Carlo codes provide information on the spectrum of the escaping light, the number of times the scattered photons are scattered, the relative importance of the different scattering mechanisms, and the length scale at which scattering occurs.

An overview of the Princeton group simulation is given in this chapter, and its treatment of light propagation is discussed. Simulated results for omni-directional and limited aperture sources located at the center of the CTF scintillator containment vessel are presented and they are compared with experimental measurements. The code is also used to study light propagation effects which could not be measured experimentally.

A. Description of the Monte Carlo

The Monte Carlo simulations developed by the Borexino collaboration are designed to model the response of the phototubes in the CTF and Borexino to ionizing radiation which impinges on the detectors. In a Monte Carlo, a large number of trials is generated. The outcome of each trial is governed by chance through the use of computer-generated random numbers. If the probabilities governing the processes included in the Monte Carlo are correct and enough trials are considered to produce good statistics, the results of the simulation will reflect reality.

The Borexino and CTF simulations allow for the generation of ionizing radiation events inside the detectors. Choices of radiation include α, β, γ, and neutrino events. The events can be generated at a specific point, on a spherical surface, in a spherical shell, or in a defined spherical volume. The Monte Carlo generates a specific number of events. Many photons are produced in each event, and each photon is tracked until it reaches a phototube or until it is lost. The photon hits are recorded so that they can be analyzed in a manner similar to that used for the experimental data from the detectors.

Behavior of the real detectors can be studied by examining the photon hits recorded in the simulations.

There are many steps involved in the simulation, including tracking of the ionizing radiation, generation of light, propagation of light, and modeling of phototube responses. Light propagation is only one of the many physical processes which are included in the simulations, but it is the process of concern in this thesis. Simulation codes have been developed by several groups in the collaboration. The code described here is the one used by the Princeton group. It was developed by Michael Lowery, R. Bruce Vogelaar, and Mark Chen. When comparisons were made, this simulation showed good general agreement with codes used by other collaboration members.

Ionizing radiation is treated in the Monte Carlo through use of the EGS4 software. EGS4 is a package of FORTRAN subroutines which is well-known in the physics community. When EGS4 is given information on a medium and the type, energy, and initial direction of ionizing radiation traveling in it, it generates a track for the radiation and calculates the energy deposited into the medium as a function of position along the track. The simulation treats α-events slightly differently than other types of radiation. No radiation track is generated for an α-event; it is treated as a point deposit of energy and all the energy of the particle is transferred to the scintillator at its point of emission.

The geometry of the detector is an input parameter for EGS4. Dimensions including the diameter of the scintillator containment vessel, the positions of the phototubes, and the shape of the light cones are provided to the program. These dimensions are used to define interfaces between media in the detector, such as those between scintillator and nylon, nylon and water, and water and glass. Data on refractive index, elastic scattering, and absorption of light as functions of wavelength are input to the simulation for each medium. Eight media are included in the CTF simulation:

scintillator, water, nylon, stainless steel, glass (phototube envelope), photocathode, acrylic (light cones), and silver (inside of light cones). The geometry and media information used in EGS4 is also used by other portions of the simulation.

The simulation converts the EGS4 data on energy deposited as a function of position into light emission. Almost all the light emission in the detector is due to radiation traveling through the scintillator. (Čerenkov light is emitted in the shielding water when high velocity electrons travel in it, but the quantity of this light is of a much smaller magnitude than that emitted in the scintillator.) Small-scale studies of light emission in the scintillator have been made in Munich and Milan.[1] Based on these studies, the simulation generates 10000 photons per MeV for β-events and 1000 photons per MeV for α-events in a scintillator consisting of 1.5 g/L of PPO in pseudocumene. It generates 4250 photons per MeV for β-events and 425 photons per MeV for α-events in a pure pseudocumene scintillator. Scintillator mixtures containing bis-MSB have not been studied as intensively as the other mixtures. The same photon yields are used for the mixture of 20 mg/L of bis-MSB and 1.33 g/L of PPO in pseudocumene as for the mixture containing only PPO. The location of photon emission along the radiation track is based on the energy deposit information from EGS4. There is some uncertainty in the number of photons emitted per MeV; this is accounted for in the simulation by randomly selecting the number of emitted photons from a Poisson or gaussian distribution with a mean value determined by the parameters mentioned above. (A gaussian distribution is used when the number of emitted photons is greater than 30.)

Photon emission does not occur instantaneously following the deposit of energy into the scintillator. The energy deposits calculated by EGS4 are made into the scintillator solvent. This energy must be transferred to the fluor and the fluor must relax in order for emission to occur. The simulation accounts for the energy transfer by using

decay time and emission spectrum parameters for the PPO-pseudocumene scintillator which are based on small-scale experimental measurements made in Milan and Perugia.[2] The decay time is represented as the sum of four exponentials. The decay times and the relative weights of the four exponentials are given in Table 7.1 for β and α excitation. (Neutrino and γ events are modeled using the β parameters because they cause scintillation due to scattered electrons.) The emission spectrum used in the Monte Carlo for the PPO-pseudocumene scintillator is shown in Figure 5.15 where it is labeled as the Perugia spectrum. The simulated decay time and emission wavelength of each photon are selected randomly based on the experimental decay curve and emission spectrum. Emission from a pure pseudocumene scintillator is modeled with a mono-exponential decay time of 27 ns and the emission spectrum shown in Figure 5.12 and labeled as the Perugia spectrum. The bis-MSB-PPO-pseudocumene scintillator is modeled using the four exponentials listed in Table 7.1 with the decay time of branch 1 changed to 3.9 ns for both types of radiation. The emission spectrum of this scintillator[3] is shown in Figure 7.1. Scintillator emission is isotropic over 4π steradians, and the direction of emission is chosen randomly. A probability for nonradiative relaxation in the scintillator is also included. It is based on the quantum yield of the scintillator mixture (0.80 for initial emission in the PPO-pseudocumene and bis-MSB-PPO-pseudocumene scintillators and 0.34 in the pure pseudocumene scintillator). No photon is emitted if nonradiative relaxation occurs, and the energy is lost.

Each photon generated in the simulation is tracked through the detector until it reaches a phototube or until it is lost. The code accounts for several light propagation phenomena while tracking the photons. In the scintillator, the photon can undergo absorption by the solvent and one or two fluors or elastic scattering. Attenuation lengths for each process are based on absorption measurements made by the Perugia group. The measurements of Chapter 5 show that the apparent absorption in the flat tail

Table 7.1. Decay parameters used in Monte Carlo. The time decay of the scintillator mixture consisting of 1.5 g/L of PPO in pseudocumene is represented as the sum of four exponentials. The decay times and relative amplitudes of the exponentials are shown here for β and α excitation. Data from Manno.[2]

	β	α
1st decay time (ns)	3.56	3.24
1st amplitude (%)	89.52	63.00
2nd decay time (ns)	17.58	13.46
2nd amplitude (%)	6.33	17.82
3rd decay time (ns)	59.39	59.83
3rd amplitude (%)	2.93	11.93
4th decay time (ns)	329.79	278.58
4th amplitude (%)	1.22	7.25

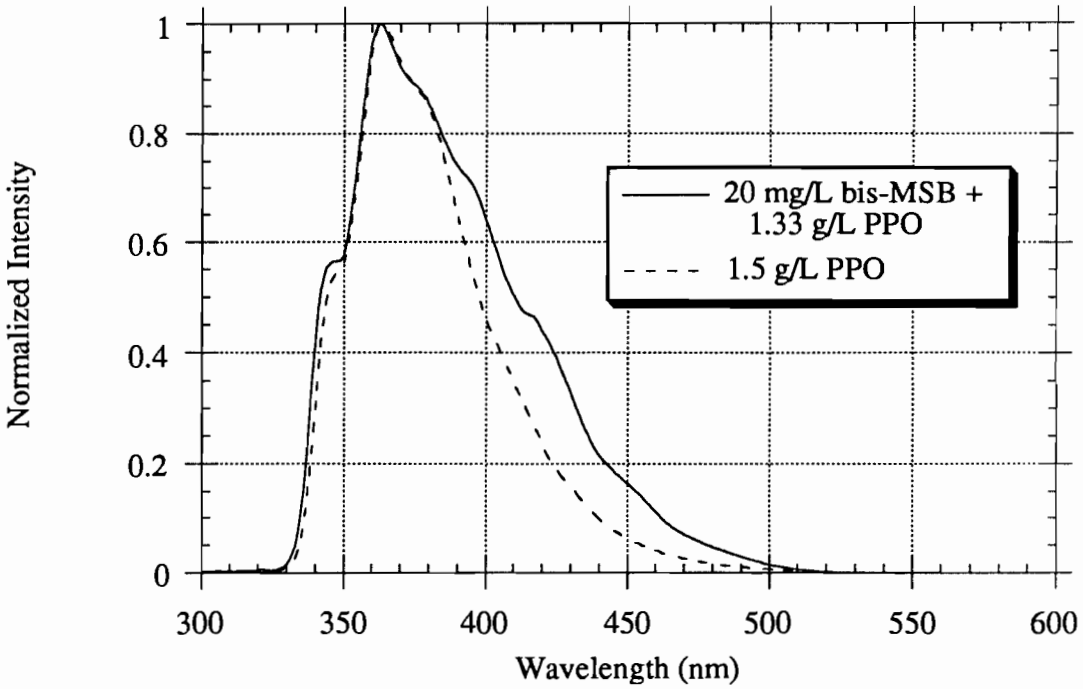

Figure 7.1. Emission spectrum of bis-MSB-PPO-pseudocumene scintillator. This emission spectrum is used in the simulation to represent the light output from a scintillator mixture of 20 mg/L of bis-MSB and 1.33 g/L of PPO in pseudocumene. It was obtained by the Perugia group following excitation of the mixture at 267 nm. The spectrum from a scintillator containing 1.5 g/L of PPO in pseudocumene is shown for comparison. The additional light output at longer wavelengths is due to emission by the bis-MSB following excitation of the solvent.

of an absorption spectrum is due to elastic scattering. The absorption spectrophotometer measurements are used to provide absorption attenuation lengths in the absorption band and elastic scattering attenuation lengths at longer wavelengths. The simulation allows absorption by pseudocumene at wavelengths below 320 nm, by PPO below 375 nm, and by bis-MSB below 440 nm. All attenuation is due to elastic scattering at longer wavelengths.

Absorption of a photon can be followed by reemission, but there is a chance for nonradiative relaxation of the absorbing molecule which depends on its quantum yield. Reemission by pseudocumene is treated in the same manner as the original emission. (A multi-exponential decay with the original or modified parameters in Table 7.1 and the spectrum of Figure 5.15 or 7.1 are used if a fluor is present. A single exponential decay with a decay time of 27 ns and the spectrum of Figure 5.12 are used in a pure pseudocumene scintillator.) Reemission by the PPO and bis-MSB fluors is modeled using single exponential decay time of 1.6 and 1.4 ns. The single component emission spectra of the fluors are used (Figure 5.15 for PPO and Figure 5.17 for bis-MSB). If reemission occurs, it is isotropic. The wavelength of reemission is selected randomly from the entire emission spectrum regardless of the wavelength of the absorbed photon. Nonradiative relaxation results in the loss of the photon, and tracking by the Monte Carlo is terminated.

If elastic scattering occurs, the photon's wavelength remains unchanged, but its direction is altered. Elastic scattering is not isotropic, but instead exhibits a $1 + \cos^2 \theta$ dependence, where θ is the angle between the incident and scattered directions. The new direction of the scattered photon is determined randomly based on this distribution. Light propagation is dominated by elastic scattering in the pseudocumene solvent at wavelengths greater than 320 nm in a pure pseudocumene scintillator, greater than 375

nm in a scintillator consisting of 1.5 g/L of PPO in pseudocumene, and greater than 420 nm in a scintillator of 20 mg/L of bis-MSB and 1.33 g/L of PPO in pseudocumene.

In the simulation, a distance is calculated at which each absorption and elastic scattering will take place. These distances are based on the attenuation lengths for the processes and they are calculated randomly. The shortest interaction distance (the one which will take place) is compared with the distance the photon must travel in its current direction before it reaches the edge of the scintillator containment vessel. If this distance is greater than that to the absorption or elastic scattering interaction, the interaction takes place as described above. If the scintillator containment vessel is reached before the interaction takes place, the interaction is ignored and the simulation examines propagation of the photon at the scintillator-nylon interface.

Once a photon reaches the edge of the scintillator medium, it must propagate through the nylon scintillator containment vessel. The simulation allows for absorption of the photon by the nylon. The nylon essentially absorbs all photons with wavelengths below 300 nm. The attenuation length of light in the 0.05 cm thick nylon membrane changes from 0.15 cm at 300 nm (72% transmission) to 0.82 cm at 500 nm and above (94% transmission). Reflection and refraction also take place at the scintillator-nylon and nylon-water interfaces. The refractive index of nylon is 1.53, while that of the scintillator is 1.505 and that of water is 1.333. This refractive index mismatch causes reflective and refractive effects at the interfaces. (The effects are greater at the nylon-water interface because the refractive index mismatch is larger here.) Refraction changes the direction of photons escaping from the scintillator containment vessel, and some photons (1.4% of photons arriving at the nylon-water interface at an incidence of 45°) are reflected at the interfaces. The probability of reflection and the amount of refraction are modeled through the use of Fresnel's laws. If a photon is reflected back into the scintillator containment vessel, its propagation in the scintillator is treated in the same

manner as before, and a new distance to each type of interaction is calculated. If a photon passes through the scintillator-nylon and nylon-water interfaces, tracking continues in the water medium.

The only potential light propagation effect in water is elastic scattering, and the scattering attenuation length is so long (approximately 30 m) in water that the probability of scattering is small. If a photon is scattered elastically in the water, its new direction is chosen randomly using the $1 + \cos^2 \theta$ distribution. Scattered photons may return to the scintillator containment vessel; the reflection and refraction treatment at the nylon vessel interface is repeated if this occurs.

When a photon reaches a location with a radius of 2.75 m or more from the center of the scintillator containment vessel, the phototubes and light collector are accounted for by the simulation. The positions of the phototubes and their light collectors are included in the computer code. If a photon enters a light collector cone, the Monte Carlo treats reflections off the sides of the light collector as the photon is guided towards the phototube. There is a possibility of reflection at the glass of the phototube because of the refractive index mismatches between water and glass (1.333 vs. 1.474) and between glass and the photocathode (1.474 vs. 3.50). If the photon is reflected, the code continues to track it. If it passes through the glass, it is absorbed by the photocathode and the tracking is stopped. Photon tracking is also terminated if a photon passes between the light collectors and reaches a distance of 4 m from the center of the scintillator containment vessel. Photons reaching this 4 m cutoff are discarded by the simulation.

If a photon is absorbed by the photocathode, the simulation continues to consider its fate. The probability of detection of a photon absorbed by the photocathode is determined by the relative efficiency of the phototube at the wavelength of the absorbed photon. Prior to tracking of any photon, the simulation randomly determines

its probability of detection at the wavelength where the phototube is most efficient. For the CTF phototubes, this is 360 nm where the tubes have an efficiency of 23.6%. Photons not passing this test are not tracked, and over 76% of the generated photons are discarded without tracking for this reason. After absorption at the photocathode, the photon is checked against the difference between the efficiency of the phototube at 360 nm and the efficiency of the tube at the wavelength of the absorbed photon. The relative efficiency is 91% at 400 nm and 72% at 450 nm. It is only 50% at 500 nm, and it declines rapidly at longer wavelengths. If the simulation determines that an absorbed photon is detected, a photon hit is recorded for the phototube which detected it. The time at which the photon was received is also recorded. Phototube time jitter is added to the time required for the photon to propagate through the detector and reach the phototube. The time jitter is assigned randomly based on a gaussian distribution with a σ of 1 ns.

Once a photon registers as a hit on a phototube in the simulation, data regarding the photon are stored. Data storage takes place using subroutines designed to interface with the Physics Analysis Workshop (PAW) software. Data recorded during the simulation differ in many respects from those recorded using the CTF data acquisition system. One advantage of the simulation over the real CTF electronics is that each phototube can be monitored individually in the Monte Carlo. The simulation also records the arrival time of every photon, not only the first one at each phototube. The time of the event is known in the Monte Carlo, but for real data collected in the CTF the event time is not known. TDC data from the CTF show only the differences between the arrival times of photons. Time zero in the CTF is set when the number of tubes corresponding to the trigger setting receive photons within 30 ns of each other. The simulation also records other data about each photon including its wavelength, the

number of times it was scattered, what type of scattering occurred, and where the scattering took place.

There are some effects which affect the experimental results of the CTF that are not included in the simulation. One of these is the geometry of the scintillator-water interface. In the Monte Carlo, the nylon vessel geometry is perfectly spherical. The real vessel does not have this perfect shape even when fully inflated, and at times it was tessellated during operation because it was underfilled and underpressurized. Although the simulation results for reflection and refraction are correct for a spherical vessel, some deviations from simulated behavior are to be expected due to the more complicated interfacial geometry found in the actual detector. Despite some uncertainties of this nature, the simulation is able to represent the experimental behavior quite well, as described in Section 7.B.

B. Monte Carlo Scattering Results: Comparison With Experiment

The Monte Carlo code used to simulate the CTF was applied to study light scattering in the detector. In the scattering studies, α events with an energy of 5.00 MeV were generated at the center of the scintillator containment vessel to simulate the ^{214}Po events of the radon sources. This treatment modeled the quartz vials as point sources. This was acceptable because the quartz vial sources had volumes small enough compared to that of the CTF that they were essentially point sources. Each simulation generated 10000 events in order to provide good statistics for the computer results. The omni-directional sources were simulated with no changes in the code. A modification was made to simulate limited aperture sources with clear apertures of 180°. For these sources, initial light emission was allowed over only 2π steradians. The simulated limited aperture sources were oriented along the +y axis; any photon initially emitted with a negative velocity component in the y-direction was discarded. This coding

allowed more light to escape than did the actual limited aperture sources, which blocked light traveling toward the top and bottom of the detector even at the aperture. Only tubes in the front and rear quadrants (as described in Chapter 6 for the experimental limited aperture source trials) in rings 2 to 5 are used for analysis so that this slight difference in geometry does not affect the results.

Simulations of light scattering in the CTF were first carried out for a scintillator containing 1.5 g/L of PPO in pseudocumene. The simulated photon arrival time distribution for an omni-directional source at the center of the scintillator containment vessel when it is filled with this scintillator is shown in Figure 7.2. The experimental distribution is shown for comparison, and the two can be seen to match almost exactly. The simulation accurately reproduces the overall decay time of the scintillator and the small peak at 30 ns due to reflections off phototube glass. In order to compare the curves, the simulation peak was scaled so that its peak value matched that of the experimental distribution.

Simulations of limited aperture source were also performed for the PPO-pseudocumene scintillator. The ratio of the number of photons received by phototubes in the quadrant along the –y axis (viewing opaque side of source) to the number received by those in the quadrant along the +y axis (viewing clear aperture) was found to be 0.25. Only tubes in rings 2 to 5 were used in this analysis in order to treat the simulated data in the same way as the experimental data. The ratio was calculated for photons received within 20 ns after the peak in the photon arrival time distribution. This was done to mirror the 20 ns cut used in analyzing the experimental data (see Section 6.C). The detected light ratio of 0.25 corresponds to a fraction of light scattered of 0.40. The experimental results were a detected light ratio of 0.27 and a fraction of light scattered of 0.43. The simulation results are well within the error of the experimental results (see Table 6.2).

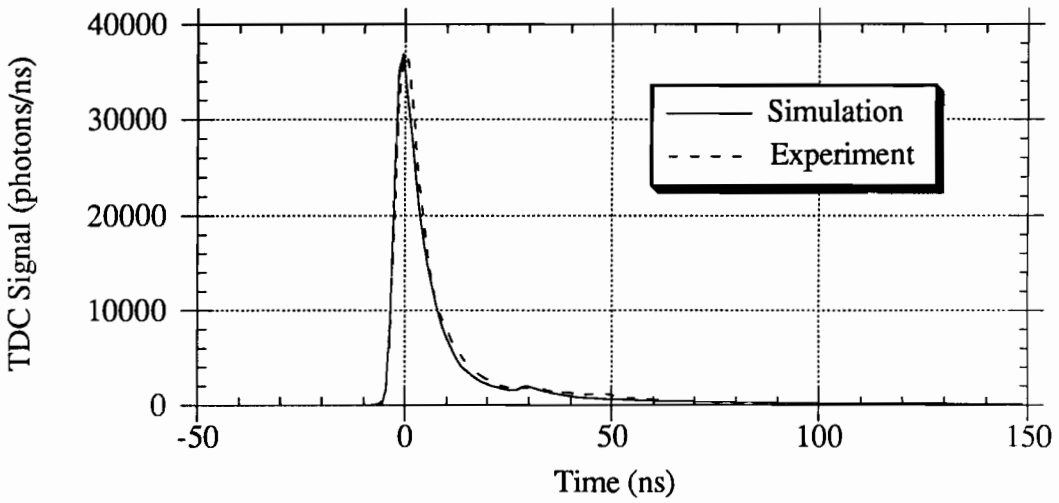

Figure 7.2. Simulated photon arrival time distribution: omni-directional source in 1.5 g/L PPO-pseudocumene. A simulated photon arrival time distribution is shown for the PPO-pseudocumene scintillator along with the experimental distribution. Both were obtained for an omni-directional source at the center of the CTF scintillator containment vessel. The two curves show good agreement.

Simulated photon arrival time distributions for a limited aperture source located at the center of the CTF scintillator containment vessel are shown for the PPO-pseudocumene scintillator in Figure 7.3. Distributions are shown for phototubes in the front and rear quadrants. Experimental arrival time distributions are shown for comparison. The simulation results were scaled so their peak heights matched the experimental heights. The simulation prediction matches very well with the experimental arrival time distribution for tubes in the front quadrant, as expected from the results with the omni-directional source. The Monte Carlo also does an adequate job of representing the distribution for tubes in the rear quadrant. The agreement is not exact in this case, but the qualitative features of the experimental curve are reproduced by the simulation. The simulation has the most difficulty in matching experimental behavior in the region around 10 ns. Here the simulation shows a faster decay of light than is measured experimentally. In this region, nylon vessel effects are important, as discussed in Chapter 6. The discrepancy may be due to a complicated vessel geometry found in the real detector that causes more reflection than a perfect sphere. The neglect of scattering by the nylon in the simulation is another possible explanation for the difference. The reflection peak at 30 ns due to phototube glass is represented well by the simulation, both in timing and in the relative heights of the main and reflection peaks.

The CTF behavior of a scintillator consisting of 20 mg/L of bis-MSB and 1.33 g/L of PPO in pseudocumene was also simulated. Simulation of an omni-directional source produced a photon arrival time distribution which agreed closely with the one measured experimentally. When a limited aperture source was simulated, the detected light ratio was found to be 0.56. This corresponds to fraction of light scattered of 0.72. These results are within the error of the experimental results of 0.51 for the detected light ratio and 0.67 for the fraction of light scattered.

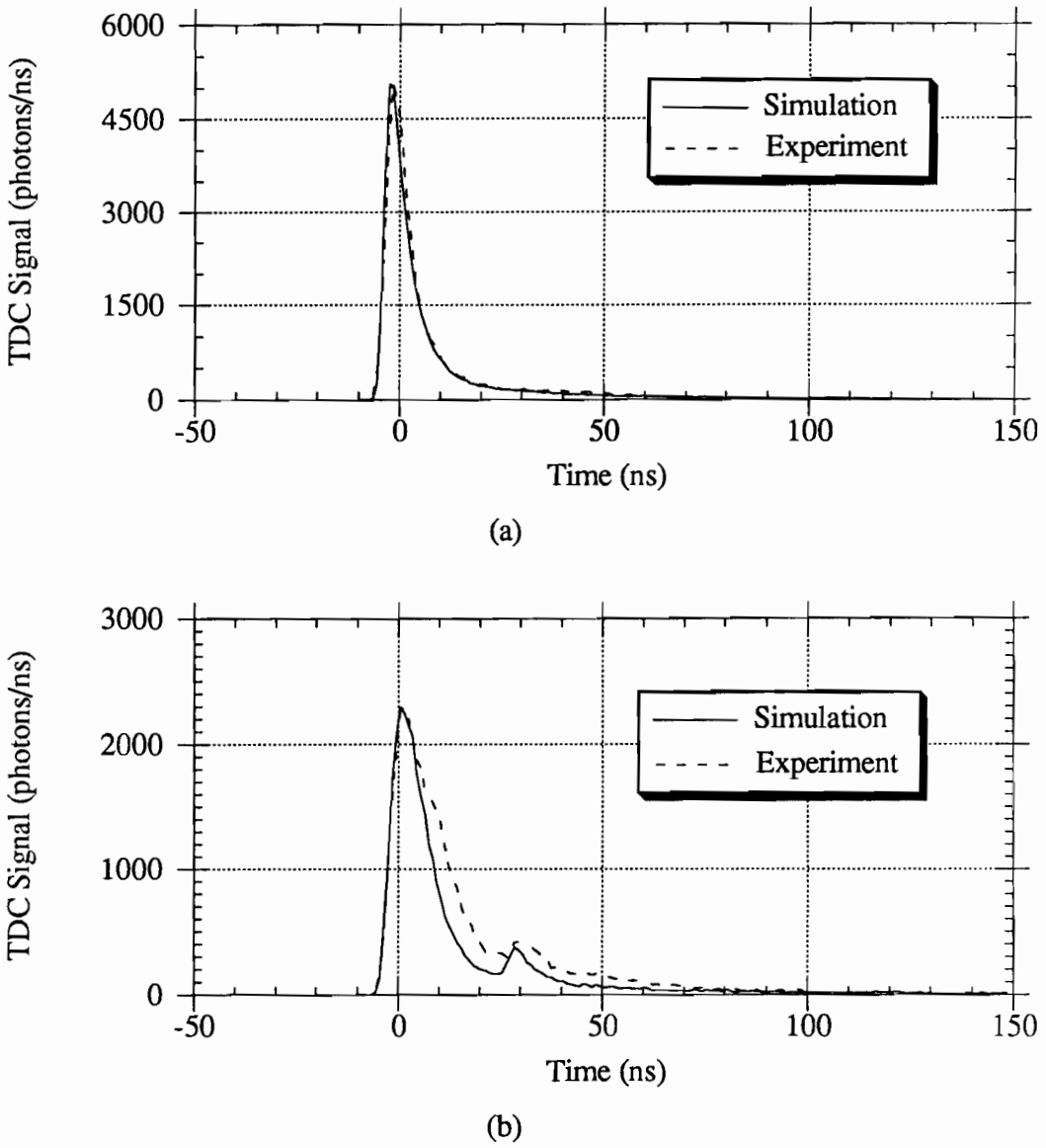

Figure 7.3. Simulated photon arrival time distributions: limited aperture source in 1.5 g/L PPO-pseudocumene. Simulated photon arrival time distributions are shown for the PPO-pseudocumene scintillator along with experimental distributions. All were obtained for a limited aperture source at the center of the CTF scintillator containment vessel. Distributions are shown for phototubes in the a) front and b) rear quadrants.

Simulated and experimentally measured photon arrival time distributions are shown for the bis-MSB-PPO-pseudocumene scintillator in Figure 7.4. Distributions are shown for tubes in the front and rear quadrants. The simulated curves are scaled so that their peak heights correspond to those of the experimental curves. The simulation and experimental results for tubes in the front quadrant agree, although the experimental curve decays slightly faster than the simulated one at times near 10 ns. The simulation also reproduces the qualitative behavior of the experimental curve the for the rear tubes. The simulation predicts a faster decay of light in the 10 ns region than found experimentally, as it did for the PPO-pseudocumene scintillator. The discrepancy is not as great for the bis-MSB scintillator. The PMT glass reflection peak is not represented as well by the simulation in Figure 7.4b as in Figure 7.3b. The timing of the peak is still correct at 30 ns, but in Figure 7.4b the relative magnitude of the peak with respect to the main peak is only half of that measured experimentally.

The behavior of the CTF was simulated for a pure pseudocumene scintillator with sources located at the center of the scintillator containment vessel. The simulated photon arrival time distribution for an omni-directional source was almost identical to the one measured experimentally. When a limited aperture source was simulated, the detected light ratio was calculated to be 0.11. This corresponds to a fraction of light scattered of 0.20. The experimental results were a detected light ratio of 0.11 and a fraction of light scattered of 0.20. The simulation results agree exactly with the experimental data for the pure pseudocumene scintillator.

Photon arrival time distributions for a limited aperture source in the pure pseudocumene scintillator are shown in Figure 7.5. Distributions are shown for tubes in the front and rear quadrants. Both simulated and experimental curves are shown in order to facilitate comparison. The simulated curves were scaled so that they had the same peak height as the experimental curves. The distributions for the front tubes agree

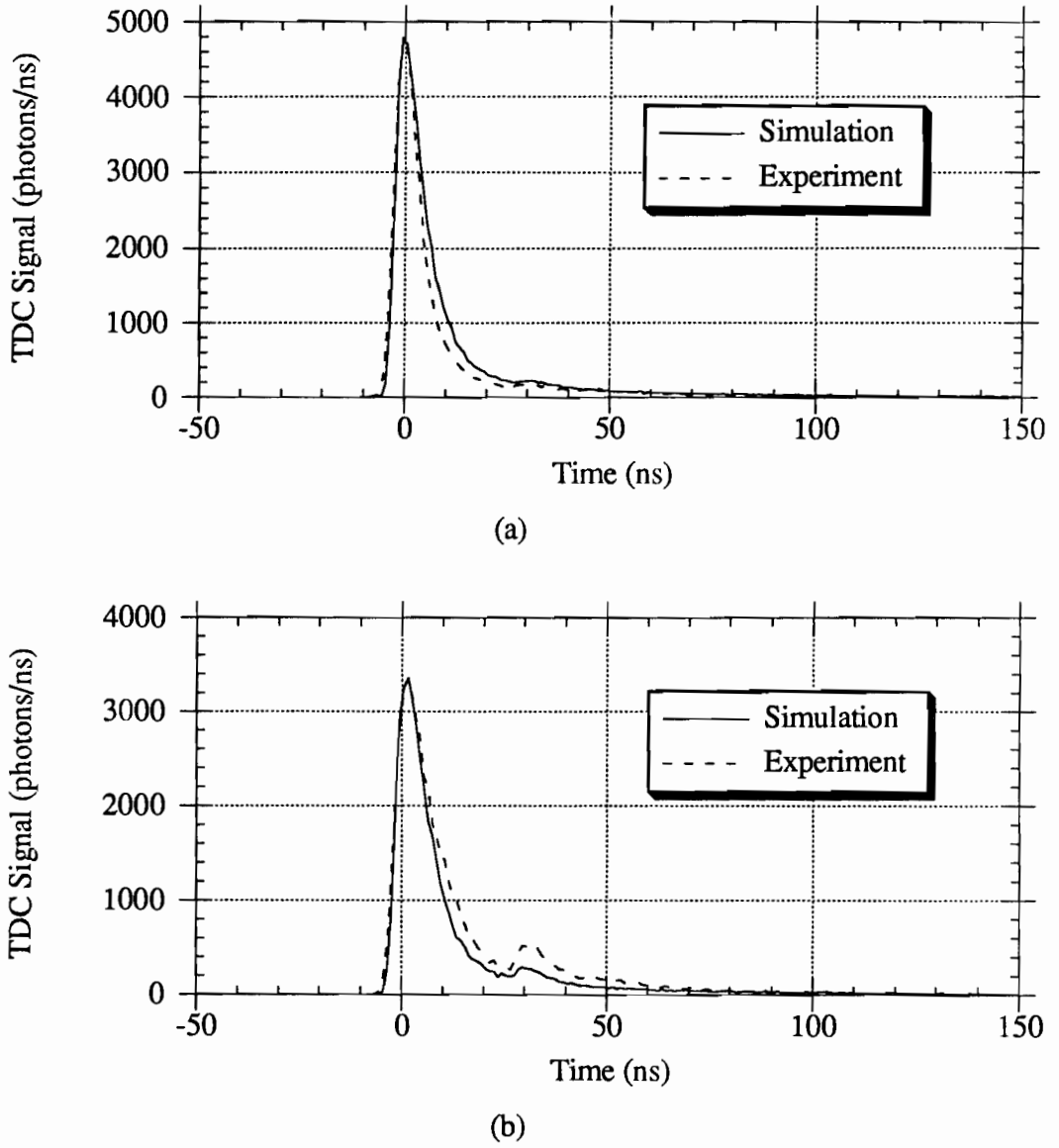

Figure 7.4. Simulated photon arrival time distributions: limited aperture source in 20 mg/L bis-MSB-1.33 g/L PPO-pseudocumene.

Simulated photon arrival time distributions are shown for the bis-MSB-PPO-pseudocumene scintillator along with experimental distributions. All were obtained for a limited aperture source at the center of the CTF scintillator containment vessel. Distributions are shown for phototubes in the a) front and b) rear quadrants.

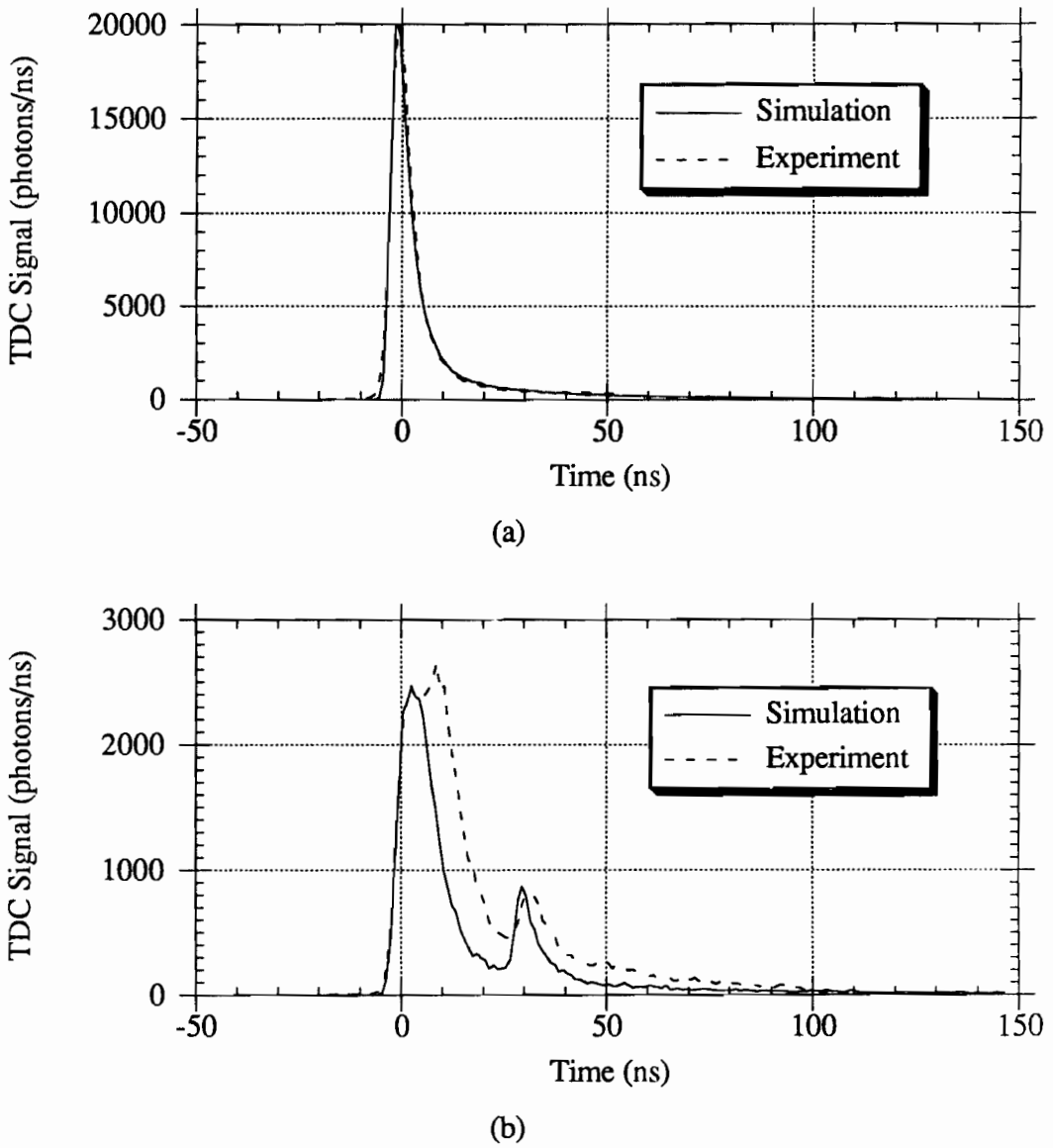

Figure 7.5. Simulated photon arrival time distributions: limited aperture source in pure pseudocumene. Simulated photon arrival time distributions are shown for the pure pseudocumene scintillator along with experimental distributions. All were obtained for a limited aperture source at the center of the CTF scintillator containment vessel. Distributions are shown for phototubes in the a) front and b) rear quadrants.

very closely. The simulation had more difficulty representing the distribution for the rear tubes. The simulated arrival time distribution does not display the plateau from 0 to 10 ns that is evident in the experimental curve. The inability of the simulation to reproduce this feature is not surprising. It is attributed to effects at the nylon vessel, and simulation of the PPO-pseudocumene and bis-MSB-PPO-pseudocumene scintillators showed that the simulation has some difficulty treating these effects. The other features of the experimental pure pseudocumene photon arrival time distribution are well-modeled by the simulation. One of these features is the reflection peak at 30 ns, which is treated accurately in both timing and magnitude.

The results presented in this section show that the Monte Carlo can accurately model the light propagation in the detector and can predict the amount of light scattered and the arrival time distribution of this light at the phototubes. The simulation does an excellent job of predicting the fraction of light scattered. The simulation results for this parameter for the three scintillator mixtures agreed within the experimental error to the results measured in Chapter 6. The photon arrival time distributions produced by the simulation agreed qualitatively with the experimental distributions. The agreement was close for the omni-directional sources, but some discrepancies were observed for the rear tubes in the limited aperture source trials.

The simulation had the most trouble reproducing the experimental photon arrival time distribution results in the area near 10 ns. The behavior here is greatly influenced by effects at the nylon vessel. These effects include reflection and elastic and inelastic scattering. Inclusion of these effects into the Monte Carlo is not likely to be useful because they are dependent on the history of the CTF. The reflections at the vessel are affected by its shape. While the simulation treats the vessel as a sphere, it was underinflated throughout much of its life. This introduced some tessellation into the vessel shape. This tessellation cannot be represented in the simulation because the exact

shape of the vessel during operation was never observed. Scattering at the vessel is also difficult to model. Measurements by the Perugia group discussed in Chapter 6 indicate that inelastic scattering in the nylon probably changed over time. Such changing conditions make the validity of any nylon scattering measurements suspect.

Difficulty representing light propagation at the nylon vessel does not significantly affect the ability of the simulation to model the CTF. The nylon only plays a major role in special situations such as the limited aperture source trials. Events in the CTF are better represented by the omni-directional sources; the simulation reproduced the photon arrival time distributions for these sources very accurately.

The success of the simulation in modeling the light scattering behavior in the CTF gives us confidence that the code accurately treats the major light scattering processes. The Monte Carlo proved to be a method which could scale the results of measurements made on milliliter-sized samples to predict the behavior of the 2 m diameter CTF. A similar Monte Carlo will be able to extrapolate the small-scale results to the 8 m Borexino detector. The simulation can also be used to learn more about light scattering in the CTF by measuring parameters which are not accessible experimentally. Its use for this study is considered in the next section.

C. Monte Carlo Scattering Results: Studies of Light Propagation

In Section 7.B, the Monte Carlo was used to simulate limited aperture source trials in the CTF, and the simulation results for the fraction of light scattered and the photon arrival time distribution were compared with the experimental ones for three scintillator mixtures. The Monte Carlo can also provide information which cannot be measured experimentally in the CTF. This information includes the spectrum of the detected light, the number of times detected photons are scattered in the CTF, and the distance scale on which the scattering takes place. These simulated results can be

studied with the assurance that they reflect the true behavior of the detector because of the ability of the code to accurately simulate measurable scattering parameters in the CTF.

The simulated data presented in this section was generated for omni-directional sources located at the center of the CTF scintillator containment vessel. Three scintillator mixtures were studied: pure pseudocumene, 1.5 g/L of PPO in pseudocumene, and 20 mg/L of bis-MSB and 1.33 g/L of PPO in pseudocumene. The initial emission in each mixture was modeled as in the studies of limited aperture sources in Section 7.B: emission from 1.5 g/L of PPO in pseudocumene for the pure pseudocumene and PPO-pseudocumene mixtures and emission from 20 mg/L of bis-MSB and 1.33 g/L of PPO in pseudocumene for the bis-MSB-PPO-pseudocumene mixture. The selection of these scintillator mixtures provides general data on light scattering in the CTF and helps to explain the results observed specifically for these compositions.

The spectrum of light detected at the phototubes for the three scintillator mixtures is shown in Figures 7.6 to 7.8. The spectrum of the photons initially emitted in each mixture is also shown. The simulated spectrum of detected light in pure pseudocumene shown in Figure 7.6 is almost identical to the emission spectrum of PPO. Only elastic scattering takes place in the pseudocumene, and this does not affect the spectral distribution of the light. A slight difference from the PPO emission spectrum is caused by the relative efficiency of the phototubes for different wavelengths of light.

Figure 7.7 shows the simulated spectrum of light detected by the phototubes in the PPO-pseudocumene scintillator. The spectrum is red-shifted from the PPO emission spectrum. Shorter wavelength photons emitted by the PPO are absorbed within a short distance and only photons of longer wavelengths escape from the detector.

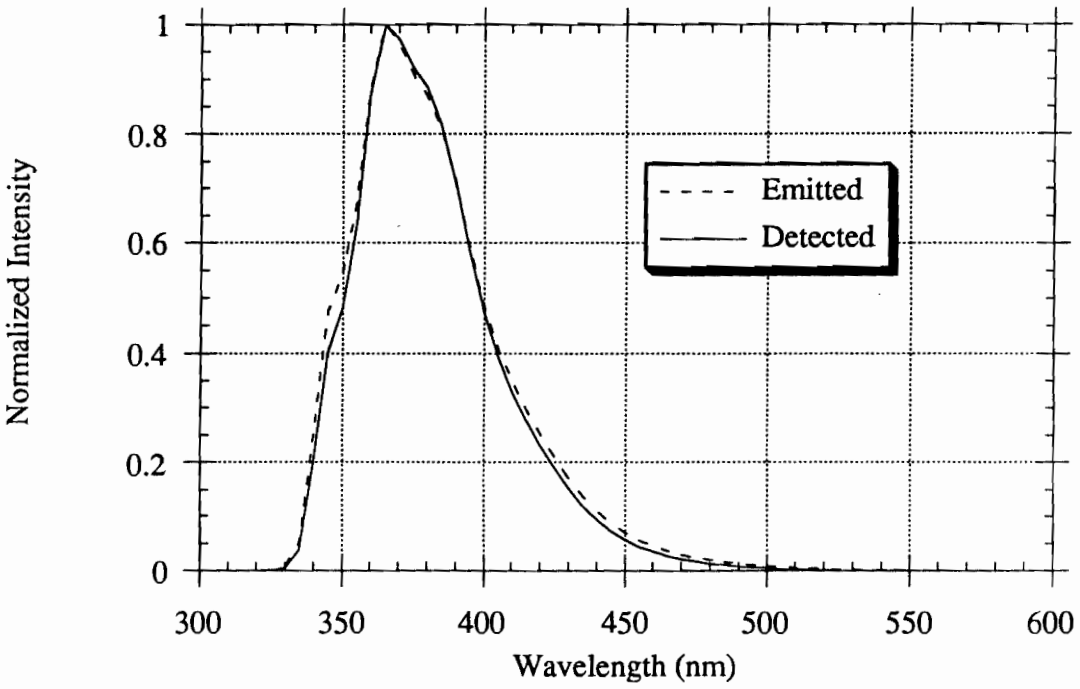

Figure 7.6. Simulated spectrum of detected light in pure pseudocumene. The spectrum of photons detected by the phototubes following emission from an omni-directional source at the center of the CTF scintillator containment vessel is shown. The bulk scintillator was pure pseudocumene and the initial emission was from 1.5 g/L of PPO in pseudocumene. The initial emission spectrum is shown for comparison.

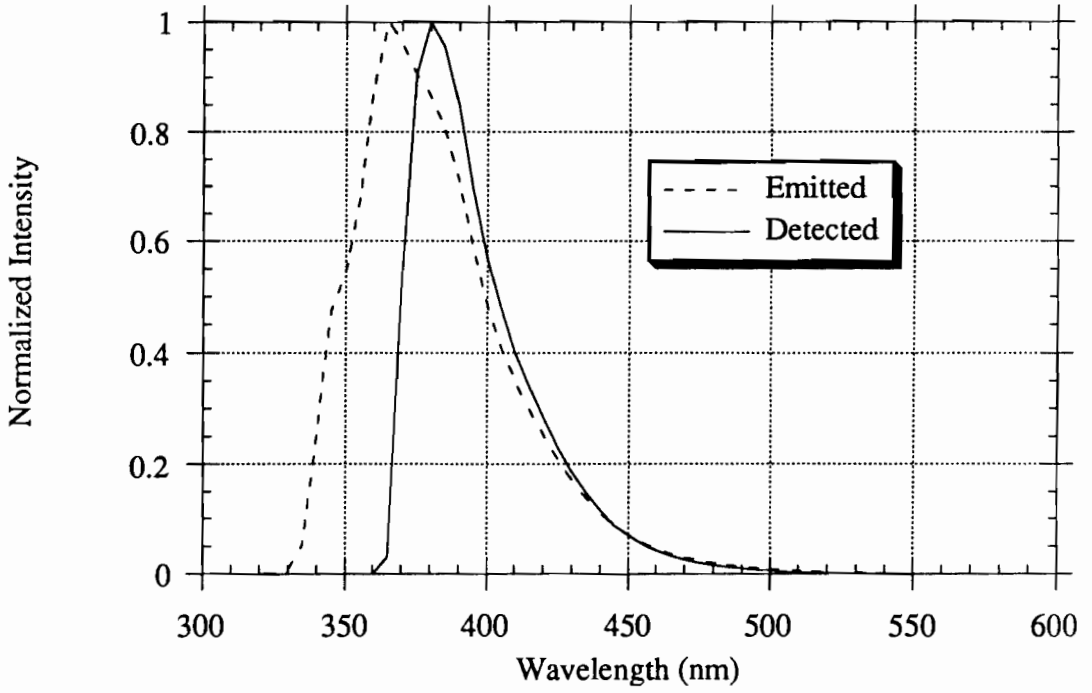

Figure 7.7. Simulated spectrum of detected light in 1.5 g/L PPO-pseudocumene. The spectrum of photons detected by the phototubes following emission from an omni-directional source at the center of the CTF scintillator containment vessel is shown. The bulk scintillator was a mixture of 1.5 g/L of PPO in pseudocumene and the initial emission was also from this mixture. The initial emission spectrum is shown for comparison.

The simulated spectrum of the detected light in the bis-MSB-PPO-pseudocumene scintillator is shown in Figure 7.8. The bis-MSB wavelength shifter has effectively shifted the initial emission spectrum which is dominated by PPO to the bis-MSB emission spectrum (see Figure 5.17). The first peak in the bis-MSB emission spectrum at 400 nm has been cut off in this figure due to self-absorption of fluorescence by the fluor.

The Monte Carlo was used to investigate the number of times that detected photons were scattered inside the CTF and what mechanisms caused the scattering. The results of this study are shown in Figures 7.9 to 7.11. Figure 7.9 shows data from simulations in the pure pseudocumene scintillator. The vast majority of these photons, 76%, is not scattered at all. Approximately 18% of the detected photons are scattered once, and 6% are scattered more than once. All the scattering in this scintillator mixture is elastic in nature. Scattering in the scintillator accounts for 90% of the total, and Rayleigh scattering in the shielding water provides the rest. An amount of light equal to 8% of the detected scattered light is reflected off the phototube glass, although this light is not counted as scattered light in the analyses of Sections 6.C and 7.B.

Figure 7.9 indicates that 24% of the detected photons were scattered in the pure pseudocumene scintillator. This is slightly higher than the fraction of light scattered of 0.20 calculated in Section 7.B and measured experimentally for the same scintillator. This discrepancy can be explained by the derivation of eq 6.1 which defines the fraction of light scattered. This derivation assumed that equal amounts of scattered light went to the phototubes in the front quadrant and in the rear quadrant. When light is emitted from a limited aperture source, it travels towards the front phototubes. At the point of scattering, the front quadrant subtends a larger solid angle than the rear quadrant. It receives more scattered photons than the rear quadrant, and eq 6.1 is not strictly correct. In spite of this approximation, the fraction of light scattered as defined in eq 6.1

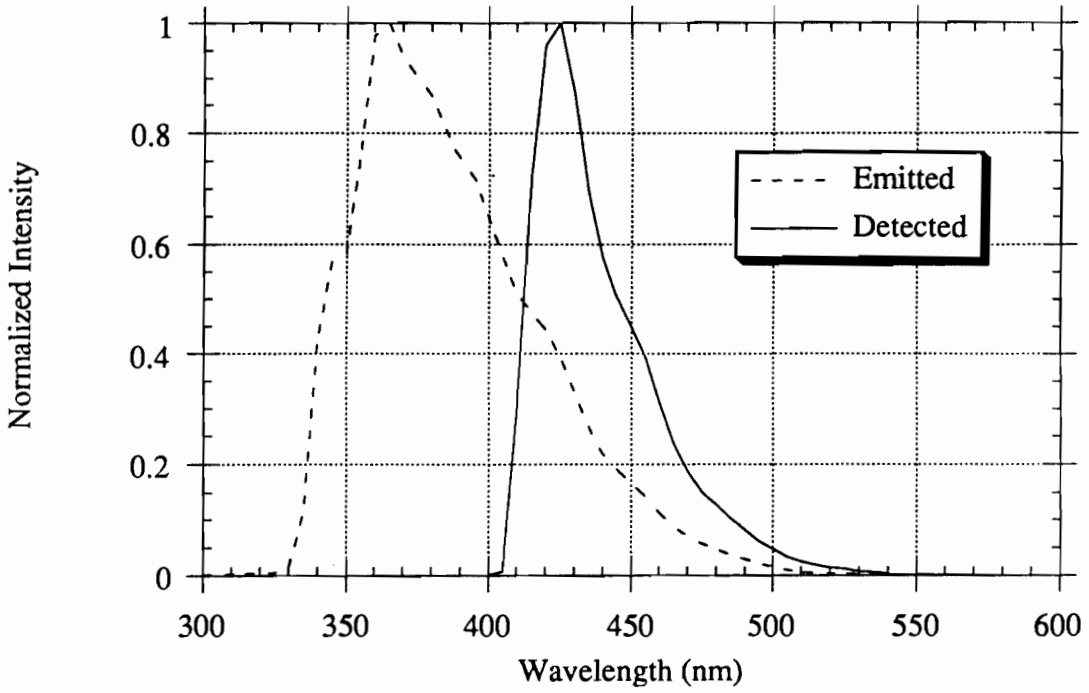

Figure 7.8. Simulated spectrum of detected light in 20 mg/L bis-MSB-1.33 g/L PPO-pseudocumene. The spectrum of photons detected by the phototubes following emission from an omni-directional source at the center of the CTF scintillator containment vessel is shown. The bulk scintillator was a mixture of 20 mg/L of bis-MSB and 1.33 g/L of PPO in pseudocumene and the initial emission was also from this mixture. The initial emission spectrum is shown for comparison.

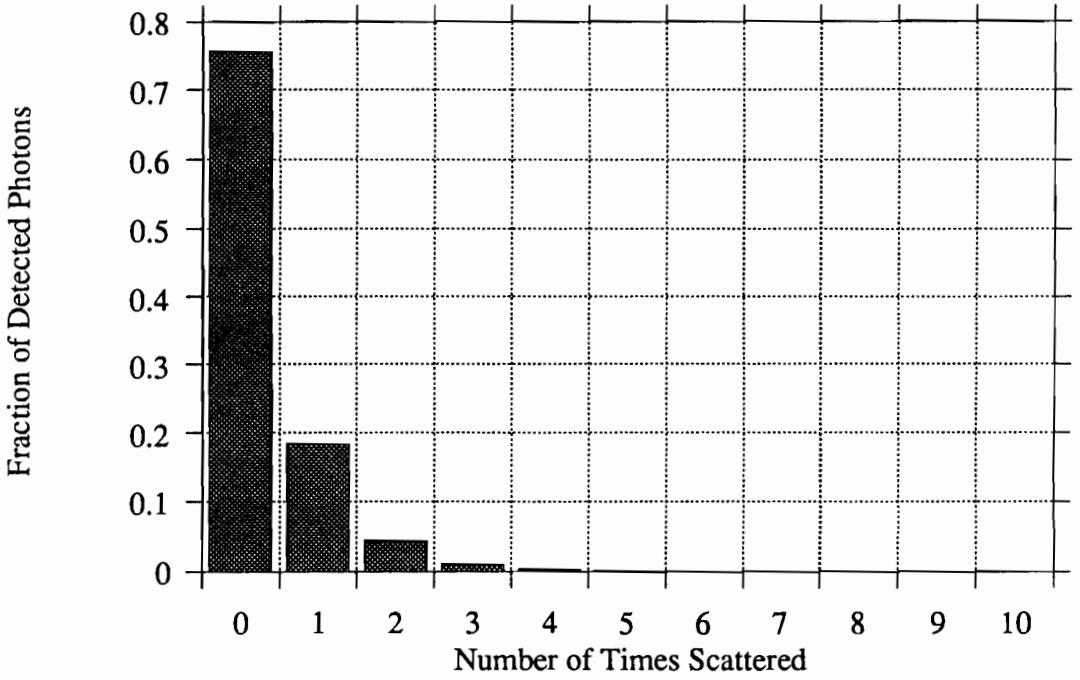

Figure 7.9. Scattering of detected photons in pure pseudocumene. The figure displays simulated results for the fraction of detected photons which were scattered the number of times indicated. The simulation modeled an omni-directional source at the center of the CTF scintillator containment vessel. The bulk scintillator was pure pseudocumene and the initial emission was from 1.5 g/L of PPO in pseudocumene.

provides a useful means of quantifying scattering in the detector. The difference between it and the percentage of photons scattered as determined by the Monte Carlo is small for all three scintillator mixtures.

Figure 7.10 presents data on the number of times detected photons were scattered in the PPO-pseudocumene scintillator. A smaller percentage, 56%, of the photons reaches the phototubes without being scattered in this scintillator mixture. Approximately 27% of the detected photons are scattered once, 11% are scattered twice, and 6% are scattered more than twice. Absorption-reemission by the PPO accounts for 67% of the scattering and Rayleigh scattering provides the remainder. Only 4% of the scattering is due to the shielding water for this scintillator mixture. Reflections off the phototube glass provide a signal of only 3% of the detected scattered light total. The amount of light reflected from the phototube glass is unchanged from the amount reflected with the pure pseudocumene scintillator. This reflection has become less significant compared to the scattering in the scintillator because the amount of scattering has increased. The importance of Rayleigh scattering in the shielding water and in the scintillator is also decreased due to the occurrence of absorption-reemission scattering in this scintillator mixture.

Data on the number of times detected photons are scattered are presented for the bis-MSB-PPO-pseudocumene scintillator in Figure 7.11. Only 27% of the detected photons reach the phototubes without being scattered. Approximately 47% of the detected photons are scattered once, 19% are scattered twice, and 7% are scattered more than twice. Absorption-reemission by the PPO and bis-MSB causes 88% of the scattering. Bis-MSB is responsible for 90% of the absorption-reemission scattering, and PPO causes the other 10%. Elastic scattering in the scintillator accounts for 11% of the total scattering, and elastic scattering in the water provides approximately 1% of the total scattering. Reflections from the phototube glass produce a signal with a magnitude

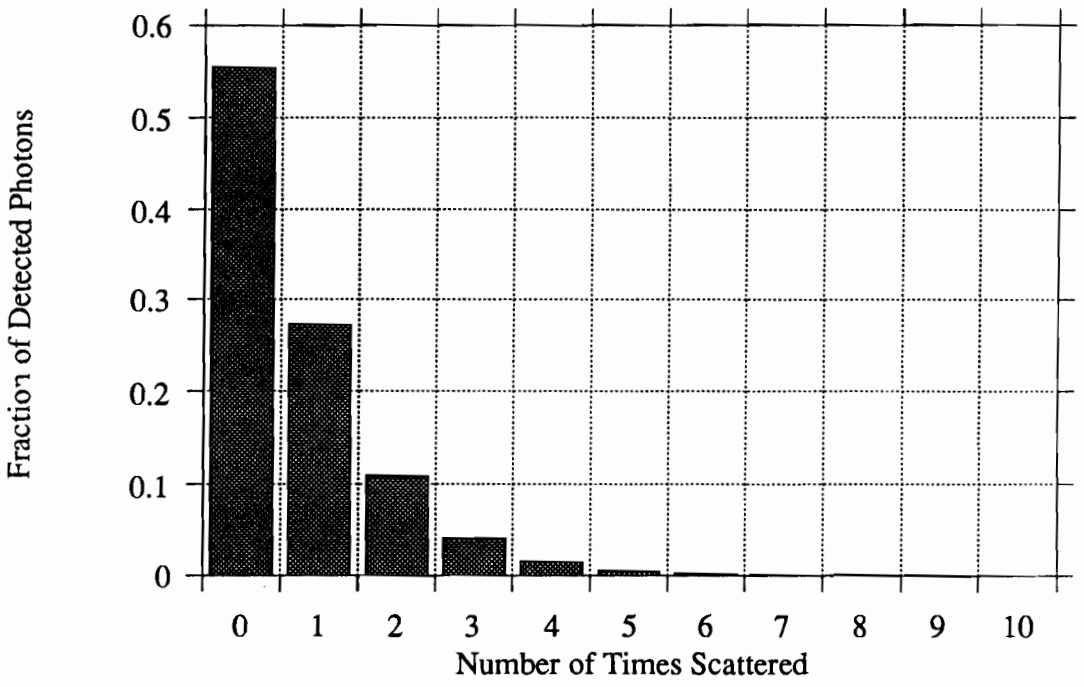

Figure 7.10. Scattering of detected photons in 1.5 g/L PPO-pseudocumene. The figure displays simulated results for the fraction of detected photons which were scattered the number of times indicated. The simulation modeled an omni-directional source at the center of the CTF scintillator containment vessel. The bulk scintillator was 1.5 g/L of PPO in pseudocumene and the initial emission was from the same mixture.

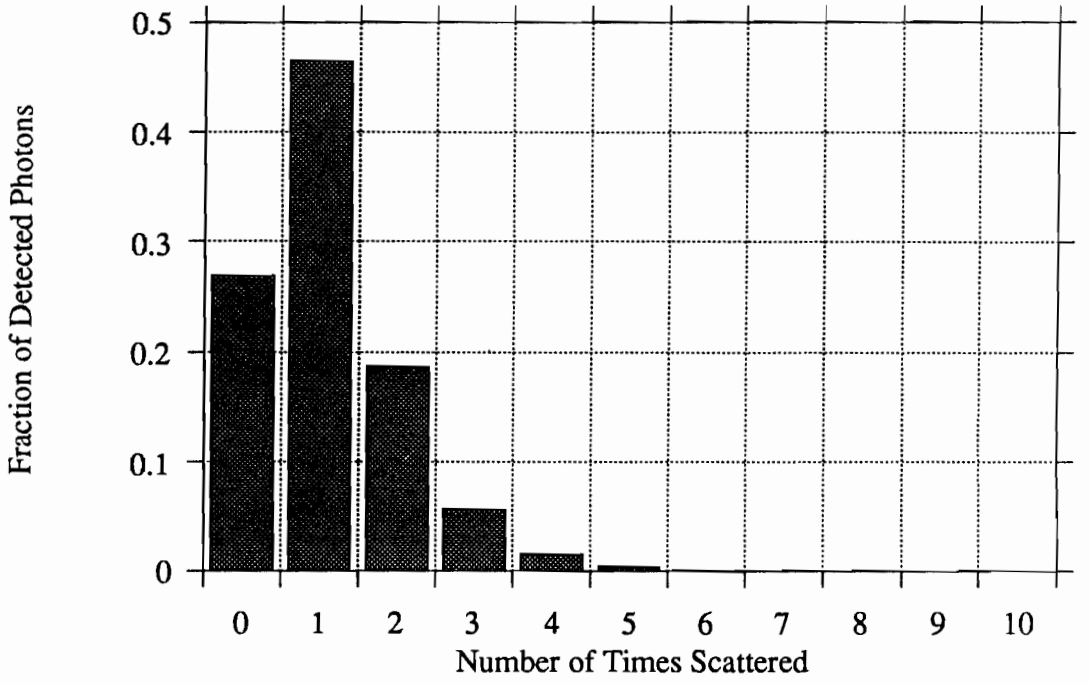

Figure 7.11. Scattering of detected photons in 20 mg/L bis-MSB-1.33 g/L PPO-pseudocumene. The figure displays simulated results for the fraction of detected photons which were scattered the number of times indicated. The simulation modeled an omni-directional source at the center of the CTF scintillator containment vessel. The bulk scintillator was 20 mg/L of bis-MSB and 1.33 g/L of PPO in pseudocumene and the initial emission was from the same mixture.

of 2% of the total scattered detected light. The relative importance of Rayleigh scattering in the shielding water and in the scintillator and reflections off the phototube glass has decreased further in this scintillator because of the increased amount of absorption-reemission.

The simulation can also be used to learn important information about the length scale on which scattering occurs. This length scale has important consequences regarding the effect of scattering on detector performance. The predicted positional resolution of the CTF is approximately 10 cm in the absence of scattering, and similar resolution is predicted in Borexino. Scattering changes the flight paths of photons in the detectors, and the arrival times of scattered photons indicate that they traveled farther in the scintillator than their position of origin would require. If this additional time is significant, it can degrade the ability of positional reconstruction codes to locate the event. Short scattering distances, especially those within the 10 cm resolution of the detector, will not have a major effect on the detector's performance. Scattering on a longer scale could hinder the capability to reconstruct events and define a fiducial volume.

Simulated results for the fraction of photons scattered as a function of radius in the CTF are shown in Figures 7.12 to 7.14. Only photons which are detected by the phototubes are included in these results. The fraction of the total scattering which occurs in each spherical shell of 1 cm thickness from the center of the scintillator containment vessel to the vessel itself is shown in the figures. Figure 7.12 shows the location of scattering in a pure pseudocumene scintillator. The fraction of light scattered as a function of radius is almost constant. All the scattering is elastic in this scintillator. The spectral distribution of the light does not change, and scattering is equally likely at each radial position. The scattering in this scintillator takes place at relatively long distances, but the overall amount of scattering is low.

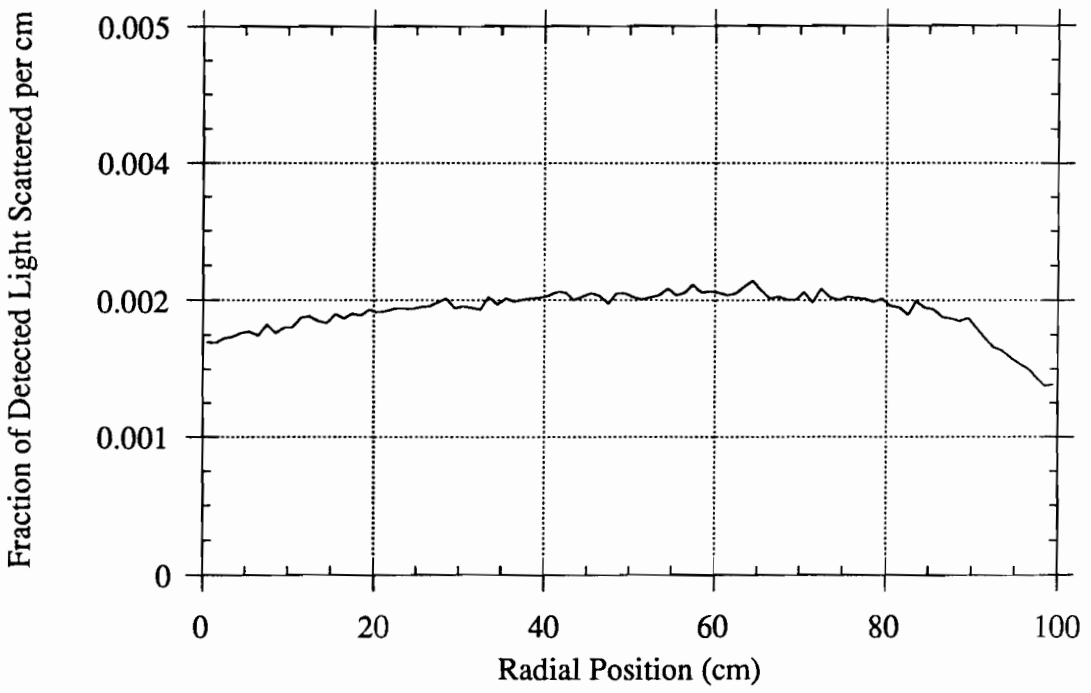

Figure 7.12. Location of scattering in pure pseudocumene. Simulated data are presented in the figure to show the fraction of the detected light which is scattered in each 1 cm thick shell of the CTF. The simulation modeled an omni-directional source at the center of the CTF scintillator containment vessel. The bulk scintillator was pure pseudocumene and the initial emission was from 1.5 g/L of PPO in pseudocumene.

Figure 7.13 shows the location of scattering in the PPO-pseudocumene scintillator. Two additional curves show the location of the absorption-reemission and Rayleigh scattering portions of the total scattering. The absorption-reemission component occurs mostly at short distances. The Rayleigh scattering takes place with equal probability at all distances, as does the scattering in pseudocumene shown in Figure 7.12. In the PPO-pseudocumene scintillator, 18% of the scattering takes place within 1 cm, 34% takes place within 5 cm, and 42% occurs within 10 cm.

The fact that in the PPO-pseudocumene scintillator only 42% of the scattered light is scattered within 10 cm of the origin of the event might cause some concern about the effect of scattering on positional reconstruction. Experimental results from the CTF with the PPO-pseudocumene scintillator have shown that the positional resolution of the CTF is approximately 10 – 15 cm. This indicates that the scattered light does not significantly degrade the resolution. The 56% of the detected light which is not scattered and the 18% which is scattered within 10 cm (74% total) provides enough of a signal from the proper origin that positional resolution is maintained. The slight decrease in the resolution of the detector from the 10 – 12 cm predicted by simulations not accounting for scattering to the 10 – 15 cm observed experimentally is a sign that the detector is operating near the boundary of acceptable performance, and any increase in the average scattering distance could degrade this performance .

The location of scattering in the bis-MSB-PPO-pseudocumene scintillator is shown in Figure 7.14. The majority of the scattering in this mixture takes place at short distances. Slightly more than 50% of the scattering takes place within 1 cm, 68% takes place within 5 cm, and 75% occurs within 10 cm. Because 27% of the detected light is unscattered and 55% of it is scattered within 10 cm (82% total vs. 74% for the PPO-pseudocumene scintillator) this scintillator should provide slightly better positional resolution than the PPO-pseudocumene scintillator.

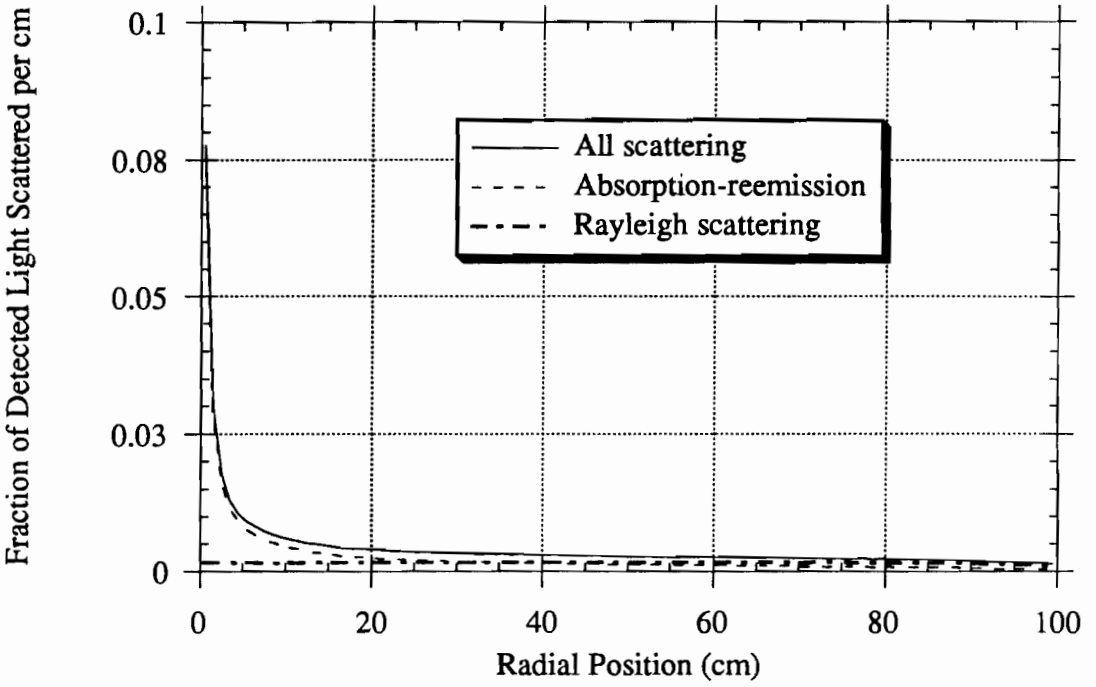

Figure 7.13. Location of scattering in 1.5 g/L PPO-pseudocumene. Simulated data are presented in the figure to show the fraction of the detected light which is scattered in each 1 cm thick shell of the CTF. The simulation modeled an omni-directional source at the center of the CTF scintillator containment vessel. The bulk scintillator was 1.5 g/L of PPO in pseudocumene and the initial emission was from the same mixture.

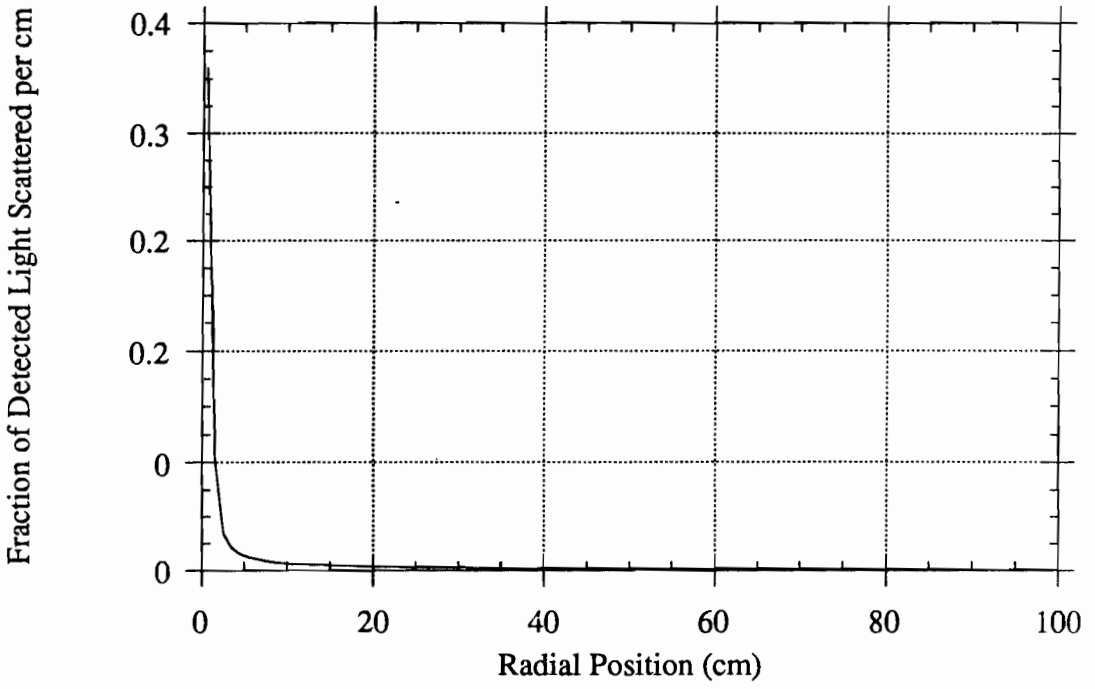

Figure 7.14. Location of scattering in 20 mg/L bis-MSB-1.33 g/L PPO-pseudocumene. Simulated data are presented in the figure to show the fraction of the detected light which is scattered in each 1 cm thick shell of the CTF. The simulation modeled an omni-directional source at the center of the CTF scintillator containment vessel. The bulk scintillator was 20 mg/L of bis-MSB and 1.33 g/L of PPO in pseudocumene and the initial emission was from the same mixture.

The Monte Carlo studies described above are useful for the information they provide about the light propagation process. Because of elastic scattering in the scintillator solvent, there is a certain amount of scattering inherent in any liquid scintillator. The addition of a fluor to obtain the light output necessary for a useful detector increases the amount of scattering. For the mixtures considered here, few detected photons are scattered more than twice and almost none are scattered more than three times. Addition of a wavelength shifter such as bis-MSB increases the amount of scattering in the detector, but helps to limit the scattering to locations closer to the origin of the event. These simulations indicate that a small improvement in positional resolution can be gained through the addition of bis-MSB to a PPO-pseudocumene scintillator.

D. Conclusions

The Monte Carlo simulations discussed in this chapter conclude the study of light propagation in a large-scale liquid scintillation detector in this thesis. The simulation was able to accurately reproduce the experimental results of light scattering in the CTF for three scintillator mixtures: pure pseudocumene, PPO-pseudocumene, and bis-MSB-PPO-pseudocumene. A combination of scattering information provided by the simulation and the experimentally determined positional resolution showed that positional resolution is 10 – 15 cm if 74% of the detected light is unscattered or scattered within 10 cm of its origin as for the PPO-pseudocumene scintillator. Simulation results also indicated that addition of bis-MSB to this scintillator may slightly improve positional resolution because more scattering would occur within 10 cm of the event.

The ability of the Monte Carlo to successfully model light propagation in the CTF has a larger significance in addition to providing a means for studying the performance of the CTF. The modeling of absorption-reemission and elastic scattering

used here can be extended to any scintillator mixture in any geometry. This thesis has compared the simulated light scattering results to the experimental results of Chapter 6 for the CTF in order to show that Monte Carlo methods are suitable for scaling light propagation parameters measured on a small scale as in Chapter 5 to large scintillation detectors. For the Borexino collaboration, this means that simulations including the correct light scattering mechanisms and accurate parameters from small-scale measurements can be used to predict the performance of the large detector with confidence. More generally, this thesis has demonstrated the need to consider absorption-reemission and Rayleigh scattering in predicting the performance of any large scintillation detector. Monte Carlo simulation provides a means of applying small-scale measurements which can be made relatively cheaply to the large detectors to alleviate the need for constructing expensive apparatus of the size of the detectors themselves to study light propagation in them.

References

1. Borexino Collaboration. "A Large Scale Low Background Liquid Scintillation Detector: The Counting Test Facility at Gran Sasso", *Nucl. Inst. and Meth. A* , in press.

2. Manno, I.; Ranucci, G. "Simulation of Absorption-Reemission Processes in C.T.F.", University of Milan: Milan, 1996.

3. Elisei, F.; Masetti, F.; Mazzucato, U., University of Perugia, private communication.